

Transverse Noise, Decoherence, and Landau Damping in High-Energy Hadron Colliders

Présentée le 21 mai 2021

Faculté des sciences de base
Laboratoire de physique des hautes énergies OS
Programme doctoral en physique

pour l'obtention du grade de Docteur ès Sciences

par

Sondre Vik FURUSETH

Acceptée sur proposition du jury

Prof. F. Mila, président du jury
Prof. O. Schneider, Dr X. Buffat, directeurs de thèse
Dr E. Chapochnikova, rapporteuse
Prof. A. Bazzani, rapporteur
Prof. M. Seidel, rapporteur

Things take time.

Acknowledgements

I wish to express my sincere gratitude to the many people without whom this thesis and the past three years would not have been the same, both for their impact on my academic life and my personal life. In particular, I would like to thank:

- Xavier Buffat, my supervisor and mentor at CERN, for never letting me be satisfied with a simple solution when he believed I could achieve a more general one. His friendly personality combined with his scientific resourcefulness were two of the main reasons why I chose this project for my thesis in the first place, and he has not disappointed me. He gave me enough freedom to shape the research as I wanted, while simultaneously helping me see what was and what was not worth my time. I will truly miss our discussions at the whiteboard, where we at times could even point at the location where an equation or graph had used to be, because we both remembered it.
- Leonid “Lenny” Rivkin, my initial thesis director at EPFL, for his positive and constructive attitude and for accepting me as his last doctoral student before his official retirement. Discussions with him helped me understand fundamental accelerator concepts. His lab also aided me financially, both to go to an international school on accelerator physics and a memorable workshop in Zermatt.
- Olivier Schneider, my final thesis director at EPFL, for taking me on after the retirement of Lenny. He has helped me focus on the requirements and possibilities towards the end of my Ph.D.
- Benoît Salvant, my colleague at CERN, for either intentionally or not taking on the role as my bonus mentor halfway through my Ph.D. He has helped me understand my audiences in various committees at CERN, to neither be interpreted as condescending nor too complex, and how to move in our scientific community.
- Elias Métral, my section leader at CERN, for always creating a positively charged work atmosphere, even in the challenging times of 2020. He has also been supportive of my ideas and results, and guided me in the world of accelerators.
- Gianluigi Arduini, my group leader at CERN, for his comments on and interest in my work. He has helped me advocate the importance of loss of Landau damping due to diffusion, as is studied in this thesis, and put this mechanism on the agenda all the way up to the LHC machine committee.
- Nicolas Mounet, an LHC impedance expert, for never believing my intuition, but always pushing me to write it down mathematically. His approach to science is different from mine, and his comments have pushed me to heights I would not have sought out myself. I hope to have taken a step in his direction since my arrival at CERN. He has also been essential to my understanding of the impact of the impedance on the beams.

Acknowledgements

- Daniel Valuch, *the* expert on the LHC transverse feedback system, for teaching me the details of how it works, from the beam position measurements, through the analog and digital filtering, to the response of the feedback kicker. He has also been an essential support in performing experiments in the LHC where the feedback system was used either to stabilize or excite the beams.
- Kevin Li, an expert on simulating transverse feedback systems, for sharing his wisdom and advice in simulating the transverse multi-bunch feedback system in the LHC.
- Rogelio Tomás, an optics expert at CERN, for his keen eye and interest in several of my projects. He has especially been helpful in suggesting small modifications that has made my research more relevant for the operation of the LHC and design of the HL-LHC.
- Sofia Kostoglou, a fellow doctoral student at CERN, for patiently sharing with me her knowledge of the noise sources in the LHC.
- Valeri Lebedev, a Fermilab scientist who visited us at CERN, for showing interest in my work and even contributing scientifically to the study on loss of Landau damping driven by diffusion.
- Juan Sebastián Pereira-Cubillo, a summer student I had the pleasure of supervising, for aiding me in the implementation of a non-white noise source in the multi-particle tracking code COMBI.
- The high-performance-computing teams at CERN and EPFL, for teaching me, enabling me, and allowing me to run heavy parallel simulations at their clusters. Nils Høimyr at CERN and Vincent Keller at EPFL deserves mention in particular.
- Andrea Høeg, my rock and best friend throughout the last decade, for always believing that I could surpass any scientific challenge, while simultaneously keeping me grounded when necessary, and also for showing me the joys of life outside of work.
- All my fellow students and young fellows at CERN, including most of the OMC team in particular, with whom I have been able to discuss my work, as well as less academic topics, in a relaxed setting.
- My family, for supporting me and listening to me explain what I do, even if they do not understand the what, the how, or the why. Thank you.

I would also like to thank “Jansons legat”, “Generaldirektør Rolf Østbyes stipendfond ved NTNU”, and the “IPAC’19 student grant” for their financial support, granting me the possibility to perform my research and share my results at international conferences.

Finally, I would like to thank both CERN and EPFL for allowing me to dive deep into the topic of long-term beam quality and stability, before I now resurface with this thesis.

Meyrin, October 21, 2020

S. V. E.

Résumé

Les collisionneurs de hadrons de haute énergie sont conçus pour générer des collisions entre particules au sein de détecteurs spécialisés. Des faisceaux de haute qualité sont nécessaires pour obtenir un grand nombre de collision. Ils sont caractérisés par une haute intensité et une faible émittance, c'est à dire par un grand nombre de particules dans une faible section transverse. Cette thèse traite de l'impact du bruit sur la qualité des faisceaux en terme de génération d'instabilités collectives ainsi que de grossissement de l'émittance. Les mécanismes de dégradation du faisceau sont décrits par le biais de nouveaux développements analytiques, de simulations numériques par traçages, de solutions numériques d'équations aux dérivées partielles ainsi que par des expériences sur le Grand Collisionneur de Hadron (LHC) du CERN.

L'impact du bruit ne peut pas être décrit proprement dans le cadre d'une perturbation de l'équation Vlasov au premier ordre, qui est communément utilisée pour l'étude des instabilités collectives. L'équation de Vlasov linéarisée est donc étendue au deuxième ordre, se traduisant par un mécanisme de diffusion causé par l'action du bruit, de la décohérence qui en résulte ainsi que de l'action des champs de sillage électromagnétiques. Cette diffusion aplati progressivement et localement la distribution de particules, résultant en une perte de l'effet Landau avec un temps de latence. Une formule analytique pour le temps de latence ainsi qu'un algorithme numérique pour la diffusion sont obtenus, donnant des prédictions en accord avec les résultats des expériences conduites sur le LHC. Cet effet peut être maîtriser en opérant la machine avec suffisamment de marge de stabilité, c'est à dire avec un étalement des fréquences plus élevé que prédit par la théorie linéaire du premier ordre pour un faisceau Gaussien. Ce résultat explique donc la raison pour laquelle le LHC a dû être opéré avec une marge de stabilité d'environ un facteur 2, déterminée empiriquement jusqu'à lors. De meilleures paramètres opérationnels réduisant le besoin en étalement des fréquences sont ainsi proposés. La théorie permet aussi d'effectuer des extrapolations pour les projets futurs, tel que le LHC Haute-Luminosité (HL-LHC), ainsi que d'estimer l'impact de composants novateurs tel que les cavités crabes.

Les sources de bruit externes ainsi que le bruit provenant du système de rétroaction transverse provoque un grossissement de l'émittance du faisceau de par la décohérence qui en résulte. La théorie existante permettant d'estimer la suppression du grossissement de l'émittance par un système de rétroaction considérant les paquets individuellement est étendue pour décrire l'impact d'un système de rétroaction traitant le signal de plusieurs paquets. L'étude numérique de cet effet est réalisée au moyen d'un nouvel algorithme parallélisé incluant deux faisceaux composés de multiple paquets. Pour un cas typique où les sources de bruit externe sont de basse fréquence et le bruit du système de rétroaction est non-négligeable, le système

Résumé

de rétroaction multi-paquets s'avère plus performante que le traitement paquet-par-paquet, car il permet de réduire le bruit généré par le système de rétroaction tout en conservant son efficacité contre le bruit externe. Une optimisation du gain et de la bande passante du système de rétroaction multi-paquet est proposée pour l'opération du LHC.

Mots clés : Accélérateur de particules, Collisionneur, LHC, Bruit, Décohérence, Diffusion, Système de rétroaction, Grossissement de l'émittance, Qualité du faisceau, Stabilité du faisceau, Amortissement Landau, Diagramme de stabilité, Champ de sillage électromagnétique, Interaction faisceau-faisceau, Simulation multi-particules.

Abstract

High-energy hadron colliders are designed to generate particle collisions within specialized detectors. A higher number of collisions is achieved with high-quality beams of low transverse emittances, meaning a small transverse cross-section, and high intensity, meaning many particles per bunch. This thesis studies how noise negatively impacts the beam quality in high-energy hadron colliders, both in terms of beam instabilities and emittance growth. The impact is analyzed through the derivation of new theories, multi-particle tracking simulations, the numerical solving of partial differential equations, and dedicated experiments in CERN's Large Hadron Collider (LHC).

The impact of noise on beam stability cannot be treated with the first-order, linear Vlasov equation, which is commonly used to study the thresholds of collective instabilities. Therefore, the Vlasov equation has in this thesis been expanded to second order in the perturbation of the beam distribution, finding a diffusion mechanism driven by the interplay between noise, decoherence, and wakefields. The diffusion leads to a local flattening of the distribution, which can cause a loss of Landau damping after a time delay referred to as the latency. An analytical formula for the latency and a specialized numerical diffusion solver were successfully benchmarked against the latency measurements in a dedicated experiment conducted in the LHC. Precaution in the machine operation has to be taken to account for this new mechanism. In particular, it is found that the machine must be operated with a margin to the linear stability threshold. For the case of the LHC, it has previously been found empirically that the octupole current during operation must be increased by about a factor 2, and this thesis provides the explanation as to why that is. Alternative operational settings are suggested to reduce the required octupole current in the LHC. In addition, the new theory allows for extrapolations to future machines, such as the High-Luminosity LHC, as well as the estimation of the impact of new devices, such as crab cavities.

External noise and noise from the transverse beam feedback system cause an emittance growth rate due to decoherence of the noise kicks. Analytical theories for the suppression of the emittance growth rate with a bunch-by-bunch feedback have here been extended to a multi-bunch feedback. The numerical study of suppression during collision was conducted by means of a newly developed parallel multi-beam multi-bunch algorithm. For the typical case of low-frequency external noise and non-negligible feedback noise, a multi-bunch feedback has both analytically and numerically been found superior to a bunch-by-bunch feedback, as it can suppress the impact of the external noise equally well, while simultaneously reducing the noise generated by the feedback itself. Suggestions for a more optimal operation of the LHC are discussed, including a reduction of the upper cutoff frequency of the feedback system.

Abstract

Keywords: Particle accelerator, Collider, LHC, Noise, Decoherence, Diffusion, Feedback system, Emittance growth, Beam quality, Beam stability, Landau damping, Stability diagram, Electromagnetic wakefield, Beam-beam interaction, Multi-particle tracking simulation.

Contents

List of Figures	xi
List of Tables	xiii
List of Acronyms	xv
List of Symbols and Notation	xvii
Introduction	1
I ACCELERATOR PHYSICS	3
1 The Large Hadron Collider	5
1.1 Machine layout	6
1.2 Operational cycle	7
1.3 Filling scheme	8
2 Beam dynamics	9
2.1 Relativistic Lorentz force	9
2.2 Linear optics	9
2.2.1 Phase space coordinates	9
2.2.2 Action-phase coordinates	12
2.3 Nonlinear optics	14
2.3.1 Chromaticity	14
2.3.2 Landau octupoles	15
2.4 Beam quality and luminosity	16
2.5 Collective dynamics	17
2.5.1 Beam-beam interactions	18
2.5.2 Impedance and wakefields	19
2.5.3 Active beam feedback system	20
2.6 Landau damping and the linear Vlasov equation	21
3 Noise excited beam dynamics	23
3.1 Noise	23
3.1.1 External noise	23
3.1.2 Beam position monitor noise	25
3.1.3 Incoherent noise	26

Contents

3.2	Modeling coherent noise	26
3.3	Rigid single-bunch dynamics	28
3.4	Rigid multi-bunch dynamics	30
3.5	Single-bunch decoherence	31
3.5.1	Feedback and incoherent detuning	32
3.5.2	Feedback and beam-beam interactions	32
3.6	Nonlinear Vlasov equation	33
 II SINGLE-BUNCH STABILITY		35
4	Instability latency in the LHC	37
4.1	Discrepancies between linear theory and observations	37
4.2	Latency in physics fills and in simulations	38
4.3	Dedicated latency experiment in the LHC	39
4.3.1	Experimental procedure	40
4.3.2	Results	41
4.3.3	Discussion	43
4.3.4	Summary	44
5	Single-bunch evolution due to noise, decoherence, and feedback	45
5.1	Introduction	45
5.2	Theory	46
5.2.1	Change of action after a single kick	46
5.2.2	Fokker-Planck equation in action	48
5.2.3	Solving the Fokker-Planck equation	50
5.3	Numerical verification	50
5.3.1	Change of action after a single kick	50
5.3.2	Fokker-Planck vs multi-particle simulations	51
5.4	Results	53
5.4.1	Distribution and stability evolution	54
5.4.2	Relative effective detuning strength	56
5.4.3	Parameter dependence	56
5.5	Conclusion	59
6	Single-bunch evolution due to noise, decoherence, and impedance	61
6.1	Introduction	61
6.2	Noise excited wakefields	62
6.2.1	Wakefield eigenmodes – $\omega_{\mathbf{m}}$	62
6.2.2	Damped wakefield eigenmodes – $\Omega_{\mathbf{m}}$	64
6.2.3	Noise excited damped wakefield eigenmodes	66
6.2.4	Wakefield driven diffusion	67
6.2.5	Instability latency	69
6.2.6	Numerical method	73
6.3	Numerical verification	73
6.3.1	Dynamics inside the stability diagram	74
6.3.2	Wakefield driven diffusion	75

6.3.3	Diffusion or resonant motion?	76
6.4	Results	78
6.4.1	Distribution and stability evolution	78
6.4.2	Detuning margin	80
6.4.3	Dedicated latency experiment in the LHC	81
6.4.4	Physics fills in the LHC	83
6.5	Discussion	84
6.6	Conclusion	84
III	MULTI-BUNCH BEAM QUALITY	87
7	COMBIp – Pipeline algorithm for multi-beam multi-bunch simulations	89
7.1	Introduction	89
7.2	Causality caused challenges in simulations	90
7.3	Parallel algorithms	92
7.3.1	COMBI	92
7.3.2	COMBIp	93
7.4	Timing results	96
7.4.1	Strong scaling	96
7.4.2	Weak scaling	98
7.5	Discussion	100
7.6	Conclusion	100
8	Optimal transverse feedback gain and bandwidth for long-term beam quality	101
8.1	Introduction	101
8.2	Theory	102
8.2.1	Active multi-bunch beam feedback system	102
8.2.2	Emittance growth suppression with a multi-bunch feedback	104
8.3	Results	105
8.3.1	Dependence on the feedback, noise, and source of detuning	106
8.3.2	Optimal feedback in the LHC and HL-LHC	108
8.4	Conclusion	111
	Conclusion	113
A	The linearized Vlasov equation and the stability diagram	117
B	The Fokker-Planck equation	121
B.1	Master equation	121
B.2	Liouville theorem	122
C	Change of action after a kick with decoherence and feedback	125
D	PyRADISE – Radial diffusion and stability evolution	129
D.1	Change of independent variable	129
D.2	Finite volume method	130
D.3	Stability evolution	132

Contents

E Harmonically driven distribution evolution	133
Bibliography	137
Curriculum Vitae	145

List of Figures

1.1	Layout of the LHC, with descriptions of the activities in the 8 interaction regions.	6
1.2	Example of the beginning of an LHC fill (fill 2718).	7
1.3	Nominal bunch filling scheme of one beam in the LHC.	8
2.1	Co-rotating, orthogonal synchrotron coordinates (X, Y, Z) , centered at the synchronous reference particle.	10
2.2	Poincaré section of the ellipse traced out in (X, P_x) phase space.	12
2.3	Coherent beam-beam modes with 1 bunch per beam and 1 interaction point.	18
2.4	Interaction region with head-on and long-range beam-beam interactions. Also displaying the intended effect of Crab Cavities.	19
2.5	Illustration of a wakefield interaction.	19
2.6	Tune spreads in (a), of similar size, and corresponding stability diagrams in (b).	22
3.1	Illustrations of different types of noise.	23
3.2	Power Spectral Density of the ground motion in tunnels at CERN (1993).	24
3.3	Maximum acceptance level of output voltage ripple from power converters at CERN.	25
3.4	Power response of a damped harmonic oscillator to a harmonic excitation.	29
3.5	Simulation of low-frequency noise acting on 60 equidistant bunches.	30
3.6	Decoherence of 10 particles starting at $(x, p) = (x_0, 0)$.	31
4.1	Evolution of horizontal emittance in a latency experiment in the LHC.	41
4.2	Dependence of the experimental latency and rate of change of the stability threshold on the octupole current.	42
4.3	Dependence of the experimental rate of change of the stability threshold on the chromaticity.	43
5.1	Action dependence of emittance growth suppression with a feedback.	47
5.2	Simulated change of action after a single kick of amplitude k as a function of the particles' initial actions, and comparison to analytical theories.	51
5.3	1D distribution evolution with noise, decoherence, and feedback. Comparison between multi-particle simulations and theory.	53
5.4	2D distribution and stability evolution with noise, decoherence, and feedback (case 1).	54
5.5	2D distribution and stability evolution with noise, decoherence, and feedback (case 2).	55
5.6	Evolution of the relative effective detuning strength in the two test cases.	56

List of Figures

5.7	Evolution of the relative effective detuning strength (parameter scan).	58
5.8	The initial reduction of the relative effective detuning strength (parameter scan).	59
6.1	Relationship between the free and Landau damped frequency shifts of a mode.	64
6.2	Stability diagram and α given by Eq. (6.13).	65
6.3	Largest dipole moments for modes at various sidebands.	67
6.4	Shape of diffusion coefficient in frequency space due to a single Landau stabilized mode.	68
6.5	Simulated tune shift of a coherent mode outside and inside the stability diagram.	74
6.6	Numerical diffusion coefficient in 20 simulations. Comparison to theory.	75
6.7	Emittance evolutions ranging from being better described by a diffusion or by resonant motion.	77
6.8	Distribution and stability evolution due to noise excited wakefields (case 1).	78
6.9	Distribution and stability evolution due to noise excited wakefields (case 2).	79
6.10	Evolution of $\text{Im}\{\Delta Q_{LDx}\}$ in the two test cases.	80
6.11	Dependence of the latency on the detuning margin.	81
6.12	Analytical latency of the two worst horizontal modes in B1 in the LHC.	82
6.13	Comparison between experimental latencies and theory (using PyRADISE).	83
7.1	Illustration of a circular collider model.	90
7.2	Schematic of inter-beam calculations around an IP in a circular collider.	91
7.3	Gantt charts of the flow of calculations for a beam, while still ensuring causality.	95
7.4	Strong scaling with COMBI and COMBIp for different collider models.	98
7.5	Weak scaling with COMBI and COMBIp for different collider models.	99
8.1	Normalized response functions of two types of filters in time and frequency.	103
8.2	Emittance growth rate for 128 neighboring bunches due to LF noise.	106
8.3	Average emittance growth rate due to LF noise or BPM noise.	107
8.4	Average emittance growth rate due to LF noise of various spectrum widths.	107
8.5	Average emittance growth rate due to LF noise and detuning due to either octupole magnets or beam-beam interactions.	107
8.6	Average emittance growth rate in the LHC in collision ($\sigma_{\text{BPM}} = 50\sigma_{\text{ext}}$).	109
8.7	Average emittance growth rate in the LHC in collision ($\sigma_{\text{BPM}} = 25\sigma_{\text{ext}}$).	110
D.1	Illustration of the Finite Volume Method grid in PyRADISE.	130
E.1	Peak-to-peak action variation and period of action oscillation due to a harmonic excitation of particles with action dependent detuning.	136
E.2	Distribution and emittance evolution due to a harmonic excitation.	136

List of Tables

1.1	Machine and beam parameters in the LHC and HL-LHC during proton physics.	5
4.1	Important parameters during a latency experiment conducted in the LHC. . . .	41
7.1	Relative time of different calculations in the scalings.	96
8.1	Numerical parameters used in the simulations.	105
8.2	Minimal emittance growth rate and corresponding optimal gain for a given cutoff frequency, beam-beam parameter, noise ratio, and chromaticity.	111

List of Acronyms

Notation	Description	Page List
1D	One-dimensional	14
2D	Two-dimensional	14
ADT	LHC Transverse Damper	21
B1	Beam 1	7
B2	Beam 2	7
BC	Boundary condition	50
BPM	Beam Position Monitor	25
BSRT	Beam synchrotron radiation telescope	42
CC	Crab Cavity	18
CC-BY	Creative commons license	33
CERN	the European Organization for Nuclear Research	5
COM	Center of mass	20
COMBI	COherent Multi-Bunch Interactions	73
COMBIp	COherent Multi-Bunch Interactions – Pipelined	90
CPU	Central Processing Unit	92
DC	Direct Current	24
DELPHI	Discrete Expansion over Laguerre Polynomials and Headtail modes	38
EOM	Equation of motion	28
EXP	Exponential (filter)	102
Ext. BW	Extended bandwidth	102
FCC-hh	Future circular hadron collider	1
FVM	Finite Volume Method	129
HEP	High-energy physics	1

List of Acronyms

Notation	Description	Page List
HL-LHC	High-Luminosity Large Hadron Collider	1
HPC	High-performance computing	2
IBS	Intra-beam scattering	26
IP	Interaction Point	7
IR	Interaction Region	6
LBW	Low-bandwidth	102
LF	Low-frequency	31
LHC	Large Hadron Collider	1
LHS	Left-hand side	9
MPI	Message Passing Interface	92
OpenMP	Open Multi-Processing	92
OTM	One-turn-map	12
PC	Power Converter	23
PDE	Partial differential equation	49
PSD	Power Spectral Density	24
PyRADISE	Python RAdial Diffusion and Stability Evolution	46
PySSD	Python Solver for Stability Diagram	46
RF	Radio-Frequency	6
RHS	Right-hand side	9
rms	Root mean square	16
SppC	Super proton-proton Collider	1
SR	Synchrotron radiation	26
STD	Standard deviation	11
USHO	Under-damped stochastic harmonic oscillator	76

List of Symbols and Notation

The main use of symbols and notation is summarized here. Additional notation is introduced and explained locally throughout the thesis.

Mathematical notation:

$A \bmod B$	Modulo, i.e. $A \bmod 1 \in [0, 1)$ is the fractional part of A .
$\bar{\square}$	Complex conjugate of \square .
$ \square $	Absolute value of \square .
$\text{Re}\{\square\}$	Real part of \square .
$\text{Im}\{\square\}$	Imaginary part of \square .
$\dot{\square}$	Time derivative of \square .
\square'	Derivative of \square with respect to a coordinate.
$\partial_A B$	Derivative of B with respect to A .
$\langle A \rangle_B$	Expectation or average value of A from the possible values of the coordinate B or over the distribution B .
$E[A(t)]$	Expectation value of A in time after multiple stochastic kicks.
$P \int \dots$	The P denotes the principal value of the integral.
$[\square]_A^B = \square(B) - \square(A)$	The value of \square is added at B and subtracted at A .
$\mathcal{F}(\square)$	The Fourier transform of \square .
\mathcal{H}	The Hamiltonian.
\mathbf{R}	Transfer map. Examples in this thesis are matrices.
\mathbf{A}	Vector in relevant coordinates, i.e. $\mathbf{A} = (A_x, A_y, A_z)$.
$R(\Omega)$	Beam response due to excitation at frequency Ω .
\equiv	Equivalence. Often used to define a new parameter.
$[A, B]$	Poisson brackets.
$\min(\square), \max(\square)$	Minimum (maximum) value of \square .
$\min\{A, B\}, \max\{A, B\}$	Minimum (maximum) value of the discrete list $\{A, B\}$.
$\mathcal{N}(A, B)$	Normal distribution of mean A and variance B .
$f(A; B)$	Function evaluated at A given B .
$\delta_D(\square)$	Dirac delta function (distribution). Equal to zero except for when $\square = 0$. The area under the function is 1.
$\mathcal{O}(\epsilon^n)$	Potentially several terms that are proportional to the n -th or higher power of ϵ , which is assumed small.

Sub- and superscripts:

\square_{rel}	Relativistic quantity.
\square_{par}	Quantity related to a parallel simulation.

List of Symbols and Notation

\square_{rev}	Quantity related to the revolution around the synchrotron.
\square_r	Quantity at a resonance, i.e. at a specific frequency.
\square_h	Harmonic quantity, related to a sinusoidal excitation.
\square_x	Quantity in the horizontal transverse plane.
\square_y	Quantity in the vertical transverse plane.
\square_j	Quantity in either transverse plane, $j \in \{x, y\}$.
$\square_{z,s}$	Quantity in the longitudinal plane.
$\square_{\text{thr,thresh}}$	Quantity related to a stability threshold.
\square_I	Quantity related to intra-beam scattering.
\square_{coh}	Coherent quantity, typically related to a coherent mode.
\square_m	Quantity related to mode number m .
\square_b	Quantity related to bunch number b .
\square_{LD}	Quantity of a Landau damped mode.
\square_{SD}	Quantity related to the stability limit (stability diagram).
$\tilde{\square}$	A quantity that is closely related to \square . Depends on \square : e.g. $\tilde{a} = \omega_{\text{rev}} a$, $\tilde{Q} = \text{Re}\{Q\}$, $\tilde{\Delta}Q = Q - \langle Q \rangle_{\Psi}$, $\tilde{f} = f(t + \tau)$.

Coordinates:

s	[m]	Longitudinal position along the synchrotron beamline.
t	[s]	Time in units of seconds.
T	[turn]	Time in units of turns. This unit is often omitted.
(X, Y, Z)	[m]	Real co-rotating coordinates.
$(\tilde{p}_x, \tilde{p}_y, \tilde{p}_s)$	[Ns]	Real momenta.
(P_x, P_y, P_s)	[1]	Momenta normalized to the momentum of the synchronous particle.
(x, y, z)		Normalized (in transverse planes) co-rotating coordinates.
(p_x, p_y, δ)		Normalized (in transverse planes) co-rotating momenta, subtracted the momentum of the synchronous particle.
ρ		Complex position in normalized transverse phase space, $\rho_x = x + i p_x$.
δ	[1]	Relative momentum/energy offset from the synchronous particle.
I	[m]	Physical action. Also the modified Bessel function of the first kind.
J	[1]	Normalized action, $J = I/\varepsilon_0$. Also the Bessel function of the first kind.
ϕ	[rad]	Phase. The canonical conjugate of the action.
r	[1]	Radius in normalized phase space, $r = \sqrt{2J} = \sqrt{x^2 + p^2}$.

Physical quantities:

\mathbf{F}	[N]	Force.
q	[C]	Charge.
m	[kg]	Mass.
$\tilde{\mathbf{p}}$	[Ns]	Physical momenta.
\mathbf{P}	[1]	Momenta normalized to the synchronous particle, $\mathbf{P} = \tilde{\mathbf{p}}/\tilde{p}_0$.
\mathbf{E}	[N/C]	Electric field.

B	[T]	Magnetic flux density.
ρ	[m]	Bending radius.
τ_{rev}	[s]	Revolution period.
f_{rev}	[Hz]	Revolution frequency, $f_{\text{rev}} = 1/\tau_{\text{rev}}$.
f_b	[Hz]	Bunch slot repetition frequency.
f_{cutoff}	[Hz]	Cutoff frequency of a filter.
f_w, f_q	[m]	Focal length of a dipole or quadrupole magnet.
L	[m]	Length of a beamline component.
L	[s]	Latency of an instability.
τ_{noise}	[s]	Time during which a bunch is affected by noise.
c	[m/s]	Speed of light in vacuum.
β_{rel}	[1]	Relativistic beta, $\beta_{\text{rel}} = v/c$.
γ_{rel}	[1]	Relativistic gamma, $\gamma_{\text{rel}} = 1/\sqrt{1 - \beta_{\text{rel}}^2}$.
β	[m]	Optical beta function.
β^*	[m]	Optical beta function at an interaction point.
α	[1]	Optical alpha function, $\alpha = -0.5d\beta/ds$.
γ	[1/m]	Optical gamma function, $\gamma = (1 + \alpha^2)/\beta$.
ϵ	[1]	Epsilon, a small parameter.
ϵ_b	[1]	Bunch marker. 1 if bunch b exists, 0 otherwise.
ϵ	[m]	Geometrical emittance.
ϵ_n	[m]	Normalized emittance, $\epsilon_n = \epsilon\gamma_{\text{rel}}\beta_{\text{rel}}$.
N	[1]	Intensity, the number of particles per bunch.
N_p	[1]	The number of macroparticles per bunch in a multi-particle tracking simulation.
N_b	[1]	The number of bunches per beam.
Ψ		Bunch distribution function.
$\varphi(\Delta)$		Probability distribution function of the change Δ .
\mathcal{L}	[1/m ² s]	Luminosity.
I_{oct}	[A]	Current in Landau octupoles.
a_j	[1]	In-plane normalized detuning coefficient in the subscripted transverse plane, i.e. $Q_x \propto a_x J_x$.
b_j	[1]	Cross-plane normalized detuning coefficient in the subscripted transverse plane, i.e. $Q_x \propto b_x J_y$.
ξ_{BB}	[1]	Beam-beam parameter.
θ_{xing}	[rad]	Crossing angle between beams at an interaction point.
s_0	[1]	Factor related to the absorption of noise energy in coherent beam-beam modes.
r_p	[m]	Classical proton radius.
\mathcal{E}	[J]	Energy.
W	[J/C ²]	Wake function.
W_J	[1]	Width of a narrow function in normalized action space.
g	[1]	Single-bunch feedback gain.
τ_g	[turn]	Damping time due to a single-bunch feedback, $\tau_g = 2/g$.
$w_{bb'}$	[1]	Peak-normalized feedback response on bunch b based on coordinates of bunch b' .

List of Symbols and Notation

g_m	[1]	Effective multi-bunch gain on multi-bunch mode m .
$k = \Delta p$	[1]	Normalized kick, i.e. a change of the normalized momentum.
$\xi(t)$	[1]	Noise signal, consisting of normalized kicks.
$\Xi_i(z)$	[1]	Orthonormal functions used to decompose the noise signal.
U	[Hz]	Drift coefficient. Can be given in change per turn.
D	[Hz]	Diffusion coefficient. Can be given in change per turn.
S_\square		Power Spectral Density of the signal \square .
m_m	[1]	Normalized eigenfunction of headtail mode m .
χ_m	[1]	Amplitude of headtail mode m .
l_m	[1]	Angular mode number of headtail mode m .
P_m	[1]	Effective impulse from headtail mode m .
η_{mi}	[1]	Moment of headtail mode m with noise function Ξ_i .
ω	[rad/s]	Angular frequency.
μ_j	[rad]	Betatron phase advance, here assumed per turn.
Q_j	[1]	Number of betatron rotations per turn, $2\pi Q_j = \mu_j = \omega_j / f_{\text{rev}}$.
Q_s	[1]	Number of synchrotron rotations per turn.
Q' or ω'	[1]	Linear chromaticity. How much the betatron rotation frequency or tune depends on the relative momentum offset, i.e. $Q \propto Q'\delta$.
ΔQ	[1]	Tune shift from the bare machine tune.
$\tilde{\Delta}Q$	[1]	Tune shift from the average tune of the bunch, i.e. $\tilde{\Delta}Q = Q - \langle Q \rangle_\Psi$.
ΔQ_{coh}	[1]	Coherent tune shift of a mode without tune spread.
ΔQ_{LD}	[1]	Coherent tune shift of a mode when including the impact of Landau damping due to a tune spread.
ΔQ_{SD}	[1]	Stability diagram, marking the limit of which ΔQ_{coh} can be stabilized with a given tune spread.
ΔQ_R	[1]	Tune shift with a vanishing positive imaginary part, used to calculate ΔQ_{SD} .
γ_\square	[Hz]	Growth rate of a mode, i.e. $\gamma_\square = \text{Im}\{\omega_\square\}$.

RMS values:

σ_I	Intra-beam scattering noise.
σ_{ext}	External noise.
σ_{BPM}	BPM error (how wrong the momenta are measured/predicted).
σ_k	Total dipolar noise in a machine. If the external noise is dipolar, $\sigma_k^2 = \sigma_{\text{ext}}^2 + g^2 \sigma_{\text{BPM}}^2$.
$\sigma_{x,y,s}$	Bunch size in the subscripted plane.
σ_δ	Relative momentum/energy offset from the synchronous particle.

PyRADISE discretization:

$C_{i,j}$	Finite volume cell in 2D, with number i in the horizontal plane and j in the vertical plane.
$c_{i,j}$	Center of cell $C_{i,j}$.
$e_{i,j}$	Midpoint of eastern edge of cell $C_{i,j}$.
$w_{i,j}$	Midpoint of western edge of cell $C_{i,j}$.
$n_{i,j}$	Midpoint of northern edge of cell $C_{i,j}$.
$s_{i,j}$	Midpoint of southern edge of cell $C_{i,j}$.

Introduction

High-energy hadron colliders are today one of the main tools used to gain a deeper understanding of fundamental particles and the interactions between them. The high-energy physics (HEP) community needs high-quality beams for their experiments to reach the number of collisions required to detect rare events. In modern high-energy hadron colliders, such as the Large Hadron Collider (LHC), two beams are stored in separate rings, which mainly consist of a multitude of superconducting magnets, and are brought into collision only within specialized detectors. The beams are subject to many deteriorating mechanisms that reduce the beam quality. External sources of noise are especially problematic if the noise contains frequency components at similar or higher frequencies compared to the beam revolution frequency. Furthermore, a beam acts on itself through wakefields, electron clouds, and space charge forces, and the other beam through beam-beam interactions. Uncorrelated noise kicks can lead to emittance growth through decoherence, while correlated or self-amplified kicks can drive the beams unstable. This thesis studies how different sources of noise negatively impact the beam quality in high-energy hadron colliders, both in terms of beam instabilities and emittance growth, and how this impact is affected by other mechanisms.

Beam stability is of utmost importance for the safe operation of high-energy hadron colliders, as instabilities can cause a significant reduction of the beam quality, induce a dump of the entire beam, or even potentially damage the collider. Some stabilization is commonly achieved with Landau damping, stabilizing coherent oscillations due to a spread in the single-particle oscillation frequencies. Therefore, Landau damping has been studied extensively and successfully in the past, often in terms of the linear Vlasov equation. Yet, there have been observations of beam instabilities developing in the LHC after prolonged stays in configurations that were predicted to be stable by such linear theories. Consequently, the LHC has been operated with an additional unexplained safety margin of approximately a factor two times the frequency spread predicted to prevent instabilities. That has been acceptable in the LHC, since the installed octupole magnets, generating the frequency spread, are sufficiently strong to cope with the additional requirements. However, a proper understanding of the underlying mechanism behind this loss of Landau damping is crucial to know how to mitigate it and achieve the desired performance also in future colliders, such as the High-Luminosity Large Hadron Collider (HL-LHC), the future circular hadron collider (FCC-hh), and the Super proton-proton Collider (SppC). Partly because Landau damping is sensitive to small variations from the commonly assumed Gaussian transverse bunch distribution, and partly due to the existence of a nonzero latency, the hypothesis investigated in this thesis is that the loss of Landau damping is caused by a noise driven evolution of said transverse bunch distribution.

A small and steady emittance growth rate can also significantly reduce the long-term beam quality. The emittance growth rate due to noise can be suppressed by active transverse beam feedback systems. Such feedback systems work by measuring the position of each bunch, and then partially kicking the bunches back onto their closed orbit each turn. They can either be operated bunch-by-bunch, or also be dependent on the measurements of the neighboring bunches in a multi-bunch configuration. Since the beam position measurements have a finite precision and accuracy, the transverse feedback system introduces additional noise on the beam. This noise has been identified as a potential performance limitation for future colliders, due to the long-term emittance growth and thereby degradation of the beam quality. This thesis aims at determining how to optimally operate the transverse feedback system, taking into account the technological limitations, to ensure both beam stability and high long-term beam quality.

The main body of this thesis is split into three. In Part I, an introduction to the relevant accelerator physics is presented. An introduction of the LHC is given in Ch. 1. The relevant Hamiltonian beam dynamics, as can be found in the literature, is described in Ch. 2. And finally, the impact of noise on the beam dynamics is introduced in Ch. 3.

In Part II, a study on the loss of Landau damping in single bunches is presented. A set of key experimental observations, which were made in the past, and a dedicated experiment on loss of Landau damping in the LHC are discussed in Ch. 4. A particle diffusion mechanism, caused by the interplay between noise, decoherence, and the feedback system, is derived from a master equation and discussed in Ch. 5. Another diffusion mechanism, caused by the interplay between noise, decoherence, and wakefields, is derived from a nonlinear Vlasov equation and discussed in Ch. 6.

In Part III, a study on the preservation of the full beam quality by the transverse feedback system is presented. Simulating full beams, not just single bunches, requires state-of-the-art parallel algorithms that fully exploit the potential of high-performance computing (HPC). A new parallel algorithm that has been developed is discussed and benchmarked in Ch. 7. The noise driven emittance growth rate is then both derived analytically and simulated in Ch. 8. The optimal bandwidth and gain of the transverse feedback system in the LHC is found numerically.

ACCELERATOR PHYSICS **Part I**

1 The Large Hadron Collider

The hadron collider with the highest collision energy in the world, at the time of writing, is the LHC [1]. Because this research work was conducted in collaboration with the European Organization for Nuclear Research (CERN), the relevant experimental observations were done in the LHC, and the derived analytical and numerical models have been applied to the LHC and to its future upgrade, the HL-LHC. Therefore, for the reader to understand what is to come, some knowledge of this collider is required. A subset of key parameters, which will be explained later, are given in Table 1.1.

Table 1.1: Machine and beam parameters in the LHC and HL-LHC during proton physics, unless otherwise specified [1–5].

Parameter	Unit	LHC		HL-LHC
		(Nominal)	(2018)	(standard)
Number of bunches, N_b	[1]	2808	2556	2760
Injection proton energy	[GeV]	450	450	450
Injection tunes, (Q_x, Q_y)	[mod 1]	(0.28, 0.31)	(0.275, 0.295)	(0.27, 0.295)
Proton energy	[TeV]	7	6.5	7
Relativistic gamma, γ_{rel}	[1]	7461	6928	7461
Fractional tunes, (Q_x, Q_y)	[mod 1]	(0.31, 0.32)	(0.31, 0.32)	(0.31, 0.32)
Synchrotron tune, Q_s	$[10^{-3}]$	1.90	1.91	2.12
Revolution frequency, f_{rev} ¹	[kHz]	11.245	11.2455	11.2455
Total RF voltage	[MV]	16.0	12.0	16.0
RF frequency	[MHz]	400.8	400.8	400.8
Harmonic number	[1]	35640	35640	35640
Bunch spacing	[ns]	25	25	25
Intensity, N	$[10^{11} \text{ p/b}]$	1.15	1.1	2.3
Norm. transverse emittance, ε_n	[μm]	3.75	2	2.5
Bunch length, σ_s	[cm]	7.55	8.0	7.55
rms momentum spread, σ_δ	$[10^{-4}]$	1.129	1.03	1.1
Hor. intra-beam scattering time	[h]	80 to 106	~ 100	21 to 26

¹ Precision update in the revolution frequency since the LHC design report [1].

1.1 Machine layout

The LHC is a 27 km long ring, illustrated from above in Fig. 1.1 [1]. It consists of injection and extraction points for the beams, superconducting magnets that steer and focus the beams, Radio-Frequency (RF) cavities that accelerate the beams, and 8 Interaction Regions (IRs) where various important activities are performed on and between the beams. The magnets are supported by a sophisticated cryogenic system, keeping the magnets at 1.9 K.

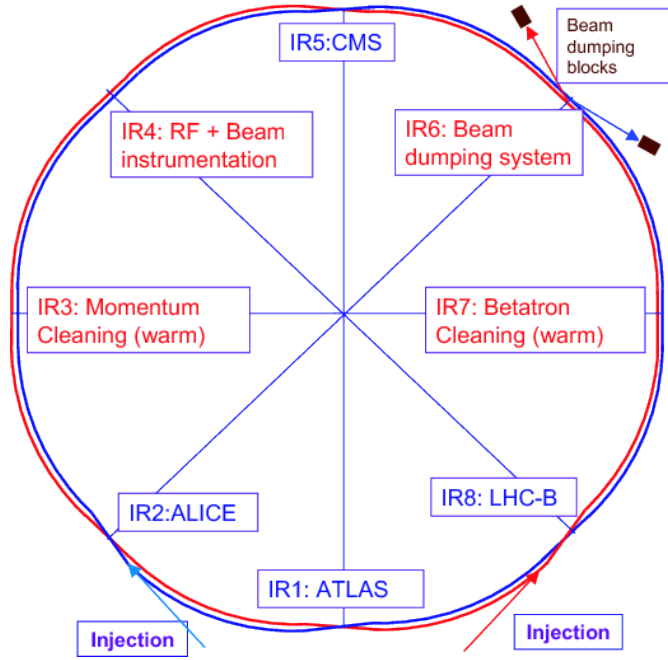


Figure 1.1: Layout of the LHC, with description of the main activity in each of the 8 interaction regions (IRs). Beam 1 (B1) is blue and moves clockwise, while Beam 2 (B2) is red and moves counterclockwise. The experiments are conducted at IR1, IR2, IR5 and IR8, where the beams are crossing. Courtesy of [6].

The beams do not start in the LHC, but are injected from a sequence of pre-accelerators. The structure of the injector chain yields the filling scheme that will be discussed in Sec. 1.3, but is otherwise not of direct relevance to this thesis. At the end of a fill, or if the continued circulation of the beam may endanger the machine safety, the beams are extracted and dumped in specialized dumping blocks.

The main types of magnets, and their uses, are:

- Dipole magnets, used to bend the beam around in a circle.
- Quadrupole magnets, used to focus the beam.
- Sextupole magnets, used to counteract the linear chromaticity (discussed in Sec. 2.3.1).
- Octupole magnets, used to create a transverse amplitude dependent detuning (discussed in Sec. 2.3.2).
- Kicker magnets, used either for injection, feedback, or extraction of the beam. It is essentially a strong dipole magnet, but with a fast rise/fall time of the field strength.

Since the LHC is a collider, it transports two beams in opposite directions, Beam 1 (B1) and Beam 2 (B2), which typically are colored blue and red, respectively. The beams are kept in separate vacuum chambers except for the 4 experiments ATLAS, ALICE, CMS and LHCb. At the Interaction Point (IP) at the center of these experiments, the beams are meant to collide to create events that can be studied by the HEP community. Only a small fraction of the particles collide at each passing. One advantage of a circular collider over a linear collider is that the particles that do not collide, can circle back and possibly collide on the next turns.

1.2 Operational cycle

The steps required to go from an empty LHC to collisions is illustrated in Fig. 1.2. During **injection**, groups of bunches are injected from the pre-accelerators at the injection energy, seen by the gradual increase of the intensity of both beams. Then, the individual particle energy is **ramped** from the injection energy to the steady operational energy. Some actions are then performed during **flat-top**, including the transition from injection to collision tunes, before the transverse cross-section of the beams is **squeezed** in the experiments, illustrated by the reduction of β^* . The LHC is then **adjusted** to get the beams into collision, seen by the increase of the luminosity in the various experiments. When this procedure is finished, the machine enters the phase when **physics** events are registered in the experiments. This phase normally lasts up to ~ 12 h (the record is > 24 h) [8], during which the intensity and luminosity gradually drops, before the beams are extracted and dumped.

There are different operational challenges in the different phases of the cycle. This thesis focuses on beam stability at full energy before collision (flat-top and squeeze) and optimal long-term beam quality during physics, to get the maximum luminosity.

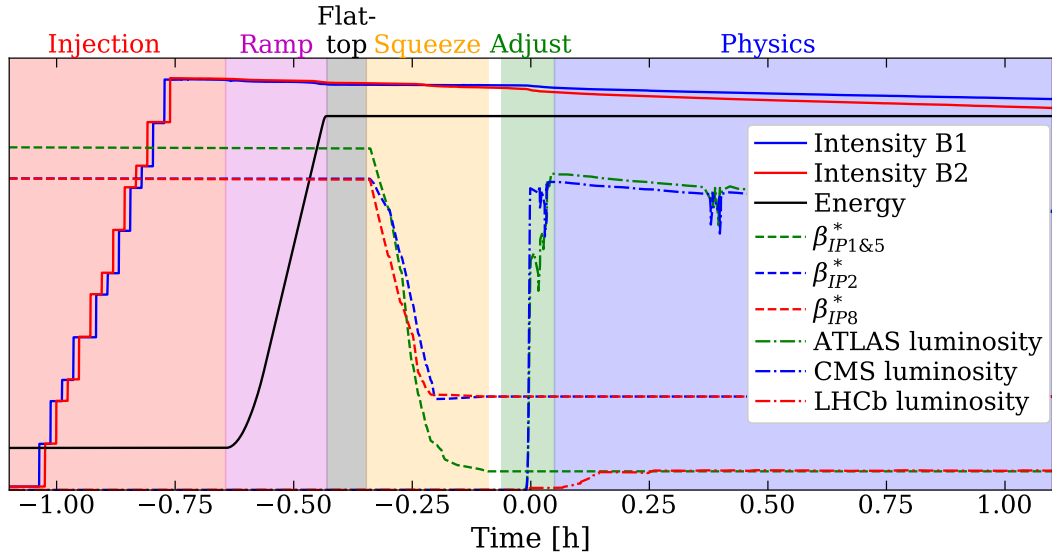


Figure 1.2: Example of the beginning of an LHC fill (fill 2718). The values plotted are the intensities per beam, the energy per proton, the optical transverse β -function at the IPs of the experiments, and the luminosity in three of the experiments. Courtesy of [7].

1.3 Filling scheme

The beams in the LHC are bunched, rather than being continuous streams of hadrons. This is a consequence of accelerating the beams with RF cavities [9]. The RF cavities in the LHC are operated at a frequency of 400.8 MHz, creating 35640 RF buckets spaced by 2.5 ns. At most every tenth bucket will in operation contain a bunch. In other words, the bunch slots are spaced by 25 ns. Furthermore, not every bunch slot is filled in the LHC, some are kept empty to allow for extraction and injection in the different rings using kicker magnets with rise and fall times exceeding 25 ns. In the nominal filling scheme, 2808 bunch slots contain bunches, organized as in Fig. 1.3. Alternative filling schemes exist. The number of interactions between the bunches in the experiments depends on the filling scheme.

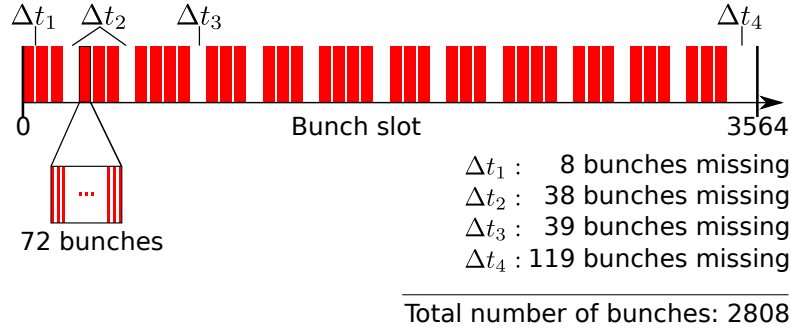


Figure 1.3: Nominal bunch filling scheme of one beam in the LHC. 2808 out of 3564 (79%) bunch slots are filled with bunches. The bunches are gathered in trains consisting of 72 bunches, with various numbers of empty bunch slots in between the trains. Courtesy of (based on) [1].

2 Beam dynamics

The relevant concepts in noise-free beam dynamics will be introduced in this chapter. This thesis will, where reasonable, follow the notation style and definitions in the text book by A. Wolski [10], where a more thorough introduction can be found.

2.1 Relativistic Lorentz force

Charged particles are affected by electro-magnetic fields. The Lorentz force on a particle of charge q and velocity \mathbf{v} moving through an electric field \mathbf{E} and magnetic field \mathbf{B} is

$$\mathbf{F} = \frac{d\mathbf{p}}{dt} = q(\mathbf{E} + \mathbf{v} \times \mathbf{B}). \quad (2.1)$$

Electrostatic fields are not used in high-energy accelerators, partially due to dielectric breakdown of high field strengths. Strong magnetic fields are used instead, for which the force scales with the speed. Assuming a uniform vertical magnetic field of magnitude $|\mathbf{B}| = B$, particles will move in horizontal circles of radius ρ found by comparison of the Lorentz force and the centrifugal force $\gamma_{\text{rel}} m v^2 / \rho$,

$$B\rho = \frac{\gamma_{\text{rel}} m v}{q}. \quad (2.2)$$

The left-hand side (LHS) of Eq. (2.2) describes the machine, while the right-hand side (RHS) describes the particles. The expression is called the beam rigidity, and models how the particles resist bending at higher energy. The rigidity explains why the LHC is large. If one wants to accelerate particles of high momentum in a synchrotron, one must achieve a high product of the magnetic field and the curvature radius of the bending magnets. The magnetic field is limited by technology, but the size of the machine is mostly limited by the budget.

2.2 Linear optics

2.2.1 Phase space coordinates

Synchrotrons have a reference orbit, on which the reference or synchronous particle moves. If the beamline is designed and operated properly, this orbit will move through the center of the

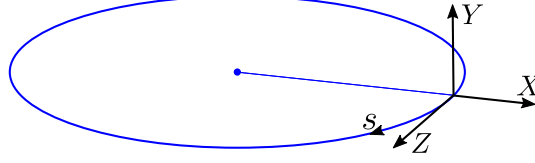


Figure 2.1: Co-rotating, orthogonal synchrotron coordinates (X, Y, Z) , centered at and following the circulating reference particle per bunch. The synchrotron is illustrated as a circle, but will in reality consist of both curves and straight sections.

magnets, as far away as possible from the physical aperture, the inner walls of the beam pipe. The position \mathbf{X} of the particles will be given in the co-rotating coordinates (X, Y, Z) illustrated in Fig. 2.1. The momentum of a particle in the new coordinates is given as

$$\mathbf{P} = (P_x, P_y, P_z) = \frac{\gamma_{\text{rel}} m \dot{\mathbf{X}}}{\tilde{p}_0}, \quad (2.3)$$

where γ_{rel} is the relativistic factor. The momentum is given in units of the reference momentum of the synchronous particle in the lab frame, $\tilde{p}_0 = \gamma_{\text{rel}0} m v_0$. The longitudinal phase space coordinates are

$$Z = \frac{s}{\beta_{\text{rel}0}} - ct, \quad (2.4)$$

$$P_z = \frac{\tilde{p}_s - \tilde{p}_0}{\tilde{p}_0} = \frac{\Delta \tilde{p}}{\tilde{p}_0}, \quad (2.5)$$

where $\beta_{\text{rel}0} = v_0/c$. In the relevant ultra-relativistic limit, $\beta_{\text{rel}0} = 1$.

In high-energy hadron colliders, one can typically make use of the paraxial approximation $P_x \ll P_s \approx P_0 = 1$. This gives in the horizontal plane

$$X' = \frac{dX}{ds} = \frac{P_x}{P_s} \approx P_x. \quad (2.6)$$

When the particles are accelerated to higher energies, they are accelerated longitudinally. Hence, $\tilde{p}_0 \approx \tilde{p}_s \propto \gamma_{\text{rel}}$ increases, while \tilde{p}_x remains constant, causing $X' \approx P_x \propto 1/\gamma_{\text{rel}}$ to decrease. This effect is called adiabatic damping.

A synchrotron is a particle lens system, consisting of an array of carefully designed, manufactured and positioned magnets and other components. The impact of beamline components on the transverse phase space coordinates can be considered with transfer maps \mathbf{R} as

$$\begin{bmatrix} X \\ P_x \\ Y \\ P_y \end{bmatrix}_{s_0+L} = \mathbf{R} \begin{bmatrix} X \\ P_x \\ Y \\ P_y \end{bmatrix}_{s_0}. \quad (2.7)$$

Only linear transfer maps will be considered at the moment, which can be given as matrices.

The transfer matrix of an empty drift space of length L is

$$\mathbf{R}_{\text{drift}} = \begin{bmatrix} 1 & L & \cdot & \cdot \\ \cdot & 1 & \cdot & \cdot \\ \cdot & \cdot & 1 & L \\ \cdot & \cdot & \cdot & 1 \end{bmatrix}, \quad (2.8)$$

where the dots represent zeros. The empty drift space of length L changes the position of the particles by $P_j L$ in the transverse plane $j \in \{x, y\}$, but not the momentum.

The job of a dipole magnet is to bend the reference orbit into the horizontal circle illustrated in Fig. 2.1. The transfer matrix of a weak (not affecting the position) dipole magnet of length L and bending curvature equal to the curvature of the reference orbit is

$$\mathbf{R}_{\text{dip}} = \begin{bmatrix} 1 & L & \cdot & \cdot \\ -1/f_w & 1 & \cdot & \cdot \\ \cdot & \cdot & 1 & L \\ \cdot & \cdot & \cdot & 1 \end{bmatrix}, \quad (2.9)$$

where f_w is the focal length of the weak horizontal focusing. The dipole magnet does kick the horizontal physical momentum independently of the coordinates. However, since this matrix is given in units of the co-rotating coordinates, this kick is already included.

The job of a quadrupole magnet is to focus the beam. The transfer matrix of a weak quadrupole magnet of length L and horizontal focal length f_q is

$$\mathbf{R}_{\text{quad}} = \begin{bmatrix} 1 & L & \cdot & \cdot \\ -1/f_q & 1 & \cdot & \cdot \\ \cdot & \cdot & 1 & L \\ \cdot & \cdot & 1/f_q & 1 \end{bmatrix}. \quad (2.10)$$

Note that if the magnet is focusing in the horizontal plane, corresponding to a positive horizontal focal length $f_q > 0$, then the magnet is defocusing in the vertical plane. A combination of quadrupole magnets are needed to get a net focusing in both planes.

How an ensemble of particles is transported through the beamline is characterized by the optical β -function, which is related to the standard deviation (STD) of the particles as

$$\langle (X - \langle X \rangle_\Psi)^2 \rangle_\Psi(s) = \varepsilon_x \beta_x(s), \quad (2.11)$$

where the angle brackets imply an average over the subscripted value, in this case the full bunch distribution Ψ , and ε_x is the geometrical beam emittance, which will be explained in Sec. 2.4. Note that the β -function only depends on the magnetic lattice, not the bunch distribution.

Since a synchrotron can be seen as a periodic beamline, the β -function is a periodic function with the machine circumference. If one chooses a specific location s along the synchrotron, and measures the transverse phase coordinates of a particle, one finds that they trace out an

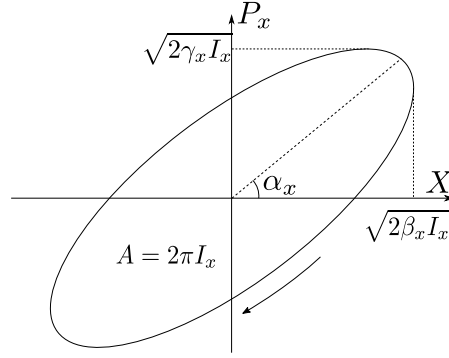


Figure 2.2: Poincaré section showing the link between the coordinates (X, P_x) , the physical action I_x , and the horizontal optical functions β_x , α_x and γ_x . This ellipse will be traced out by a single particle as it passes the same location in the machine turn by turn.

ellipse as in Fig. 2.2. This can be modeled with a one-turn-map (OTM)

$$\mathbf{R}_{\text{OTM}} = \begin{bmatrix} \mathbf{R}_{\text{OTM}x}^{2 \times 2} & \cdot \\ \cdot & \mathbf{R}_{\text{OTM}y}^{2 \times 2} \end{bmatrix}, \quad \mathbf{R}_{\text{OTM}j}^{2 \times 2} = \begin{bmatrix} \cos(\mu_j) + \alpha_j \sin(\mu_j) & \beta_j \sin(\mu_j) \\ -\gamma_j \sin(\mu_j) & \cos(\mu_j) - \alpha_j \sin(\mu_j) \end{bmatrix}, \quad (2.12)$$

where γ_j and α_j are the additional optical Twiss functions, related to the β -function as

$$\alpha_j = -\frac{1}{2} \frac{d\beta_j}{ds}, \quad (2.13)$$

$$1 = \beta_j \gamma_j - \alpha_j^2, \quad (2.14)$$

and μ_j is the phase advance in plane j , which is related to the bare tune of the machine

$$Q_j = \frac{\mu_j}{2\pi}. \quad (2.15)$$

The tune is the number of betatron oscillations during one revolution of the machine. It is important to keep the tune away from rational numbers of low denominators, as nonlinearities can cause resonances and particle losses at such tunes. The corresponding angular betatron frequency in units of rad/s is

$$\omega_j = 2\pi f_{\text{rev}} Q_j = \omega_{\text{rev}} Q_j, \quad (2.16)$$

where f_{rev} is the revolution frequency of the beam around the full machine.

In this section, the optics were considered to be uncoupled, i.e. the motion in the horizontal and vertical phase space are independent of each other. This is not exact, but remains a useful representation of an ideal machine.

2.2.2 Action-phase coordinates

If there exist stable trajectories around the orbit, a particle will trace out an ellipse of constant shape in the transverse phase space coordinates, as was illustrated in Fig. 2.2. It can be shown that there is a conserved property in this motion, the area within the ellipse, which is

proportional to the physical action I_j . When the ellipse is evolving along the beamline, it is due to the change of the optical functions, while the action remains constant.

The horizontal (and equivalently the vertical and longitudinal) phase space coordinates of the ellipse can be expressed in terms of action-phase coordinates as

$$X = \sqrt{2\beta_x I_x} \cos(\phi_x), \quad (2.17a)$$

$$P_x = \frac{dX}{ds} = -\sqrt{\frac{2I_x}{\beta_x}} [\sin(\phi_x) + \alpha_x \cos(\phi_x)], \quad (2.17b)$$

where the phase ϕ_x is the canonical conjugate of the action I_x . The horizontal action of a particle can be calculated as

$$I_x = \frac{1}{2} (\gamma_x X^2 + 2\alpha_x X P_x + \beta_x P_x^2). \quad (2.18)$$

Similarly, there is an oscillation in the longitudinal parameters, caused by the RF cavities. At low speeds, a particle with slightly larger kinetic energy will move faster and spend less time on one revolution around the ring. However, as the speed of light is approached, increased energy does not cause a much higher speed. Simultaneously, the path length traveled by the particle increases in general with the energy due to the beam rigidity. Hence, at energies above a transition energy, the particles of higher energy than the reference particle will move backwards relative to the reference particle, and the particles of lower energy will move forward, i.e. the particles will oscillate counterclockwise in a (Z, P_z) phase space. The machines of interest in this thesis are operated above transition. The longitudinal motion can be described by action-phase coordinates and optical functions as

$$z \equiv Z = \sqrt{2\beta_z I_z} \cos(\phi_z), \quad (2.19a)$$

$$\delta \equiv P_z = -\sqrt{\frac{2I_z}{\beta_z}} \sin(\phi_z), \quad (2.19b)$$

where α_z has been assumed to be 0, by the smooth focusing approximation, and the standard notation δ for the relative momentum and energy deviation has been introduced.

The OTM of the action and phase can be found from an effective Hamiltonian with Hamilton's equations [11]

$$\mathcal{H}_0 = I_x \omega_x + I_y \omega_y - I_z \omega_s, \quad (2.20a)$$

$$\dot{I}_j \equiv \frac{dI_j}{dt} = -\frac{\partial \mathcal{H}_0}{\partial \phi_j} = 0, \quad \dot{I}_z = -\frac{\partial \mathcal{H}_0}{\partial \phi_z} = 0, \quad (2.20b)$$

$$\dot{\phi}_j = \frac{\partial \mathcal{H}_0}{\partial I_j} = \omega_j, \quad \dot{\phi}_z = \frac{\partial \mathcal{H}_0}{\partial I_z} = -\omega_s, \quad (2.20c)$$

where the conservation of the action is ensured, the angular betatron frequency in Eq. (2.16) has returned, and ω_s is the angular synchrotron frequency, which is here defined to be positive above transition. Note that the subscript s is used instead of z for the synchrotron frequency, as it is the standard notation.

The transverse phase space ellipse can be transformed to a normalized phase space circle

$$x = \frac{X}{\sqrt{\beta_x \varepsilon_{x0}}} = \sqrt{2J_x} \cos(\phi_x), \quad (2.21a)$$

$$p_x = \beta_x \frac{dx}{ds} = -\sqrt{2J_x} \sin(\phi_x), \quad (2.21b)$$

where ε_{x0} is the emittance used to normalize the coordinates, typically equal to the initial emittance. The evolution of the normalized transverse phase space coordinates can be written

$$x + ip_x = \sqrt{2J_x} \exp[-i(\phi_{x0} + \omega_x t)]. \quad (2.22)$$

The phase ϕ_x is unchanged, but the normalized action J_x is

$$J_x = \frac{I_x}{\varepsilon_{x0}} = \frac{1}{2} (x^2 + p_x^2). \quad (2.23)$$

The longitudinal phase space coordinates are on the other hand kept unnormalized, $(z, \delta) \equiv (Z, P_z)$, as defined in Eq. (2.19). The evolution of the normalized action-phase coordinates can be found by insertion in Eq. (2.20)

$$\mathcal{H}_0 = \varepsilon_{x0} J_x \omega_x + \varepsilon_{y0} J_y \omega_y - I_z \omega_s, \quad (2.24a)$$

$$\dot{J}_j = -\frac{1}{\varepsilon_{j0}} \frac{\partial \mathcal{H}}{\partial \phi_j} = 0, \quad (2.24b)$$

$$\dot{\phi}_j = \frac{1}{\varepsilon_{j0}} \frac{\partial \mathcal{H}}{\partial J_j} = \omega_j. \quad (2.24c)$$

In a transverse one-dimensional (1D) model, or in a two-dimensional (2D) model with $\varepsilon_{x0} = \varepsilon_{y0}$, the Hamiltonian could have been divided by ε_{j0} for simplicity. However, when introducing higher-order action terms in the following, it is better to keep it on this form.

2.3 Nonlinear optics

In theory, only linear elements that can be treated with matrices are needed to create a synchrotron for single particles. In reality, alignment and powering errors, magnetic imperfections, particle to particle energy spread, and collective effects introduce nonlinearities and sources of instabilities. This creates the need for higher-order magnets with nonlinear transfer maps.

2.3.1 Chromaticity

Chromaticity is the variation of the transverse tunes due to the momentum mismatch

$$Q_j = Q_{j0} + Q'_j \delta + Q''_j \delta^2 + \mathcal{O}(\delta^3), \quad (2.25)$$

where the linear coefficient Q'_j often is called the linear chromaticity. The (linear) chromaticity can be modeled by the introduction of a one-turn Hamiltonian

$$\mathcal{H}_{\text{chroma}} = (\omega'_x \varepsilon_x J_x + \omega'_y \varepsilon_y J_y) \delta, \quad (2.26)$$

where $\omega'_j = \omega_{\text{rev}} Q'_j$. This Hamiltonian also affects the longitudinal motion. However, it can be found that it is negligible compared to the synchrotron motion described in Eq. (2.19) [12, 13].

The momentum mismatch δ oscillates with the synchrotron frequency, and will therefore cause a modulation of the transverse motion. By insertion of Eq. (2.19) in Eq. (2.25), one finds

$$\begin{aligned} \cos[\phi_j(t)] &= \cos \left[\omega_{j0} t + \int_0^t \omega'_j \delta dt \right] \\ &= \cos \left[\omega_{j0} + \frac{\omega'_j \sqrt{2I_z / \beta_z}}{\omega_s} \sin \left(\omega_s t - \phi_{z0} - \frac{\pi}{2} \right) \right] \\ &= \sum_{n=-\infty}^{\infty} J_n \left(\frac{\omega'_j \sqrt{2I_z / \beta_z}}{\omega_s} \right) \cos \left[(\omega_0 + n\omega_s) t - n \left(\phi_{z0} + \frac{\pi}{2} \right) \right], \end{aligned} \quad (2.27)$$

where $J_n(\cdot)$ are the Bessel functions of the first kind of order n , not to be confused with the normalized actions, acting as coefficients of the various synchrotron sidebands.

Chromatic aberration in visual light optics is the dependence of the bending angle through a lens on the momentum of the photons. Similarly, the bending of the particles in magnetic fields depends on their momentum (magnetic rigidity). In particular, the quadrupole magnets generate a natural (negative) chromaticity. However, a large chromaticity can be detrimental to the beam. Therefore, it is typical to counteract the natural chromaticity with sextupole magnets. As an example, the LHC is typically operated with a chromaticity $Q'_j \in [0, 15]$.

2.3.2 Landau octupoles

Landau octupoles are put in a machine to produce a tune spread in order to keep the beam stable through Landau damping, which will be introduced in Sec. 2.6 [14]. The octupoles cause an action dependent tune spread in both transverse planes, relative to the bare machine tune, which can be expressed as

$$\Delta Q_{x/y} = A_{x/y} I_{x/y} + B_{x/y} I_{y/x},$$

where $A_{x/y}$ are the in-plane detuning coefficients and $B_x = B_y$ are the cross-plane detuning coefficients, as defined in [14]. In terms of the normalized actions introduced in Eq. (2.23) and used in this thesis, the octupole tune spread, relative to the bare tune, can instead be given as

$$\Delta Q_{x/y} = a_{x/y} J_{x/y} + b_{x/y} J_{y/x}, \quad (2.28)$$

or equivalently for the angular frequency shift

$$\Delta \omega_{x/y} = \tilde{a}_{x/y} J_{x/y} + \tilde{b}_{x/y} J_{y/x}, \quad (2.29)$$

where $\tilde{a}_j = \omega_{\text{rev}} a_j$. The integrated impact of the octupole magnets along the machine can be included in an effective one-turn Hamiltonian as

$$\mathcal{H}_{\text{oct}} = \frac{\tilde{a}_x}{2} \varepsilon_x J_x^2 + \frac{\tilde{a}_y}{2} \varepsilon_y J_y^2 + \tilde{b}_x \varepsilon_x J_x J_y. \quad (2.30)$$

Note that in the last term on the RHS, $\tilde{b}_x \varepsilon_x = \omega_{\text{rev}} B_{x/y} \varepsilon_x \varepsilon_y = \tilde{b}_y \varepsilon_y$.

The magnitude of the detuning is determined by the (normalized) detuning coefficients, which in the horizontal plane of B1 in the LHC are

$$\begin{aligned} a_x &= +543.2 \frac{6.5/0.938}{\gamma_{\text{rel}}} I_{\text{oct}} \varepsilon_x, \\ b_x &= -383.6 \frac{6.5/0.938}{\gamma_{\text{rel}}} I_{\text{oct}} \varepsilon_y, \end{aligned} \quad (2.31)$$

where I_{oct} is the octupole current, limited to maximum ± 570 A. The prefactors (543.2, -383.6) are calculated based on the optical functions at the locations of the octupole magnets in the LHC during the main experiments referred to in this thesis [15], for a particle energy of 6.5 TeV. In B2 they are (531.3, -383.4). The prefactor for a_y is slightly different, while the prefactor is equal for b_y , for each beam separately, but this is of little relevance in this thesis. The deflection achieved by the magnets is inversely proportional to the energy, explained in Eq. (2.2). Since the coefficients are relative to the normalized actions, the detuning coefficients are proportional to the geometrical emittance, which is also inversely proportional to the energy. The detuning coefficients can be increased further by a factor $\in (2, 4)$ by use of telescopic optics [16].

It will in some chapters be relevant to discuss the tune spread relative to the average tune of all the particles

$$\begin{aligned} \tilde{\Delta} Q_{x/y} &= Q_{x/y} - \langle Q_{x/y} \rangle_{\Psi} \\ &= a_{x/y} (J_{x/y} - \langle J_{x/y} \rangle_{\Psi}) + b_{x/y} (J_{y/x} - \langle J_{y/x} \rangle_{\Psi}), \end{aligned} \quad (2.32)$$

which will be denoted by the tilde across the Δ in $\tilde{\Delta} Q$, and mentioned in the text when relevant. The root mean square (rms) tune spread is $\sqrt{a_j^2 + b_j^2}$, assuming a Gaussian distribution.

2.4 Beam quality and luminosity

So far, the description has only considered single particles moving through a linear beamline. However, as introduced in Ch. 1, the particles are gathered in bunches of multiple particles. These ensembles will here be described by probability density functions, with several important macroscopic quantities.

The bunch distribution can be given as a probability function of the 6 phase space coordinates, $\Psi(x, p_x, y, p_y, z, \delta)$. In high-energy hadron colliders, the distributions are often assumed uncoupled to first order

$$\Psi(x, p_x, y, p_y, z, \delta) = \Psi_x(x, p_x) \Psi_y(y, p_y) \Psi_z(z, \delta). \quad (2.33)$$

Furthermore, the transverse distributions are often assumed to be Gaussian in the normalized coordinates

$$\Psi_x(\phi_x, J_x) = \frac{1}{2\pi} \exp\left(-\frac{x^2 + p_x^2}{2}\right) = \frac{1}{2\pi} \exp(-J_x), \quad (2.34)$$

which is uniformly distributed in the phase coordinate, ϕ_x . Therefore, one can rather use the 1D distribution $\Psi_x(J_x) = 2\pi\Psi_x(\phi_x, J_x)$.

Key macroscopic quantities of a bunch include:

- The bunch intensity N , which is the number of particles in a bunch.
- The transverse geometrical emittances ε_j , related to the bunch size by Eq. (2.11).
- The rms relative momentum and energy spread σ_δ .
- The bunch length σ_s , often calculated as the STD of the particles' longitudinal position assuming a Gaussian distribution. The value given for the bunch length is often $4\sigma_s$, as in Table 4.1, which would include 95% of the particles in a Gaussian distribution.

The emittance of a beam on orbit is the average transverse physical action of the particles

$$\varepsilon_j = \langle I_j \rangle_\Psi. \quad (2.35)$$

Due to adiabatic damping, the geometrical emittance decreases with the energy, while

$$\varepsilon_{nj} = \gamma_{\text{rel}} \beta_{\text{rel}} \varepsilon_j, \quad (2.36)$$

called the normalized emittance, remains constant.

The key goal of a hadron collider is to generate hadronic collisions for the experiments, the more the merrier. The rate of hadron collisions is measured in terms of the luminosity. For two equal, round Gaussian bunches colliding head-on, the luminosity is given by

$$\mathcal{L} = \frac{N^2 f_{\text{rev}} N_b}{4\pi \beta_j^* \varepsilon_j} \propto \frac{N^2}{\varepsilon_j}, \quad (2.37)$$

where N is the bunch intensity in both beams, N_b is the number of bunches that collide per beam, and β_j^* is the value of the optical β_j -function at the location of the collisions. As indicated in the equation, to get a high luminosity one requires high bunch intensity and small transverse emittances. Therefore, in this thesis, a high beam quality refers to a bunch with a high intensity and small transverse emittances, and preserving the beam quality refers to the goal of minimizing the particle loss rate and emittance growth rate.

2.5 Collective dynamics

Collective dynamics in an accelerator beam is mechanisms that depend on the beam distribution. Such mechanisms can drive collective instabilities. If there is a transverse force that to first order is proportional to the transverse offset from the reference path, it can drive transverse oscillations around that reference path. These oscillations evolve like $\exp(-i\omega_{\text{coh}} t)$, with a complex frequency $\omega_{\text{coh}} = \omega_0 + \Delta\omega_{\text{coh}}$ consisting of a bare frequency ω_0 and a frequency

shift $\Delta\omega_{\text{coh}} = \omega_{\text{rev}}\Delta Q_{\text{coh}}$ driven by the collective dynamics. If $\text{Im}\{\omega_{\text{coh}}\} > 0$, the coherent mode of oscillation is unstable and its amplitude will (initially) grow exponentially.

2.5.1 Beam-beam interactions

When the proton beams are put into collision to produce luminosity for the experiment at an IP, an unavoidable byproduct are low-angle deflections between the non-colliding protons. In the weak-strong model, one can calculate the deflection and detuning of a test particle caused by an opposing rigid Gaussian bunch. If the bunch is round, the detuning in 1D is [17]

$$\Delta Q_{\text{BB}}(J) = -\xi_{\text{BB}} \cdot \frac{2}{J} \left[1 - I_0\left(\frac{J}{2}\right) \exp\left(-\frac{J}{2}\right) \right], \quad (2.38)$$

where I_0 is the modified Bessel function of the first kind, J is the action of the test particle normalized to the opposing bunch, and ξ_{BB} is the linear beam-beam parameter, which for round high-energy beams is

$$\xi_{\text{BB}} = \frac{Nr_p\beta_{\text{rel}}}{4\pi\epsilon_n}, \quad (2.39)$$

where r_p is the classical proton radius. The rms tune spread is approximately $0.168\xi_{\text{BB}}$ [18]. The largest absolute tune shift is ξ_{BB} and is experienced by test particles of zero action, whereupon the tune shift approaches zero for larger actions. In 2D, the tune spread is illustrated in Fig. 2.6a. If there are multiple IPs, the beam-beam parameter can be added up to a total beam-beam parameter $\xi_{\text{BB,tot}}$. By comparing Eq. (2.39) to the luminosity in Eq. (2.37), it is clear that a higher luminosity in general will generate stronger beam-beam interactions.

In reality, both beams are affected by each other, and this can drive coherent beam-beam modes. In the case of 1 bunch per beam, the coherent modes are the 0-mode and π -mode, named after their phase difference at the IP as illustrated in Fig. 2.3. If not damped, these modes can drive the beams unstable. The coherent tune shift of the 0-mode is 0, while the coherent tune shift of the π -mode is $1.2\xi_{\text{BB}} - 1.3\xi_{\text{BB}}$ [19], depending on the bunch shape, and is thus outside the incoherent tune spectrum in Eq. (2.38).

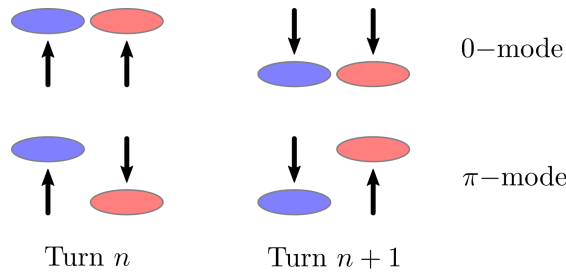


Figure 2.3: Coherent beam-beam modes with 1 bunch per beam and 1 interaction point.

In the LHC, there are several bunches per beam. As a consequence, as illustrated in Fig. 2.4, there are both a head-on interaction at each IP and several parasitic interactions on both sides. Therefore, the beams are typically made to collide with a nonzero crossing angle such that the parasitic interactions become long-range, thus reducing their impact. However, this reduces the overlap between the colliding bunches at the IP as well. Crab Cavities (CCs) are

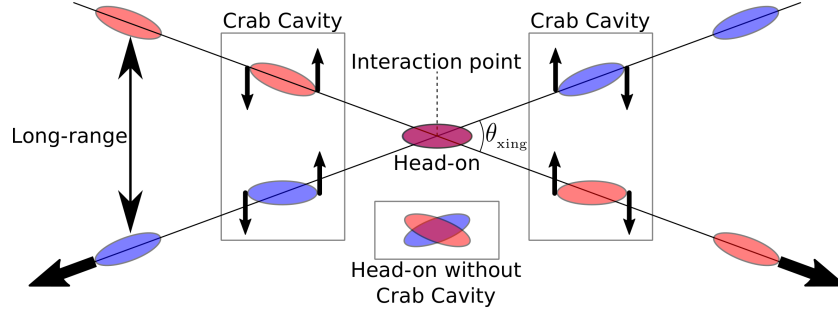


Figure 2.4: Interaction region with a crossing angle θ_{xing} , displaying both head-on and long-range beam-beam interactions. The intended effect of the Crab Cavities is also illustrated: Tilting the bunches so that they collide with maximum overlap, while still ensuring a large crossing angle θ_{xing} to reduce the impact of the long-range interactions.

designed to tilt the bunches at the IP, as illustrated in Fig. 2.4, by kicking the head and tail of the bunches in opposite directions [20]. The bunches are tilted back after the IP. This is done to increase the luminosity, while simultaneously allowing for a significant separation of the bunches at the long-range interactions. CCs are not implemented in the LHC, but are part of the design for the HL-LHC.

2.5.2 Impedance and wakefields

When charges move through a beamline, image charges and currents are induced in the walls of the beam pipe [10], which induce their own electro-magnetic fields. In the ultra-relativistic limit, these fields can only affect trailing bunches. The wakefields depend both on the interacting charges, as illustrated in Fig. 2.5, and the beam pipe itself, either through a finite resistivity or geometry variations along the beam pipe.

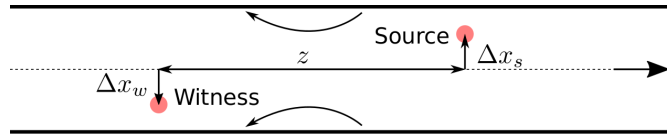


Figure 2.5: Illustration of a wakefield interaction. A source charge traverses the machine, produces an electromagnetic response, and affects the trailing witness charge.

The horizontal wake force, F_x , from the source particle on the witness particle, integrated over a distance of the machine, causes an energy change [21]

$$\begin{aligned} \Delta \mathcal{E}_x &= \int F_x(\Delta x_s, \Delta x_w, z; s_s) ds_s = -q_s q_w W_x(\Delta x_s, \Delta x_w, z) \\ &\approx -q_s q_w [W_{x0}(z) + W_{xD}(z) \Delta x_s + W_{xQ} \Delta x_w], \end{aligned} \quad (2.40)$$

where $z = s_w - s_s$ is the distance from the source to the witness, and W_x is the horizontal wake function, which models the wakefields in time domain. The impedance, being the Fourier transform of the wake function, models the wakefields in frequency domain. In the ultra-relativistic case, the wake function is 0 for $z > 0$, and also approaches 0 for $z \rightarrow -\infty$. To get the

impact of the entire beam on the witness charge, the wake function must be convoluted with the charge distribution ahead of it, including the witness charge itself at previous turns. The wake functions differ between various components of the beamline. These can, as a useful approximation, be combined into a single effective wake function for the entire machine.

The wake function can be Taylor expanded in terms of the transverse offsets of the source and witness charges, as is done in the second line of Eq. (2.40): $W_{x0}(z)$ is the zeroth-order wake function and will typically be zero for symmetrical structures; $W_{xD}(z)$ is the dipolar wake function, which can drive modes with complex coherent tune shift $\Delta\omega_{\text{coh}}$; $W_{xQ}(z)$ is the quadrupolar wake function, which can cause an additional tune shift. The tune shift, along with other details of the modes, can be calculated with numerical Vlasov solvers as DELPHI [22] or circulant matrix solvers as BimBim [7]. These modes will be treated more carefully in Ch. 6.

2.5.3 Active beam feedback system

The active beam feedback system is different from the inherent collective effects treated so far, in that it is intentionally included in the machine and it is controlled by the operators. In short, the transverse bunch feedback system, sometimes called the damper, measures the transverse position of the bunches turn-by-turn, and if it oscillates around the synchronous orbit, a kicker magnet is used to reduce the transverse offset [1, 23]. Hence, if operated correctly, it induces a negative imaginary coherent tune shift, which can prevent instabilities. As will be seen in Ch. 3, the feedback can also reduce the emittance growth rate.

Since the bunches are moving at almost the speed of light, the bunch cannot be acted on at the same turn as the position measurements. Instead, the feedback system must use measurements from previous turns to predict the current transverse offset. For this reason, it is important to know the tunes of the particles accurately. Otherwise, the feedback system may drive the beam unstable [24]. A key parameter when considering the stability of the feedback loop is the group delay of the feedback filter, how far into the future the prediction is made [25]. Much work has been put into designing optimal multi-turn filters, damping a bunch based on the measurements from more than one turn. Different filters have different stability limits [26].

A dipolar feedback system predicts the average transverse momentum of bunch b and reduces it by a gain g_j as

$$p_{jb} \rightarrow p_{jb} - g_j p_{jb} = p_{jb}(1 - g_j). \quad (2.41)$$

This is called a bunch-by-bunch feedback, since each bunch is damped independently of the other bunches. If all the particles in a bunch have the same tune, and there are no other forces included, it can be shown that the feedback reduces the center of mass (COM) radius in phase space as

$$\sqrt{\langle x \rangle_\Psi^2 + \langle p \rangle_\Psi^2} \propto \exp\left(-\frac{gT}{2}\right) \equiv \exp\left(-\frac{T}{\tau_g}\right), \quad (2.42)$$

where the damping time $\tau_g = 2/g$ has been defined in units of turns. There also exist feedback systems that reduce the headtail motion of the bunch [27], but that is not of interest in this thesis.

If the beam consists of bunch trains, as introduced in Sec. 1.3, then it can in some cases be preferential from a physics point of view to use a multi-bunch feedback

$$p_{jb} \rightarrow p_{jb} - g_j \sum_{b'} w_{bb'} p_{jb'}, \quad (2.43)$$

where $w_{bb'}$ is the peak-normalized response over all the bunches. It is defined as 1 for bunch b , and then decreasing for larger $|b - b'|$. This is the case for the LHC Transverse Damper (ADT). More details about the multi-bunch feedback will be introduced in Ch. 8.

2.6 Landau damping and the linear Vlasov equation

Landau damping is essential for the successful operation of high-energy hadron colliders. Without it, some of the modes driven by collective effects would be unstable. It was first described in plasma physics [28], as the damping of a small plasma vibration due to a spread of the particles' velocities. This mechanism and description has been adopted by the accelerator community, with some modifications.

Landau damping in accelerator physics can be described as “a physical process in which an ensemble of harmonic oscillators ... that would otherwise be unstable is stabilized by a spread in the natural frequencies of the oscillators” [29]. In other words, a mode that is unstable without a tune spread among the particles, can be stabilized if there is a tune spread. That is why many machines include Landau octupoles, which were described in Sec. 2.3.2, as the name hints at. However, it is essential that the same particles that are involved in the coherent (possibly unstable) oscillation are also involved in the incoherent tune spread. Furthermore, it should be noted that Landau damping in accelerator physics is not actually damping of an instability, but rather the absence of one [30].

To evaluate Landau damping, it is common to start with Liouville's theorem [11]. In a collision-free Hamiltonian system, Liouville's theorem states that the distribution function Ψ is constant along any trajectory of the system in phase space. For non-colliding particles, the Liouville theorem can be stated mathematically by the Vlasov equation [12, 22, 31–33]

$$\frac{d\Psi}{dt} = \frac{\partial \Psi}{\partial t} + [\Psi, \mathcal{H}] = 0, \quad (2.44)$$

where \mathcal{H} is the Hamiltonian of the system and the brackets are the Poisson brackets.

The question now is whether or not unstable coherent modes with frequencies $\omega_{\text{coh}j}$ can be stabilized by Landau damping, changing the frequencies to $\Omega_{\text{LD}j}$ with a negative imaginary part, due to an action dependent spread of the incoherent frequencies $\omega_j(J_x, J_y)$. Under the weak headtail approximation, one can linearize the Vlasov equation, as in App. A [34], and get an integral relation between these quantities

$$\frac{-1}{\Delta\omega_{\text{coh}j}} = \int_0^\infty \int_0^\infty dJ^2 \frac{J_j \frac{d\Psi(J_x, J_y)}{dJ_j}}{\Omega_{\text{LD}j} - \omega_j(J_x, J_y)} = 2R(\Omega_{\text{LD}j}), \quad (2.45)$$

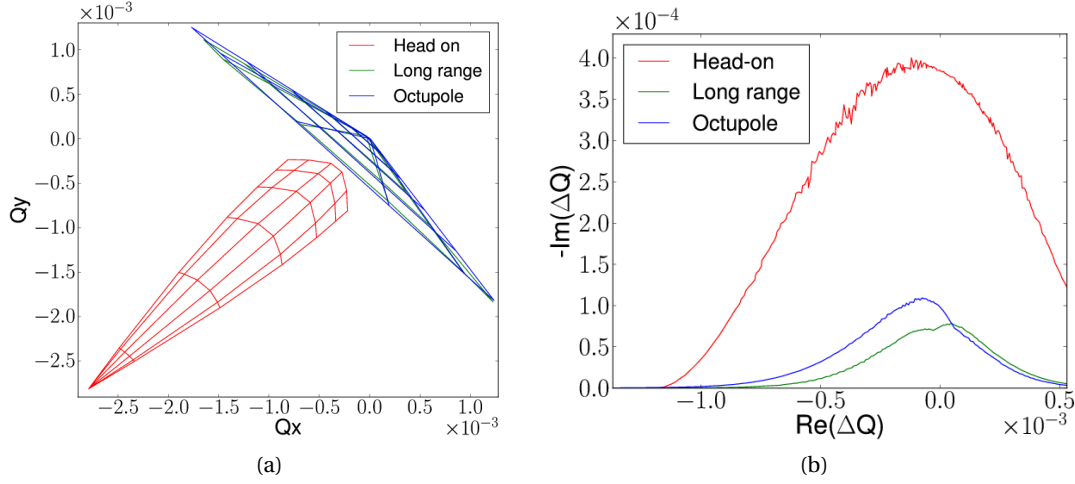


Figure 2.6: Tune spreads in (a), of similar size, and corresponding stability diagrams in (b). The grids in (a) correspond to particles at various numbers of the STD of the distributions. The stability diagrams in (b) mark the limit of stability. If a coherent mode has a tune shift ΔQ_{coh} that is inside/below this curve, the mode will be stabilized by that detuning. If it is outside/above, it will be unstable. The octupole tune spread corresponds to a negative octupole current. For a positive current, the stability diagram in (b) would have been mirrored horizontally around $\text{Re}\{\Delta Q\} = 0$. Courtesy of [30, 35].

where $R(\Omega_{\text{LD}j})$ is the response function. Instead of evaluating each mode individually, it is simpler to find the limit of stability. The stability diagram is the set of tune shifts $\Delta\omega_{\text{SD}j}$ of coherent modes that are barely stabilized with a given frequency spread $\omega_j(J_x, J_y)$, i.e.

$$\frac{-1}{\Delta\omega_{\text{SD}j}} = \int_0^\infty \int_0^\infty dJ^2 \frac{J_j \frac{d\Psi(J_x, J_y)}{dJ_j}}{\Omega_{Rj} - \omega_j(J_x, J_y)} = 2R(\Omega_{Rj}), \quad (2.46)$$

where Ω_{Rj} has a vanishing positive imaginary part. The stability diagram in terms of the tunes is found by multiplying both sides by ω_{rev} .

Various tune footprints and stability diagrams are given in Fig. 2.6, where the sources of the detuning are octupole magnets operated with a negative current, head-on beam-beam interactions, and long-range beam-beam interactions [30, 35]. Even though the footprints are of similar size up to 6 beam sigmas, the stability diagrams are quite different. Most importantly, the stability diagram due to head-on beam-beam interactions is much larger than the other two. This is because the head-on interactions cause the largest tune spread for particles in the core of the bunch, while the other two cause the largest tune spread for particles in the tail of the bunch. Both the distribution and the tune spread matter.

3 Noise excited beam dynamics

3.1 Noise

‘Noise’ will in this thesis refer to stochastic transverse kicks applied to the particles in a bunch, changing their (normalized) momenta as

$$p \rightarrow p + \Delta p, \quad (3.1)$$

and thereby their actions as

$$J_0 \rightarrow \frac{x^2 + (p + \Delta p)^2}{2} = J_0 + p\Delta p + \frac{\Delta p^2}{2} \equiv J_k. \quad (3.2)$$

Various types of noise are illustrated in Fig. 3.1. The sources of noise will be explained in the following, and all noise amplitudes are given in the normalized coordinates, i.e. in units of the ‘beam sigma’ (1 STD). Since the focus in this thesis is transverse dynamics, the subscript j , denoting the transverse plane, has been omitted when possible for ease of notation.

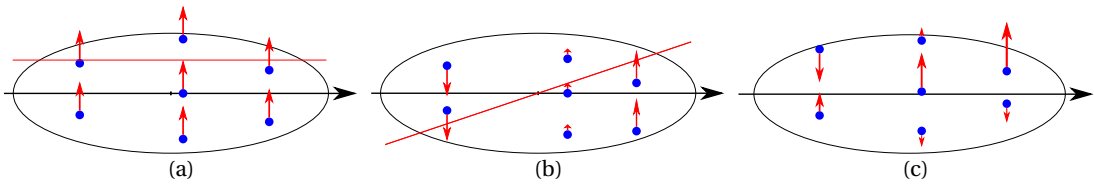


Figure 3.1: Different types of noise. (a) Rigid/dipolar noise, where all particles experience the same kick each turn, but the kick is stochastic from turn to turn. (b) Headtail noise, where each kick is correlated along the bunch. The illustration is of a linear correlation along the bunch, but higher order correlations can exist as well. (c) Incoherent noise, where there is no correlation between the kicks experienced by individual particles.

3.1.1 External noise

‘External noise’ will in this thesis refer to noise that is independent of the beam itself. Examples of sources of external noise are ground motion [36], Power Converter (PC) ripples [37], including 50Hz lines [38], and amplitude or phase noise in CCs [20]. For a full bunch length of

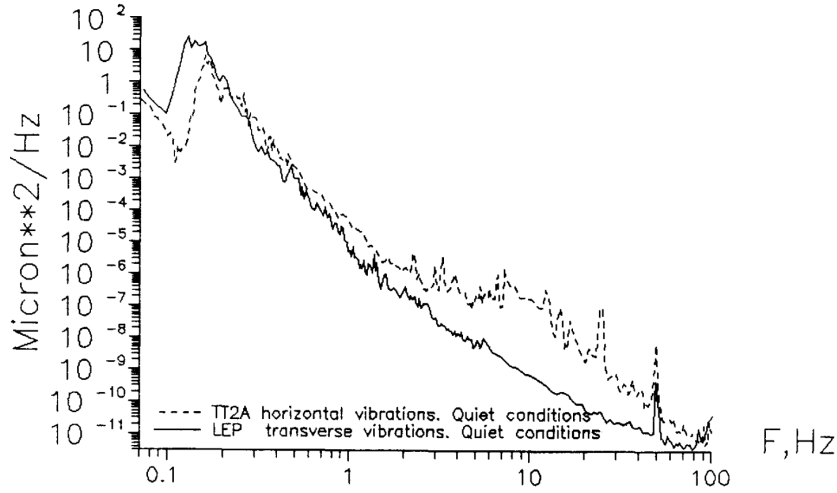


Figure 3.2: Power Spectral Density of the ground motion in tunnels at CERN, measured in 1993. The LEP tunnel is now the LHC tunnel. Courtesy of [40].

~ 1 ns, as in the LHC, the noise needs power in frequencies close to or above ~ 1 GHz to not be constant along the bunch. External noise is, for various reasons, typically strongest at low frequencies [39]. Therefore it tends to affect all particles in a bunch equally, as illustrated in Fig. 3.1a, with crab cavity amplitude noise being the exception.

The noise amplitude of ground motion is in general weak at high frequencies, as illustrated in Fig. 3.2. Noise at such small frequencies can be problematic in that it shifts the closed orbit of the particles, and therefore generates a beam offset at the IP, but it is less problematic within the scope of this thesis.

PCs are used to deliver Direct Current (DC) voltage to the superconducting magnets in the LHC. Ripples in the output from a PC lead to a ripple in the current in the magnets, and thereby a ripple in the magnetic field seen by the particles. The maximum acceptance level of the PC output ripple is given in Fig. 3.3. This voltage will be damped by self-inductance in the electromagnets, giving an additional factor $1/f^2$ in the power of the output magnetic field ripple. Furthermore, the magnetic field ripple will be damped by the beam screen [39]. Hence, the Power Spectral Density (PSD) of the PC ripple noise acting on the beam will be much weaker at large frequencies, and therefore be dipolar in nature.

The magnitude of the resulting dipolar external noise on the beam is, however, challenging to quantify. Dedicated emittance growth measurements have been performed with proton beams in the LHC [41, 42]. The effective noise amplitude per turn was $\sigma_{\text{ext}} \sim 5 \times 10^{-5}$ in units of the beam sigma with a normalized emittance of $2 \mu\text{m}$ at an energy of 6.5 TeV. This assumed a flat PSD, as due to white noise. Other beam measurements have found that the spectrum is not flat, but contains peaks at integer multiples of 50 Hz, at frequencies where they can affect the beam [38]. If the beam spectrum contains such a 50 Hz line, it would be detrimental for the beam. A full understanding of the noise is needed to calculate the impact on the beam. In the following, the noise is considered to have a flat spectrum up to a maximum frequency.

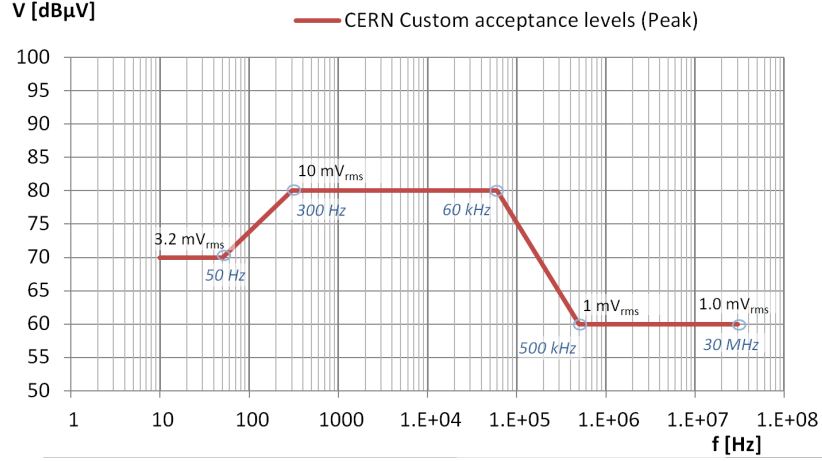


Figure 3.3: Maximum acceptance level of output voltage ripple from power converters at CERN, which deliver current to the electromagnets in the machine. Courtesy of [37].

Crab cavity amplitude noise is slightly different. CCs are designed to tilt the bunches at the IP, as was illustrated in Fig. 2.4. Small inaccuracies in the CC kick amplitude will lead to an overall unwanted tilt of the bunch after the IR. Hence, the crab cavity amplitude noise is of the form illustrated in Fig. 3.1b. The impact of crab cavity amplitude noise will not be studied in detail in this thesis, but may require studies in the future, especially with regards to long-term beam stability. Nevertheless, the formalism that will be developed is general enough, such that it can be directly applied to crab cavity amplitude noise or even higher frequencies.

3.1.2 Beam position monitor noise

A Beam Position Monitor (BPM) measures the transverse position of the beam at a given position along the accelerator. A set of BPMs is usually dedicated to the feedback system, which can reduce the beam offset from the closed path, as explained in Sec. 2.5.3. However, the measured positions are not exact, leading to an error between the predicted momentum p_{bp} and the actual momentum p_b in either transverse plane. Thus, the effect of a bunch-by-bunch feedback in Eq. (2.41) changes to

$$p_b \rightarrow p_b - g p_{bp} = p_b(1 - g) + g \delta_{bp}, \quad (3.3)$$

where δ_{bp} is the BPM error, which can be assumed to be drawn from a normal distribution $\delta_{bp} \sim \mathcal{N}(0, \sigma_{\text{BPM}}^2)$, and it was assumed that the prediction of the momentum did not introduce additional error, requiring a small gain and correct tune knowledge. The effective BPM error amplitude in the LHC was measured to be $\sigma_{\text{BPM}} \approx 2.3 \times 10^{-5}$, in units of the beam sigma with a normalized emittance of $2\mu\text{m}$ at an energy of 6.5 TeV [41, 42]. This BPM error is then filtered by the feedback system before it affects the beam. The resulting unwanted kick from the feedback system on the beam is in this thesis referred to as the BPM noise. For a bunch-by-bunch feedback, the kick is $g \delta_{bp}$, which is drawn from a normal distribution with variance $g^2 \sigma_{\text{BPM}}^2$. The BPM noise with a multi-bunch feedback is studied in Ch. 8.

3.1.3 Incoherent noise

Unlike the noise sources considered above, incoherent noise affects all particles differently. One source of incoherent noise is intra-beam scattering (IBS) [43], which is the process where particles in the same bunch scatter elastically off each other. Macroscopically, this noise causes an emittance growth. The horizontal IBS time in the LHC is reported in Table 1.1, corresponding to a relative emittance growth rate of approximately 2%/h, while the vertical emittance growth rate due to IBS is approximately 0.

Another source of incoherent noise is synchrotron radiation (SR) [44], which microscopically is the process where particles emit photons stochastically as they are bent around the synchrotron by the dipoles. The photon emission leads to a reduction of the momentum, which is compensated by the RF cavity only in the longitudinal direction. Hence, the macroscopic effect is a reduction of the emittance, even though the individual particles experience a random walk. The energy loss through SR from a beam in a synchrotron is inversely proportional to the particle mass to the fourth power, $\Delta\mathcal{E} \propto 1/m^4$. Hence, it is a dominant effect for electrons, while it is more negligible in proton colliders built so far.

There exist sophisticated models of both IBS and SR. Here, the impact will be simplified as a single incoherent kick per particle per turn $\Delta p \sim \mathcal{N}(0, \sigma_{Ij}^2)$. Each kick will lead to a change of the action, for each particle individually, given by Eq. (3.2). The incoherent noise will lead to a uniform diffusion of the distribution governed by

$$\frac{\partial \Psi}{\partial t} = \sum_{j=\{x,y\}} \frac{\partial}{\partial J_j} \left(J_j D_{Ij} \frac{\partial \Psi}{\partial J_j} \right), \quad D_{Ij} = \frac{\sigma_{Ij}^2}{2\tau_{\text{rev}}}, \quad (3.4)$$

which can be found as in App. B.1. Macroscopically, this gives a relative emittance growth rate

$$\frac{\dot{\epsilon}_j}{\epsilon_{j0}} = \frac{\sigma_{Ij}^2}{2\tau_{\text{rev}}}, \quad (3.5)$$

where it has been assumed that the SR damping is negligible as the focus here is hadron colliders. The diffusion coefficient D_{Ij} is here, and in the rest of this thesis, defined such that a uniform diffusion in phase space corresponds to a constant diffusion coefficient. An alternative convention, which is also common in the literature, is to call $J_j D_{Ij}$ the diffusion coefficient.

3.2 Modeling coherent noise

Coherent noise affects all particles at the same point in space-time equally. This noise can be modeled as a force $\mathbf{F}_{\text{noise}}(s; t)$. Here, it is neglected that a small part of the noise force may also depend on the transverse coordinates, e.g. due to noise in the focusing fields. The change of momentum is the time integral of this force, also known as the noise impulse.

There are several noise sources along the beamline. Noise source l affects the beam with kicks of PSD $S_l(\omega)$. Assuming no correlation between the noise sources, the PSD of the full coherent

noise is

$$S_{\text{noise}}(\omega) = \sum_l S_l(\omega). \quad (3.6)$$

Similarly, the noise amplitude variance acting on a particle, not per kick, but per time, can be calculated over N turns as

$$\sigma_{\text{noise}}^2 = \langle \Delta p^2 \rangle_t = \lim_{N \rightarrow \infty} \frac{1}{N\tau_{\text{rev}}} \sum_{n=1}^{n=N} \sum_l \Delta p_{ln}^2 = \sum_l \sigma_l^2, \quad (3.7)$$

where Δp_{ln} is the impulse from noise source l on turn n . Each noise source will act on the particles only once per turn. Hence, individual particles will only sample each noise source with sampling frequency equal to the revolution frequency f_{rev} . Noise at frequencies above the Nyquist frequency $f_{\text{rev}}/2$ will still affect the particles, but aliased into lower frequencies.

Instead of modeling all the noise sources separately, the effect can be modeled as a single source $\xi(t)$. This noise kicks each particle only once per turn. The model noise shall have the same PSD as given by Eq. (3.6), and variance per kick

$$\sigma_{\xi}^2 = \sigma_{\text{noise}}^2 \tau_{\text{rev}}, \quad (3.8)$$

which depends on the period between each kick, here set equal to the revolution period τ_{rev} .

Assume for now that the noise is white. White noise is characterized by having uncorrelated kicks of zero mean, defined mathematically as

$$\langle \xi(t) \rangle_t = 0, \quad \langle \xi(t) \xi(t + \tau) \rangle_t = \sigma_{\text{noise}}^2 \delta_D(\tau), \quad (3.9)$$

where $\delta_D(\cdot)$ is the Dirac delta distribution — However, note that $\langle \xi(t) \xi(t) \rangle_t = \sigma_{\text{noise}}^2$, it is well defined and finite — The PSD of a continuous white noise signal is flat, and is by the Wiener-Khinchin theorem equal to the Fourier transform of the autocorrelation function [45]

$$S_{\xi}(\omega) = |\mathcal{F}[\xi(t)]|^2 = \mathcal{F}[\langle \xi(t) \xi(t + \tau) \rangle_t] = \sigma_{\text{noise}}^2 = \sigma_{\xi}^2 f_{\text{rev}}. \quad (3.10)$$

The noise on a specific particle is not continuous, it consists of individual kicks of variance σ_{ξ}^2 with a repetition frequency f_{rev} . The PSD of the white noise on a particle can in this case be modeled as

$$S_{\xi}(\omega) = \begin{cases} \sigma_{\xi}^2 f_{\text{rev}} & , \omega \in [0, \pi f_{\text{rev}}] \\ 0 & , \text{otherwise,} \end{cases} \quad (3.11)$$

only extending to the Nyquist frequency.

So far, the focus was the effective noise acting on a particle. Now, the focus is the effective noise acting on a bunch. The noise may differ between the head and the tail of the bunch, as illustrated in Fig. 3.1b. To model this, the noise function $\xi(t)$ can be decomposed as

$$\xi(t) \equiv \sum_i \xi_i(t_c) \Xi_i(z), \quad (3.12)$$

in a small interval around t_c , the time when the synchronous particle reaches the effective noise source. Here, $\Xi_i(z)$ are orthogonal functions, square normalized over the initial bunch

distribution $\Psi_0(z)$

$$\langle \Xi_i(z)^2 \rangle_{\Psi_0} = 1, \quad (3.13)$$

and $\xi_i(t_c)$ are the amplitudes of the noise components across the bunch. For the machines of interest in this thesis, the only two components of interest are a constant one $\Xi_0 \propto z^0$ and a linear headtail component $\Xi_1(z) \propto z$. Thus, the variance of the noise kick amplitude is

$$\langle \xi(t)^2 \rangle_t = \sigma_{\text{noise}}^2 = \sigma_{\xi}^2 f_{\text{rev}} = (\sigma_{\xi_0}^2 + \sigma_{\xi_1}^2) f_{\text{rev}}, \quad (3.14)$$

averaged over all the particles in a bunch.

As mentioned in Sec. 3.1.1, noise at sufficiently low frequencies will affect all particles in a bunch equally, as in Fig. 3.1a, and almost all noise in the LHC is of such low frequencies. The CC will be the main contributor to the noise component $\Xi_1(z)$ in the HL-LHC, but they do not exist in the LHC. Hence, in the LHC, a valid approximation is $\sigma_{\xi}^2 \approx \sigma_{\xi_0}^2 \equiv \sigma_k^2$. Here, the variance of the rigid dipole kick has been renamed σ_k^2 , consisting of external noise (without CCs) and BPM noise

$$\sigma_k^2 = \sigma_{\text{ext}}^2 + g^2 \sigma_{\text{BPM}}^2. \quad (3.15)$$

The frequency spectrum of this noise is typically not of great importance when studying a single bunch, unless it contains narrow peaks, for example due to the 50Hz lines in the LHC. However, in Ch. 8, the noise spectrum will be important as it can correlate multiple neighboring bunches.

3.3 Rigid single-bunch dynamics

In a rigid bunch, the distance in phase space between all particles is fixed. It is a simple, yet useful, model of a bunch, and it is accurate in the limit that all the particles have the same tune and the noise is purely dipolar. The dynamics of a rigid bunch can be considered purely by studying the COM of the bunch, represented here with the coordinates (x, p) for ease of notation. In one transverse plane, the dynamics can be described with a Hamiltonian as in Eq. (2.24)

$$\mathcal{H} = \frac{\omega_0}{2} (x^2 + p^2) - x \Delta p, \quad (3.16a)$$

$$\dot{x} = \frac{\partial \mathcal{H}}{\partial p} = \omega_0 p, \quad (3.16b)$$

$$\dot{p} = -\frac{\partial \mathcal{H}}{\partial x} = -\omega_0 x + \Delta p, \quad (3.16c)$$

where Δp models impulses scaled per time unit. This gives the equation of motion (EOM)

$$\ddot{x} + \omega_0^2 x = \omega_0 \Delta p. \quad (3.17)$$

If the kicks Δp in Eq. (3.17) are due to a bunch-by-bunch feedback, as described in Sec. 2.5.3, $\Delta p = -g f_{\text{rev}} p$, where f_{rev} is required to scale the feedback gain from per turn to per second.

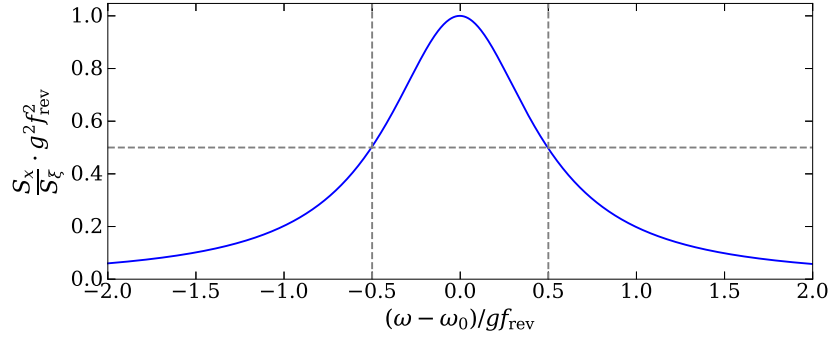


Figure 3.4: Power response of a damped harmonic oscillator of natural frequency ω_0 to a noise signal ξ at different frequencies. This is in the relevant limit of weak damping, $g f_{\text{rev}} \ll \omega_0$.

By use of Eq. (3.16b), the EOM becomes

$$\ddot{x} + g f_{\text{rev}} \dot{x} + \omega_0^2 x = 0, \quad (3.18)$$

where the feedback enters as a damping term on the LHS, as it should. Solving this with an exponential ansatz, $x \propto \exp(\lambda t)$, returns the expression for the damping time in Eq. (2.42).

If the kicks Δp in Eq. (3.17) are due to a white dipolar noise source, the COM will perform a random walk. The action of the COM will, after a kick $\Delta p = k$, be changed from $J_0 \rightarrow J_k$, as given by Eq. (3.2). By taking the average over all possible kicks, the expected change of action is

$$\langle J_k - J_0 \rangle_k = \left\langle p k + \frac{k^2}{2} \right\rangle_k = \frac{\sigma_k^2}{2}. \quad (3.19)$$

Assuming that the initial COM action is zero, $J(0) = 0$, the expected action after T turns (assuming one kick per turn) is

$$\text{E}[J(T)] = \frac{\sigma_k^2 T}{2}, \quad (3.20)$$

where the notation on the LHS stands for the expected value in time after multiple kicks.

If there are both a feedback and a noise source, $\xi(t)$, the EOM can be written

$$\ddot{x} + g f_{\text{rev}} \dot{x} + \omega_0^2 x = \omega_0 \xi(t). \quad (3.21)$$

By taking the Fourier transform, one can find that the PSD of the COM position is

$$S_x(\omega) = |\mathcal{F}(x)|^2 = \frac{|\omega_0^2| S_\xi(\omega)}{(\omega_0^2 - \omega^2)^2 + g^2 f_{\text{rev}}^2 \omega^2}. \quad (3.22)$$

The response to the noise power S_x/S_ξ is illustrated in Fig. 3.4. The response is greatest at $\omega = \omega_0$, and drops off quickly from there, being halved at $|\omega - \omega_0| = g f_{\text{rev}}/2$. Assume a white noise with a flat PSD $S_\xi(\omega) = \sigma_k^2 f_{\text{rev}}$. By use of the Wiener-Khinchin theorem, as in Eq. (3.10),

it can be shown in the limit of weak damping that

$$\lim_{t \rightarrow \infty} E[x(t)^2] = \frac{1}{2\pi} \int_{-\infty}^{\infty} S_x(\omega) d\omega = \frac{\sigma_k^2}{2g} = \lim_{t \rightarrow \infty} E[J(t)]. \quad (3.23)$$

The COM will reach an equilibrium offset due to a balance between the noise and the feedback. Note, as this is important, that if the noise instead has zero power at the frequencies close to the bunch's betatron frequency and corresponding alias frequencies, the bunch will not be significantly affected.

3.4 Rigid multi-bunch dynamics

There are typically multiple bunches in a beam, whose motion can be coupled. Consider a beam consisting of M equidistant bunches, with revolution frequency f_{rev} and transverse (non-integer) tune Q . The bunch repetition frequency is $f_b = M f_{\text{rev}}$. These bunches can oscillate in M different multi-bunch modes with phase difference between neighboring bunches [46]

$$\Delta\phi = \frac{m}{M} 2\pi, \quad (3.24)$$

where $m \in \{0, 1, \dots, M-1\}$ is the mode number. These modes have frequencies

$$f_m = f_{\text{rev}} \cdot \min\{m + Q, M - (m + Q)\} < \frac{f_b}{2}, \quad (3.25)$$

i.e. all frequencies below $f_b/2$ whose alias is $f_{\text{rev}} \cdot \min\{Q, 1 - Q\}$ with a sampling frequency f_{rev} .

Similar to the result for a single bunch in Eq. (3.22), a multi-bunch mode will only gain energy from the noise if the noise contains energy close to the betatron frequency of the mode. This

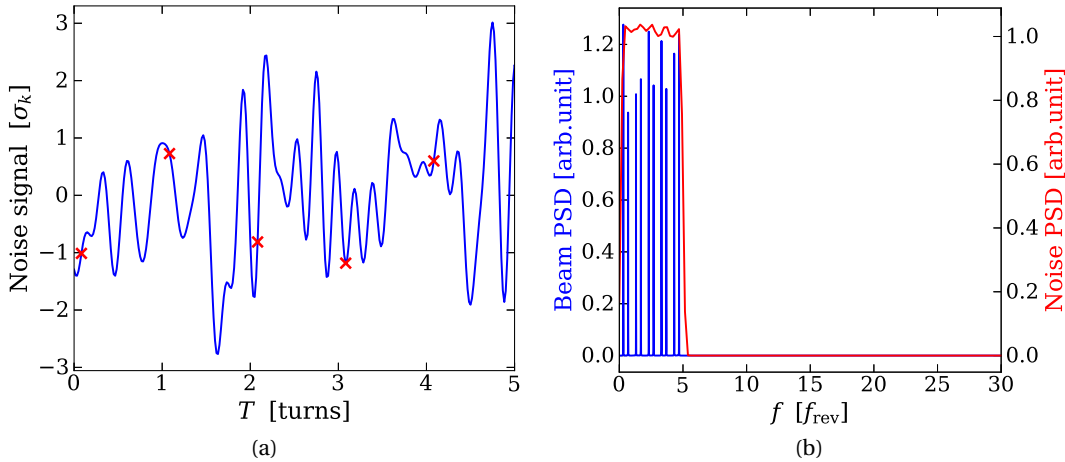


Figure 3.5: Simulation of low-frequency noise acting on 60 equidistant bunches, with $Q = 0.31$ and $g = 0.01$. (a) The noise signal in the first 5 turns, acting on each bunch once per turn. The red crosses mark the subsequent kicks on one of the bunches. (b) The PSD of both the noise in red, which is flat up to $5f_{\text{rev}}$, and the beam in blue.

can be understood intuitively if one considers, as an example, a low-frequency (LF) noise signal whose amplitude changes slowly with time. The noise will affect neighboring bunches similarly, and will therefore tend to drive multi-bunch modes with small phase differences between neighboring bunches. A numerical example is shown in Fig. 3.5, with $M = 60$ bunches affected by a noise signal with a PSD that is flat up to $f_{\max} = 5f_{\text{rev}}$ and zero above. Only the 10 multi-bunch modes with frequencies below $5f_{\text{rev}}$ are excited by the noise.

3.5 Single-bunch decoherence

Most often, real bunches do not fully behave as rigid bunches, because a tune spread is required to achieve Landau damping, as was explained in Sec. 2.6. When there is a tune spread among the particles, the COM will not oscillate indefinitely, but will decohere over time. This process will modify the distribution and bring the COM offset to 0, as illustrated in Fig. 3.6.

Consider again the change of action after a normalized kick $\Delta p = k$ in Eq. (3.2). Assuming a bunch with uniform phase distribution, the average change of action immediately after the kick is independent of the initial action J_0

$$\langle J_k - J_0 \rangle_{\phi_0} = \left\langle -\sqrt{2J_0} \sin(\phi_0) k + \frac{k^2}{2} \right\rangle_{\phi_0} = \frac{k^2}{2}. \quad (3.26)$$

What happens next depends on the feedback system and the tune spread. If there is a feedback and no tune spread, the COM will be damped back to zero without modifying the distribution. However, if there is no feedback and the bunch decoheres completely, the actions remain as they were immediately after the kick, resulting in a relative emittance growth

$$\frac{\Delta \varepsilon}{\varepsilon_0} = \frac{k^2}{2}. \quad (3.27)$$

If the kick is large, the distribution will change qualitatively [47]. However, if the kick is small, an initially Gaussian distribution will remain Gaussian, but with a larger cross-section.

The beams are not kicked once, but are continuously affected by various noise sources. The impact of the single kick can be extended to a series of uncorrelated small kicks, e.g. drawn

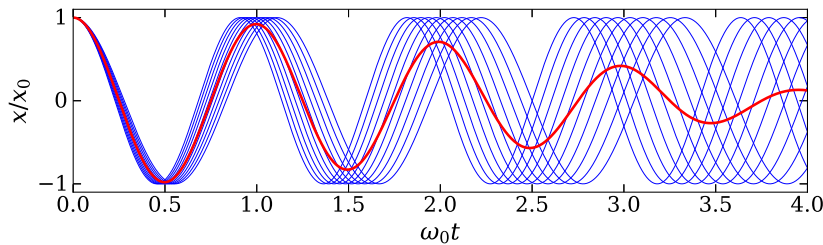


Figure 3.6: Decoherence of 10 particles starting at $(x, p) = (x_0, 0)$ with uniform frequency spread around ω_0 . The blue curves are the positions of the individual particles and the bold red curve is the COM.

from a normal distribution, $k \sim \mathcal{N}(0, \sigma_k^2)$. Due to the decoherence, the resulting distribution evolution is equivalent to the case with incoherent noise, governed by the uniform diffusion equation in Eq. (3.4) and emittance growth rate in Eq. (3.5), but with $\sigma_I \rightarrow \sigma_k$. This can be verified by both derivations of the Fokker-Planck equation in App. B. An essential assumption in these derivations is that one can average over a uniform phase distribution. This requires a fast phase relaxation, due to detuning, compared to the diffusion time in action space.

3.5.1 Feedback and incoherent detuning

If there is both a feedback system and a source of detuning, the distribution evolution will depend on the balance between the two. The change of action of a particle with incoherent tune shift $\tilde{\Delta}Q$, relative to the average tune $\langle Q \rangle_\Psi$ of all the particles in the bunch, is derived in App. C. Here, the term ‘incoherent detuning’ refers to a detuning which is independent of the bunch distribution. An example of a source of incoherent detuning are Landau octupoles. By taking the average of Eq. (C.14), both over the distribution and over the possible kicks, the familiar expression [48] for the expected relative emittance growth rate is found to be

$$\frac{\dot{\varepsilon}}{\varepsilon_0} = \frac{\sigma_k^2}{2\tau_{\text{rev}}} \left\langle \frac{\left(1 - \frac{g}{2}\right)^2 4 \sin^2(\pi \tilde{\Delta}Q)}{\left(\frac{g}{2}\right)^2 + \left(1 - \frac{g}{2}\right) 4 \sin^2(\pi \tilde{\Delta}Q)} \right\rangle_\Psi, \quad (3.28)$$

which is zero for $\tilde{\Delta}Q = 0$ and equal to the rms value of Eq. (3.27) for $g = 0$, as it should be.

3.5.2 Feedback and beam-beam interactions

In most of the operation cycle of the LHC, the main source of detuning is beam-beam interactions. In this case, the detuning does depend on the bunch distribution, and the result in Eq. (3.28) is not accurate. One main difference is that the beam-beam interactions can drive discrete modes, as introduced in Sec. 2.5.1. Additionally, the emittance growth will be shared equally between the two bunches if the noise only acts on one of the beams. Assuming that both beams are affected by white dipolar noise of kick variance σ_k^2 , the emittance growth rate with a single head-on beam-beam interaction and a transverse feedback is [49]

$$\frac{\dot{\varepsilon}}{\varepsilon_0} = \frac{\sigma_k^2}{2\tau_{\text{rev}}} \frac{1 - s_0}{2} \left(1 + \frac{g}{2\pi\xi_{\text{BB,tot}}} \right)^{-2}, \quad (3.29)$$

where $(1 - s_0)/2$ is the reduction due to the absorption of energy in the discrete beam-beam modes, and $\xi_{\text{BB,tot}}$ is the total beam-beam parameter. For round beams, it can be determined numerically that $s_0 \approx 0.645$. Hence, only $(1 - s_0)/2 = 18\%$ of the emittance growth from full decoherence is expected even without the feedback. The rest of the energy, which is carried by the beam-beam modes, can lead to an instability if not stabilized by a transverse feedback system. This is one of the reasons why the LHC is continuously operated with the ADT on. Equation (3.29) is also correct if there are two head-on beam-beam interactions with equal phase advances between the IPs for the two beams. However, the emittance growth rate can be larger in more complex configurations that include other sources of detuning, such as chromaticity, or additional beam-beam interactions, either long-range and/or a second

head-on interaction with different phase advances between the IPs for the two beams. In the latter case, the discrete beam-beam modes are expected to be inside the incoherent spectrum and no longer be able to prevent the emittance growth [41].

These analytical models of the emittance growth rate are useful. Nevertheless, simulations are necessary to model the full complexity of machines with noise, feedback systems, chromaticity, Landau octupoles, and beam-beam interactions. This will be done in Ch. 8.

3.6 Nonlinear Vlasov equation

Disclaimer: This section was adapted from the following article — with permissions of the co-author and publisher:

[50] **S. V. Furuseth** and X. Buffat, “Loss of transverse Landau damping by noise and wakefield driven diffusion”, *Phys. Rev. Accel. Beams* **23**, p. 114401, Nov. 2020. doi:[10.1103/PhysRevAccelBeams.23.114401](https://doi.org/10.1103/PhysRevAccelBeams.23.114401)

It was published under Creative commons license (CC-BY) 4.0.

My contribution: All results presented here.

So far, Landau damping of instabilities and decoherence of noise have been discussed separately in Ch. 2 and Ch. 3, respectively. However, both mechanisms affect the beam simultaneously, and should be treated together. Using a perturbation approach, one can write the distribution as

$$\Psi = \Psi_0 + \epsilon \Psi_1 + \epsilon^2 \Psi_2 + \mathcal{O}(\epsilon^3), \quad (3.30)$$

where Ψ_0 is the equilibrium distribution, assuming no wakefields nor noise, Ψ_1 and Ψ_2 are higher-order perturbations, and the tag ϵ denotes the size of each term as $\mathcal{O}(\epsilon) \ll 1$. The role of the tag is to imply the value of the term it is multiplied with. In the end it will be set to 1.

Similarly one can write the Hamiltonian as

$$\begin{aligned} \mathcal{H} &= \mathcal{H}_0 + \epsilon \mathcal{H}_1 + \epsilon^2 \mathcal{H}_2 + \mathcal{O}(\epsilon^3) \\ &= \mathcal{H}_0 + \epsilon (\mathcal{H}_{\text{wake}} + \mathcal{H}_{\text{noise}}) + \epsilon^2 0 + \mathcal{O}(\epsilon^3), \end{aligned} \quad (3.31)$$

where \mathcal{H}_0 is the equilibrium Hamiltonian, which models the phase space rotation etc., $\mathcal{H}_1 = \mathcal{H}_{\text{wake}} + \mathcal{H}_{\text{noise}}$ is the first-order perturbation, including both the weak wakefields driven by Ψ_1 and the noise, and $\mathcal{H}_2 = 0$ models the wakefields driven by Ψ_2 , which are assumed to be non-existent. As long as the beam is stable, the noise drives a perturbation $\Psi_1 \propto \mathcal{H}_{\text{noise}}$, which again drives wakefields $\mathcal{H}_{\text{wake}} \propto \Psi_1$. Hence, these terms should be of the same order, denoted by the tag. The perturbation representing the impact of the wakefields, $\mathcal{H}_{\text{wake}}$, models the collective wake force from the full ensemble of particles, as was first suggested by A. Vlasov [31]. The short-range interactions between individual particles are in this manner neglected, as required by the Vlasov equation. Such perturbations to the Hamiltonian can be constructed based on the dipolar wake potentials within the ultra-relativistic approximation, as have been done in [12, 13, 22, 32, 33, 51]. In this thesis, the perturbation $\mathcal{H}_{\text{wake}}$ is assumed to only represent the transverse kicks from weak dipolar wakefields.

The perturbations in Eqs. (3.30) and (3.31) can be inserted into the Vlasov equation in Eq. (2.44). By organizing the terms by order of ϵ , one gets

$$\frac{\partial \Psi_0}{\partial t} + [\Psi_0, \mathcal{H}_0] = 0, \quad (3.32a)$$

$$\frac{\partial \Psi_1}{\partial t} + [\Psi_1, \mathcal{H}_0] = -[\Psi_0, \mathcal{H}_{\text{wake}}] - [\Psi_0, \mathcal{H}_{\text{noise}}], \quad (3.32b)$$

$$\frac{\partial \Psi_2}{\partial t} + [\Psi_2, \mathcal{H}_0] = -[\Psi_1, \mathcal{H}_{\text{wake}}] - [\Psi_1, \mathcal{H}_{\text{noise}}]. \quad (3.32c)$$

Eq. (3.32a) models the evolution of the equilibrium distribution due to the unperturbed Hamiltonian. Similarly, the LHS of the subsequent equations model the evolution of the perturbations due to the unperturbed Hamiltonian. Without any driving terms on the RHS, Ψ_0 will remain as the initial distribution, typically assumed to be Gaussian in the transverse planes. The perturbations will, however, evolve with time due to the driving terms, which must be considered in detail:

- $[\Psi_0, \mathcal{H}_{\text{wake}}]$ is the excitation of the bunch by the wakefields. This term in addition to the LHS is the linear Vlasov equation, which was used to derive the stability limit in Sec. 2.6.
- $[\Psi_0, \mathcal{H}_{\text{noise}}]$ is the excitation of the bunch by the noise, as was studied in Sec. 3.3.
- $[\Psi_1, \mathcal{H}_{\text{noise}}]$ is the second-order excitation of the bunch by the noise, leading to a feedback dependent diffusion that will be studied in Ch. 5 [52].
- $[\Psi_1, \mathcal{H}_{\text{wake}}]$ is the second-order excitation of the bunch by the wakefields, leading to a diffusion that will be studied in Ch. 6 [50].

SINGLE-BUNCH STABILITY Part II

4 Instability latency in the LHC

This chapter acts as a motivation for Ch. 5 and Ch. 6, by focusing on discrepancies between predictions made with the linear Vlasov theory and observations made in the LHC. The most interesting observation is the concept of instability latency: a bunch that is initially stable can become unstable after a time delay referred to as the latency. To understand the underlying mechanism causing these observations is the main goal of this part of the thesis.

4.1 Discrepancies between linear theory and observations

The linear Vlasov theory has become the gold standard in evaluating beam stability in accelerator physics, because it manages to explain a wide variety of observations. Nevertheless, once and again observations are made that are not explained by this theory. Sometimes, the discrepancies can be caused by an improper experimental approach where the controlled variables have not been kept constant at the correct values. However, it can also point to physics that is not explained by the linear theory.

The possibly most concerning difference between observations in the LHC and the linear Vlasov theory is the required current in the Landau octupole magnets to keep non-colliding beams stable through Landau damping. The lowest octupole current that provides enough Landau damping to maintain beam stability will from here on be referred to as the stability threshold. Regardless of willingness to reduce the octupole current in physics fills,

“in 2018 the octupole current used for operation [was approximately] a factor 2 higher than the prediction [of the stability threshold.]” [53]

The stability margin of a factor 2 has been considered acceptable in the LHC, because the predicted threshold current of about $I_{\text{oct,thr}} \lesssim 200\text{A}$ is more than a factor 2 smaller than the maximum current of about 570A. However, in order to proceed with future designs for the HL-LHC upgrade and the FCC-hh, the cause of this discrepancy must be understood, especially whether the required stability margin to the linear theory threshold will increase or not.

Another difference between the linear theory and the observations is the value of the tune shift of the coherent modes. Both the real and imaginary parts of the tune shift, the latter of

which corresponds to the growth rate of an instability, have been found to be larger in absolute value in experiments than in simulations based on the linear theory.

“[The] factor between measurements and simulations [of the coherent tune shifts] can be estimated to be between 30% and 50%.” [54]

One possible explanation for this discrepancy, is that the impedance given as input to the linear theory is smaller than the actual impedance. The existence of an unknown ‘dark’ impedance can explain a part of the factor 2 on the stability threshold discussed above.

Another important observation was that the discrepancy between the observations and the theoretical predictions calculated numerically with DELPHI (Discrete Expansion over Laguerre Polynomials and Headtail modes) [22] depends on the linear chromaticity [55, 56].

“[F]or positive chromaticity, $Q' \geq 2$... good agreement is found between measurements and DELPHI predictions ... For negative chromaticity, $Q' < 2$, there is large disagreement between measurements and DELPHI predictions.” [56]

The threshold was severely underestimated for chromaticities close to zero, and this area is therefore typically avoided in operation. For chromaticities in the interval $Q' \in [-10, -2]$, the ideal feedback with a positive feedback gain was predicted to keep the otherwise unstable rigid mode stable without the help of octupole magnets, $I_{\text{oct,thr}} = 0\text{A}$. This was not confirmed experimentally. On the other hand, for $Q' \geq 2$, good agreement was found even without the inclusion of the ‘dark’ impedance mentioned above, suggesting that the impedance model is an accurate representation of the actual impedance.

A final important observation was that the good agreement for positive chromaticity in fact depended on the experimental approach. The experimental stability threshold is typically found by starting with a large octupole current, and then gradually reducing it step by step until the beam goes unstable.

“[M]easurements performed by reducing the octupoles in short steps of ≈ 1 minutes lead to results compatible with the model [[55]], whereas experiments with longer steps (≈ 10 minutes) revealed a difference of about a factor 2 [[57]].” [53]

The dependence on how long the machine is kept in a constant configuration implies that time is an important factor and that something is changing slowly.

4.2 Latency in physics fills and in simulations

On May 16, 2017, a bunch went unstable in the LHC after being stable in a constant machine configuration at flat-top (see Sec. 1.2) for ≈ 40 min [58]. In other words, Landau damping was lost after a slow change of a quantity that was not measured. By studying the expression in Eq. (2.45), the three possible candidates are:

- The mode frequency shift $\Delta\omega_{\text{coh}}$, relative to the stability limit $\Delta\omega_{\text{SD}}$.
- The detuning $\omega(J_x, J_y)$.
- The distribution $\Psi(J_x, J_y)$.

The mode could in principle change, with an uncontrolled shift of the chromaticity, and the detuning itself could change, both due to a dynamical change of the field strength in the superconducting magnets. However, a significant dynamical change of fields on such time scales were excluded [59]. This supported the hypothesis that it was the transverse bunch distribution that changed from the assumed Gaussian distribution to something non-Gaussian, such that a coherent mode that previously was inside the stability diagram and stable, would become outside and unstable. This type of mechanism is obviously not explained by the linear Vlasov theory, where the equilibrium distribution is assumed constant.

The detrimental change of the stability diagram, due to a modification of the transverse distribution, had previously been measured in a simulation with an artificial harmonic excitation [7]. After the measurement in operation, this effect required further studies. In simulations with external rigid white noise, transverse feedback, octupole detuning, and wakefields corresponding to the LHC impedance model, bunches that were predicted to be stable, were found to repeatedly go unstable after a significant time delay and a slow and steady distribution evolution [58]. The length of this delay, referred to as the latency of the instability, was found to have clear dependencies on the simulation parameters. Hence, the instabilities were not random events, but caused by a mechanism that steadily modified the distribution and corresponding stability diagram. Such a mechanism would explain the dependence of the experimental stability threshold on the length of the time steps when decreasing the octupole current, discussed in Sec. 4.1. The mechanism may also explain the factor 2 between the operational stability threshold and the predicted threshold, assuming Gaussian transverse distributions.

4.3 Dedicated latency experiment in the LHC

Disclaimer: This section was adapted from the following documents — with permissions of the co-authors:

- [15] **S. V. Furuseth**, X. Buffat, E. Métral, D. Valuch, B. Salvant, D. Amorim, N. Mounet, M. Söderén, S. A. Antipov, T. Pieloni, and C. Tambasco, “MD3288: Instability latency with controlled noise”, CERN, Geneva, Switzerland, Rep. CERN-ACC-NOTE-2019-0011, Apr. 2019.
- [60] **S. V. Furuseth**, D. Amorim, S. A. Antipov, X. Buffat, N. Mounet, E. Métral, T. Pieloni, B. Salvant, and C. Tambasco, “Instability Latency in the LHC”, in *Proc. 10th Int. Particle Accelerator Conf. (IPAC’19)*, Melbourne, Australia, May 2019, pp. 3204–3207. doi:[10.18429/JACoW-IPAC2019-WEPTS044](https://doi.org/10.18429/JACoW-IPAC2019-WEPTS044)

The first document is an open source CERN note, while the second document was published under CC-BY 3.0. Neither of the documents were officially peer-reviewed.

My contribution: The analysis and post-processing of the experiment. The planning and execution was performed in collaboration with the co-authors.

A dedicated experiment was conducted in the LHC on June 14 and July 26, 2018, to investigate the latency of single-bunch instabilities [15, 60]. The hypothesis at the time was that a loss of Landau damping could be caused by a change of the distribution, driven by an external rigid-bunch noise. The goals were first to confirm the hypothesis that external noise could lead to loss of Landau damping, and secondly to measure the dependence of the latency on a few key machine and beam parameters as well as the external noise amplitude.

4.3.1 Experimental procedure

The experiment was conducted over three fills in the LHC. Up to 13 proton bunches per beam were injected into the machine, with separations of 5.25 μ s or more [15]. The bunches were arranged longitudinally in each beam such that all beam-beam interactions were avoided. The ADT was used both as a feedback system and to act on the bunches as an external source of white noise up to 40 MHz, which was Gaussian in the time domain. A few key parameters are listed in Table 4.1.

The experiment was conducted as follows (two examples are presented in Fig. 4.1):

1. Accelerate the bunches to flattop with $\beta^* = 1$ m under nominal conditions.
2. For a given configuration, act on a group of 4 bunches with different noise amplitudes.
3. Wait for the bunches to go unstable. The time it took before an instability was visible on the emittance measurement is referred to as the latency.

Different machine configurations were tested systematically:

- In fill 1, the octupole current, I_{oct} , was varied.
- In fill 2, the chromaticity, Q' , was varied.
- In fill 3, the transverse feedback gain, g , was varied.

In fill 1, the noise only acted horizontally, while in fills 2 and 3, the noise acted in both transverse planes. The external background noise in the machine was assumed to be negligible compared to the applied noise. This assumption was later supported by analyzing the emittance growth rates.

The experiment was given a total time window of 16h. Therefore, if the latencies for a given configuration were too high, the current in the Landau octupoles was eventually reduced stepwise, to measure how much the stability threshold had changed in a given time. The difference between the actual octupole current when the bunches went unstable, $I_{\text{oct,thr}}^{\text{emp}}$, and the predicted octupole stability threshold, $I_{\text{oct,thr}}^{\text{the}}$, is denoted

$$\Delta I_{\text{oct,thr}} = I_{\text{oct,thr}}^{\text{emp}} - I_{\text{oct,thr}}^{\text{the}}. \quad (4.1)$$

The predictions have been calculated with DELPHI [22], assuming a Gaussian distribution with the measured intensity, emittances and bunch length at the time the noise was turned on. The rate of change of the stability threshold will be presented as $\Delta I_{\text{oct,thr}} / \tau_{\text{noise}}$, where τ_{noise} is the time during which a given bunch was affected by the external noise before it went unstable. A high rate of change of the stability threshold means that the configuration is prone to experience instabilities of short latencies, and such configurations should be avoided.

4.3. Dedicated latency experiment in the LHC

Table 4.1: Important parameters during a latency experiment conducted in the LHC [15, 60]. The bunch parameters are averaged values in e.g. the horizontal plane of beam 1 (B1H).

Parameter	Unit	Fill 1	Fills 2 & 3
Energy per proton	[TeV]	6.5	6.5
Horizontal tune, Q_x	[mod 1]	0.275	0.275
Vertical tune, Q_y	[mod 1]	0.295	0.295
Synchrotron tune, Q_s	[1]	0.00191	0.00191
Revolution frequency	[kHz]	11.2455	11.2455
Total RF voltage	[MV]	12.0	12.0
Normalized emittance B1H ¹	[μm]	1.86	1.91
Normalized emittance B1V ¹	[μm]	1.14	1.18
Normalized emittance B2H ¹	[μm]	0.87	1.37
Normalized emittance B2V ¹	[μm]	1.48	1.24
Intensity	[10^{11} p/b]	0.91	1.10
Bunch length, $4\sigma_s$	[ns]	1.12	1.07
rms momentum spread, σ_δ	[10^{-4}]	1.08	1.04

¹ Measured with the beam synchrotron radiation telescope (BSRT).

4.3.2 Results

The evolution of the emittance of two groups of bunches in B2 in fill 1 is presented in Fig. 4.1. The chromaticity was $Q' \approx 15$, and the feedback damping time in the horizontal plane of B2 was $\tau_g \approx 170$ turns. The first group was first acted on with a small noise for ≈ 10 min, which was found to be too small. Therefore the noise was doubled. The part of the latency with the smaller noise has been included with a scaling of 1/4, assuming that the latency is inversely proportional to the noise amplitude squared, as discussed later in Ch. 6. The octupole current was 452 A, while the stability thresholds predicted with DELPHI at the time

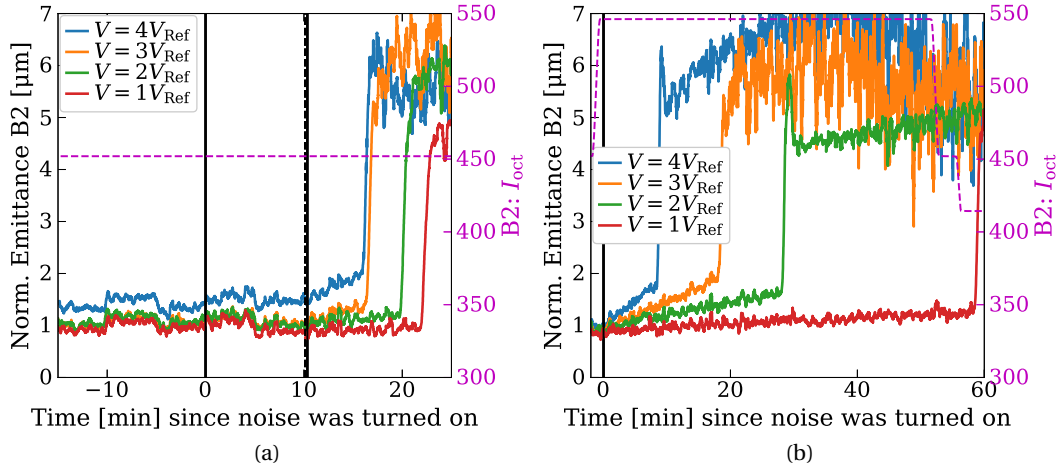


Figure 4.1: Evolution of normalized horizontal emittance for two groups of 4 bunches in Beam 2 (B2), with linearly spaced external noise amplitudes V . Displayed emittance is a rolling average over the 25 closest values measured with the BSRT. $Q' \approx 15$ and $\tau_g \approx 170$ turns. The vertical black solid (dashed) lines indicate where the noise was turned on (off).

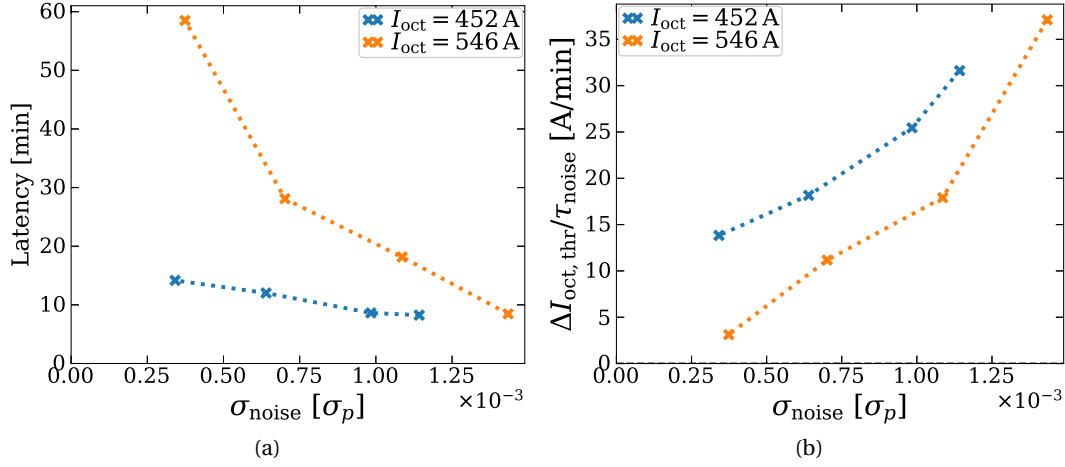


Figure 4.2: Scan of octupole current in B2, with a chromaticity $Q' \approx 15$ and damping time $\tau_g \approx 170$ turns in both transverse planes. The values for I_{oct} when the noise was turned on is given in the legends. (a) shows the latency. (b) shows the rate of change of the stability threshold.

the larger noise was turned on were $I_{\text{oct,thr}}^{\text{the}} = [193 \text{ A}, 234 \text{ A}, 235 \text{ A}, 257 \text{ A}]$, in order of decreasing noise. Hence, the operational octupole current when the bunches went unstable was a factor ~ 2 larger than the predicted threshold. Note that all the emittances measured with the beam synchrotron radiation telescope (BSRT) oscillated nonphysically during this measurement. These oscillations have been treated as an additional source of uncertainty on the measured emittance, adding up to the device specification of 10% [61]. As a result, also the predicted stability thresholds for these bunches have a higher uncertainty.

The second group, and all the subsequent groups, was only acted on by noise once. The initial octupole current for the second group was 546 A, while the stability thresholds predicted with DELPHI at the time the noise was turned on were $I_{\text{oct,thr}}^{\text{the}} = [232 \text{ A}, 221 \text{ A}, 232 \text{ A}, 225 \text{ A}]$, in order of decreasing noise. Hence, the operational octupole current when the first three bunches went unstable was a factor ~ 2.4 larger than the predicted threshold. The last bunch did not go unstable until the operational octupole current had been reduced to 414 A.

The latencies of the bunches in Fig. 4.1 are presented as a function of the noise amplitude in Fig. 4.2a. The latency was longer for a higher octupole current and a larger noise amplitude, as confirmed in simulations [58]. Note that the longest latency of ≈ 60 min was measured after a reduction of the octupole current, and is therefore most likely a lower limit on the latency. The corresponding average rate of change of the stability threshold is presented in Fig. 4.2b, being higher for a lower octupole current and higher noise amplitude.

Different chromaticities were tested with three groups in both beams of fill 2. The chromaticities were set to be $Q' \in \{0, 5, 15\}$, but were spread around these values by 2 – 4 units in both planes of both beams, according to measurements at the end of the fill. The rate of change of the stability thresholds for both beams are presented in Fig. 4.3. A non-monotonic trend was found in both beams, the rate was high for $Q' \approx 0$, low for $Q' \approx 15$ and negligible for $Q' \approx 5$.

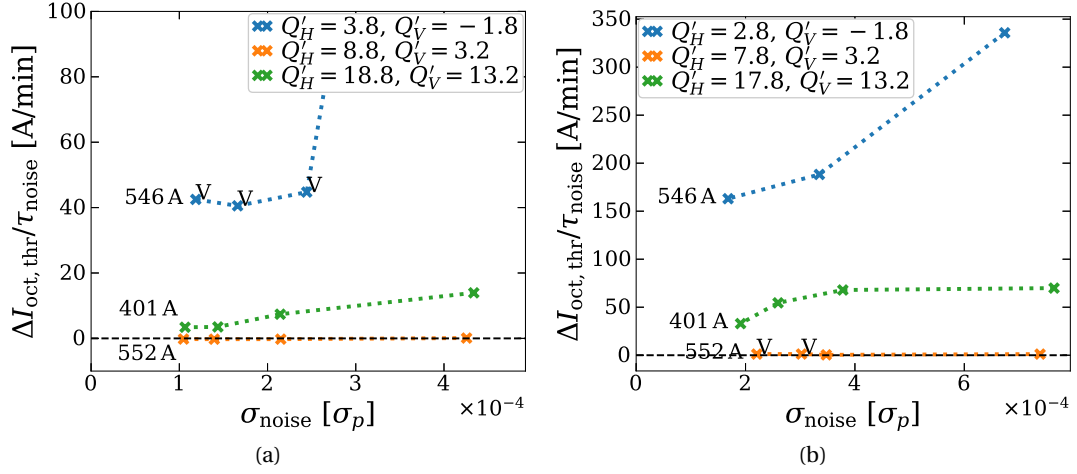


Figure 4.3: Scan of chromaticity in both beams. B1 is in (a), where the last point is at $(4.7 \times 10^{-4} \sigma_p, 404 \text{ A/min})$. B2 is in (b). The points marked with a ‘V’ became unstable vertically. The values for I_{oct} when the noise was turned on are annotated next to the lines. The damping time was $\tau_g \sim 200$ turns.

The dependence on the feedback gain was also scanned with multiple groups in fill 3. At low gains, zero bunches went unstable while affected by the noise. The noise was therefore turned off, and the gain was increased to test a new group. Many of the bunches tested at low feedback gains became unstable shortly after the gain was increased to the nominal, corresponding to $\tau_g \sim 200$ turns. However, no clear trend could be observed in the rate of change of the stability threshold [15]: at a low noise amplitude the rate was higher with a low gain, while at a high noise amplitude, the rate was higher with a high gain.

4.3.3 Discussion

The emittance is expected to grow in the presence of noise, which was also measured. Comparison between the experimental emittance growth rate and that in comparable simulations was used to estimate the noise amplitude in B1 and B2, separately. Assuming still a Gaussian distribution, the stability threshold octupole current should then have been reduced. However, Landau damping was instead lost, supporting the hypothesis of a modification of the distribution through an amplitude dependent diffusion. Because the distribution evolution is understood to be driven by the noise, it was expected that the latency would be shorter for a higher noise, as was measured.

The experiment further confirmed that with a higher I_{oct} , it takes a longer time to lose Landau damping. Moreover, with a lower I_{oct} , when the bunch is closer to its stability threshold, the rate of change of the stability threshold is higher. This supports the idea that the noise induced coherent motion, of the modes closest to their stability thresholds, participates strongly in this mechanism. This will be investigated in Ch. 6.

In this experiment it was found that the rate of change of the stability threshold was by far highest for $Q' \approx 0$. This can be explained by either an underestimation of $I_{\text{oct,thr}}^{\text{the}}$ with DELPHI,

as referred to in Sec. 4.1, or by a much shorter latency than at higher chromaticities. Therefore, no conclusion can be drawn on the dynamics around $Q' \approx 0$, based on this experiment.

Finally, the latency seemed to be shorter with a higher feedback gain in the experiment, at odds with simulations with an ideal feedback, where the latency was proportional to the feedback gain [58]. This apparent discrepancy might be explained by the additional noise introduced by the feedback itself, but requires further studies.

4.3.4 Summary

In this experiment it was successfully shown that Landau damping can be lost due to external noise, with a stability margin of more than a factor 2. This mechanism might explain why it is typically necessary to use an octupole current in the LHC about a factor 2 larger than what is predicted from a stability diagram approach assuming a Gaussian distribution.

The latency of the instabilities, which is the time from the external noise was turned on to the time when the bunches became unstable, depends on key machine parameters:

- A higher noise amplitude leads to a shorter latency.
- A higher octupole current leads to a longer latency.
- The dependence on chromaticity was non-monotonic, the latency was longest with $Q' \approx 5$, intermediate with $Q' \approx 15$ and shortest with $Q' \approx 0$.
- A higher feedback gain seemed to lead to a shorter latency in the experiments.

The latter is not compatible with results obtained in simulations, but might be explained by the noise introduced by the feedback, and requires further studies.

Another measurement presented was the rate of change of the stability threshold octupole current from the predicted value, assuming a Gaussian bunch, to the value of I_{oct} when the bunch actually went unstable. These values are more straightforward to compare than the pure latencies, as they partly filter out dependencies on a few bunch-to-bunch and group-to-group variations. The rate of change was higher with a higher noise amplitude. It was lower with a higher octupole current, implying that the process is faster as the instability threshold is approached. The dependence on chromaticity was again non-monotonic, the rate of change was negligible for $Q' \approx 5$, higher for $Q' \approx 15$, and highest for $Q' \approx 0$. The dependence on the feedback gain could not be properly resolved experimentally. Note that no bunch went unstable while the LHC was operated with a gain lower than the nominal one, although they were acted upon by noise at such gains. This was not expected, and will require further studies.

The existence of a mechanism that causes a finite instability latency for initially stable bunches has been verified in this experiment. The experimental results have given some hints on how this mechanism works. For instance, the higher rate of change of the stability threshold for a lower octupole current implies that the process is related to the least stable modes themselves. In the following two chapters, two mechanisms that can change the transverse bunch distribution are studied in detail. The ultimate goal is to have an analytical model that predicts how fast the stability threshold is approached, to guide the search for optimal machine and beam parameters, mitigating such instabilities by maximizing the latency, relevant for HL-LHC and other future projects.

5 Single-bunch evolution due to noise, decoherence, and feedback

Disclaimer: This chapter was adapted from the following articles — with permissions of the co-author and publishers:

[62] **S. V. Furuseth** and X. Buffat, “Change of beam distribution due to decoherence in the presence of transverse feedback”, in *J. Phys.: Conf. Ser.* **1350**, May 2019, p. 012118. doi:[10.1088/1742-6596/1350/1/012118](https://doi.org/10.1088/1742-6596/1350/1/012118)

[52] **S. V. Furuseth** and X. Buffat, “Long-term evolution of Landau damping in the presence of transverse noise, feedback, and detuning”, *Phys. Rev. Accel. Beams* **23**, p. 034401, Mar. 2020. doi:[10.1103/PhysRevAccelBeams.23.034401](https://doi.org/10.1103/PhysRevAccelBeams.23.034401)

Both were published under a CC-BY, 3.0 and 4.0, respectively.

My contribution: All results presented here.

5.1 Introduction

In the experiment discussed in Ch. 4, Landau damping was lost after being affected by a controllable external source of noise over an extended period of time. The working hypothesis is that this loss of Landau damping was caused by a noise induced change of the transverse bunch distribution, away from the commonly assumed Gaussian distribution.

In this chapter, an analytical theory is derived, explaining how the transverse equilibrium distribution changes in the presence of transverse noise, due to the combined effects of a transverse action dependent detuning and a transverse feedback system. The mechanism is modeled by the Fokker-Planck equation. It corresponds to a diffusion that is zero for particles with tune equal to the average tune of the bunch, and which is growing quadratically with the tune shift in the vicinity. The slow change of the distribution due to the wakefields themselves has at this stage been neglected, and will be discussed separately in Ch. 6. The stability of the slowly evolving beam is at each time step evaluated by the linearized Vlasov equation through the stability diagram.

5.2 Theory

The calculation consists of 4 steps:

1. Derive an expression for the change of the action for each particle after a kick, taking into account both the tune spread and the transverse feedback.
2. Consider the change of action as a Wiener process with a drift, and derive the Fokker-Planck equation for the particle density distribution of the bunch.
3. Solve the Fokker-Planck equation numerically to get the time evolution of the distribution. This is achieved with the code PyRADISE (Python Radial Diffusion and Stability Evolution), which is described in App. D.
4. Calculate the correspondingly evolving stability diagram, given by Eq. (2.46), numerically with the code PySSD (Python Solver for Stability Diagram) [35]. PySSD is integrated in PyRADISE, and is also described in App. D.

The 4-step calculation may be applied to various sources of tune spread. In this thesis, the focus is when the tune spread is achieved with Landau octupoles, as described in Sec. 2.3.2.

5.2.1 Change of action after a single kick

The goal of this section is to model the change of the action of each individual particle after a kick, when there is both a transverse tune spread and a transverse feedback. There already exists an expression for the subsequent emittance growth in such a configuration [48]. A similar approach will be taken here. The change of action is found to depend on the feedback gain g and the offset of the single particle tune from the average tune

$$\tilde{\Delta}Q = Q(J_x, J_y) - \langle Q \rangle_\Psi. \quad (5.1)$$

Note the distinction between $\tilde{\Delta}Q$ and ΔQ , which is the offset from the bare tune. The change of action after a kick k , given in units of the beam divergence, can in this formalism be given as

$$\begin{aligned} \Delta J &= \frac{k^2}{2} \frac{\left(1 - \frac{g}{2}\right)^2 4\pi^2 \tilde{\Delta}Q^2}{\left(\frac{g}{2}\right)^2 + \left(1 - \frac{g}{2}\right) 4\pi^2 \tilde{\Delta}Q^2} + k\sqrt{2J_0} \left(1 - \frac{g}{2}\right) \frac{\cos(\phi_0) \left(\frac{g}{2}\right) 2\pi \tilde{\Delta}Q - \sin(\phi_0) \left(1 - \frac{g}{4}\right) 4\pi^2 \tilde{\Delta}Q^2}{\left(\frac{g}{2}\right)^2 + \left(1 - \frac{g}{2}\right) 4\pi^2 \tilde{\Delta}Q^2} \\ &= \frac{1}{2} k^2 L^2 + k\sqrt{2J_0} [M \cos(\phi_0) + N \sin(\phi_0)] \\ &= \frac{1}{2} k^2 L^2 + k\sqrt{2J_0} \sqrt{M^2 + N^2} \cos\left(\phi_0 - \text{atan}\left(\frac{M}{N}\right)\right), \end{aligned} \quad (5.2)$$

where L , M and N are functions of $\tilde{\Delta}Q$ and g in this chapter only. The step-by-step derivation is given in App. C. The first term of Eq. (5.2) is an average growth, while the second term is a spread based on the phase of the particle. By averaging over the distribution, one gets the same expression for the emittance growth as in [48], assuming a uniform phase distribution. Equation (5.2) simplifies to Eq. (3.2) in the limit $g \ll \tilde{\Delta}Q$, and to 0 in the limit $g \gg \tilde{\Delta}Q$.

Equation (5.2) was derived under the assumption that the reduction of the transverse offset comes from the transverse feedback, not the decoherence ($g \gg \tilde{\Delta}Q$). The weighting functions

L^2 , M^2 , and N^2 are related to each other by the expression

$$M^2 + N^2 = L^2 + \frac{\left(1 - \frac{g}{2}\right)^2 \left(\frac{g}{4}\right)^2 (2\pi\tilde{\Delta}Q)^4}{\left[\left(\frac{g}{2}\right)^2 + \left(1 - \frac{g}{2}\right) (2\pi\tilde{\Delta}Q)^2\right]^2}, \quad (5.3)$$

where the second term on the RHS is negligible for all relevant values of $\tilde{\Delta}Q$ and g . Hence, one can rewrite Eq. (5.2) as

$$\Delta J = \frac{1}{2}k^2 L^2 + k\sqrt{2J_0}L\cos(\tilde{\phi}_0), \quad (5.4)$$

where $\tilde{\phi}_0 = \phi_0 - \text{atan}\left(\frac{M}{N}\right)$, which will still be uniformly distributed for each J_0 , and

$$L^2(g, \tilde{\Delta}Q) = \frac{\left(1 - \frac{g}{2}\right)^2 4\pi^2 \tilde{\Delta}Q^2}{\left(\frac{g}{2}\right)^2 + \left(1 - \frac{g}{2}\right) 4\pi^2 \tilde{\Delta}Q^2}, \quad (5.5)$$

with a maximum value of $(1 - g/2) \approx 1$.

The focus of this investigation is the dynamics caused by the combination of the active transverse feedback and detuning caused by Landau octupoles, because of its relevance for operation of the LHC. The detuning is given by Eq. (2.28), with in-plane detuning coefficient a_j and cross-plane coefficient b_j . In a simplified model with only horizontal noise and $b_x = 0$, L^2 takes the shape illustrated in Fig. 5.1.

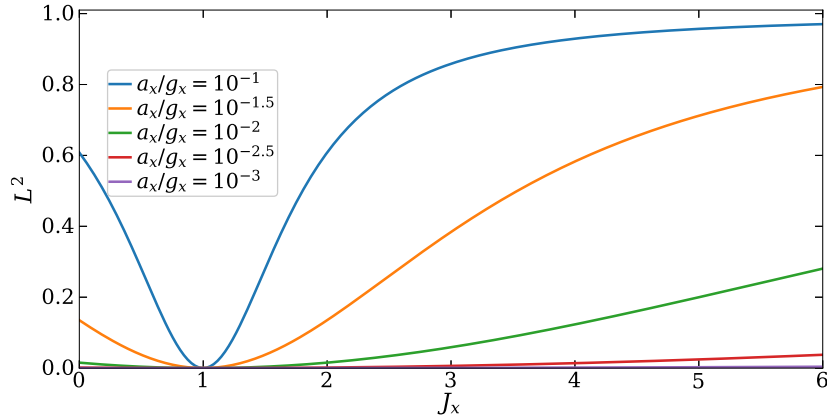


Figure 5.1: Action dependence of L^2 for a horizontal feedback gain $g_x = 0.01$ and different values for the octupole detuning coefficient a_x , in the simplified case that $b_x = 0$.

In the derivation of Eq. (5.4), the incoherent tune offset $\tilde{\Delta}Q$ was assumed constant. However, in general it depends on J , which changes during this process. Right after the kick, the action is changed to J_k , given by Eq. (3.2). Due to the feedback, the action will be reduced back towards J_0 . The variation of action during the process will be taken into account by calculating the

average of Eq. (5.4) from J_0 to J_k in the following manner:

$$\begin{aligned}
 \overline{\Delta J} &= \frac{1}{J_k - J_0} \int_{J_0}^{J_k} \Delta J(J_0) + (J' - J_0) \left. \frac{\partial \Delta J}{\partial J} \right|_{J=J_0} dJ' \\
 &= \Delta J(J_0) + \frac{J_k - J_0}{2} \left. \frac{\partial \Delta J}{\partial J} \right|_{J=J_0} \\
 &= \Delta J(J_0) + \frac{1 - \frac{g}{4}}{1 - \frac{g}{2}} \cdot \frac{k^2}{2} J_0 \frac{\partial L^2}{\partial J} + \mathcal{O}(k^4).
 \end{aligned} \tag{5.6}$$

Note that the only impact of the variation of J after the kick is through the action dependence of $\tilde{\Delta}Q(J)$. The values of J_0 and ϕ_0 are supposed to be taken prior to the kick. Terms that will become zero when averaging over ϕ_0 were dropped.

5.2.2 Fokker-Planck equation in action

The change of action after a kick k in Eq. (5.6), $\overline{\Delta J}(k, J_0, \phi_0, \tilde{\Delta}Q_0, g)$, will from here on be referred to as Δ . The next step is to derive how this change of action will change the distribution Ψ . When extending from a single kick to a sequence of kicks, modeled as a coherent white noise source, the change of action can be considered a stochastic process described by the Fokker-Planck equation derived in App. B.1 [63]

$$\partial_t \Psi = -\partial_J (U \Psi) + \partial_J^2 (J D \Psi), \tag{5.7}$$

where the drift and diffusion coefficients are given by

$$U(J, \Psi) = \int_{-\infty}^{\infty} \frac{\Delta}{\tau_{\text{rev}}} \varphi(\Delta; J, \Psi) d\Delta, \tag{5.8a}$$

$$D(J, \Psi) = \frac{1}{J} \int_{-\infty}^{\infty} \frac{\Delta^2}{2\tau_{\text{rev}}} \varphi(\Delta; J, \Psi) d\Delta, \tag{5.8b}$$

where τ_{rev} is the time interval between each kick, set equal to the revolution period. The division of D by J , in comparison to the alternative diffusion coefficient $\tilde{D} = JD$, will be convenient in the following. For this process to be modeled well by the Fokker-Planck equation, the detuning must be fast enough, relative to the noise amplitude, to achieve the required phase relaxation. For increasingly large noise amplitudes, this model is therefore gradually less able to accurately represent the dynamics.

The probability distribution for the change of action after a kick, derived from Eq. (5.6), can be written as

$$\varphi(\Delta; J, \Psi) = \frac{F(k) dk}{\pi \sqrt{2Jk^2 L^2 - \left[\Delta - \frac{k^2}{2} \left(L^2 + \frac{1 - \frac{g}{4}}{1 - \frac{g}{2}} J \frac{\partial L^2}{\partial J} \right) \right]^2}}, \tag{5.9}$$

and it is defined only between the singularities. $F(k)$ is the probability distribution of the kicks, assumed to have zero mean and STD σ_k .

The next step is to calculate the coefficients $U(J, \Psi)$ and $D(J, \Psi)$. The integral over Δ must be done first, as its limits depend on k . When assuming a uniform phase distribution, the coefficients become

$$D(J, \Psi) = \frac{\sigma_k^2}{2\tau_{\text{rev}}} L^2, \quad (5.10a)$$

$$U(J, \Psi) = D + \frac{1 - \frac{g}{4}}{1 - \frac{g}{2}} J \frac{dD}{dJ}. \quad (5.10b)$$

The second term of U comes from the inclusion of the dynamically evolving $\tilde{\Delta}Q$ during the decoherence process, i.e. by using $\overline{\Delta J}$ instead of ΔJ .

The last step is to insert the expressions for U and D of Eq. (5.10) into the Fokker-Planck equation of Eq. (5.7). The first term of U cancels $\partial_J[\partial_J(J)D\Psi]$. In the assumed limit of small g , the second term cancels the term $\partial_J[J\partial_J(D)\Psi]$. Thus, the Fokker-Planck equation turns into the well-known diffusion equation

$$\partial_t \Psi = \partial_J [JD\partial_J(\Psi)]. \quad (5.11)$$

This equation could also be obtained by assuming a time reversal symmetry on the microscopic level. That is, the probability of going from J_a to J_b is equal to the process of going back, or $\varphi(J_b - J_a; J_a) = \varphi(J_a - J_b; J_b)$.

If one would have assumed constant tunes during the feedback and decoherence process of a single kick, the D in Eq. (5.11) would have been inside the inner derivative. That partial differential equation (PDE) would have corresponded to a stochastic process where the probabilities of reducing and increasing the action by Δ from an initial action J_0 were equal, or $\varphi(\tilde{\Delta} + \Delta; J_0) = \varphi(\tilde{\Delta} - \Delta; J_0)$, where $\tilde{\Delta} = k^2 L^2 / 2$ is assumed small. It is a subtle, but important distinction from the process modeled by Eq. (5.11), and it will be highlighted in Sec. 5.3.

This theory will now be extended to a general 2D Fokker-Planck equation like

$$\partial_t \Psi = \sum_{j=0}^1 \frac{\partial}{\partial J_j} \left[-U_j \Psi + \sum_{i=0}^1 \frac{\partial}{\partial J_i} \left(\sqrt{J_j J_i} D_{ji} \Psi \right) \right], \quad (5.12)$$

where the indexes i and j go over the two transverse planes, with definitions of U_j and D_{ji} as before. This equation can be obtained by doing a 2D Taylor expansion as in App. B.1. As for a single plane, it is still true that $U_j \propto \sigma_{kj}^2 + \mathcal{O}(\sigma_{kj}^4)$ and $D_{jj} \propto \sigma_{kj}^2 + \mathcal{O}(\sigma_{kj}^4)$. Since the external noise in the two planes is considered to be uncorrelated, $\langle k_x k_y \rangle_t = 0$, the coupling diffusion coefficients can be considered negligible, because $D_{xy} = D_{yx} \propto \sigma_{kx}^2 \sigma_{ky}^2 \ll D_{jj}$. The Fokker-Planck equation in 2D transverse action space, which corresponds to Eq. (5.11) for one transverse plane, can therefore be written as

$$\frac{\partial \Psi}{\partial t} = \frac{\partial}{\partial J_x} \left(J_x D_{xx} \frac{\partial \Psi}{\partial J_x} \right) + \frac{\partial}{\partial J_y} \left(J_y D_{yy} \frac{\partial \Psi}{\partial J_y} \right). \quad (5.13)$$

The diffusion coefficients are given as before,

$$D_{jj} = \frac{\sigma_{kj}^2}{2\tau_{\text{rev}}} L^2 [g_j, \tilde{A}Q_j(J_x, J_y)], \quad (5.14)$$

where it has been written explicitly that L^2 depends on the detuning and feedback gain in the given transverse plane.

5.2.3 Solving the Fokker-Planck equation

To get the evolution of the bunch distribution, one must either solve Eq. (5.11) in 1D or Eq. (5.13) in 2D. Without the feedback, $\tilde{A}Q \gg g$, there will be no action dependence of the diffusion coefficient, and the distribution will simply widen, as in Eq. (3.4). In another extreme limit, $g \gg \tilde{A}Q$ and $\tilde{A}Q \rightarrow 0$, the diffusion coefficient will be zero. The offsets from the kicks will be damped, without modifying the distribution at all.

In the interesting regime, when both the feedback and the detuning will be relevant, the coefficients will depend on the transverse actions, and a numerical solver is required to determine how the distribution will change. To do so, a PDE solver named PyRADISE has been developed. It is described in detail in App. D. In the results that follow, the boundary condition (BC) at $J_{\text{max}} = 20$ is absorbing, representing a physical aperture in a real machine, the COM tune, $\langle Q \rangle$, is kept constant, and the grid is 700×700 in 2D. The stability diagram is calculated numerically after each discrete time step, using PySSD [35] to perform the integral in Eq. (2.46) with a uniform trapezoidal discretization in (J_x, J_y) .

5.3 Numerical verification

In this section, the objective is to numerically test and verify the theory derived in Sec. 5.2 by means of particle tracking simulations. The radius in transverse phase space is defined as

$$r = \sqrt{2J}, \quad (5.15)$$

and will at times be referred to instead of the action.

5.3.1 Change of action after a single kick

The change of action after a kick and the subsequent decoherence was derived and found to be given by Eq. (5.6). Here, this will be tested with 1D toy models without dependence on the vertical plane, with $g_x = 0.1$, $a_x = 5 \times 10^{-4}$ and $b_x = 0$. Simulations of this configuration have been run with 10^7 macroparticles for 150 turns, after a single horizontal kick of various amplitudes k . Macroparticles are used in simulations to represent multiple particles, e.g. representing a bunch of $N = 10^{11}$ protons with $N_p = 10^7$ macroparticles of higher mass and charge. The phase advance per particle has been kept constant in one set of simulations, and evolving dynamically as J changes in another. The first abides by the assumptions used to derive Eq. (5.4), while the second is the actual beam dynamics, which is modeled by Eq. (5.6).

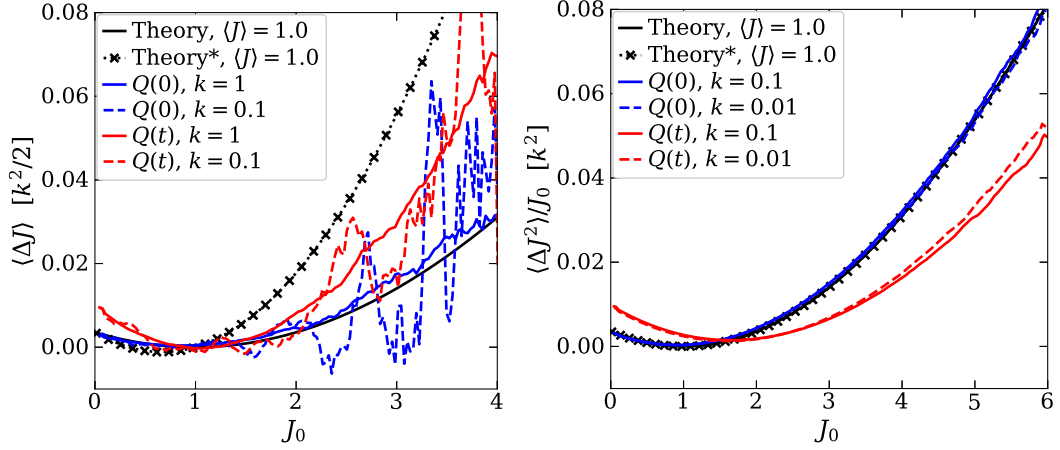


Figure 5.2: Change of action after a single kick of amplitude k as a function of the particles' initial actions. Multi-particle simulations were run with constant tunes corresponding to the initial actions, $Q(0)$, and dynamically evolving tunes corresponding to the evolving actions, $Q(t)$. The simulations are compared to a theory assuming constant tunes, and a modified theory, denoted in the legend by *, given by Eq. (5.4) and Eq. (5.6), respectively.

The dependence of $\langle \Delta J \rangle_\phi$ and $\langle \Delta J^2 \rangle_\phi$ on J_0 is presented in Fig. 5.2. They are compared to the theory given by Eq. (5.4) and modified theory including dynamical tunes given by Eq. (5.6). The modification did not change the expected value for $\langle \Delta J^2 \rangle_\phi$ to first order. The simulated curves for $\langle \Delta J \rangle_\phi$ have more statistical noise, as the average is proportional to k^2 , while the spread is proportional to $k\sqrt{J_0}$, which is why the curves stop at $J_0 = 4$ and were not calculated for $k < 0.1$. The agreement is excellent between Eq. (5.4) and the simulations with constant tune, denoted by $Q(0)$. The expression in Eq. (5.4) has thus been verified numerically, using the same assumptions. There is a difference between the modified theory and the simulations run with dynamically evolving tunes, denoted by $Q(t)$. The dependence on the dynamical tunes does have an impact. The difference appears not to diminish for smaller kicks k . The difference between the simulations and the modified theory is similar for $\langle \Delta J \rangle_\phi$ and $\langle \Delta J^2 \rangle_\phi$. Hence, the agreement is considered acceptable for this study. If this mechanism would have been found to be critical for long-term beam stability, it could deserve further studies.

5.3.2 Fokker-Planck vs multi-particle simulations

The importance of modeling the evolution of the tunes, due to the change of action following a kick, seemed to not modify the qualitative behavior significantly in Sec. 5.3.1. Here, the change of the distribution after multiple infinitesimal kicks is considered. A 1D toy configuration will be studied, with $a_x = 5 \times 10^{-3}$, $b_x = 0$ and $g_x = 0.2$.

In the derivation of Eq. (5.4), it was assumed that the amplitude of the stochastic process was solely dependent on the particle parameters before the kick. This can be modeled by either the Fokker-Planck equation in Eq. (5.7), without the second term on the RHS of Eq. (5.10b), or with a multi-particle simulation with a centered incoherent noise of variance $\sigma_k^2 \cdot L^2$ over T turns. The distribution evolutions, predicted by the Fokker-Planck solver and measured in

the simulation after $\sigma_k^2 \cdot T = [0, 1, \dots, 4] \cdot 25/6$ turns, are shown to have a perfect agreement in Fig. 5.3a. The time is scaled to hours of operation of the LHC, with a noise of $\sigma_k = 5.77 \times 10^{-4}$, comparable to the noise amplitude in the experiment described in Ch. 4.

The more accurate description of the beam dynamics includes the dynamical evolution of the tune of the incoherent particles. Such a multi-particle simulation has been run, using 4×10^6 macroparticles and 4×10^6 turns. The distribution is shown in Fig. 5.3b after T turns such that $\sigma_k^2 \cdot T = [0, 1, \dots, 8] \cdot 25/6$ turns. The evolution of multiple edges in the simulation can be a numerical artifact. Clearly, this distribution evolution is qualitatively different from the one in Fig. 5.3a.

The distribution evolution modeled by the Fokker-Planck equation in Eq. (5.11) is given in Fig. 5.3c. This evolution is in better agreement with the realistic multi-particle simulation. According to the new theory, an edge develops at $r = \sqrt{2} \approx 1.4$, where $\tilde{\Delta}Q = 0$. This is the effect of the diffusion: Ψ increases at $J \lesssim J(\tilde{\Delta}Q = 0)$ and at large J , and is depleted at $J \gtrsim J(\tilde{\Delta}Q = 0)$ and at $J \sim 0$. In other words, Ψ flattens in the two regions separated by $J(\tilde{\Delta}Q = 0) = 1$, with a step in between.

The expected distribution evolution due to multiple small uncorrelated kicks is governed by Eq. (5.11). This works well for continuous distribution functions and non-zero diffusion coefficients. However, in this case, the distribution evolves towards a hard step with a singular derivative at the action of zero diffusion coefficient, $J(\tilde{\Delta}Q = 0)$, making the product $D\partial_J\Psi$ in Eq. (5.11) undefined and inaccurately evaluated with the numerical solver. Therefore, even though discontinuities have been observed also in multi-particle simulations, the evolution calculated numerically based on the Fokker-Planck equation becomes inaccurate as the distribution approaches this hard step.

The mechanism at hand, the evolution of the stability diagram due to amplitude dependent transverse diffusion, caused by the combined effect of amplitude dependent detuning and active feedback, is difficult to assess with multi-particle simulations. Relevant parameters for this effect in the LHC are $g \sim 0.1$, $\tilde{\Delta}Q \sim 10^{-4}$, $\sigma_k \sim 10^{-4}$, $N \sim 10^{11}$ particles per bunch, $T \sim 10^7$ turns. There are multiple numerical obstacles: (i) The process is according to Fig. 5.1 strongly dependent on the ratio $\tilde{\Delta}Q/g \sim 10^{-3} \ll 1$, and altering it will correspond to a different machine configuration; (ii) The COM offset depends on the noise and feedback gain as $\sqrt{\langle x \rangle_\Psi^2} = \sigma_k / \sqrt{2g} \sim 2 \times 10^{-4} \ll 1$, neglecting the damping from the decoherence. If the COM offset becomes significantly larger, e.g. if one increases σ_k to reduce the necessary number of turns in the simulation, the detuning per particle will be averaged over a wider range, leaving the assumption of a weak noise perturbation, and the diffusion becomes closer to uniform; (iii) Due to a limited number of N_p macroparticles, the ideal feedback causes unphysical, numerical stochastic cooling [64, 65]. This effect is weaker for larger N_p/g ; (iv) The rate of change in the distribution is for small $\tilde{\Delta}Q/g$ proportional to $T\sigma_k^2\tilde{\Delta}Q^2/g^2$. Bringing it all together, a good simulation will have a large $N_p T \cdot \tilde{\Delta}Q^2/g^2 \cdot \sigma_k^2/g \sim N_p T \cdot 4 \times 10^{-14}$. The complexity of the simulations will approximately be proportional to $N_p T$, which will have to be large. Experience has shown that $N_p T \geq 10^{13}$, with $N_p \sim T$, is necessary to get an estimate of this effect, but with further improvement achievable for higher $N_p T$. Assuming a perfect simulation, it is also required to have an even higher N_p to interpolate the multi-particle bunch to get an agreeable expression for $\partial_J(\Psi)$, which enters in Eq. (2.46) for the stability

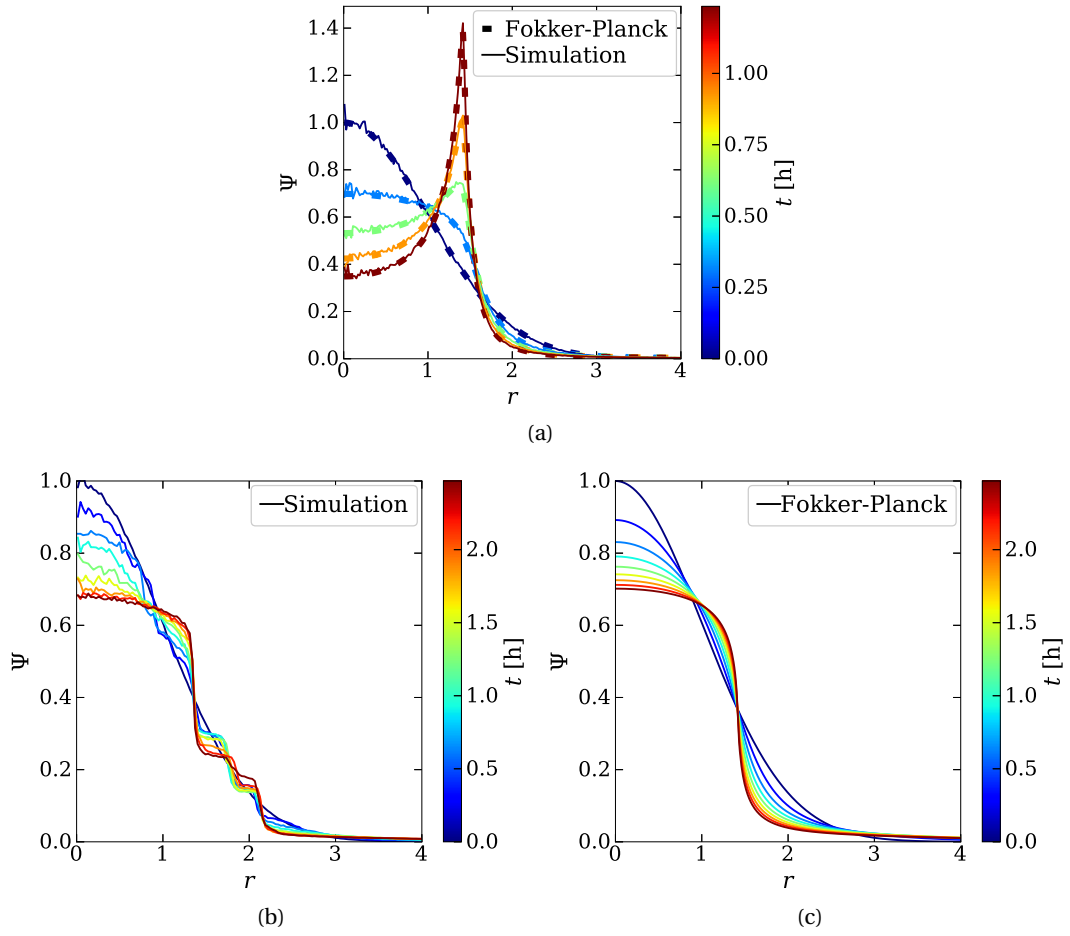


Figure 5.3: Distribution evolution in units of $r = \sqrt{2J}$ with $a_x = 5 \times 10^{-3}$, $b_x = 0$, $g_x = 0.2$, and equivalent noise of $\sigma_k = 10^{-3}/\sqrt{3}$. (a) shows the process modeled by ΔJ given by Eq. (5.4), and a multi-particle simulation with incoherent noise of variance $\sigma_k^2 \cdot L^2$. (b) shows a realistic multi-particle simulation of this process, using 4×10^6 macroparticles and 4×10^6 turns. (c) shows the process modeled by ΔJ given by Eq. (5.6).

diagram. For numerical calculations of the stability diagram, good statistics up to $r = 6$ is necessary.

5.4 Results

In this section, results obtained by solving the Fokker-Planck Eq. (5.13) with PyRADISE will be presented. First, two test cases are presented in Sec. 5.4.1, focusing on the distribution evolution in 2D and corresponding evolution of the stability diagram. Then, the effective detuning strength will be defined in Sec. 5.4.2. Finally, the effective detuning strength will be studied in several scans of the relevant parameters in Sec. 5.4.3. Symmetry is assumed between the detuning coefficients and feedback gains in the transverse planes in all configurations, i.e. $a_x = a_y = a$, $b_x = b_y = b$ and $g_x = g_y = g$. Hence, the subscripts will not be included in the following.

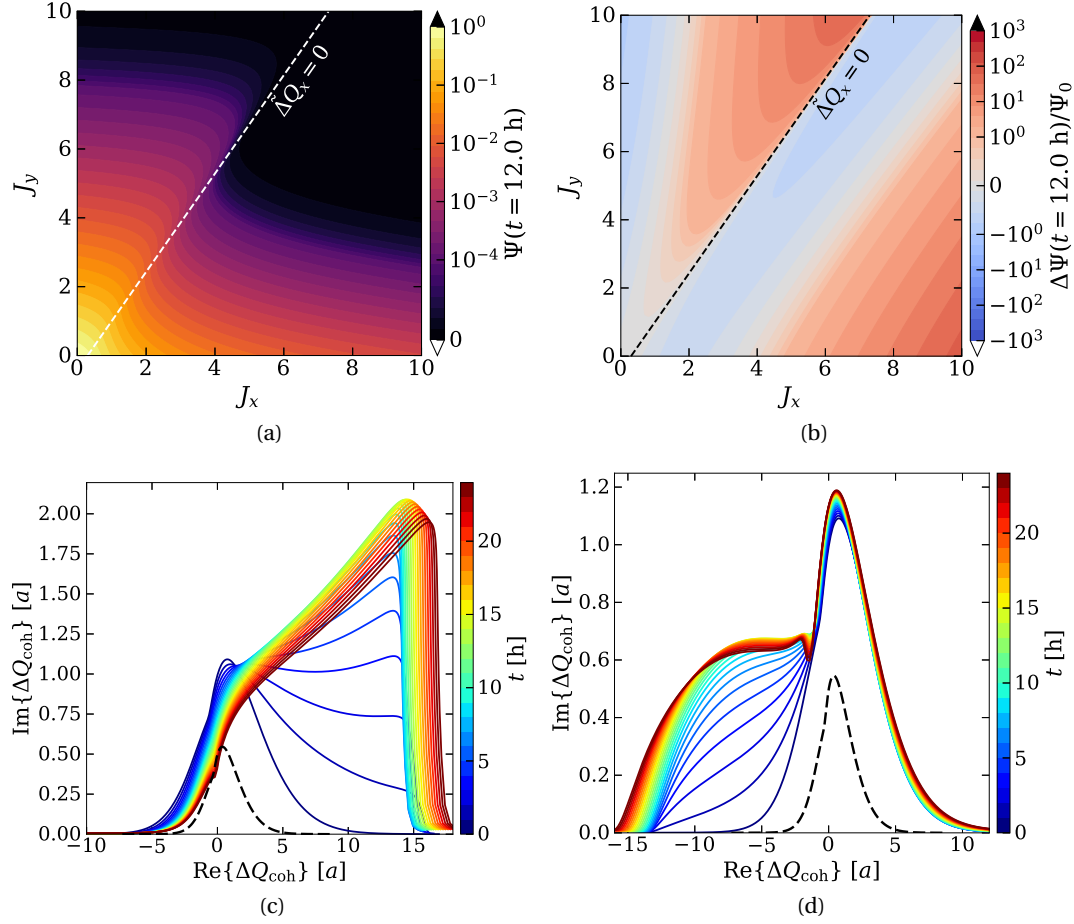


Figure 5.4: Evolution with noise in the horizontal plane only: (a) distribution after 12h; (b) corresponding relative change of the distribution; (c) and (d) stability diagrams in the horizontal and vertical planes, respectively. The black dashed curves in the stability diagrams correspond to the stability diagrams of the initial distribution with half the detuning strength.

5.4.1 Distribution and stability evolution

Now, a more realistic model for the LHC will be considered, with $a = 5 \times 10^{-5}$, $b = -3.5 \times 10^{-5}$, $g = 0.01$, and $\sigma_{kj} = 5 \times 10^{-4}$. This noise amplitude is compatible with the experiment in the LHC that is described in Ch. 4. First, a configuration with noise only in the horizontal plane is considered. Secondly, a configuration with equal noise in both planes will be considered. The number of turns T have been scaled to a time variable $t = T/f_{\text{rev}}$, where f_{rev} is the revolution frequency in the LHC.

The distribution and relative change of the distribution after 12h, with noise only in the horizontal plane, is displayed in Figs. 5.4a and 5.4b, respectively. This is an equivalent trend for each value of J_y , as the one in Fig. 5.3c, except for that $J_x(\tilde{\Delta}Q_x = 0)$ now depends on J_y . Therefore, it is more difficult to see that the projection of the new distribution in the (x, y) plane is not Gaussian, than with $b = 0$. The stability in the horizontal plane evolves as in Fig. 5.4c, and in the vertical plane as in Fig. 5.4d. After 24 h, the horizontal stability diagram is partly inside the

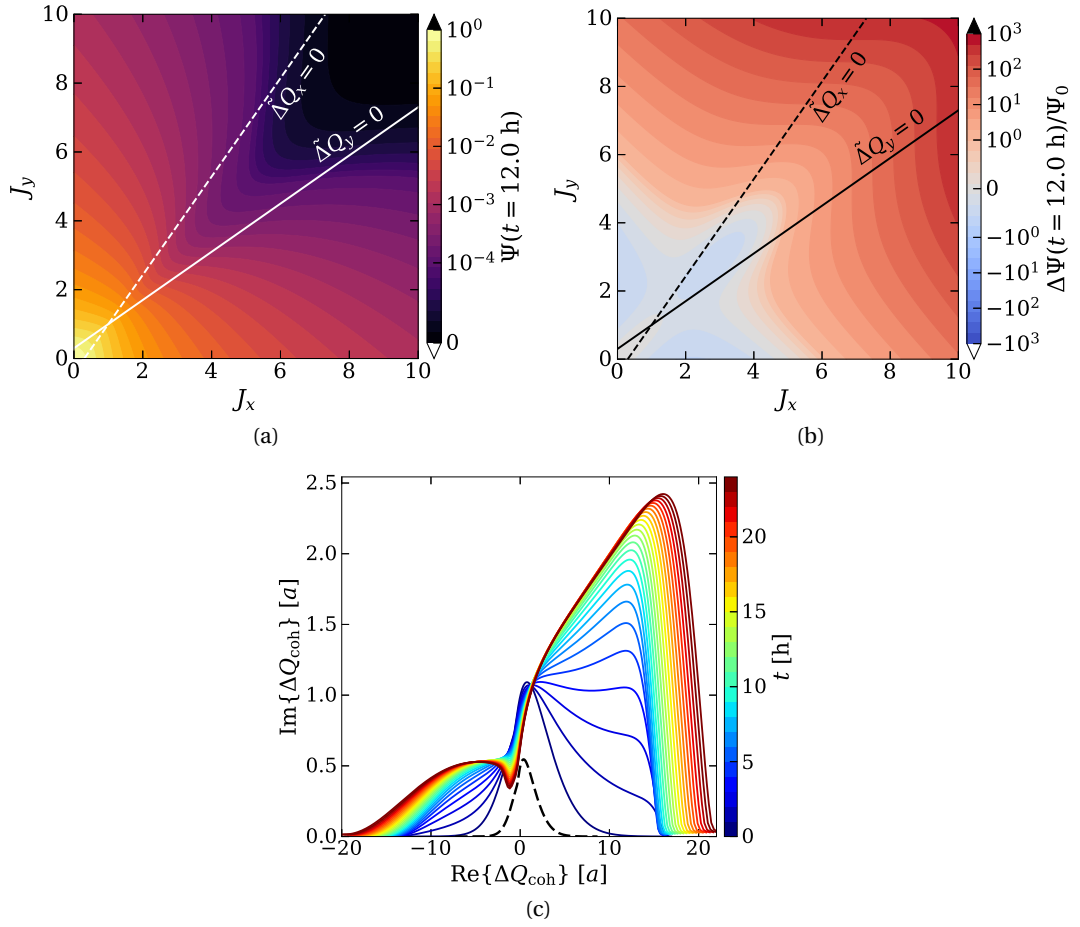


Figure 5.5: Evolution with equal noise and detuning in both planes: (a) distribution after 12h; (b) corresponding relative change of the distribution; (c) stability diagram. The stability diagram evolves equally in both planes, due to symmetry. The black dashed curve in the stability diagram corresponds to the stability diagram of the initial distribution with half the detuning strength.

black dashed curve, which is the stability diagram of the initial distribution with half the detuning strength. The vertical stability decreases initially slightly at positive $\text{Re}\{\Delta Q_{\text{coh}}\}$, but there is no extreme reduction of the stability for any real tune shift. However, at $\text{Re}\{\Delta Q_{\text{coh}}\} \approx -1.6a$, the drilling of a hole has begun. This is due to the uncommon appearance of a positive distribution derivative, $\partial\Psi/\partial J_y > 0$, close to $\tilde{\Delta}Q_x = 0$.

The distribution and relative change of the distribution after 12h, with equal noise in both transverse planes, is displayed in Figs. 5.5a and 5.5b, respectively. The evolution is driven by both horizontal and vertical diffusion. Where the horizontal diffusion is zero, the particles only diffuse vertically, leading to a zero distribution derivative, $\partial\Psi/\partial J_y \approx 0$. Due to perfect symmetry between the two planes, in noise, decoherence, and feedback, the stability in both planes evolves as in Fig. 5.5c. The evolution of the stability diagram is in this case qualitatively similar to the sum of the evolutions in both planes when there was only horizontal noise. There is a reduction of the stability limit at $\text{Re}\{\Delta Q_{\text{coh}}\} \sim 0$, especially for weakly negative real

coherent tune shifts, where the most problematic coherent modes in the LHC reside [66]. After 24 h, the stability limit has been reduced to almost that of the initial distribution with half the detuning strength.

5.4.2 Relative effective detuning strength

A stability diagram has been calculated for each distribution $\Psi(t = t_k)$ with the correct detuning coefficients, as described in App. D and presented in Figs. 5.4 and 5.5. In addition, stability diagrams have been calculated for the initial Gaussian distribution $\Psi(t = 0)$ with scaled detuning coefficients $(a_s, b_s) = s \cdot (a, b)$. The relative effective detuning strength at time t_k is defined as the largest factor s that corresponds to a stability diagram that is completely inscribed in the stability diagram for distribution $\Psi(t = t_k)$. It represents a pessimistic characterization of the potential reduction of Landau damping at a given time.

The evolution of the relative effective detuning strengths for the two cases in Sec. 5.4.1 are presented in Fig. 5.6. The decrease of the stability limit is evident, except in the vertical plane when there was no vertical noise. The effective detuning strengths are after 24 h, in these cases, reduced to as low as 42% of the octupole detuning one actually has in the machine. That the relative effective detuning strength eventually becomes smaller than 0.5, is visualized by the red curves in Fig. 5.4c that cross the dashed black line corresponding to a relative detuning strength of $s = 0.5$. As seen by the evolution of the stability diagrams in the previous section, the stability does also increase for certain values of $\text{Re}\{\Delta Q_{\text{coh}}\}$, the relative effective detuning strengths correspond to a worst-case scenario.

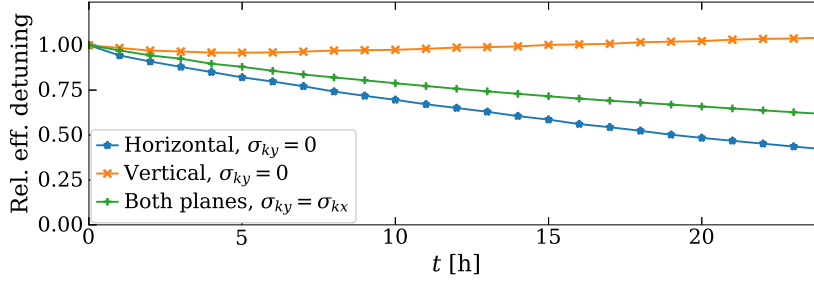


Figure 5.6: Evolution of the relative effective detuning strengths, corresponding to the distribution evolutions in Figs. 5.4 and 5.5.

5.4.3 Parameter dependence

It is of both academic and operational interest to investigate how the impact of this mechanism scales with the most important parameters, a , b , g and σ_{kj} . These parameters have been varied to look for the optimal and worst configurations. The parameters were varied relative to $a_0 = 5 \times 10^{-5}$, $b_0 = -0.7a_0$, $g_0 = 0.01$, $\sigma_{kx0} = \sigma_0 = 5 \times 10^{-4}$ and $\sigma_{ky0} = 0$, as in the configuration in Fig. 5.4.

In the limit $g \gg a$, which is relevant for machine operation, the diffusion coefficients in Eq. (5.14) mostly depend on the parameter $\sigma_{kj}a/g$. This is confirmed by the scans of a/a_0 ,

g_0/g and σ_{kx}/σ_0 , presented in Figs. 5.7a, 5.7b and 5.7c, respectively. There is a small difference for the largest values of a/g , as expected. Note that the largest two values of $\sigma_{kx}a/g$ are included for completeness, but they are not realistic in the LHC as of now. The scans of a/a_0 and g_0/g were repeated while keeping $\sigma_{kx}a$ and σ_{kx}/g constant, respectively. In these scans, there were no clear dependences on a or g . Note that an increase of a corresponds to an increase of the stable area for ΔQ_{coh} . Here, the focus is the *relative* change of this area. With a larger a , there is a larger initial margin for a given mode to go unstable, but the reduction of the margin is also faster, according to these results.

The ratio b/a has also been studied. This ratio is typically about -0.7 in the LHC, but it is possible to operate with other ratios, as it mainly depends on the ratio of the transverse β -functions at the locations of the octupoles [34]. Note that varying b/a will change the shape of the stability diagram. The ratio b/a is typically negative, which generates Landau damping for coherent modes of both positive and negative $\text{Re}\{\Delta Q_{\text{coh}}\}$ [67]. The modes in the LHC have in general a negative tune shift, $\text{Re}\{\Delta Q_{\text{coh}}\} < 0$. Hence, it could be desired to keep $\{a, b\} < 0$. However, this is not possible in the LHC. The scan of b/a is presented in Fig. 5.7d. The evolution of the vertical stability is worst for $b/a \in \{-1, 1\}$. In these configurations, the horizontal and vertical isotune curves (curves of equal tunes) in 2D action space are equal. Therefore, the positive derivative $\partial\Psi/\partial J_y$, which is visible in Fig. 5.4b, will add up for certain Q in Eq. (2.46), such that the stability limit on $\text{Im}\{\Delta Q_{\text{coh}}\}$ becomes negative. Note that $b_x/a_x \propto \varepsilon_y/\varepsilon_x$. Hence, a bunch in the LHC with larger vertical than horizontal emittance can have $b/a = -1$. This was approximately the case for several of the bunches in the experiment in Ch. 4. However, vertical latencies of ~ 10 h are far above what was measured. The evolution of the horizontal stability is not strongly dependent on b/a .

Next, the vertical noise was increased, and the scan is shown in Fig. 5.7e. The noise amplitudes σ_{kx} and σ_{ky} were varied such that $\max\{\sigma_{kx}, \sigma_{ky}\} = \sigma_0$, and the relative difference $\text{rel}(\sigma_{kx} - \sigma_{ky})$ was scanned, which has been defined as

$$\text{rel}(\alpha - \beta) = \frac{\alpha - \beta}{\alpha + \beta}, \quad \alpha, \beta \geq 0. \quad (5.16)$$

Due to an otherwise perfect symmetry, the change of the relative effective horizontal detuning strength for $\text{rel}(\sigma_{kx} - \sigma_{ky}) = d$ is equal to the relative effective vertical detuning strength for $\text{rel}(\sigma_{kx} - \sigma_{ky}) = -d$. The relative effective detuning strength in a plane is reduced the fastest with noise in only that plane, and the least with noise in only the other plane, as was already seen in Sec. 5.4.1.

At last, an incoherent noise of amplitude σ_{Ij} has been introduced, to model in a simplified manner the stochastic process generated by IBS. The incoherent noise amplitude corresponds to a uniform diffusion coefficient $D_I = \sigma_I^2/2\tau_{\text{rev}}$. Such a uniform diffusion will cause a distribution to become more Gaussian, and will therefore counteract the destabilizing change in the distribution, driven by the coherent noise. A scan with noise in the horizontal plane only is shown in Fig. 5.7f. The vertical noise was kept at zero. The horizontal noise amplitudes σ_{kx} and σ_{Ix} were varied to scan $\text{rel}(\sigma_{kx} - 10\sigma_{Ix})$ from -1 to 1 , keeping $\sigma_{kx} = \sigma_0$, except for when the relative difference is -1 , in which case $\sigma_{kx} = 0$ and $\sigma_{Ix} = \sigma_0/2$. The incoherent noise is beneficial for long-term beam stability. However, after ~ 4 h, there was a reduction of the

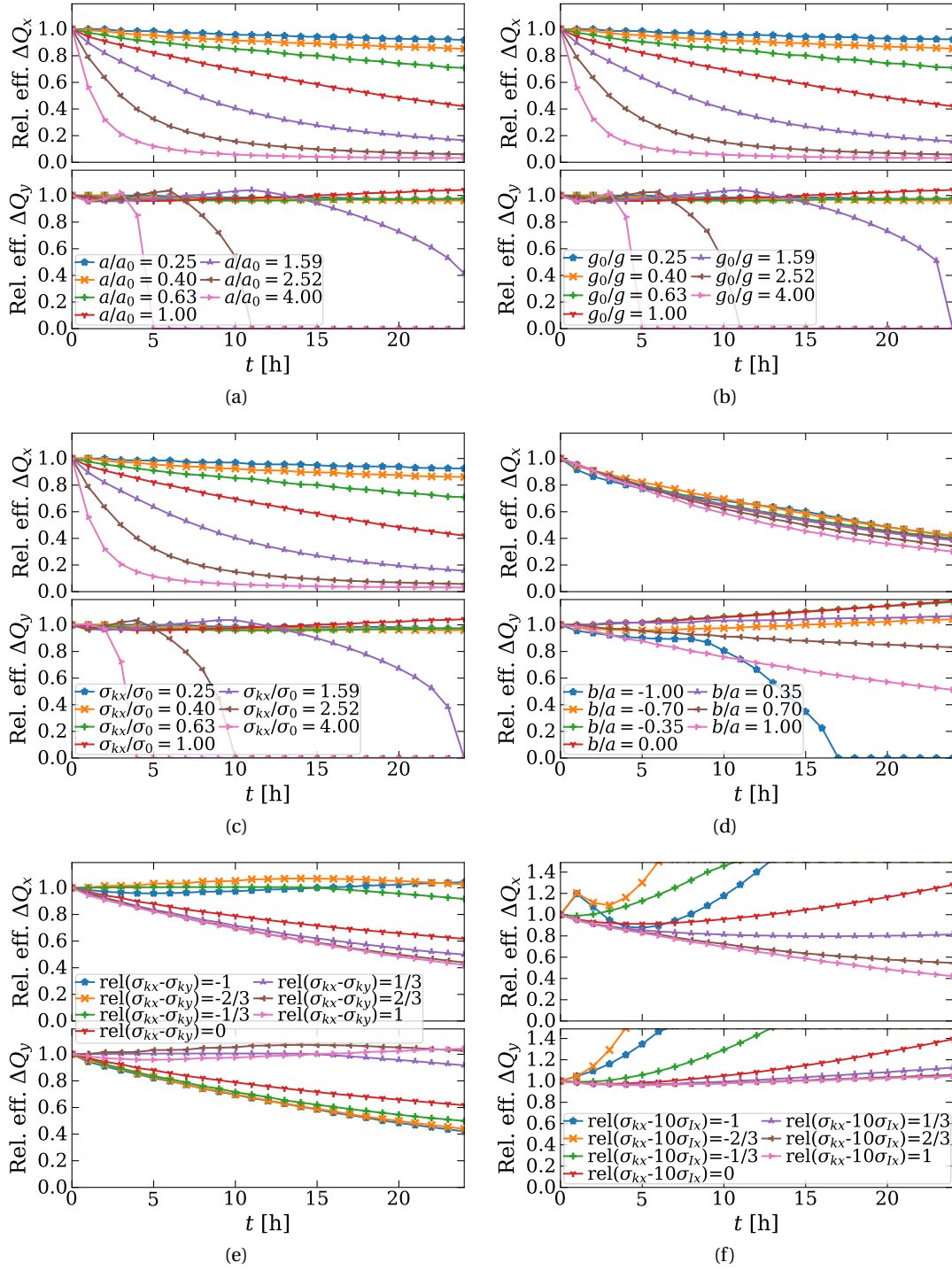


Figure 5.7: Scan of a , g , σ_{kx} , σ_{ky} , σ_{Ix} and b/a , given by the legends. The relative effective detuning strength is explained in Sec. 5.4.2. The relative difference in (e) and (f) is given by Eq. (5.16). The configuration in Fig. 5.4 is the same as $a/a_0 = 1$, $g_0/g = 1$, $\sigma_{kx}/\sigma_0 = 1$, $b/a = -0.7$, $\text{rel}(\sigma_{kx} - \sigma_{ky}) = 1$ and $\text{rel}(\sigma_{kx} - 10\sigma_{Ix}) = 1$, respectively in order from (a) to (f).

stability for $\text{rel}(\sigma_{kx} - 10\sigma_{Ix}) \leq -0.67$. It has been found that this happens because the beam size grows towards the aperture at J_{\max} , such that the beam becomes Gaussian with its tails collimated at a certain amplitude [67, 68]. With the strongest incoherent noise, the beam size was doubled after 142 min, and 83% of the bunch intensity was lost after 24 h. For strong incoherent noise, the non-uniform diffusion due to the coherent noise is actually beneficial for long-term stability. The increase of the relative effective detuning strength beyond 1.5 is not of interest.

The change of the relative effective detuning strength over the first hour, for all the parameter scans, is presented in Fig. 5.8. The reduction is faster due to noise in the same plane, with $b/a = -1$, and with no incoherent noise. To a certain extent, it does not matter how one changes $\sigma_{kx}a/g$. Except at large values of this parameter, there is never a reduction of the relative effective detuning strength faster than 10%/h. Hence, this effect cannot reduce the stability substantially within a latency time of $\lesssim 30$ min, which has been observed in the LHC [60].

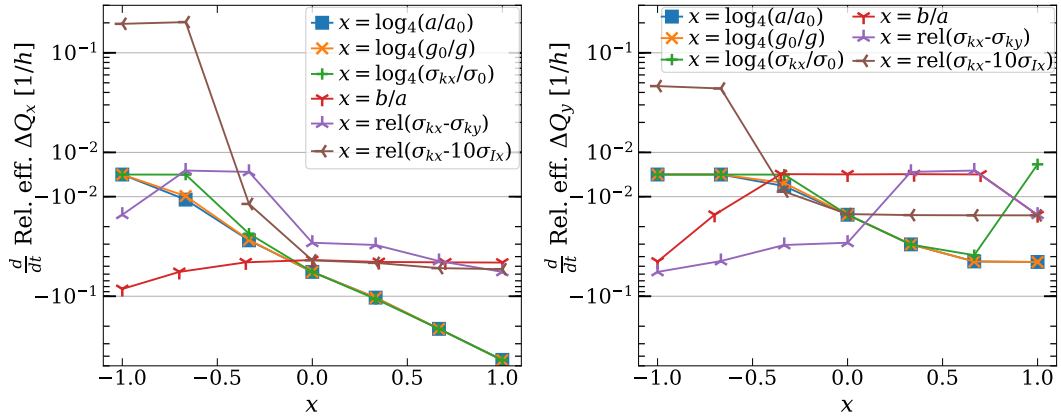


Figure 5.8: The initial reduction of the relative effective detuning strength, from the scans that are given in more detail in Fig. 5.7. The value corresponds to the change during the first hour, after starting with a Gaussian transverse distribution. The vertical scale is linear on the interval $[-10^{-2}, 10^{-2}]$, and logarithmic otherwise.

5.5 Conclusion

The collective motion of the particles in 6D phase space have in this study been considered in detail. It has been found that due to the combined mechanism of linear detuning and transverse feedback, the change of action after a kick depends on the tune of the individual particle, relative to the average tune of the distribution. By considering the change of action after an initial kick, due to a noise source, as a stochastic process, the Fokker-Planck equation has been derived from a master equation. The resulting diffusion coefficient is 0 for particles with tune equal to the average tune of the bunch, and grows quadratically with the tune from there. While incoherent noise, such as IBS, causes the distribution to tend to a Gaussian, the coherent noise causes the distribution to tend to a step function.

The change in the distribution from a Gaussian towards a step, changes the stability diagram as well. The change of the stability limit has been studied through the change of the relative effective detuning, a worst-case measure. The relative effective detuning strength in the horizontal plane decreased faster, and thus approached an instability faster, with:

- Larger absolute values of the detuning coefficients a and b ($\Delta Q_x = aJ_x + bJ_y$).
- Smaller horizontal feedback gain g_x .
- Stronger coherent noise in the same plane σ_{kx} .
- Coherent noise in only the opposite plane, combined with $b/a = -1$.
- Larger ratio of the coherent noise amplitude in the same plane to that in the other plane, σ_{kx}/σ_{ky} .
- Larger ratio of the coherent noise to the incoherent noise in the same plane, σ_{kx}/σ_{Ix} .

The relative effective detuning strength was reduced by up to 58% in a realistic configuration without IBS, over a time period of 24h. It was not found a reduction of the relative effective detuning strength higher than 10%/h with LHC relevant parameters. Hence, this mechanism does not explain the latencies measured in the LHC.

6 Single-bunch evolution due to noise, decoherence, and impedance

Disclaimer: This chapter was adapted from the following articles — with permissions of the co-author and publishers:

[50] **S. V. Furuseth** and X. Buffat, “Loss of transverse Landau damping by noise and wakefield driven diffusion”, *Phys. Rev. Accel. Beams* **23**, p. 114401, Nov. 2020. doi:[10.1103/PhysRevAccelBeams.23.114401](https://doi.org/10.1103/PhysRevAccelBeams.23.114401)

[69] **S. V. Furuseth** and X. Buffat, “Noise and possible loss of Landau damping – Noise Excited Wakefields”, in *Proc. of ICFA mini workshop on Mitigation of Coherent Beam Instabilities in particle accelerators*, Zermatt, Switzerland, Sep. 2019, pp. 262–269, Rep. CERN-2020-009. doi:[10.23732/CYRCP-2020-009](https://doi.org/10.23732/CYRCP-2020-009).

Both were published under CC-BY 4.0.

My contribution: All results presented here, except for: The BimBim calculations, which return the details of the wake driven eigenmodes.

6.1 Introduction

In the experiment discussed in Sec. 4.3, Landau damping was lost after the bunches were affected by a controllable external source of noise over an extended period of time. The working hypothesis is that this loss of Landau damping was caused by a noise induced change of the transverse bunch distribution, away from the commonly assumed Gaussian distribution.

In this chapter, a mechanism is introduced where the coherent wakefield driven modes are excited by noise in the machine, whereupon they act back on the individual particles through wakefields and are damped by decoherence. If the modes are stable, the energy they carry is typically assumed to be infinitesimal. However, since the beam is excited by external noise sources, the modes will be excited to finite amplitudes and carry a non-negligible energy. Hence, it is necessary to go beyond a first-order perturbation theory, as was explained in Sec. 3.6.

6.2 Noise excited wakefields

The mechanism introduced in this chapter can cause a loss of Landau damping by diffusion. The mathematical explanation of noise excited wakefields consists of 4 steps:

1. The wakefields drive eigenmodes with complex coherent eigenfrequencies $\omega_m \equiv \omega_{\text{coh}}$, found from the linearized Vlasov equation, assuming no tune spread and no noise. This is discussed in Sec. 6.2.1. The mode number m is an iterative index over different modes. The subscripts m are omitted for brevity, except for when it is the only subscript, as it will be clear from context which mode is treated.
2. Due to the tune spread, the discrete modes mix with the continuous incoherent spectrum, and the complex eigenfrequencies are changed to $\Omega_m \equiv \Omega_{\text{LD}}$, which are found in Sec. 6.2.2. If $\text{Im}\{\Omega_m\} > 0$, the mode is already unstable. The interesting case is when $\text{Im}\{\Omega_m\} < 0$. The detuning will be assumed to be due to Landau octupoles, as was introduced in Sec. 2.3.2.
3. An external noise drives the initially stable eigenmodes to finite amplitudes that depend on the noise amplitude and damping rates of the modes.
4. The noise excited modes drive wakefields that act on the incoherent particles. By considering the wake force as a stochastic excitation, in the framework of the Liouville equation, a diffusion equation will be derived in Sec. 6.2.4.

The diffusion will be found to be narrow in frequency space, and thus also in action space, causing a local flattening of the equilibrium distribution. Other mechanisms can cause a similar frequency dependent diffusion, but will not systematically be peaked at a critical frequency: the frequency of a mode that requires stabilization by Landau damping. The distribution evolution can correspond to the drilling of a borehole in the stability diagram, i.e. a local reduction of the imaginary part of the curve. Hence, initially stable regions are changed into unstable ones at the real frequencies of the coherent modes. In relevant and reasonable limits, an analytical expression for the latency of an initially stable mode is derived in Sec. 6.2.5. However, in a different and less relevant limit, the flattening does not cause a drilling. It is in general better to solve the diffusion and corresponding stability evolution numerically, as explained in Sec. 6.2.6. The stability of the evolving bunch is continuously evaluated by the linearized Vlasov equation through the stability diagram in Eq. (2.46).

6.2.1 Wakefield eigenmodes – ω_m

It is common to assess beam stability by neglecting noise and assuming weak wakefield driven perturbations, in which case Eq. (3.32) becomes the linearized Vlasov equation. The dipolar wake force is only dependent on z , not δ . It is common to model it as one effective kick $\Delta p = P_{\text{coh}}(z, t)$ per turn. One can solve the Vlasov equation with a normal mode analysis, assuming that the distribution perturbation in either transverse plane can be written as a sum of orthogonal modes [12]

$$\begin{aligned} \Psi_1 &= \sum_m \Delta \Psi_m(\phi, J, \phi_z, I_z, t) \\ &= \sum_m f_m(\phi, J, I_z) e^{-i\phi_m(t, \phi_z, z)}, \end{aligned} \tag{6.1}$$

with phases

$$\phi_m(t, \phi_z, z) = \phi_{m0} + (\omega_m + l_m \omega_s) t - l_m \phi_z - \frac{z \omega'}{\omega_s \beta_z}. \quad (6.2)$$

Here, $\omega_m = \omega_0 + \Delta\omega_m$ is the coherent frequency of mode $m \neq 0$, $\Delta\omega_m$ is the complex frequency shift generated by the wakefields, l_m is the angular mode number, ω_0 is the bare betatron frequency of the synchronous particle, and the last term is the headtail phase factor. Here, it has been assumed that a mode consists of a single angular spatial frequency.

The individual particles are oscillating in longitudinal phase space, as given by Eq. (2.19). The phase of the mode at the location (ϕ_z, I_z) of an individual particle is

$$\phi_{\Delta m}(t) = (\phi_{m0} - l_m \phi_{z0}) + \omega_m t - \frac{z(t) \omega'}{\omega_s \beta_z}, \quad (6.3)$$

where the synchrotron frequency has been canceled. This phase evolves with time equally to the transverse phase of the single particle in Eq. (2.27), illustrating that the coherent mode in fact consists of the motion of synchronized individual particles.

The average transverse complex offset of the distribution in the y plane, following the longitudinal motion of the single particles, can be written in terms of normalized, fixed eigenfunctions $m_m(\phi_z, I_z)$ with time dependent amplitudes $\chi_m(t)$ as

$$\chi_m(t) m_m(\phi_z, I_z) = \int_0^\infty dJ \int_0^{2\pi} d\phi (y + i p_y) \Delta \Psi_m(\phi_z + \omega_s t). \quad (6.4)$$

The normalization of m_m is done over the equilibrium distribution [70]

$$\langle \overline{m_m} m_m \rangle_\Psi = \int_0^\infty dI_z \int_0^{2\pi} d\phi_z \Psi_0(\phi_z, I_z) |m_m(\phi_z, I_z)|^2 = 1, \quad (6.5)$$

where the horizontal line on the LHS implies a complex conjugation.

The evolution of these modes with time is governed by the following equation of motion

$$\ddot{\chi}_m m_m + \omega_m^2 \chi_m m_m = 0. \quad (6.6)$$

The eigenmodes m_m and eigenfrequencies ω_m can be found with numerical Vlasov solvers, such as DELPHI [12], or circulant matrix solvers, such as BimBim [7].

The wake impulse of mode m can be found by moving the impedance dependent terms to the RHS as

$$\begin{aligned} \ddot{\chi}_m m_m + \omega_0^2 \chi_m m_m &= (\omega_0^2 - \omega_m^2) \chi_m m_m \\ &= \omega_0 P_m(\phi_z, I_z, t). \end{aligned} \quad (6.7)$$

To drive modes of shape $m_m(\phi_z, I_z)$, with a discrete frequency shift $\Delta\omega_m$, an effective wake kick P_m can be found that is proportional to the mode m_m . It can be evaluated as the average

kick on particles starting at (ϕ_z, I_z) , over the synchrotron motion

$$P_m(\phi_z, I_z, t) = \left\langle P_{\text{coh}}[z(t'), t'] e^{i\phi_{\Delta m}(t')} \right\rangle_{t'} e^{-i\phi_{\Delta m}(t)}. \quad (6.8)$$

6.2.2 Damped wakefield eigenmodes – Ω_m

Whether a mode is stabilized by Landau damping or not is typically assessed with the mapping given by Eq. (2.45), which is valid only in the weak headtail approximation. The stability diagram is calculated as $\Delta\omega_m \rightarrow \Delta\omega_{\text{SD}}$ in the limit $\text{Im}\{\Delta\Omega_m\} \rightarrow 0^+$, given by Eq. (2.46). If one desires the rise time τ_m of a mode m that is outside/above the stability diagram, this can be found as $\tau_m = 1/\text{Im}\{\Omega_m\} > 0$ [71].

Obtaining the damping time of a mode that is inside/below the stability diagram, as is of interest in this chapter, is a greater challenge. The mapping in Eq. (2.45) has a hole in its domain inside the stability diagram. N. G. Van Kampen has addressed this issue in plasma physics [72]. Inside the stability diagram, there will exist a continuous spectrum in addition to the discrete modes. However, if the continuous motion is damped faster than the discrete modes, an arbitrary initial distribution may after a short transient time behave like a superposition of damped discrete modes. This requires that the continuous spectrum is damped faster than the discrete modes [73]. In the following, it will be assumed that the beam motion can be described sufficiently accurately with a single damped mode. This hypothesis will be tested with particle tracking simulations.

An algorithm is needed to extend the mapping in Eq. (2.45) inside the stability diagram. The challenge is illustrated in Fig. 6.1. The goal is to obtain an expression relating $M_{\text{coh}} = \Delta\omega_m - \Delta\omega_{\text{SD}}$ and $M_{\text{LD}} = \Delta\Omega_m - \Delta\Omega_R$, the margins of the free and damped mode frequencies, for a mode that is barely damped. The free margin M_{coh} will be chosen to be purely imaginary.

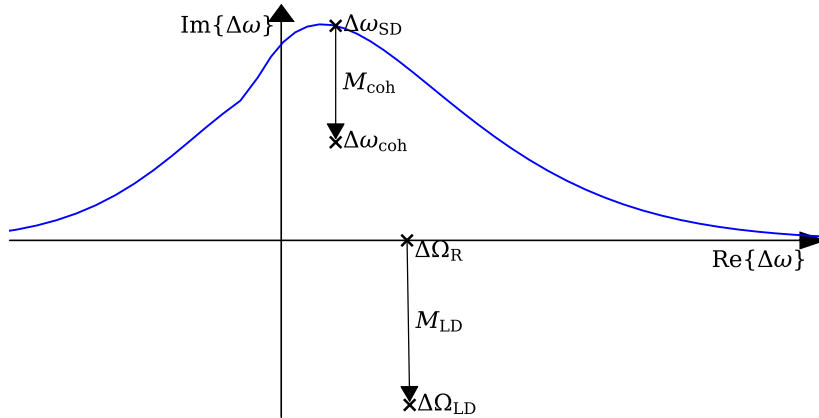


Figure 6.1: Illustration of the problem of finding the damped frequency $\Delta\Omega_{\text{LD}} = \Delta\Omega_m$ corresponding to the undamped frequency $\Delta\omega_{\text{coh}} = \Delta\omega_m$ that is inside the stability limit in blue, commonly referred to as the stability diagram. The marginally stable point $\Delta\Omega_R$ corresponds to the point on the stability diagram $\Delta\omega_{\text{SD}}$, given by Eq. (2.46).

For the solution to be physical, the damped frequency shift $\Delta\Omega_m$ should change continuously through the artificial discontinuity of the mapping at zero growth rate. If there is no frequency spread, there is no hole in the mapping, and

$$\frac{-1}{\Delta\omega_m} = \frac{-1}{\Delta\Omega_m} \implies M_{LD} = M_{coh}. \quad (6.9)$$

When including a frequency spread, one can do a Taylor expansion of Eq. (2.45), assuming $|M_{coh}| \ll |\Delta\omega_{SD}|$ and $|M_{LD}| \ll |\Delta\Omega_R|$. The LHS becomes

$$\frac{-1}{\Delta\omega_m} = \frac{-1}{\Delta\omega_{SD} + M_{coh}} = \frac{-1}{\Delta\omega_{SD}} \left(1 - \frac{M_{coh}}{\Delta\omega_{SD}} \right), \quad (6.10)$$

where the higher order terms of $M_{coh}/\Delta\omega_{SD}$ have been omitted. Doing the same for the integrand on the RHS gives

$$\frac{1}{\Delta\Omega_R(J_x, J_y) + M_{LD}} = \frac{1}{\Delta\Omega_R(J_x, J_y)} - \frac{M_{LD}}{\Delta\Omega_R(J_x, J_y)^2}, \quad (6.11)$$

where $\Delta\Omega_R(J_x, J_y) = \Omega_R - \omega(J_x, J_y)$. After performing the integral, the first term becomes $-1/\Delta\omega_{SD}$, the first term in Eq. (6.10). Next, assume that the mean squared will be of the same order as the squared mean, $\langle 1/\Delta\Omega_R^2 \rangle \sim \langle 1/\Delta\Omega_R \rangle^2$. Thus, the second terms on the RHS of Eqs. (6.10) and (6.11) give

$$\frac{M_{coh}}{\Delta\omega_{SD}^2} = \frac{1}{\alpha} \frac{M_{LD}}{\Delta\omega_{SD}^2} \implies M_{LD} = \alpha M_{coh}, \quad (6.12)$$

where α is a correction factor, which is 1 without a frequency spread as in Eq. (6.9). Based on this derivation, one cannot determine what α is with detuning, but one can assume that it is close to 1.

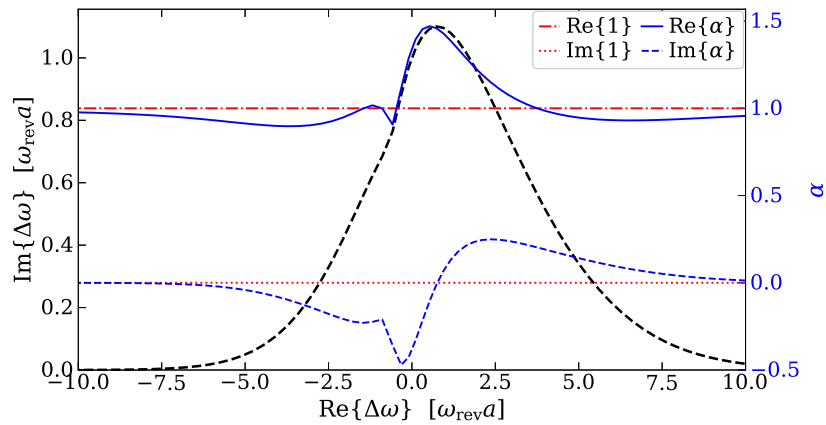


Figure 6.2: Stability diagram (black dashed line) and α given by Eq. (6.13), in comparison to the estimate $\alpha = 1$. The configuration corresponds to linear detuning coefficients $a = 1 \times 10^{-4}$ and $b = -0.7a$.

Since the mapping in Eq. (2.45) works for positive growth rates, one can calculate α in this domain as

$$\alpha \approx \frac{\partial M_{\text{LD}}}{\partial M_{\text{coh}}} = \lim_{\Delta\Omega_m \rightarrow \Delta\Omega_R} \frac{\Delta\Omega_m - \Delta\Omega_R}{\Delta\omega_m - \Delta\omega_{\text{SD}}}, \quad (6.13)$$

and assume that α varies negligibly for small negative growth rates. In other words, one assumes that M_{LD} is a smooth function of M_{coh} , in addition to being continuous. The complex α , for a Gaussian distribution, is displayed in Fig. 6.2. For large real frequency shifts, one finds $\alpha \rightarrow 1$, as expected. Equation (6.12) can be considered a correction to the zeroth-order expression in Eq. (6.9). This expression works well for small $\text{Im}\{M_{\text{coh}}\} > 0$. Here, it is postulated that it also works for small $\text{Im}\{M_{\text{coh}}\} < 0$, inside the stability diagram. This is tested numerically in Sec. 6.3.1.

6.2.3 Noise excited damped wakefield eigenmodes

The particle beam in an accelerator is continuously excited by external noise sources. The noise has been neglected in the derivation so far. By adding a noise term to the RHS of Eq. (6.6), using the damped frequency Ω_m , multiplying by $\overline{m_m}$, and taking the average over the longitudinal distribution, one finds

$$\ddot{\chi}_m + \Omega_m^2 \chi_m = \Omega_m \sum_i \langle \overline{m_m} \Xi_i \rangle_{\Psi} \xi_i, \quad (6.14)$$

where the noise has been decomposed as in Eq. (3.12). The excitation per noise component is proportional to the modes' noise moments $\eta_{mi} \in \mathbb{R}$, defined as

$$\eta_{mi} = |\langle \overline{m_m} \Xi_i \rangle_{\Psi}|. \quad (6.15)$$

The spectrum of the mode amplitudes can be found in the standard way by Fourier transforming Eq. (6.14)

$$\mathcal{F}(\chi_m) = \frac{\Omega_m \sum_i \langle \overline{m_m} \Xi_i \rangle_{\Psi} \mathcal{F}(\xi_i)}{\text{Re}\{\Omega_m^2\} - \omega^2 + i\text{Im}\{\Omega_m^2\}}. \quad (6.16)$$

This derivation has modeled the ensemble of oscillators making up the mode as a single damped stochastic oscillator with frequency found in Sec. 6.2.2. The approximation is valuable, as it allows the analytical latency formula below in Sec. 6.2.5. On the other hand, due to the frequency spread of the individual harmonic oscillators, the frequencies could also be mapped with Eq. (2.45). That corresponds to a change of $\omega \rightarrow \omega_{\text{SD}}$ and $\Omega_m \rightarrow \omega_m$ in Eq. (6.16). In the already assumed limit of small tune shifts, so that $\Omega_m^2 - \omega_0^2 = 2\Omega_m \Delta\Omega_m$, this changes Eq. (6.16) for a dipolar noise to Eq. (A.14).

The noise in the LHC is of sufficiently low frequency to be modeled as dipolar noise. Hence, only the dipolar noise moment of the modes is of interest, $\eta_{m0} = |\langle m_m \rangle|$. Dipolar moments can be calculated analytically, e.g. for an airbag bunch using Eq. (6.186) in [13]. However, calculating the dipolar moments for a Gaussian bunch that is perturbed by the transverse feedback system and wakefields will here be done numerically with BimBim. In an LHC like configuration, but without transverse feedback, the dipole moments of the prevalent modes are presented as a function of the linear chromaticity in Fig. 6.3. At nonzero chromaticity, the

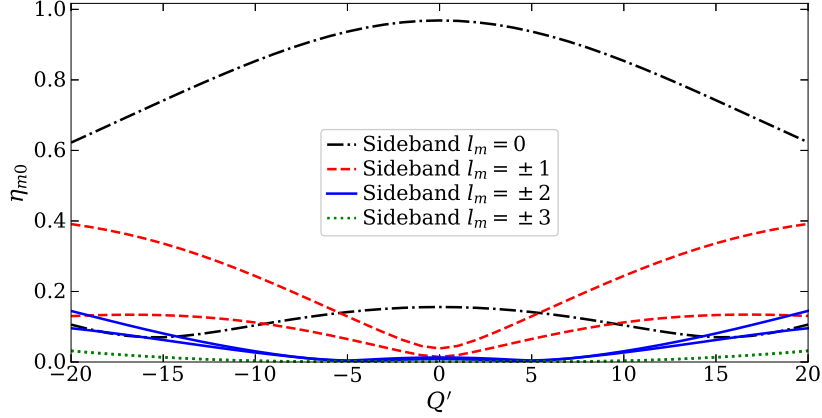


Figure 6.3: Largest dipole moments for modes at various sidebands, with various chromaticities and zero transverse feedback. The values have been calculated numerically with BimBim, for the experiment in the LHC described in Sec. 4.3.

dipolar moment of the angular headtail modes ($l_m \neq 0$) is nonzero, and can thus be excited by a dipolar noise. These are the most problematic modes in the LHC as of 2018, since the transverse feedback can stabilize the dipolar modes efficiently. In the following, the noise will be assumed to be white and dipolar, as illustrated in Fig. 3.1a, acceptable over the frequency span of a single bunch in a machine without CCs. The PSD of this noise on a particle can be modeled as in Eq. (3.11), equal to $\sigma_k^2/\tau_{\text{rev}}$ for a frequency below $f_{\text{rev}}/2$.

6.2.4 Wakefield driven diffusion

The noise and wakefields do not only affect the coherent modes, but also the individual particles. Describing the individual particles by their amplitudes y and frequencies $\omega(J_x, J_y)$, their motion in one transverse plane is governed by

$$\begin{aligned} \ddot{y} + \omega^2 y &= \omega \xi(t) + \omega P_{\text{wake}} \\ &= \omega \xi(t) + \sum_m \frac{\omega}{\omega_0} (\omega_0^2 - \omega_m^2) \chi_m m_m. \end{aligned} \quad (6.17)$$

The first term on the RHS models the direct impact of the noise. This term was studied in detail in Ch. 5 and found to not be detrimental for stability in the LHC. The second term is the main focus in this chapter, modeling the indirect impact of the noise through the wakefields. Here, the first term will be neglected, and it will be shown that this is an acceptable approximation, since the second term will dominate the diffusion.

To better understand the single-particle dynamics driven by the stochastic force in Eq. (6.17), it is modeled by a perturbed Hamiltonian as in Eq. (3.31). Focusing only on the complex effective wake force, the perturbation is given by

$$\epsilon \mathcal{H}_1 = -\text{Re}\{(y + i p_y) \overline{P_{\text{wake}}}\}, \quad (6.18)$$

which returns the normal $-yP_{\text{wake}}$ when $P_{\text{wake}} \in \mathbb{R}$ [12, 13, 22, 51]. The change of the quickly varying phases due to the perturbation is negligible, while the change of the action is by Hamilton's equations only caused by the perturbation as

$$\dot{J} = -e \frac{\partial \mathcal{H}_1}{\partial \phi} = -\sqrt{2J} \text{Re}\{i e^{-i\phi} \overline{P_{\text{wake}}}\}. \quad (6.19)$$

This requires that the unperturbed Hamiltonian \mathcal{H}_0 only depends on the actions, not the transverse phases of the particles. Note that ϕ is the transverse phase of the particle, given in Eq. (2.27), and that $P_{\text{wake}} \propto \exp(-i\phi_{\Delta m})$, with phase given by Eq. (6.3). Hence, the headtail phase shifts cancel.

If the stochastic forces are sufficiently weak to accurately be modeled as a perturbation, they drive a diffusion of the individual particles that can be modeled by [74, 75]

$$\frac{\partial \Psi_{\text{eq}}}{\partial t} = \frac{\partial}{\partial J} \left[J D_{\text{wake}} \frac{\partial \Psi_{\text{eq}}}{\partial J} \right], \quad (6.20)$$

$$D_{\text{wake}} = \lim_{t_{\text{tot}} \rightarrow \infty} \frac{1}{2J t_{\text{tot}}} \int_{t_0}^{t_0+t_{\text{tot}}} dt \int_{t_0}^{t_0+t_{\text{tot}}} ds \langle \dot{J}(t) \dot{J}(s) \rangle_{\phi}, \quad (6.21)$$

which is derived in App. B.2.

In the interesting regime, the modes are uncoupled. Therefore, the force from the different modes have zero expected correlation, and the diffusion coefficient can be given as

$$D_{\text{wake}} = \frac{1}{2} \sum_m S_{P_m}[\omega(J_x, J_y), I_z], \quad (6.22)$$

where $S_{P_m}(\omega)$ is the PSD of the wake force due to mode m on a particle, calculated by combining Eqs. (6.16) and (6.17). Here, it was used that $S_{P_m}(\omega)$ is the Fourier transform of the autocorrelation function of the wake force acting on a particle, after the cancellation of the headtail phase shift.

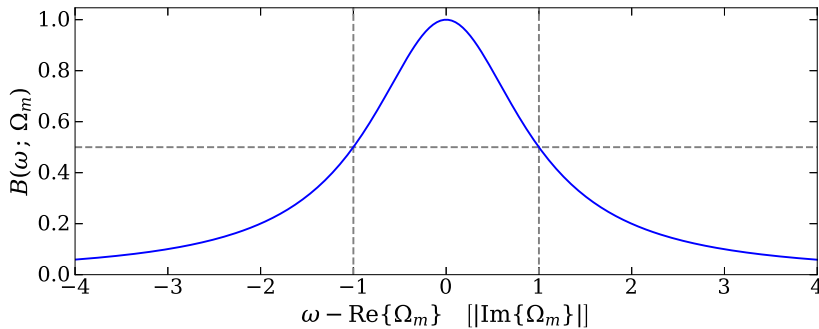


Figure 6.4: Shape of diffusion coefficient in frequency space due to a single Landau stabilized mode, given by Eq. (6.23c). The half width at half maximum is equal to $|\text{Im}\{\Omega_m\}|$, the damping rate of the mode.

In general, the diffusion coefficient in Eq. (6.22) depends on the longitudinal action I_z , in addition to the transverse actions, since $S_{P_m} \propto \langle \overline{m_m} m_m \rangle_{\phi_z}$. Since only the transverse diffusion is of concern, and the longitudinal distribution is expected to not evolve, the average over I_z can be taken, for which the normalization of m_m in Eq. (6.5) is of use. The diffusion coefficient, only dependent on the transverse single-particle frequency $\omega(J_x, J_y)$, can be written as

$$D_{\text{wake}}(\omega) = \sum_m D_{\text{max}}^m B(\omega) C, \quad (6.23a)$$

$$D_{\text{max}}^m = \frac{\sigma_k^2 \eta_{m0}^2 |\Delta\omega_m|^2}{2\tau_{\text{rev}} \text{Im}\{\Omega_m\}^2}, \quad (6.23b)$$

$$B(\omega) = \frac{\text{Im}\{\Omega_m^2\}^2}{(\text{Re}\{\Omega_m^2\} - \omega^2)^2 + \text{Im}\{\Omega_m^2\}^2}, \quad (6.23c)$$

$$C = \left| 1 + \frac{\Delta\omega_m}{2\omega_0} \right|^2 \frac{|\Omega_m|^2}{\text{Re}\{\Omega_m\}^2}, \quad (6.23d)$$

where the noise has been assumed to be dipolar. In the relevant limit of small wake driven frequency shifts $\Delta\omega_m, \Delta\Omega_m \ll \omega_0$, one can ignore corrections proportional to the frequency shifts of second or higher power, and get

$$B(\omega) = \frac{\text{Im}\{\Omega_m\}^2}{(\text{Re}\{\Omega_m\} - \omega)^2 + \text{Im}\{\Omega_m\}^2},$$

$$C = 1.$$

The B function, illustrated in Fig. 6.4, expresses the dependence of the diffusion coefficient on the single-particle frequency ω . It has a maximum value of 1 and half width at half maximum of $\Delta\omega = |\text{Im}\{\Omega_m\}|$. The C function contains the higher-order terms, and will typically be close to 1. To express the diffusion coefficient as a function of the tune, one writes $\omega = \omega_{\text{rev}} Q$. Every factor ω_{rev} will cancel.

Going from diffusion in 1D to 2D is elementary. The noise is already assumed to be centered, $\langle \xi_i(t_c) \rangle = 0$. By further assuming no correlation between the horizontal and vertical noise, and no horizontal wakefields from a vertical offset, there is no cross-plane diffusion. Hence, the wakefield driven diffusion equation in 2D is

$$\frac{\partial \Psi}{\partial t} = \frac{\partial}{\partial J_x} \left[J_x D_{xx} \frac{\partial \Psi}{\partial J_x} \right] + \frac{\partial}{\partial J_y} \left[J_y D_{yy} \frac{\partial \Psi}{\partial J_y} \right], \quad (6.24)$$

$$D_{jj}(J_x, J_y) = D_{\text{wake}j}[\omega_{\text{rev}} Q_j(J_x, J_y)],$$

where $D_{\text{wake}j}$ includes the noise and details of the modes in the transverse plane j .

6.2.5 Instability latency

The diffusion derived in Sec. 6.2.4 will locally flatten the distribution around the actions resonant with the frequency of the least stable mode. Since the derivative of the distribution appears in the integral in Eq. (2.46), a change of the stability diagram is expected. In general, the diffusion modeled by Eq. (6.24) requires a numerical technique to be solved accurately,

as will be done in Sec. 6.2.6. Nevertheless, the latency can be calculated analytically under certain assumptions, as will be done here. For ease of notation, the complex frequencies will, in this subsection only, be written with an alternative notation as

$$\begin{aligned}\omega &= \text{Re}\{\omega\} + i\text{Im}\{\omega\} = \tilde{\omega} + i\gamma, \\ \Omega &= \text{Re}\{\Omega\} + i\text{Im}\{\Omega\} = \tilde{\Omega} + i\Gamma,\end{aligned}$$

using the subscripts already introduced in Fig. 6.1. Furthermore, only horizontal noise, and thus diffusion, will be considered, and it is assumed that only one dominant horizontal mode drives the diffusion.

In 1D, the stability diagram can be calculated as [30]

$$\begin{aligned}\lim_{\epsilon \rightarrow 0^+} \int_{-\infty}^{\infty} \frac{f(x) dx}{g(x) + i\epsilon} &= P \int_{-\infty}^{\infty} \frac{f(x) dx}{g(x)} - i\pi \int_{-\infty}^{\infty} f(x) \delta_D[g(x)] dx \\ &= P \int_{-\infty}^{\infty} \frac{f(x) dx}{g(x)} - i\pi \sum_{\substack{x_r \text{ s.t.} \\ g(x_r)=0}} \frac{f(x_r)}{|g'(x_r)|},\end{aligned}\tag{6.25}$$

where $f(x), g(x) \in \mathbb{R}$, P denotes the principal value, $g'(x) = \partial_x g(x)$, and the sum is over all zeros x_r of the function $g(x)$.

The penultimate goal of this section is to calculate the imaginary part of the stability diagram at the real frequency $\tilde{\omega}_m$ of the least stable mode, $\gamma_{\text{SD}}(\tilde{\omega}_m) = \gamma_{\text{SD}r}$, where the subscript r denotes the resonance condition. By considering the imaginary part of Eq. (2.46), one finds

$$\frac{\gamma_{\text{SD}r}}{|\Delta\omega_{\text{SD}r}|^2} = -\pi \iint_{00}^{\infty\infty} dJ^2 J_x \Psi' \delta_D[\tilde{\Omega}_{Rr} - \omega(J_x, J_y)],\tag{6.26}$$

where $\Psi' = \partial\Psi/\partial J_x|_{(J_x, J_y)}$. Consider linear detuning, as given by Eq. (2.29). Assuming that \tilde{a} is nonzero, there will for each vertical action be only one resonating horizontal action J_{xr} , defined by

$$\Delta\tilde{\Omega}_{Rr} = \tilde{a}J_{xr}(J_y) + \tilde{b}J_y.\tag{6.27}$$

Furthermore, in the limit of large relative real tune shifts $|\Delta\tilde{\omega}_{\text{SD}r}| \gg |\gamma_{\text{SD}r}|$, which is true for the least stable modes in the LHC, and assuming that the real part changes negligibly, since Ψ' only will change close to the resonance, the imaginary part can be approximated by

$$\frac{\gamma_{\text{SD}r}}{|\Delta\tilde{\omega}_{\text{SD}r}|^2} = -\frac{\pi}{|\tilde{a}|} \iint_{00}^{\infty\infty} dJ^2 J_x \Psi' \delta_D[J_x - J_{xr}(J_y)].\tag{6.28}$$

The imaginary part of the stability diagram, at the critical frequency, is under these assumptions proportional to the derivative of the distribution at the resonant actions. Thus, the local flattening of the distribution will lead to a reduction of $\gamma_{\text{SD}r}$, which can be illustrated as the drilling of a borehole in the stability diagram at this critical frequency. See a visual illustration of this process in Fig. 6.8. If this process carries on for long enough uninterrupted, it can lead

to a loss of Landau damping as $\gamma_{\text{SD}r} \rightarrow \gamma_m^+$. Note that in the limit of small relative real tune shifts, $|\Delta\tilde{\omega}_{\text{SD}r}| \ll |\gamma_{\text{SD}r}|$, $\gamma_{\text{SD}r}$ would be proportional to the inverse of the RHS of Eq. (6.28), and a local flattening would initially lead to an increase of the imaginary part of the stability diagram. This special case will be investigated in more detail numerically in Sec. 6.4.1.

To evaluate the evolution of $\gamma_{\text{SD}r}$, one must evaluate the evolution of Ψ' . Taking the action derivative of the diffusion equation in Eq. (6.24) gives

$$\frac{\partial \Psi'}{\partial t} = \frac{\partial^2}{\partial J_x^2} [J_x D_{xx} \Psi']. \quad (6.29)$$

It is only the evolution of Ψ' at the center of the diffusion coefficient in Fig. 6.4 that is of interest. However, this evolution also depends on the diffusion close to it. To evaluate the macro-diffusion, the finite difference of the RHS of Eq. (6.29) has been taken at $\{J_{xr} - W_J, J_{xr}, J_{xr} + W_J\}$, where $W_J = |\Gamma_m / \tilde{a}|$ is the half width at half maximum in the horizontal action coordinate. By assuming a Gaussian initial distribution in transverse phase space, equal to an exponential distribution in action $\Psi_0(J_x, J_y) = \exp(-J_x - J_y)$, Eq. (6.29) becomes

$$\frac{1}{\Psi'_r} \frac{\partial \Psi'_r}{\partial t} = -\frac{D_{\max}}{W_J^2} [J_{xr} + W_J^2 - J_{xr} W_J^2 + \mathcal{O}(W_J^3)], \quad (6.30)$$

where $\Psi'_r = \Psi'(J_{xr}(J_y), J_y)$. For the relevant cases, it has already been stated that $|\Delta\tilde{\omega}_{\text{SD}r}| \gg |\gamma_{\text{SD}r}|$, and that the mode is close to the stability threshold, $\gamma_m \lesssim \gamma_{\text{SD}r}$. Furthermore, it is illustrated in Fig. 6.2 that $\max(\gamma_{\text{SD}r}) \approx \tilde{a}$, when \tilde{b} is small wrt to \tilde{a} . It follows that $W_J \ll 1$. Hence, the first term on the RHS of Eq. (6.30) will dominate, except when $J_{xr} \approx 0$. If $\tilde{b} \neq 0$, then $J_{xr}(J_y)$ is not constant, and one can calculate a nonzero effective action, as will be done in the following. Therefore, all but the first term on the RHS will be neglected.

If the RHS of Eq. (6.30) would have been constant, the distribution derivative would have evolved as

$$\Psi'_r(t) = \Psi'_r(0) \exp\left(-\frac{J_{xr} D_{\max}}{W_J^2} t\right),$$

where the flattening would gradually slow down. This is not correct. As Ψ'_r is flattened, $\gamma_{\text{SD}r}$ is reduced while γ_m stays put, such that Γ_m approaches 0 and D_{\max}/W_J^2 increases. This evolution has to be solved self-consistently.

The ultimate goal of this section is to get the latency, i.e. the time it takes for $\gamma_{\text{SD}r} \rightarrow \gamma_m^+$ and $\Gamma_m \rightarrow 0^-$. Combining Eqs. (6.28) and (6.30), returns an expression for the relative time derivative of $\gamma_{\text{SD}r}$

$$\frac{1}{\gamma_{\text{SD}r}} \frac{\partial \gamma_{\text{SD}r}}{\partial t} = -\frac{J_{x,\text{eff}} D_{\max}}{W_J^2}, \quad (6.31a)$$

$$J_{x,\text{eff}} = \frac{\int_0^\infty \int_0^\infty dJ_x^2 J_x^2 \Psi' \delta_D[J_x - J_{xr}(J_y)]}{\int_0^\infty \int_0^\infty dJ_x^2 J_x \Psi' \delta_D[J_x - J_{xr}(J_y)]}, \quad (6.31b)$$

using that only Ψ' depends on time. Assuming that $\tilde{a}\tilde{b} \leq 0$ and $\tilde{a} \neq 0$, as in the LHC, one gets

$$J_{x,\text{eff}} = \min(J_{xr}) + \frac{b}{b-a} + \frac{\left(\frac{b}{b-a}\right)^2}{\min(J_{xr}) + \frac{b}{b-a}} \geq \frac{2b}{b-a}, \quad (6.32)$$

expressed in a and b , as the factors ω_{rev} have canceled out. The value $\min(J_{xr})$ is the minimum horizontal action of a resonant particle, being equal to $\max\{0, \Delta\tilde{\Omega}_{Rr}/\tilde{a}\}$. The most critical modes in the LHC have $\Delta\tilde{\Omega}_{Rr} < 0$. For a positive octupole current, $\tilde{a} > 0$, one then gets $\min(J_{xr}) = 0$. For a negative octupole current, on the other hand, one gets $\min(J_{xr}) > 0$ and the effective action $J_{x,\text{eff}}$ will be larger.

To get the evolution of Γ_m , one combines Eqs. (6.31a) and (6.12), assuming that α will stay constant. This assumption is a simplification of the physics, necessary to reach an analytical expression for the latency, and it is the main difference in this derivation from what a numerical solver can model. Since γ_m is constant, it follows that $\partial_t \Gamma_m = -\text{Re}\{\alpha_0\} \partial_t \gamma_{\text{SD}r}$. One gets

$$\frac{1}{\text{Re}\{\alpha_0\} \gamma_{\text{SD}r}} \frac{\partial \Gamma_m}{\partial t} = \frac{J_{x,\text{eff}} D_{\text{max}}}{W_J^2} = \frac{J_{x,\text{eff}} D_{\text{max}0} \Gamma_{m0}^2 \tilde{a}^2}{\Gamma_m^4}, \quad (6.33)$$

where the subscript 0 denotes that the values should be taken at time $t = 0$, when the diffusion process starts. Note that $\Gamma_m < 0$ when stable, such that a positive time derivative takes it towards 0 and a possible loss of Landau damping. The latency L can finally be calculated as

$$L = \frac{1}{J_{x,\text{eff}} D_{\text{max}0} \Gamma_{m0}^2 \tilde{a}^2} \int_{\Gamma_{m0}}^0 \frac{\Gamma_m^4 d\Gamma_m}{\text{Re}\{\alpha_0\} \gamma_m - \Gamma_m}, \quad (6.34)$$

where the fraction outside the integral is a constant only dependent on the initial condition.

The latency integral in Eq. (6.34) can be approximated as the integrand is always positive and its denominator goes from $\text{Re}\{\alpha_0\} \gamma_{\text{SD}r0}$ to $\text{Re}\{\alpha_0\} \gamma_m$, which should be a small relative change according to the assumptions. A lower estimate can be calculated by assuming the initial value, and a maximum value can be calculated by assuming $\gamma_m = 0$

$$\frac{(\gamma_{\text{SD}r0} - \gamma_m) W_{J0}^2}{5 \gamma_{\text{SD}r0} J_{x,\text{eff}} D_{\text{max}0}} \equiv L_L \leq L \leq L_L \frac{5}{4}. \quad (6.35)$$

Inserting the physical quantities gives

$$\begin{aligned} \frac{L_L}{\tau_{\text{rev}}} &= \frac{\gamma_{\text{SD}r0} - \gamma_m}{\gamma_{\text{SD}r0}} \frac{(\gamma_{\text{SD}r0} - \gamma_m)^4}{2.5 \tilde{a}^2 |\Delta\omega_m|^2} \frac{\text{Re}\{\alpha_0\}^4}{J_{x,\text{eff}} \sigma_k^2 \eta_{m0}^2} \\ &= \frac{(\text{Im}\{\Delta Q_{\text{SD}r0} - \Delta Q_{\text{coh}}\})^5}{2.5 \text{Im}\{\Delta Q_{\text{SD}r0}\} a^2 |\Delta Q_{\text{coh}}|^2} \frac{\text{Re}\{\alpha_0\}^4}{J_{x,\text{eff}} \sigma_k^2 \eta_{m0}^2}. \end{aligned} \quad (6.36)$$

As τ_{rev} is the revolution period in the machine, the RHS of Eq. (6.36) gives the lower estimate of the latency in number of turns. Remember that $\Delta Q_{\text{SD}r0}$ is the point on the stability diagram at the same real tune as the coherent mode, $\text{Re}\{\Delta Q_{\text{SD}r0}\} = \text{Re}\{\Delta Q_{\text{coh}}\}$. Furthermore, note that

α_0 to zeroth order can be approximated by $\alpha_0 = 1$, as illustrated in Fig. 6.2. This expression can serve as a guide in designing future high-energy hadron colliders to avoid this diffusion driven instability mechanism.

The latency is, according to this analytical calculation, proportional to $W_{j0}^2 / J_{x,\text{eff}} D_{\text{max}0}$. In words, the latency is shorter for a fast diffusion that is narrow in action space. Such a diffusion will efficiently reduce Ψ' at the resonant actions without increasing the overall beam size. The latency is also proportional to $(\gamma_{\text{SD}r0} - \gamma_m) / \gamma_{\text{SD}r0}$. This is a measure on how much the stability diagram must be lowered, for the mode to reach the stability threshold. At first glance, it may look like the latency is shorter for a larger detuning coefficient a , which would be counterintuitive, but note that a larger a also leads to a more negative Γ_m , which in total leads to a longer latency.

6.2.6 Numerical method

The diffusion modeled by Eq. (6.24) must be solved numerically to be solved accurately. Numerical estimates are also needed to lift the assumptions, such as the one of large relative real tune shifts, taken in Sec. 6.2.5. The results that will be presented in the following have been produced with a PDE solver named PyRADISE, which is described in detail in App. D. The 2D transverse action space has been discretized into a 700×700 grid, going from 0 to $J_{\text{max}} = 20$, which is equidistant in \sqrt{J} . Thus, the minimal grid spacing is $\min(\Delta J) = 4 \times 10^{-5}$, and the grid spacing increases for larger actions where the distribution is less dense.

It has been assumed that a single mode is dominant, even though this is not required by the code. The diffusion coefficient has been recalculated at each time step during the diffusion process, whereupon the diffusion has been solved with an implicit backward differentiation formula for the following time step. Using an implicit scheme is necessary, as the maximum value of the diffusion coefficient will grow as the instability is approached, eventually rendering an explicit solver numerically unstable. Calculating the diffusion coefficient requires the calculation of the tune $Q_{\text{LD}} = \Omega_{\text{LD}} / \omega_{\text{rev}}$ of the damped mode. This is done using the algorithm in Sec. 6.2.2 and a numerical trapezoidal integrator implemented in PySSD [35], which has been imported in PyRADISE. If $\text{Im}\{Q_{\text{LD}}\}$ eventually becomes positive, the bunch will be considered to have become unstable.

6.3 Numerical verification

In this section, various aspects of the new theory derived in Sec. 6.2 will be tested with multi-particle simulations run with the tracking code COMBI (Coherent Multi-Bunch Interactions) [7, 76, 77]. The source of detuning is always assumed to be due to Landau octupoles, and only the detuning in the plane of the noise and coherent mode is of importance. A detuning symmetry is assumed for simplicity in all configurations, i.e. $a_x = a_y = a$ and $b_x = b_y = b$. Hence, the subscripts denoting the plane will in general not be included in the following.

6.3.1 Dynamics inside the stability diagram

The response of the beam to an external noise has been modeled as a single under-damped harmonic oscillator, with a complex frequency that is found by Eqs. (6.12) and (6.13). To verify this, simulations have been run with 10^6 macroparticles. The simulations were run with an anti-damper inducing a complex tune shift $\Delta Q_{\text{coh}} = -1.47 \times 10^{-4} + 1.25 \times 10^{-5} i$. This mode is stabilized with $a = a_{\text{thresh}} = 5.0 \times 10^{-5}$ and $b = -0.7a$. The real and imaginary tune shifts, in the simulations and according to Eqs. (6.12) and (6.13), are presented in Fig. 6.5. Each point is the average of 10 simulations, from which the STD has been used as an error bar. The Taylor algorithm works equally well for modes outside and just inside the stability diagram. For this complex tune shift, the approximation $\alpha = 1$ has a minimal impact close to a_{thresh} , compared to finding α by Eq. (6.13).

The simulations presented here were initialized with nonzero initial horizontal amplitudes, to get a measurable evolution from which to calculate the negative imaginary frequency. With a nonzero initial offset, some bunches that were supposed to be barely stabilized by Landau damping, eventually became unstable. This was caused by a similar mechanism to the one introduced in this chapter, except that the noise over multiple turns was combined into a single kick. Furthermore, according to the law of large numbers, the average of N_p numbers drawn from a centered Gaussian distribution of spread σ_x , will itself be drawn from a Gaussian distribution with zero mean and spread $\sigma_x / \sqrt{N_p}$. Therefore, the imaginary part of the frequency has been calculated based on the initial damping until the COM reached $4 \times 10^{-3} \sigma_x$, which occurs earlier for a larger a and smaller initial offset, causing a larger error bar at these points. The real part of the frequency has been calculated based on the

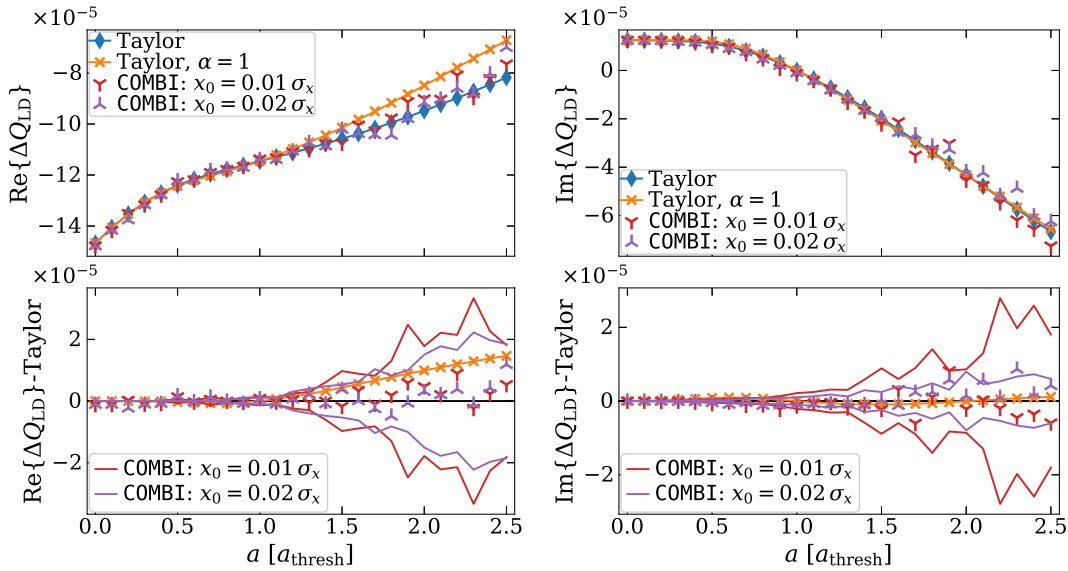


Figure 6.5: Tune shift of a coherent mode outside and inside the stability diagram. The theoretical curves have been calculated with Eq. (6.12), using both $\alpha = 1$ and α given by Eq. (6.13). The error margin (solid lines) is the STD of 10 simulations, for each value of a separately.

turn-by-turn position, using an interpolated Fast Fourier Transform implemented in the code Harpy [78]. The real part did not change systematically with time for each calculation separately.

6.3.2 Wakefield driven diffusion

In Sec. 6.2, the impact of the wakefields was modeled as a diffusion, with diffusion coefficient given by Eq. (6.23). Here, this expression will be compared to a numerical diffusion coefficient

$$D_{\text{num}}(J_0) = \frac{\langle \Delta J^2 \rangle_\phi}{2TJ_0}, \quad (6.37)$$

where J_0 is the initial action of a particle and ΔJ is the change of action after T turns. Without loss of generality, the diffusion coefficient is in this section given in units of action variance per action per turn, instead of per second.

The test configuration includes a dipolar mode with complex coherent tune shift $\Delta Q_{\text{coh}} = -1.47 \times 10^{-3} + 1.25 \times 10^{-4}i$, detuning given by $a_{\text{thresh}} = 5 \times 10^{-4}$, $a = 1.5a_{\text{thresh}}$, $b = -0.7a$, $Q' = 0$, and a noise of $\sigma_k = 10^{-4}$. 20 simulations have been run with $N_p = 10^7$ particles over $T = 10^4$ turns. This many particles were needed to make the numerical noise negligible, and this few turns were necessary to avoid a significant change of the distribution and thereby the stability. The individual and average numerical diffusion coefficients are presented in Fig. 6.6a, in comparison to the theory given by Eq. (6.23). The numerical diffusion coefficients in the individual simulations have not reached the expectancy value, but the average has. The apparent small difference in the real tune shift of the coherent mode may be attributed to the Taylor technique used to map ΔQ_{coh} to $\Delta Q_{\text{LD}} = -1.06 \times 10^{-3} - 1.987 \times 10^{-4}i$. The width of the average numerical diffusion coefficient is slightly larger than in the new theory, which may cause an underestimation of the latency, analytically found to be proportional to the width squared in Eq. (6.35). Note that the peak wake diffusion of $\sim 3 \times 10^{-7}/\text{turn}$ is significantly larger than the direct diffusion of $5 \times 10^{-9}/\text{turn}$, as stated in Sec. 6.2.4. The direct

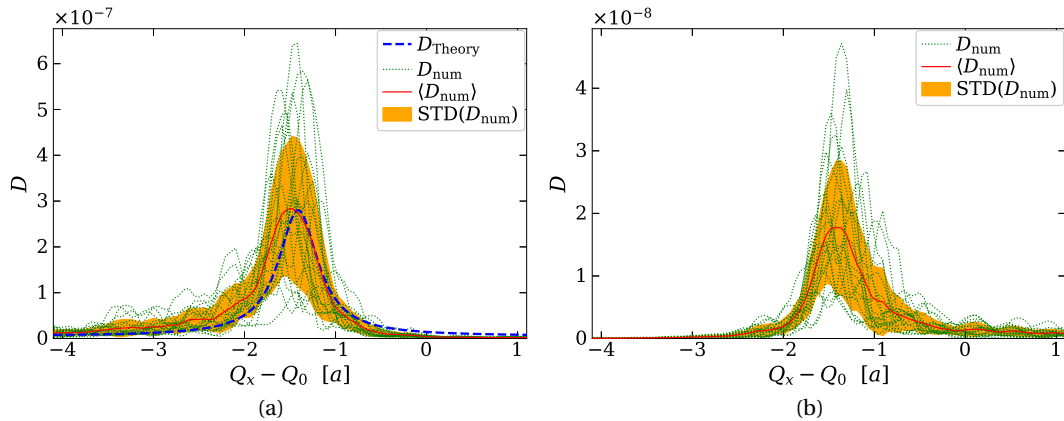


Figure 6.6: Numerical diffusion coefficient in 20 simulations and comparison to theory given by Eq. (6.23). (a) with external noise of amplitude $\sigma_k = 10^{-4}$. (b) without external noise.

diffusion would have been reduced even further in the presence of a transverse feedback, as was described in Ch. 5.

In the simulations presented in this section, an anti-damper have been used to generate the tune shift ΔQ_{coh} , so that it could be controlled perfectly. The main challenge in calculating D_{num} is that a bunch consisting of N_p particles normally distributed with zero mean and spread σ_x , will not actually have zero mean, explained by the law of large numbers. Therefore, a large number of particles is needed for the numerical noise to be negligible compared to the small controlled external noise. With 10^7 particles, the numerical diffusion coefficient without external noise is presented in Fig. 6.6b. The maximum of this average is 6% of the maximum with external noise. At least this many particles is therefore needed in simulations of this configuration.

6.3.3 Diffusion or resonant motion?

It was assumed in Sec. 6.2.4 that the impact of the noise driven wakefields was sufficiently stochastic to be modeled as a diffusion mechanism. Whether the events in the future and the past are sufficiently independent was considered by a phase mixing condition in [75]. The autocorrelation function of the under-damped stochastic harmonic oscillator (USHO) is an exponential $\exp(\text{Im}\{\Omega_m\}|t - t'|)$, which satisfies the phase mixing condition. The process will in this case converge to a diffusion process in the limit of small perturbations $\epsilon\mathcal{H}_1 \rightarrow 0$ and long times $t \rightarrow \infty$. Thus, a minimal requirement is a lower limit on the time of the process, i.e. the latency, which should be much longer than the correlation time of the USHO, $L \gg \tau_m = 1/|\text{Im}\{\Omega_m\}|$. For typical modes in the LHC, this requirement implies that the latency should be $L \gg 10\text{s}$ to be well modeled as a diffusion.

Now, consider in more detail the process at hand. To be modeled as a diffusion, the change of the distribution during a correlation time of the stochastic excitation must be limited. Therefore, the integrated change of a particle's action, κ_{wake} , due to the wake force within one correlation time must be small compared to the width of the diffusion coefficient in action space. The PSD of the noise driven wakefields was in Eq. (6.23) found to have half width at half maximum of $|\text{Im}\{\Omega_m\}|$. Since the considered detuning is caused by octupoles, the width in action space is given by $W_J = |\text{Im}\{\Omega_m\}|/\tilde{a}$. In the relevant limit of a small $\Delta\omega_m$ and a single dominating mode, one can write $P_{\text{wake}} = P_m = -2\Delta\omega_m\chi_m m_m$. The mean square amplitude of an USHO can be given as the product of the noise PSD and $\tau_m/4$. Thus, the condition for diffusion can be written as

$$\kappa_{\text{wake}} \approx \frac{\eta_{m0}\sigma_k|\Delta\omega_m|}{|\text{Im}\{\Omega_m\}|^{3/2}} \ll \left| \frac{\text{Im}\{\Omega_m\}}{\tilde{a}} \right|. \quad (6.38)$$

Due to the definition of $\sigma_k \propto \sqrt{\tau_{\text{rev}}}$, there is no direct dependence on the revolution frequency.

In the limit $\text{Im}\{\Omega_m\} \rightarrow 0$, the wake force becomes a deterministic harmonic excitation of a single frequency. The particles will oscillate around the harmonic frequency $\text{Re}\{\Omega_m\}$, causing an oscillation of the distribution and emittance, discussed in more detail in App. E. The maximum half width in action of particles oscillating around the harmonic frequency is W_h , estimated by Eq. (E.14). The period of this oscillation is estimated to be somewhat larger than

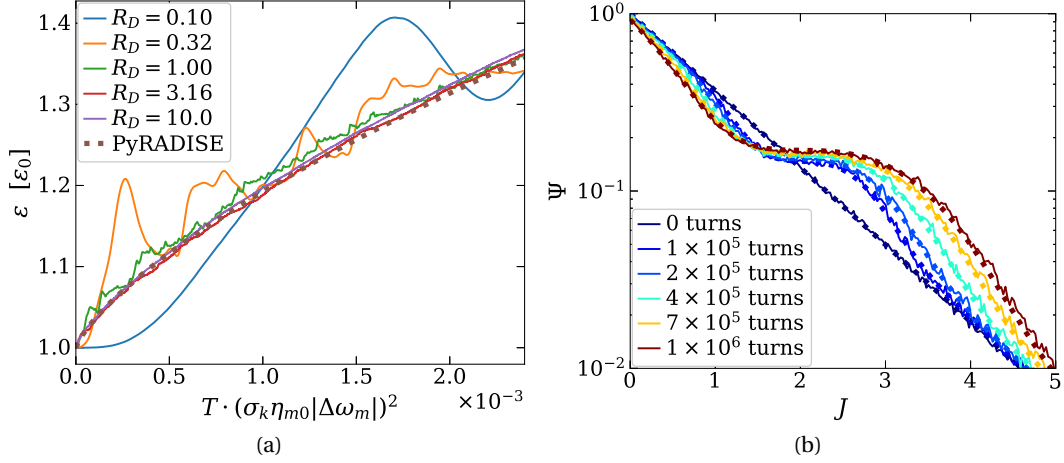


Figure 6.7: Evolution of emittance in (a) for different values of R_D given by Eq. (6.39), and of the distribution in (b) for $R_D = 10$. The solid lines correspond to multi-particle simulations in COMBI, while the dotted lines have been calculated with PyRADISE. R_D was changed by changing the external noise amplitude σ_k and the number of turns T , while keeping the product $T\sigma_k^2$ constant.

the minimal τ_{hmin} , given by Eq. (E.12). This deterministic evolution will be negligible when $W_h \ll W_D$ and $\tau_{hmin} \gg \tau_m$. Both these requirements and the requirement in Eq. (6.38) can be summarized by a condition on a single ratio of relevant parameters

$$R_D = \frac{|\text{Im}\{\Delta\Omega_m\}|^{2.5}}{a f_{\text{rev}} \sigma_k \eta_{m0} |\Delta\omega_m|} \gg 1. \quad (6.39)$$

If this condition is met, then the diffusion will dominate over the resonant motion.

The condition on R_D has been estimated by simple calculations. Simulations have been run to verify this condition, and to find how large R_D needs to be, before the process is acceptably estimated by a diffusion. The emittance evolution in 5 different simulations is presented in Fig. 6.7a and the distribution evolution for the case of $R_D = 10$ is presented in Fig. 6.7b. It was assumed in Sec. 6.2 that the least stable mode could be modeled as an USHO. To avoid the numerical noise challenges described in Sec. 6.3.2, such a stochastic oscillator has been implemented in COMBI. There is a great agreement between the simulations and the PDE solver PyRADISE for $R_D = 10$. For small values of R_D , the emittance fluctuates as in App. E, and is clearly dominated by the resonance. It seems that the evolution is fairly well modeled as a diffusion starting already at $R_D = 1$. In all the following results, it has been checked that $R_D \gg 1$ at the initial condition.

The message of this section is that the effect of the noise driven wakefields is a diffusion only if the noise is small enough. In Sec. 6.3.2, it was found that a large noise was needed to be stronger than the numerical noise. To model this mechanism self-consistently with multi-particle simulations, both of these requirements must be met. One should use a minimum of 10^7 macroparticles and $\mathcal{O}(10^6)$ turns. This is why the analytical diffusion model presented in this chapter is invaluable in evaluating this mechanism.

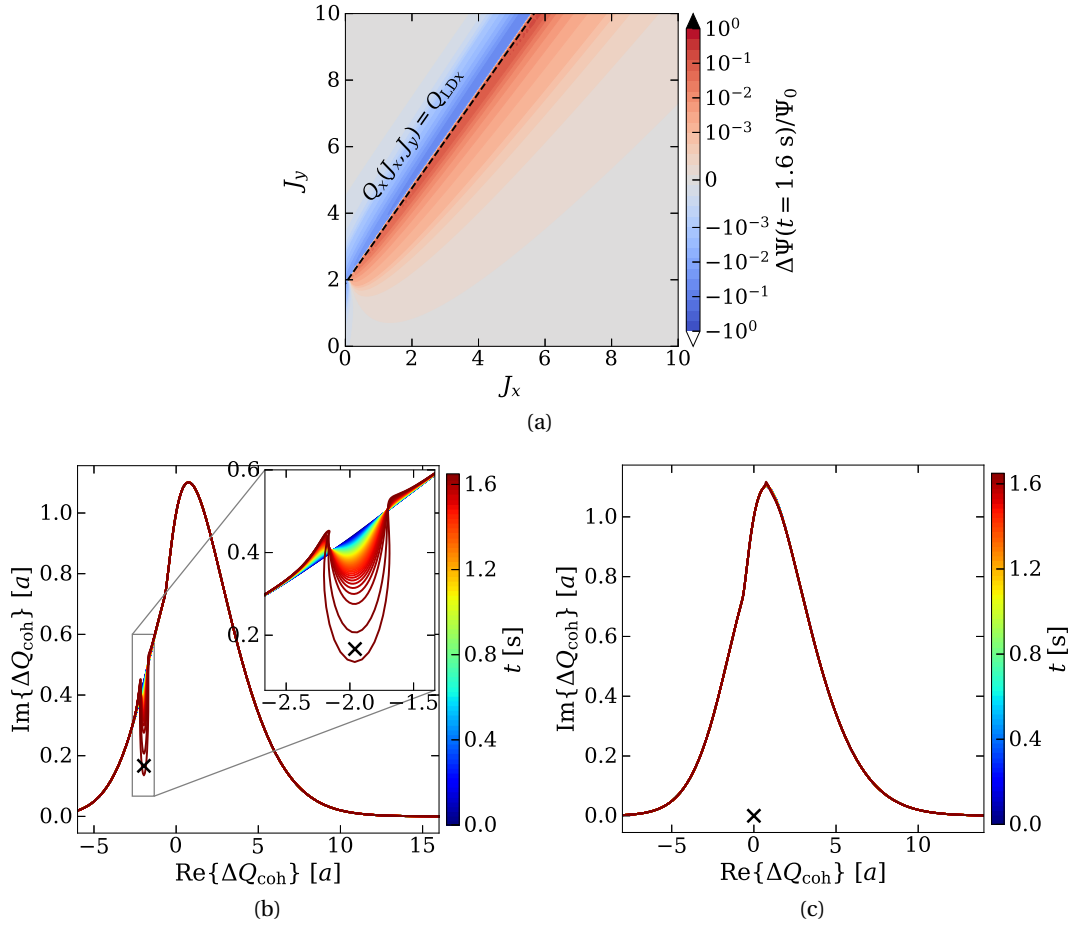


Figure 6.8: Change of distribution in (a) due to diffusion driven by horizontal wakefields, and corresponding evolution of the horizontal and vertical stability diagrams in (b) and (c), respectively. The dashed line in (a) marks the actions where $Q_x(J_x, J_y) = Q_{LDx}$. The cross at $\Delta Q_{\text{coh}x} = -1.47 \times 10^{-4} + 1.25 \times 10^{-5}i$ in (b) marks the tune shift of the least stable mode in the horizontal plane. No mode, nor noise, is included in the vertical plane.

6.4 Results

6.4.1 Distribution and stability evolution

The change of the distribution, and corresponding change of the stability diagram, will here be evaluated in two representative configurations with only horizontal noise. Both cases use $a_{\text{thresh}} = 5 \times 10^{-5}$, $a = 1.5a_{\text{thresh}}$, $b = -0.7a$, and $\eta_{m0}\sigma_k = 1 \times 10^{-4}$. The difference is the coherent tune shift in absence of Landau damping, $\Delta Q_{\text{coh}x}$. Note that the diffusion coefficient in Eq. (6.23) and analytical latency estimate in Eq. (6.34) do not depend on the absolute values of a and $\Delta Q_{\text{coh}x}$, but only on their ratio. This fact is also illustrated in Fig. 6.2, as the frequency shifts are given in units proportional to a .

In the first case, the least stable mode is at $\Delta Q_{\text{coh}x} = -1.47 \times 10^{-4} + 1.25 \times 10^{-5}i$. This is the same configuration as was tested in Sec. 6.3.1. The relative change of the distribution at the time of the instability is illustrated in Fig. 6.8a. The distribution is locally flattened in the

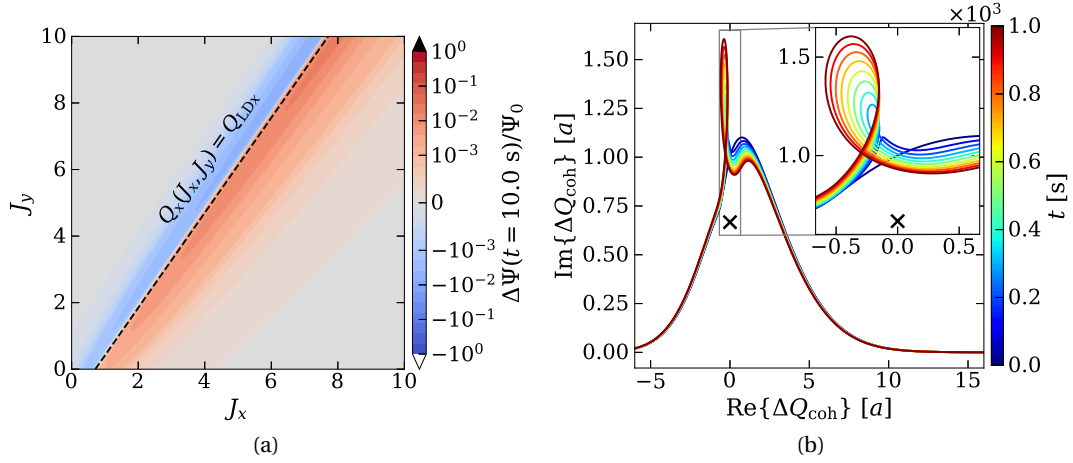


Figure 6.9: Change of distribution in (a) and evolution of the horizontal stability diagram in (b), due to diffusion driven by horizontal wakefields. The dashed line in (a) marks the actions where $Q_x(J_x, J_y) = Q_{LDx}$. The cross at $\Delta Q_{coh x} = 5.00 \times 10^{-5} i$ in (b) marks the tune of the least stable mode.

horizontal direction at the resonant actions $Q_x(J_x, J_y) = Q_{LDx}$, equivalently to the process illustrated in Fig. 6.7. The local flattening causes a change of the horizontal stability diagram that is illustrated in Fig. 6.8b. A borehole is drilled in the stability diagram directly at the frequency of the least stable mode. The drilling speeds up as the instability is approached, since $\text{Im}\{Q_{LDx}\}$ approaches 0. The vertical stability diagram in Fig. 6.8c is barely modified in this process.

In the second case, the least stable mode is at $\Delta Q_{coh x} = 5.00 \times 10^{-5} i$, which is purely imaginary. The relative change of the distribution after 10s and the evolution of the stability diagram are illustrated in Fig. 6.9. The distribution changes as in the first case, with the main difference being a shift of the resonant tune, due to the different $\text{Re}\{\Delta Q_{coh x}\}$. Instead of the drilling of a borehole in the stability diagram, the stability threshold does initially grow, before a loop starts developing. This loop is difficult to interpret and it causes challenges for the numerical algorithm used to calculate α and ΔQ_{LDx} . Therefore, the diffusion coefficient has, in the calculation presented here, been kept constant at the initial value. Similar evolutions have been calculated with a time evolving diffusion coefficient. With zero real tune shift, it was derived in Sec. 6.2.5 that a local flattening at the resonant actions would initially lead to an increased stability threshold, which has been verified.

The evolution of $\text{Im}\{\Delta Q_{LDx}\}$ for these two cases is presented in Fig. 6.10. In the derivation of the analytical latency in Sec. 6.2.5, it was assumed that α would stay constant at its initial value $\alpha(0)$. This is not correct. As the borehole is drilled, the curvature of the stability diagram will increase, leading to a reduction of $\alpha(t)$ with time. In addition to the calculations presented in Figs. 6.8 and 6.9, an additional calculation has been executed of case 1 where α has artificially been kept constant at its initial value. The latencies for case 1 in the PyRADISE calculations are 1.65s with evolving $\alpha(t)$ and 3.88s with constant $\alpha(0)$, in comparison to 3.84s estimated with the analytical theory in Eq. (6.34). Note also that even if the stability margin initially increases for case 2 with $\text{Re}\{\Delta Q_{coh x}\} = 0$, it eventually decreases. Nevertheless, the latency is

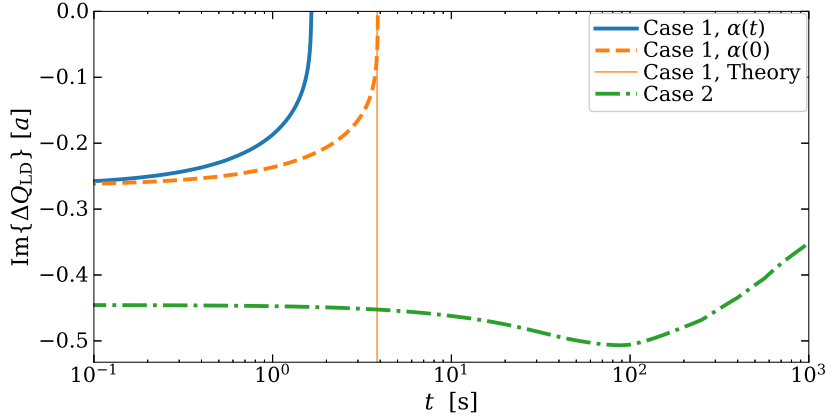


Figure 6.10: Evolution of $\text{Im}\{\Delta Q_{LD}\}$ for the two test cases illustrated in Figs. 6.8 and 6.9. The vertical line marks the latency estimated with Eq. (6.34) for the calculation represented by the dashed line (“Case 1, $\alpha(0)$ ”).

longer than the 87.0s that would have been wrongly estimated with Eq. (6.34), which assumed $|\text{Re}\{\Delta Q_{coh}\}|/|\text{Im}\{\Delta Q_{coh}\}| \gg 1$.

6.4.2 Detuning margin

Test case 1 in Sec. 6.4.1 is representative of the type of modes that typically are the least stable modes in the LHC. The drilling of a borehole in the stability diagram can be expected, and this drilling speed increases as the instability is approached. The latency for the least stable mode $\Delta Q_{coh} = -1.47 \times 10^{-4} + 1.25 \times 10^{-5}i$, affected by noise such that $\eta_{m0}\sigma_k = 1 \times 10^{-4}$, is presented with different detuning margins in Fig. 6.11. By scaling the detuning margin by 1 order of magnitude, from 10% to 100%, the latency increases by more than 4 orders of magnitude.

Note the three different sets of points calculated with PyRADISE: (i) For the points labeled “ $\alpha(0)$ ”, the factor α has been kept constant at its initial value, as was assumed in the analytical latency in Eq. (6.34). The agreement between these points and the approximative analytical latency is striking for $a < 2a_{\text{thresh}}$; (ii) The points labeled “ $\alpha(t)$ ” are considered to best represent the physics at hand, self-consistently solving for both α and the diffusion coefficient as the distribution changes. However, for large stability margins, $a > 2a_{\text{thresh}}$, the linear extrapolation of the damped mode becomes increasingly inaccurate at $t = 0$. Furthermore, as the borehole is drilled this deep for this mode, $\alpha = \partial M_{LD}/\partial M_{coh}$ is quickly varying due to an increased curvature of the stability diagram. Thus, a small inaccuracy in the initial $\text{Re}\{\Delta Q_{LD}\}$ will cause an unphysical drift of $\text{Re}\{M_{LD}\}$ by use of Eq. (6.12) for $|M_{coh}| \gg \epsilon$. This can prevent the instability in the numerical calculation, by nonphysically varying the resonant action; (iii) Therefore, for the points labeled “ $\alpha(t) \in \mathbb{R}, \text{Re}\{\Delta Q\}(0)$ ”, the real tune of the damped mode has been forced constant at the initial value, while α has been allowed to evolve in time, but forced to be real. This is considered the best approximation of the drilling at large detuning margins for this mode.

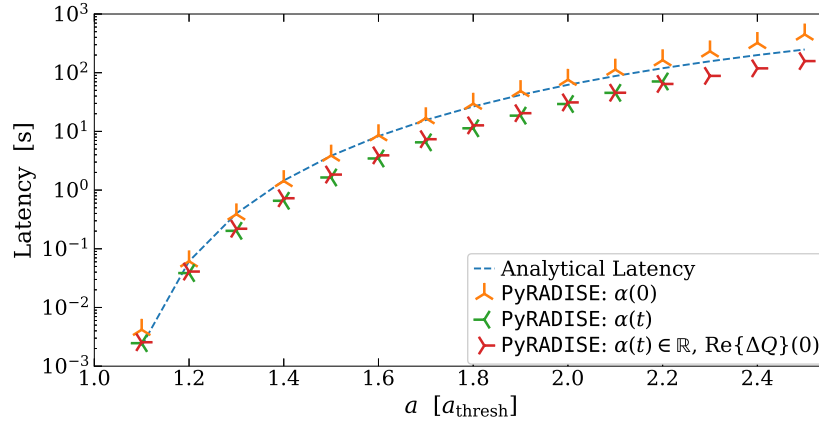


Figure 6.11: Latency for a mode of coherent tune $\Delta Q_{\text{coh}} = -1.47 \times 10^{-4} + 1.25 \times 10^{-5}i$, stabilized by octupole detuning with $a_{\text{thresh}} = 5 \times 10^{-5}$ and $b = -0.7a$.

6.4.3 Dedicated latency experiment in the LHC

This theory has been tested against the experiment conducted in the LHC that was reported in Sec. 4.3 [15, 60]. While at flattop, subsets of the bunches were excited by a controllable noise source, acting equally on all particles per bunch per turn with effectively a white spectrum over multiple turns. Only latencies between 1 min and 60 min were acceptable, due to constraints of the theory and the allotted time with the machine. The condition for diffusion in Eq. (6.37) has been found to be met for all investigated bunches with $R_D \gtrsim 200$.

The latency for a specific bunch depends strongly on the individual bunch parameters, especially the emittance and intensity. This can mask the dependence on the machine parameters. The analytical latency for the worst mode, given by Eq. (6.34), is illustrated as a function of the chromaticity and feedback gain in Fig. 6.12a. The second shortest latency is given in Fig. 6.12b, in units of the shortest latency, hinting at whether a single mode is sufficient in modeling the latency or not. Note that the predicted latencies vary by more than 6 orders of magnitude in this limited parameter space, where neither the octupole current, nor the noise amplitude, nor the bunch specific parameters have been varied.

The latencies of the 8 bunches in B2 in fill 1 in Fig. 4.1 have been investigated in more detail, including the bunch specific parameters, such as the intensity, emittances, bunch length, and applied noise amplitude. The comparison between the experimental latencies and the latencies calculated with PyRADISE is given in Fig. 6.13a. The first set of bunches (450-1350) was the first intentional experimental realization of this mechanism. These bunches were acted on by external noise in two intervals, with an emittance measurement that was subpar by chance, giving cause for the large error bars. They went unstable with $a \approx 2a_{\text{thresh}}$, assuming a Gaussian bunch. The second set of bunches (1950-2850) was acted on in slightly better conditions, allowing for a better quantitative comparison to the diffusion model. The first three of these bunches went unstable with $a \approx 2.4a_{\text{thresh}}$, assuming a Gaussian bunch. Bunch 2850 did not go unstable during the experiment. The chromaticity was $Q' = 15$, and the damping time due to the feedback was 170 turns. For this configuration, all modes with positive $\text{Im}\{\Delta Q_{\text{coh}}\}$ and centered maximally 10 synchrotron sidebands from the bare

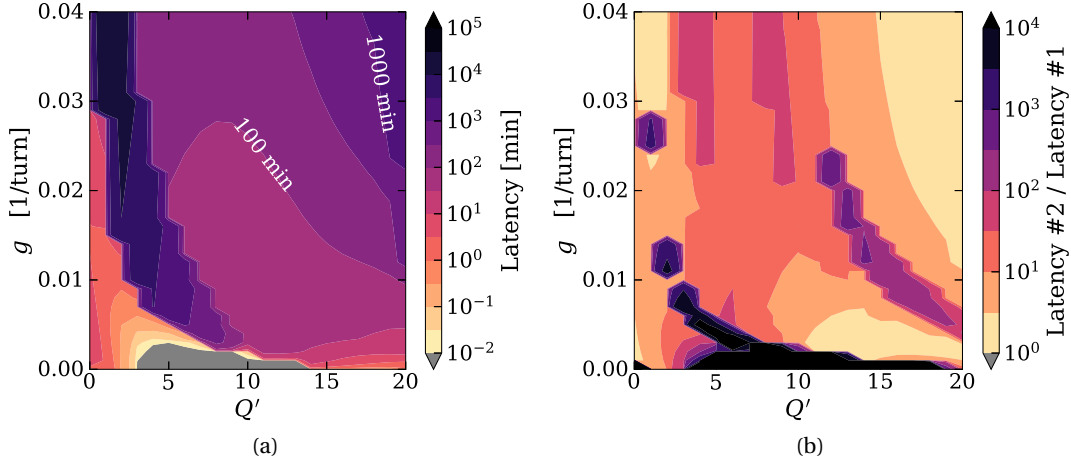


Figure 6.12: Analytical latency of the worst horizontal mode in B1 in the LHC in (a) and second worst mode in (b), for the parameter values: normalized emittance $\varepsilon_{nj} = 1.4 \mu\text{m}$; bunch length $4\sigma_s = 1.05 \text{ ns}$; intensity $N = 1.1 \times 10^{11}$ p/b; noise amplitude $\sigma_k = 1 \times 10^{-4}$; octupole current $I_{\text{oct}} = 400 \text{ A}$. Latencies below 0.6 s have been marked as if the bunch was already unstable.

tune, $|l_m| \leq 10$, are displayed in Fig. 6.13b. Since one mode stands out, a single mode should represent the diffusion well.

The error bars in Fig. 6.13a are large, because the latency scales quadratically or faster with a set of uncertain parameters, as given by Eq. (6.36). The considered most significant uncertainties are: (i) The emittance measured with the BSRT was found in 2018 to have a 10% accuracy [61]. During the measurement of bunches 450-1350, the emittance measurement of all bunches displayed an unphysical oscillatory drift. The total uncertainty in the emittance of these bunches has therefore been estimated to 25%. As the linear detuning coefficients in Eq. (2.31) are proportional to the emittance, this uncertainty affects the knowledge of the stability margin. Furthermore, the horizontal noise σ_k is given in units of the beam divergence, such that $\sigma_k^2 \varepsilon_{nx}$ is constant. Thus, the larger emittance corresponds to the upper error bar on the latency. A 10% uncertainty in the emittance causes an uncertainty of a factor ~ 2 on the latency for these detuning margins. Remember that the dependence is rather on the stability margin than the absolute emittance. Hence, this factor should not be used in general. It was found in 2018 that the BSRT on average underestimated the emittance, favoring the upper error bar [4]; (ii) The noise amplitude was experimentally known with low accuracy. By comparing the emittance growth of these bunches in B2 with multi-particle simulations, the noise amplitude has been scaled by a factor 3.85 ± 0.30 to $\sigma_k \in [3.4, 14.3] \times 10^{-4}$, ignoring the uncertainty; (iii) The feedback gain is considered to be estimated with approximately 10% margin; (iv) The chromaticity was not measured on the day of the fill presented in Fig. 6.13. It is therefore only estimated with accuracy ± 1 . The uncertainty in the feedback gain and chromaticity causes an uncertainty in ΔQ_{coh} and η_{m0} . The shortest and longest latency has been calculated with $Q' = 15 \pm 1$ and $g = (12 \pm 1) \times 10^{-3}$. The uncertainty in gain and chromaticity only causes a small part of the total error bar on the latency, in comparison to that caused by the uncertainty in the emittance.

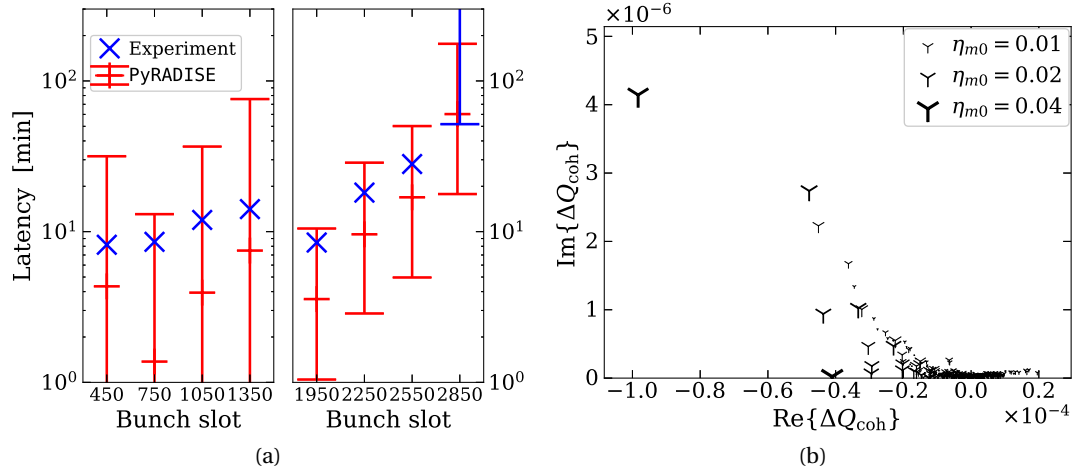


Figure 6.13: Comparison between an experiment in the LHC [15, 60] and the latency found by PyRADISE solving the diffusion equation introduced in this chapter in (a), for the worst mode found by BimBim in (b). The error bars in (a) are due to uncertain measurements of the emittances, chromaticity, feedback gain, and external noise amplitude during the experiment. Predicted latencies below 1 min are not shown, as the dynamics require more time to be modeled accurately as a diffusion (see Sec. 6.3.3). Bunch 2850 did not go unstable before I_{oct} was reduced after 52 min.

The experiment was repeated in similar conditions, but with the chromaticity set to $Q' = 5$. No instabilities were reached during the experiment at the initial octupole current. Furthermore, by reducing I_{oct} , it was found that the stability threshold had barely been modified by the noise. This is in qualitative agreement with the predictions in Fig. 6.12a, where the latency is more than an order of magnitude longer for $g \sim 0.01$ and $Q' \sim 5$, than for $g \sim 0.01$ and $Q' \sim 15$. The alternative settings, with $Q' \sim 5$, would allow for a reduction of the required stability margin in operation. Nevertheless, other instability mechanisms have been observed with low positive chromaticities [55]. They may limit the range of acceptable chromaticities for the operation of the LHC.

6.4.4 Physics fills in the LHC

This study was mainly motivated by the observations reported in Ch. 4. Instabilities were developing when the beam was maintained in a steady configuration for a few to tens of minutes, with an octupole current less than twice the required value expected from linear Vlasov theory with a Gaussian distribution. Consequently, the LHC was operated with at least twice as much octupole current as initially expected to mitigate this instability [3, 53]. The detuning coefficients in normal operation in 2018 were on average close to the ones in the experiment described in the previous section, with an average normalized emittance of $1.9 \mu\text{m}$ and octupole current $I_{\text{oct}} = 280 \text{ A}$. The noise was measured at approximately $\sigma_k = 6 \times 10^{-5}$, with the operational gain of $g = 0.01$ [41]. The predicted latency for the average bunch at $Q' = 15$ and $g = 0.01$ is 120 min, which is slightly larger than the value in Fig. 6.12, due to the lower noise amplitude. With a 15% lower emittance, the expected latency drops to 9.9 min, illustrating again how sensitive the latency is to the individual bunch parameters. Similar

reductions of the latency occur from an equal reduction of I_{oct} or increase of the intensity. We note that the latencies obtained with the formula in Eq. (6.34) are usually overestimated with respect to the numerical estimates. Nevertheless, such latencies seem compatible with safe operation of the LHC. Hence, this study confirms the observed efficiency of the mitigation strategy of operating with a margin in the octupole current, initially implemented based on empirical evidence only.

6.5 Discussion

The analytical latency and simulated results that have been presented have assumed that a single mode was dominant. The ratio of the second shortest latency in B1 in the LHC to the shortest latency was presented in Fig. 6.12b. In the configurations that have been studied, the shortest latency is at least an order of magnitude shorter than the second shortest, and is thus dominant. In configurations where two modes are relevant, one of three things can happen:

- The modes flatten the distribution at exactly the same frequency, reducing the latency by maximally a factor 2 for uncoupled modes.
- The modes flatten the distribution at close but different frequencies, widening and increasing the diffusion, causing either an increase or decrease of the latency, depending on the separation in frequency.
- The modes flatten the distribution at well separated frequencies, with no impact on one another.

A case-by-case study is required for exact predictions of the impact of the second worst mode.

In this chapter, only the wake driven diffusion has been considered. It is found to be a strong candidate for the driver of the instabilities of long latencies observed in the LHC. Diffusion that can counteract the drilling in the stability diagram has not been studied in detail here. The diffusion due to the first term on the RHS of Eq. (6.17) and due to IBS were included in [69], and found to only marginally increase the latency in an LHC-like configuration. The effect of IBS will depend on the ratio between the latency and the IBS driven emittance doubling time, which is in the order of days in the horizontal plane of the LHC at flattop. The IBS is essentially negligible in the vertical plane. If the latency, ignoring the IBS, is similar to the IBS driven doubling time, it may be increased indefinitely. However, instabilities with that long latencies are not a problem for operation of the LHC.

6.6 Conclusion

Transverse instabilities with latencies from a few to tens of minutes have been observed in the LHC, both in regular operation and in dedicated experiments. In this chapter, the hypothesis that such instabilities are due to a long-term evolution of the transverse distribution, which leads to a loss of Landau damping have been considered. The mechanism that has been studied in detail here, is that external sources of noise excite the beam, which then acts back on itself through electromagnetic wakefields. The coherent response of the beam has been modeled as a set of damped harmonic oscillators, representing the least stable wakefield driven modes. The impact of the wakefields on the individual particles has been modeled as a diffusion, which is narrow in frequency space around the real frequency of the least stable

mode. Thus, the diffusion is also narrow in action space around the resonant action, causing a local flattening of the distribution in 2D action space. Numerical calculations with PyRADISE have shown that the distribution evolution efficiently drills a borehole in the stability diagram at the frequency of the least stable mode, if the absolute value of the real tune shift of the coherent mode is large compared to the imaginary part. This can cause an instability with a latency. One of the most effective techniques to extend the latency, and thus mitigate this instability mechanism, is to operate with a large stability margin, i.e. more detuning than required to stabilize a Gaussian beam. An analytical expression for the latency has been derived in Eq. (6.34) under strict assumptions, and found to consistently be a factor ~ 2 longer than the latency found with PyRADISE. The predicted latency is sensitive to the input, being proportional to the second or higher power of multiple parameters. Consequently, the latencies of the configurations considered in this chapter vary by more than 8 orders of magnitude.

The new theory has been compared with a dedicated latency experiment conducted in the LHC [15, 60]. The latencies measured in the experiment have been reproduced, albeit with large error bars, eventually causing instabilities with more than twice the required detuning strength for a Gaussian distribution. The latencies in regular LHC operation are also in agreement with the new theory. Thus, it can be concluded that the loss of Landau damping observed in the LHC is most probably caused by noise excited wakefields driving a diffusion of individual particles. One important result is the confirmation that the latency is approximately an order of magnitude longer at an intermediate chromaticity $Q' \approx 5$ with a feedback driven damping time of 200 turns, than at $Q' \approx 15$. This constitutes an alternative working point for the LHC worth considering in view of relaxing intensity limits that may arise due to this mechanism.

MULTI-BUNCH BEAM QUALITY

Part III

7 COMBIp – Pipeline algorithm for multi-beam multi-bunch simulations

Disclaimer: This chapter was adapted from the following article — with permissions of the co-author and publisher:

[79] **S. V. Furuseth** and X. Buffat, “Parallel high-performance multi-beam multi-bunch simulations”, *Computer Physics Communications* **244**, pp. 180–186, 2019. doi:[10.1016/j.cpc.2019.06.006](https://doi.org/10.1016/j.cpc.2019.06.006)

It was published under CC-BY 4.0.

My contribution: All results presented here.

7.1 Introduction

Coherent multi-bunch interactions can cause severe impacts on the beams in circular colliders [66]. To understand the dynamics of such interactions, the accelerator physics community relies both on analytical models and high-performance tracking codes. Each beam consists of multiple bunches. The bunches are affected by external electromagnetic fields, such as those produced by the machine, and by interactions with each other. There are:

- Independent, intra-bunch effects, such as the forces from the various magnets.
- Intra-beam, inter-bunch interactions, such as the kicks from electromagnetic wakefields, space charge forces, electron clouds, or feedback systems.
- Inter-beam, inter-bunch interactions close to the IPs, called beam-beam interactions.

The different effects, as they are modeled in simulations, will be referred to as calculations.

There exists a wide library of simulation codes developed specifically for circular particle colliders, exploiting the parallel infrastructure of modern computers in different ways. How a code is parallelized depends on what the code is designed to study. BeamBeam3D is a parallel particle-in-cell code designed to model beam-beam interactions in three dimensions in detail [80]. Each bunch is represented by multiple macroparticles, and six phase space coordinates represent each macroparticle. The parallelization is done with a particle-field decomposition, slicing each bunch longitudinally, and distributing the slices on separate processes. The impact of the slices of Beam 1 (B1) on the slices of Beam 2 (B2) is calculated in order. PyHEADTAIL studies the interplay of a single multi-bunch beam with the machine

through electromagnetic wakefields [81]. In the multi-bunch version, multiple bunches are allocated to each process. The same calculation is performed for all bunches simultaneously. The parallelization scheme in COMBI differs from BeamBeam3D and PyHEADTAIL as it was designed for multi-bunch beam-beam interactions, and was later extended to study the interplay with other effects, such as wakefields [7, 76, 77]. Each bunch is allocated to its own process, and all bunches are controlled by a master process. The bunches are distributed on a circular grid as in a collider, and synchronized at the end of each calculation to ensure causality.

An unbreakable rule of physics is causality. When simulating coherent multi-beam multi-bunch effects, causality puts strict constraints on the order of the calculations. However, the parallel algorithm in COMBI was more inefficient than necessary when considering various types of interactions with different computing and communication requirements [7]. Based on the analysis of the inherent constraints and the shortcomings of the original algorithm, a new parallel algorithm has been designed and implemented in the code. It was inspired by putting the calculations for each bunch in separate pipelines, and is referred to as COMBIp (Coherent Multi-Bunch Interactions – Pipelined). Finally, the performance of COMBIp will be analyzed and compared to that of the old parallel algorithm.

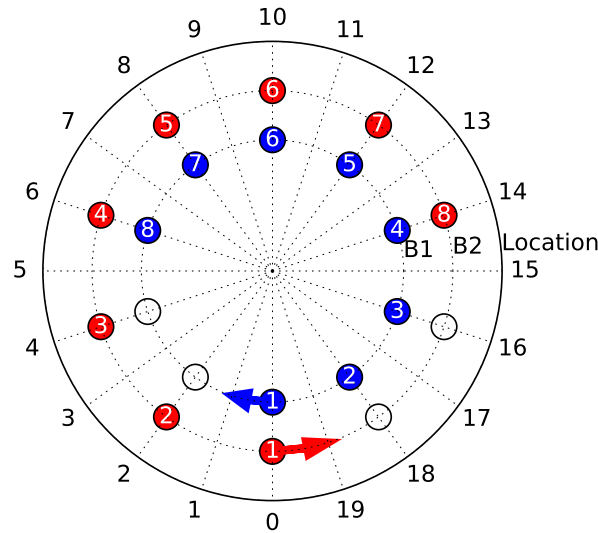


Figure 7.1: A circular collider model where two beams (B1 in blue, B2 in red) move in opposite directions. Both beams have 8 bunches in a row followed by two empty slots. There are twice as many locations for calculations as bunch slots, to be able to model beam-beam interactions.

7.2 Causality caused challenges in simulations

A circular collider contains two beams that are moving in opposite directions, as shown in Fig. 7.1. This example with 8 bunches per beam will be discussed repetitively in this chapter. The locations must be traversed in order, meaning 19, 0, 1, ... for a bunch in B1, and 1, 0, 19, ... for a bunch in B2, to ensure causality. At each location there may be a calculation to be performed, or not. The different types of necessary calculations, and their impact on ensuring causality, will now be discussed.

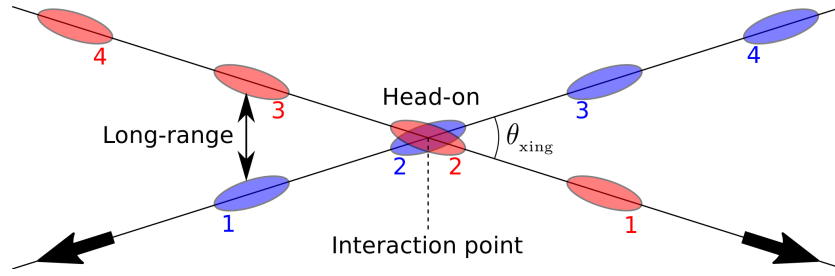


Figure 7.2: Schematic of inter-beam calculations around an IP in a circular collider. Each bunch may experience one head-on calculation in the center and a number of long-range calculations on both sides. The number labels at the head of each bunch are the bunch numbers, given that the IP is in location 0 in Fig. 7.1.

Independent, intra-bunch calculations only depend on the affected bunch, and require no communication between the bunches. That is for example the bending and focusing from the magnets around the machine. It can also be the case for simplified models of inter-bunch calculations, such as the weak-strong model of beam-beam interactions [82]. These calculations have to be done in order for each bunch separately, to ensure causality. However, in a multi-bunch simulation, these calculations do not require any synchronization between the bunches.

Intra-beam, inter-bunch calculations, from now on referred to as intra-beam calculations, can be represented as in Fig. 2.5. A source charge traverses the machine and leaves some remnant mark on its surroundings, either as remnant electromagnetic fields or as measurements by the BPMs that lead to a kick from the feedback system. In the ultra-relativistic limit, a bunch cannot affect bunches ahead of itself. From here on wakefields are referred to as an example of these interactions. The effect of wakefields is typically weaker the greater the distance is between the source and the witness. The wakefields produced by each bunch can numerically be calculated simultaneously for all the bunches in the same beam. Then the wakefields must be communicated to the trailing bunches, before the kicks from the wakefields can be calculated. Hence, a bunch cannot overtake another bunch beyond this calculation. Without inter-beam calculations, the individual bunches can easily be parallelized, by performing each calculation simultaneously for every bunch. That is how it is done in PyHEADTAIL [81].

Inter-beam calculations can be represented as in Fig. 7.2. In modern circular colliders, the two beams are kept separated except for close to the points where the beams are brought into collision. For example, assume that there is a head-on calculation at location 0 in Fig. 7.1, and a long-range calculation at locations 1 and 19. To preserved causality, bunch n of B1 (B1b n) must first interact with bunch $n - 1$ of B2 at location 19, then bunch n at location 0 and finally bunch $n + 1$ at location 1, given that these bunches exist. Extending this rule to all the bunches, the calculations must be done in the following order:

1. B1b1 interacts with B2b1 at location 0. Every other bunch must wait.
2. B1b2 interacts with B2b1 at location 19 and B1b1 interacts with B2b2 at location 1.
3. B1b2 interacts with B2b2 at location 0.

And so on. With equal number of bunches per beam and beam-beam interactions, this can be parallelized efficiently by letting the bunches do different calculations simultaneously.

That was the inspiration of the old algorithm in COMBI. With more bunches than beam-beam interactions the calculations can still be parallelized efficiently by overlapping multiple turns. If there is no intra-beam calculations, nor filling of every bunch slot in the collider model, the third step above would then be:

3. B1b2 interacts with B2b2 at location 0 (turn 1), and B1b1 with B2b1 at location 0 (turn 2).

The bottleneck, preventing these parallel multi-beam multi-bunch simulations from being efficient, arises when one includes both intra-beam and inter-beam calculations in the same simulation. The intra-beam calculations prefer the bunches to do the same calculation in parallel, while the inter-beam calculations prefer the bunches to do different calculations in parallel. As a result, there is a sizable amount of empty time when no calculation can be done for a given bunch, due to causality. To maximize the efficiency of a parallel multi-beam multi-bunch simulation, these periods of waiting bunches must not correspond to the stalling of processing units.

7.3 Parallel algorithms

7.3.1 COMBI

COMBI is implemented with a hybrid OpenMP-MPI parallelization. The MPI (Message Passing Interface) parallelization employs a master-worker algorithm, with one master process overall, and one worker process per bunch [83]. Each calculation is parallelized internally in each worker process with OpenMP (Open Multi-Processing) [7]. The algorithm is shown in detail in Algorithm 1. The bunches of each beam are fixed to a circular grid as in Fig. 7.1, and rotated synchronously to their next locations in the collider model. The master process tells all workers what the bunches have to do, whether it is a calculation or nothing. After the workers are done, they send a completion confirmation each to the master. Therefore, all workers have to wait for the slowest calculation to finish, before the bunch grids are rotated to their next locations.

The Gantt charts for the bunches in B1 in Fig. 7.1 are shown for three illustrative examples in Fig. 7.3: (i) Independent and intra-beam calculations; (ii) Independent and inter-beam calculations; (iii) Intra-beam and inter-beam calculations. The charts on the left include the synchronization in the COMBI algorithm, while the charts on the right display the optimal flows that still ensure causality. Since there is only one bunch per worker process, these are efficiently the Gantt charts for the worker processes. Therefore, the white gaps between the calculations correspond to wasted Central Processing Unit (CPU) hours. Note that this example only considers 8 bunches. The LHC holds up to 2808 bunches [1], for which the efficiency would approach zero.

This algorithm was developed with beam-beam calculations in mind. It limits the efficiency especially when the number of bunches outnumbers the number of calculations, or when the calculations are of varying numerical complexity. The wall time per turn, assuming that the number of bunches is larger than the number of calculations, is expected to be in the order of

$$t_{\text{par}} \sim \max_i \{t_i\} \cdot \max_j \{N_{bj}\} \cdot \frac{N_{b1} + N_{b2}}{N_{\text{core}}}, \quad (7.1)$$

Algorithm 1 COMBI (old)

```

1: procedure MASTER(rank)
2:   PARSE input files
3:   SEND bunch details to Workers
4:   CREATE collider
5:   // list of calculations at location
6:   for turn in numberOfTurns do
7:     for step in numberOfLocations do
8:       Rotate bunch grids one step
9:       SEND calculations to Workers
10:      RECEIVE confirmation from Workers
11:    end for
12:  end for
13:  SEND Abort to Workers
14: end procedure

15: procedure WORKER(rank)
16:  RECEIVE bunch details from Master
17:  CREATE bunch
18:  while TRUE do
19:    RECEIVE message from Master
20:    if message is calculation then
21:      Perform calculation
22:      SEND confirmation to Master
23:    else if message is Abort then
24:      BREAK
25:    end if
26:  end while
27: end procedure

```

Algorithm 2 COMBIp (new)

```

1: procedure PIPELINE(rank)
2:   PARSE input files
3:   CREATE bunches for this rank
4:   SET bunch.step to 0
5:   CREATE bunch.pipeline
6:   // all calculations for one bunch
7:   while all bunches are not done do
8:     for bunch in bunches do
9:       if bunch is done then
10:        CONTINUE
11:      end if
12:      SET calculation to pipeline[step]
13:      if need to send then
14:        TEST if previous message is read
15:        SEND new message (non-blocking)
16:      else if need to receive then
17:        PROBE if message is sent
18:        RECEIVE message (non-blocking)
19:      end if
20:      if communication failed then
21:        CONTINUE
22:      end if
23:      Perform calculation
24:      INCREMENT step
25:      Update whether the bunch is done
26:    end for
27:  end while
28: end procedure

```

where t_i is the wall time of the calculation at location i with 1 core, N_{bj} is the number of bunches in beam j , and N_{core} is the total number of cores. This formula is meant for comparison with the new algorithm, not for predicting the actual wall time.

7.3.2 COMBIp

The new parallelization algorithm, COMBIp, is detailed in Algorithm 2. The key advances from the original algorithm are:

- The bunches are autonomous.
- All calculations for each bunch are put in individual pipelines.
- The communication between the bunches is asynchronous, and only done when information is required.
- There can be multiple bunches per process.

The processes are still parallelized with MPI. The communication between the bunches is handled with MPI as well, even if the bunches are on the same process. Additional memory is allocated for the messages, to prevent the memory from being overwritten before it is received. The size of this additional memory is negligible compared to the memory required to store the phase space coordinates of the macroparticles that constitute the bunches. Each calculation handled by the processes is still parallelized with OpenMP. Hence, each bunch can maximally exploit the cores on one full compute node.

Since the bunches are autonomous, the need for the master process is gone. Therefore, the communication from and to the master is no longer needed. Since the bunches' calculations are in separate pipelines, the bunches are no longer waiting after each calculation for all the other bunches to finish. Since the communication is asynchronous, the processes do not have to stall while waiting for other processes to respond, freeing up the processing power. To achieve this, the calculations that require communication with other bunches have been split in two, first sending and then receiving the required information. This separation is especially useful for the intra-beam calculations, where each bunch must communicate with all other bunches in the same beam. Due to the first 3 advances, the Gantt charts for the bunches are the most efficient ones shown on the right in Fig. 7.3.

It is still of utmost importance to ensure that causality is preserved. Because the calculations are in separate pipelines, the independent calculations are automatically performed in the correct order. Mistakes can only arise from the calculations that require communication between the bunches. However, when a bunch arrives at a location where the calculation requires communication, the bunch knows which bunch(es) it is supposed to communicate with. First, it will test if the previous message(s), using the assigned memory buffer, has been received with `MPI_Test`. If yes, it will non-blockingly send the new message(s) with `MPI_Isend` to the bunch(es) it is interacting with. Then, the process allows the other bunches on the process to do their next calculations. Next, the bunch will non-blockingly check with `MPI_Iprobe` if the message(s) from the bunch(es) it is interacting with has been sent. If yes, it will start receiving the message(s) with `MPI_Recv`. The bunch can and will wait till after it has sent its message(s) and received the required message(s), before it performs the calculation. Thus, the minimum required synchronization is achieved, and causality is preserved, due to how the inter-bunch communication is implemented.

The main goal of this work was to make efficient simulations including both intra-beam and inter-beam calculations. It was displayed in Fig. 7.3f that in such simulations, individual bunches would have to wait due to causality, even if the synchronization was minimal. However, when bunch 1 has to wait in this example, bunch 5 can perform its calculations. Since the new algorithm allows for having multiple bunches per process, a process does not have to stall when a bunch has to wait. This last key advance, thus allows the simulation efficiency to go beyond the most efficient flow of calculations shown on the right of Fig. 7.3. The wall time per turn is expected to be in the order of

$$t_{\text{par}} \sim \sum_i t_i \cdot \frac{N_{b1} + N_{b2}}{N_{\text{core}}}. \quad (7.2)$$

Hence, the new algorithm can be up to $\max_j \{N_{bj}\}$ times faster than the old algorithm.

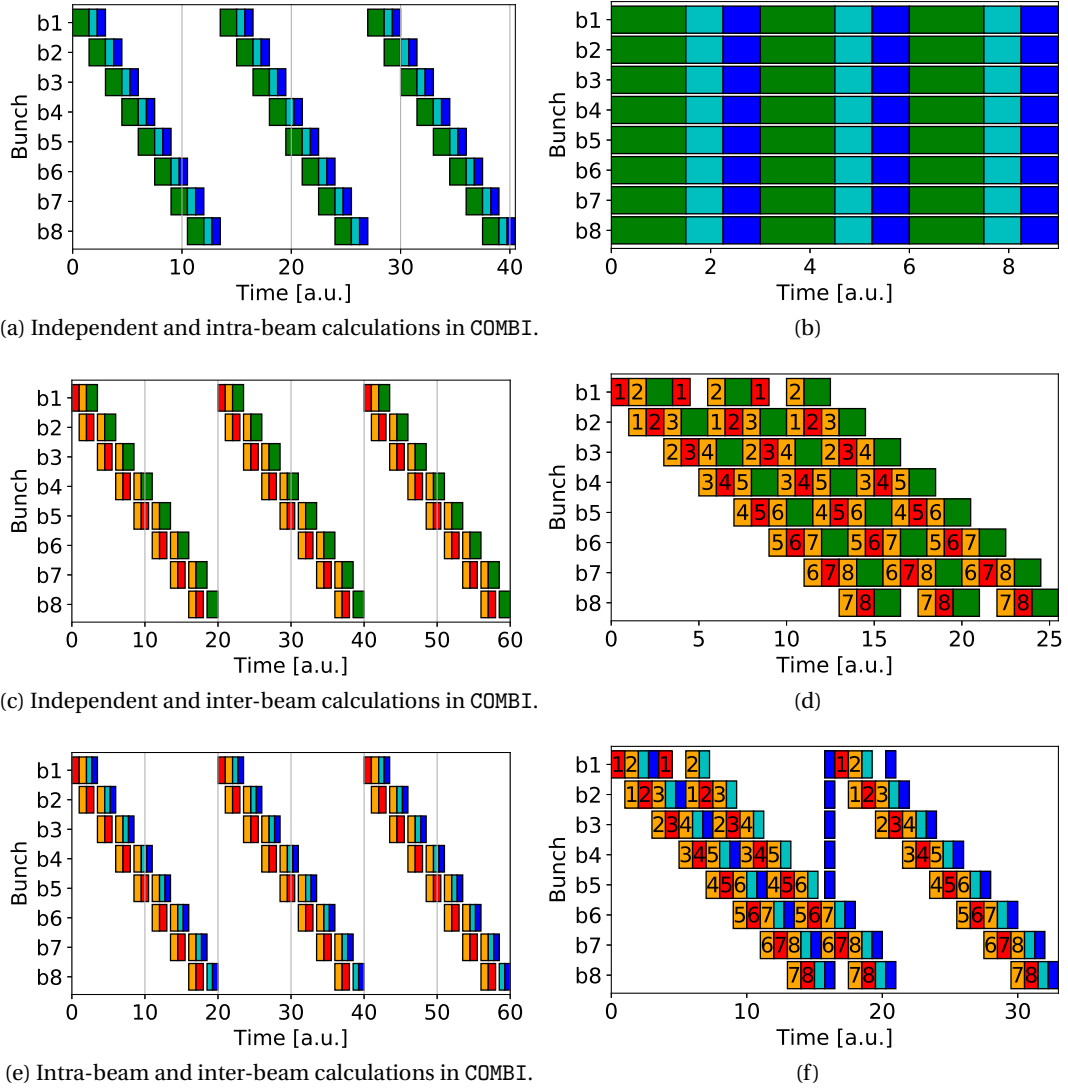


Figure 7.3: Gantt charts [84] of the flow of calculations for 8 bunches (b1-b8) of one beam, while still ensuring causality. The charts on the left, (a), (c), (e), include the synchronization after each calculation in COMBI. The charts on the right, (b), (d), (f), are the most efficient flows possible, including only the strictly necessary synchronization to ensure causality. The order of the calculations for each bunch is read left to right. If there is a white gap, it means that the next calculation cannot yet be initiated, because it requires input from another bunch. **Green** is independent calculations, **Light blue** is the calculation of that bunch's wakefields, **Blue** is the impact of other bunches' wakefields, **Red** is the head-on beam-beam calculation, and **Orange** is a long-range beam-beam calculation. The numbers on the beam-beam calculation blocks on the right refer to which bunch of the other beam the calculation is with, assuming the head-on calculation is in location 0 in Fig. 7.1. The necessary calculations for 3 turns are displayed. The time of the different types of calculation is set artificially. These charts are only meant to show the inter-bunch dependencies.

7.4 Timing results

The parallel algorithms have been tested in detail for their performance in relevant configurations. All simulations have been run on the Deneb cluster at EPFL, with nodes containing 2 Ivy Bridge processors running at 2.6 GHz, with 8 cores each [85]. They have been run with 10^6 particles per bunch, for 100 turns. They were run 4 times, whereupon the average wall time was calculated. The wall time per turn and efficiency will be presented. The efficiency is a measure of how well a parallel algorithm exploits additional computing resources [86], and is here defined as

$$\text{Efficiency} = \frac{t_{\text{ref}}}{t_{\text{par}}} \cdot \frac{N_{\text{cores,ref}} / s_{\text{ref}}}{N_{\text{cores,par}} / s_{\text{par}}}, \quad (7.3)$$

where t , N_{core} and s are the wall time, number of cores and problem size of a simulation. The subscripts ref and par correspond to a reference simulation and the parallel simulation for which the efficiency is sought after. Typically $N_{\text{cores,ref}} = 1$, but the more general definition in Eq. (7.3) is more suitable for this study. For a perfectly scaling algorithm, the efficiency is 1. The speedup from the reference simulation to a parallel simulation is here defined as

$$\text{Speedup} = \frac{t_{\text{ref}}}{t_{\text{par}}}. \quad (7.4)$$

The timings have been measured for models like the ones presented in Fig. 7.3. The models consisted of various combinations of the following:

- A linear phase advance including linear chromaticity, independent for each bunch.
- A section with one head-on beam-beam calculation and one long-range beam-beam calculation on each side.
- A wakefield calculation.

The relative wall times of the different types of calculations, neglecting the communication, are presented in Table 1. These values are meant to show the ratio between the different calculations, not to be compared to the integrated wall time per turn that will be presented.

Table 7.1: Relative time of different calculations in the scalings.

Calculation	Time [t_{BB}]
Independent	9.6
Beam-beam ¹	1
Wakefield	0.84
Bunch moments ²	1.64

¹ Head-on and long-range calculations have equal numerical complexity.

² Calculated after each turn and prior to communication in beam-beam and wakefield calculations.

7.4.1 Strong scaling

The strong scaling of an algorithm is how the wall time varies with the number of cores for a fixed total problem size. That is, $s_{\text{ref}} = s_{\text{par}}$ in Eq. (7.3) [86]. The reference simulation was calculated with COMBIp with 1 core. In this case, the speedup of a perfectly scaling algorithm

would be equal to $N_{\text{cores,par}}$. For the following simulations, the strong scaling will be presented for three schemes, the first with the old algorithm and the last two with the new algorithm:

- COMBI: Start with $(N_{b1} + N_{b2}) + 1$ processes of 1 thread, then add more threads.
- OpenMP→MPI: Scale 1 process up to 16 threads, then add more processes.
- MPI→OpenMP: Scale up to $(N_{b1} + N_{b2})$ processes, then add more threads per process.

One exception will be noted in the text.

All simulations have 8 bunches per beam. Hyper-threading has been forced off to get reliable scaling data. The reduction of wall time is fitted to Amdahl's law, and the parallel part p is given in the legends for the new algorithm [86]. The expected and actual scaling depend on the required synchronization of the calculations in the collider model, as discussed in Sec. 7.2.

Consider first one beam requiring a single independent calculation per turn. The new algorithm with one core is expected to finish slightly faster than the old algorithm with $N_{b1} + 1$ cores. This is because the master-worker algorithm requires communication for the synchronization and work organization, and only one worker is computing at a time. The scaling is presented in Fig. 7.4a. In this case, COMBI using 9 cores achieves a speedup of 0.89 (efficiency of 0.099) from the serial version of COMBIp, approximately as expected. The results are rather independent of how one increases the number of cores with the new algorithm, both schemes show that the simulation has a parallel part of 99.7%. Because this collider model requires neither communication nor synchronization between the bunches, this is assumed to be the best performance achievable by the COMBIp-algorithm.

For simulations with one wakefield calculation and one independent calculation per turn, the scaling is presented in Fig. 7.4b. It is slightly better to increase the number of processes before the number of threads. That could be because these simulations require a substantial amount of MPI communication, including organization of the incoming wakefield kicks, which is performed by only one thread per process. COMBI using 9 cores achieves again a speedup of 0.89 (efficiency of 0.099) from the serial version of COMBIp. The efficiency of the new algorithm for this collider model is close to the best performance found above, as expected.

For simulations with one head-on calculation and one long-range calculation on each side, in addition to one independent calculation, the scaling is as in Fig. 7.4c. COMBI requires a minimum of 17 cores, with which it achieves a speedup of 2.0 (efficiency of 0.12) from the serial version of COMBIp. COMBIp scales equally well for the two schemes, independently of how the cores are added. The efficiency of the new algorithm for this collider model is close to the best performance found above, as expected.

For simulations with three beam-beam interactions, as above, and one wakefield calculation, the scaling is as in Fig. 7.4d. The MPI→OpenMP scaling of this configuration was performed in three ways, by initially going to 4, 8 and 16 MPI processes, before adding more threads per process. This was done to emphasize the bottleneck introduced in Sec. 7.2, which limits the performance in simulations with both intra-beam and inter-beam calculations, if there is only 1 bunch per MPI process. The 16 bunches were distributed evenly over the MPI processes. With only 1 bunch per process, the efficiency dropped to 0.4 with only 16 cores. There is a clear improvement by having multiple bunches on the same process. For this collider model, it is sufficient to have 4 bunches per MPI process. By allowing for bunches to share a process, the reduction of the performance due to the bottleneck has been avoided.

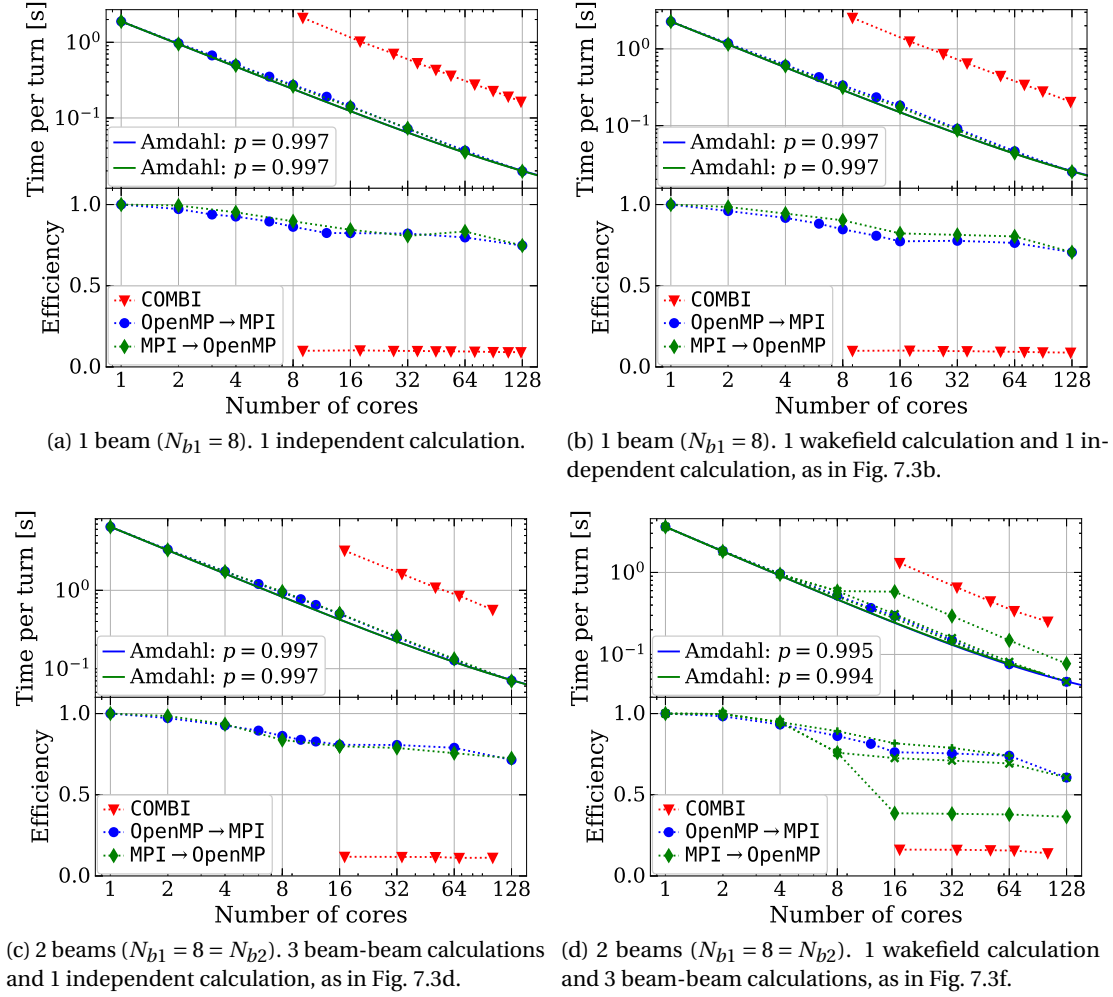


Figure 7.4: Strong scaling with COMBI and COMBIp for different collider models, including independent, beam-beam and wakefield calculations. In (d) “MPI \rightarrow OpenMP” goes to 4 (+), 8 (x) and 16 (◆) MPI processes, before it scales further with multiple threads per process.

7.4.2 Weak scaling

The weak scaling of an algorithm is how the wall time varies with the number of cores for a fixed problem size per core [86]. Hence, the efficiency is equal to the speedup given by Eq. (7.4). To test the weak scaling, the bunch sizes were kept constant, while the total number of bunches were equal to the number of cores, subtracted 1 for the master process. It is typically easier to achieve a good weak scaling than strong scaling, hence the names. However, in multi-beam multi-bunch simulations it can be more challenging to keep a high efficiency as the number of bunches increases, as will be shown. The collider models are the same as in Fig. 7.4, plus one as in Fig. 7.4d also including two independent calculations per turn. The models with beam-beam calculations have $N_{\text{core}}/2$ bunches per beam, while the others have N_{core} bunches in the first beam only. As the beam-beam calculations do not make sense for one bunch, the scalings start at a reference simulation for 8 bunches. The weak scaling is presented in Fig. 7.5.

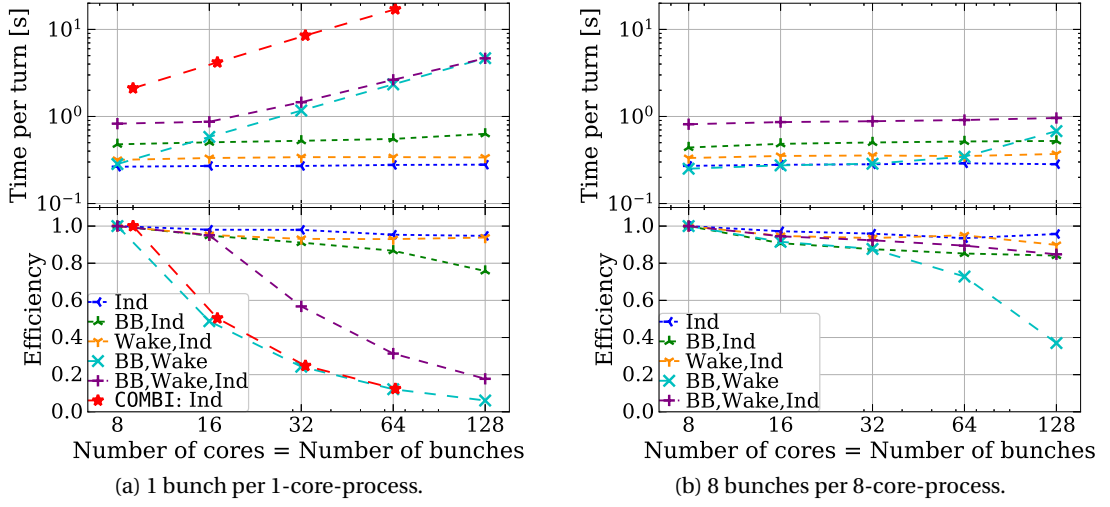


Figure 7.5: Weak scaling with COMBIp for different collider models, with independent (Ind), beam-beam (BB) and wakefield (Wake) calculations. The weak scaling was also calculated with COMBI, but only with the independent calculation and only for 1 bunch per worker process.

Note that the efficiency of COMBI is calculated relative to a reference simulation that is also run with COMBI, to better show the behavior as the problem size increases.

The weak scaling with 1 bunch per 1-core-process is presented in Fig. 7.5a. The efficiency of the COMBI algorithm falls quickly as the number of bunches increases, due to the synchronization after each calculation that was illustrated in Fig. 7.3. Note that the COMBI simulations were run with only the independent calculation, and should be compared to the blue curve labeled “Ind”, which was simulated with COMBIp. The bottleneck discussed in Sec. 7.2 for collider models with both intra-beam and inter-beam calculations is clearly visible on the curves labeled “BB,Wake” and “BB,Wake,Ind”, which both drop below an efficiency of 0.2. The simulations with beam-beam calculations, but without wakefield calculations, become less effective starting from 64 cores. This can partly be explained by the white triangles in the beginning and end of Fig. 7.3d, because only 100 turns are simulated. A part of the work required by the wakefield calculations scales with the number of bunches. This scaling is negligible up to 128 bunches, according to these results.

The weak scaling with 8 bunches per 8-core-process is presented in Fig. 7.5b. There is a clear improvement by having multiple bunches on the same process in COMBIp. The root limitation, as discussed in Sec. 7.2 qualitatively and shown here quantitatively, is how many bunches causality allows to be calculated in parallel. The solution is therefore to distribute more bunches on each process, such that each calculation takes a shorter wall time, instead of trying to calculate every bunch in parallel. That is what COMBIp does. By achieving better load balancing in this manner, the impact of the bottleneck is pushed to a higher number of cores, such that the achievable speedup is higher.

7.5 Discussion

The goal of the new algorithm in this thesis is to study the long-term evolution of the beam quality in collision in the LHC, requiring a machine specific noise and feedback model, as well as beam-beam interactions. The solution to the inherent bottleneck was to distribute the bunches over fewer processes, and instead parallelize maximally each calculation within each process. The speedup of this method is limited by how many cores there are on each node in the utilized cluster. One could go one step further by dividing each individual bunch over multiple nodes on separate processes, but this would require a significant amount of additional communication and implementation, and is expected to lead to an increased efficiency only in marginal cases. Therefore, there is a limited, albeit large, speedup that can be achieved by the new algorithm for a given simulation.

The scalings in Sec. 7.4 were calculated with a limited number of bunches, and simple collider models. In realistic models for the LHC, there will be more independent calculations, up to about 120 long-range and 4 head-on beam-beam calculations for each bunch, and up to 2808 bunches per beam [1]. Although the simulations will be computationally heavy, multiple bunches can be calculated simultaneously. Hence, a large number of processes can be active with good load balancing in COMBIp, and a significant speedup can be achieved.

7.6 Conclusion

The constraints due to causality in multi-beam multi-bunch simulations have been discussed in this chapter. Simulations with either intra-beam or inter-beam calculations can easily be performed efficiently. In simulations including both of them, causality leads to a bottleneck of how many bunches that can be calculated in parallel.

A new parallel algorithm has been implemented in COMBI, named COMBIp, to improve the efficiency. The key points of the new algorithm are that each bunch is autonomous, their calculations are ordered in a pipeline, the required communication between bunches is performed asynchronously, and there can be multiple bunches per process. The new algorithm has achieved a speedup of up to the number of bunches per beam, compared to the previous algorithm implemented in the code. The performance is close to independent of causality constraints when simulating collider models with either only inter-beam calculations or intra-beam calculations in the ultra-relativistic limit. The predicted bottleneck for collider models with both inter-beam and intra-beam calculations is now a limit on the number of compute nodes that can be used efficiently, instead of a limit on the number of bunches that can be simulated efficiently. The new algorithm is designed to efficiently simulate realistic models of the LHC.

8 Optimal transverse feedback gain and bandwidth for long-term beam quality

Disclaimer: This chapter was adapted from the following article — with permissions of the co-authors and publisher:

[87] **S. V. Furuseeth**, X. Buffat, J. S. Pereira-Cubillo, and D. Valuch, “Emittance growth suppression with a multibunch feedback in high-energy hadron colliders: Numerical optimization of the gain and bandwidth”, submitted for publication.

My contribution: All results presented here, except for: The module for generation of non-white noise in COMBI and the generation of the peak-normalized response functions for the ADT multi-bunch feedback.

8.1 Introduction

A transverse feedback system can effectively mitigate the emittance growth caused by external noise sources. However, as its action on the beam depends on beam position measurements (BPM) of finite accuracy, it introduces additional BPM noise on its own. The amplitudes of the external noise and the BPM noise can be added in squares as in Eq. (3.15), assuming a bunch-by-bunch feedback. The external noise is in general strongest at low frequencies. In the LHC, this noise may be dominated by voltage ripples in PCs, which are currently understood to be strongest at frequencies below 10 kHz [38]. Such a low-frequency (LF) noise can only excite multi-bunch modes of equally low frequencies, as was illustrated in Fig. 3.5. Hence, the feedback is less needed at high frequencies. In this chapter, the two theories in Sec. 3.5, for the suppression of the noise induced emittance growth rate with a bunch-by-bunch feedback, will be extended to a multi-bunch feedback.

The ultimate goal is to find the optimal transverse feedback bandwidth and gain, determined by the minimization of the total emittance growth rate while still maintaining beam stability. The optimum depends on the ratio between the amplitudes of the BPM error and the external noise, the PSD of the external noise, the response of the feedback filters, and the magnitude and details of the detuning. In this chapter, the optimum is found numerically. It was also attempted to do so experimentally in the LHC as part of this study, but it was inconclusive due to limited accuracy in the emittance measurement, as well as other experimental challenges [88].

8.2 Theory

8.2.1 Active multi-bunch beam feedback system

A multi-bunch/low-bandwidth (LBW) feedback works by acting on multiple bunches based on the measurement of one bunch, or equivalently acting on one bunch b based on the measurements of multiple bunches b' . This can be denoted as

$$p_b \rightarrow p_b - g \sum_{b'} \epsilon_{b'} w_{bb'} p_{b'p}, \quad (8.1)$$

where the coefficient

$$\epsilon_{b'} = \begin{cases} 1 & , \text{bunch } b' \text{ exists} \\ 0 & , \text{otherwise,} \end{cases} \quad (8.2)$$

marks the bunches, $w_{bb'}$ is the peak-normalized response function of the filter, and $p_{b'p} = p_{b'} - \delta_{b'p}$ is the predicted value of the momentum of bunch b' . The error $\delta_{b'p}$ in the prediction is mainly due to the BPM error in the measurements, while the possible additional error due to the prediction itself is assumed negligible. The error will be modeled as drawn from a centered normal distribution, $\delta_{b'p} \sim \mathcal{N}(0, \sigma_{\text{BPM}}^2)$.

Response functions for two types of low-pass filters, with various cutoff frequencies f_{cutoff} , are visualized in Fig. 8.1a. The corresponding transfer functions are displayed in Fig. 8.1b. The extended bandwidth (Ext. BW) is for all intents and purposes a bunch-by-bunch feedback. The response function for the exponential filter (EXP) is the exponential function,

$$w_{bb'}^{\text{EXP}} = \exp(-2\pi f_{\text{cutoff}} \Delta t |b - b'|), \quad (8.3)$$

where Δt is the bunch-to-bunch separation. The response functions labeled “ADT” include all the filtering in the digital signal processing and the analogue chain frequency response of the LHC transverse feedback system, assuming known bunch measurements [23]. In addition to the measured center bunch b , the response extends symmetrically over the 32 closest bunch slots on both sides. The currently lowest reasonable cutoff frequency for the ADT is 0.5 MHz. The ADT also operates with a high-pass filter of lower cutoff frequency, required to make a bandpass filter. However, it is not considered here as it affects frequencies far below the beam oscillations frequencies.

The LBW feedback is most valuable when the beam oscillates with LF modes, as driven by an LF noise. To appreciate the effect of an LBW feedback, the transverse beam oscillation at the BPM can be decomposed into a single coherent mode $p_{bm} = A_m \cos(2\pi f_m t_b + \phi_{b0}) = A_m \cos(\phi_b)$ and an incoherent momentum $p_{bi} \sim \mathcal{N}(0, \sigma_i^2)$. Equation (8.1) can, with this decomposition, be rewritten as

$$\begin{aligned} p_b &\rightarrow p_b - g \sum_{b'} \epsilon_{b'} w_{bb'} (p_{b'm} + p_{b'i} - \delta_{b'p}) \\ &= p_{bm}(1 - g_{bm}) + p_{bi}(1 - g) + g\delta_{b\sigma i} + g\delta_{b\sigma p} + gA_m \sin(\phi_b) \sum_{b'} \epsilon_{b'} w_{bb'} \sin(\phi_{b'} - \phi_b), \end{aligned} \quad (8.4)$$

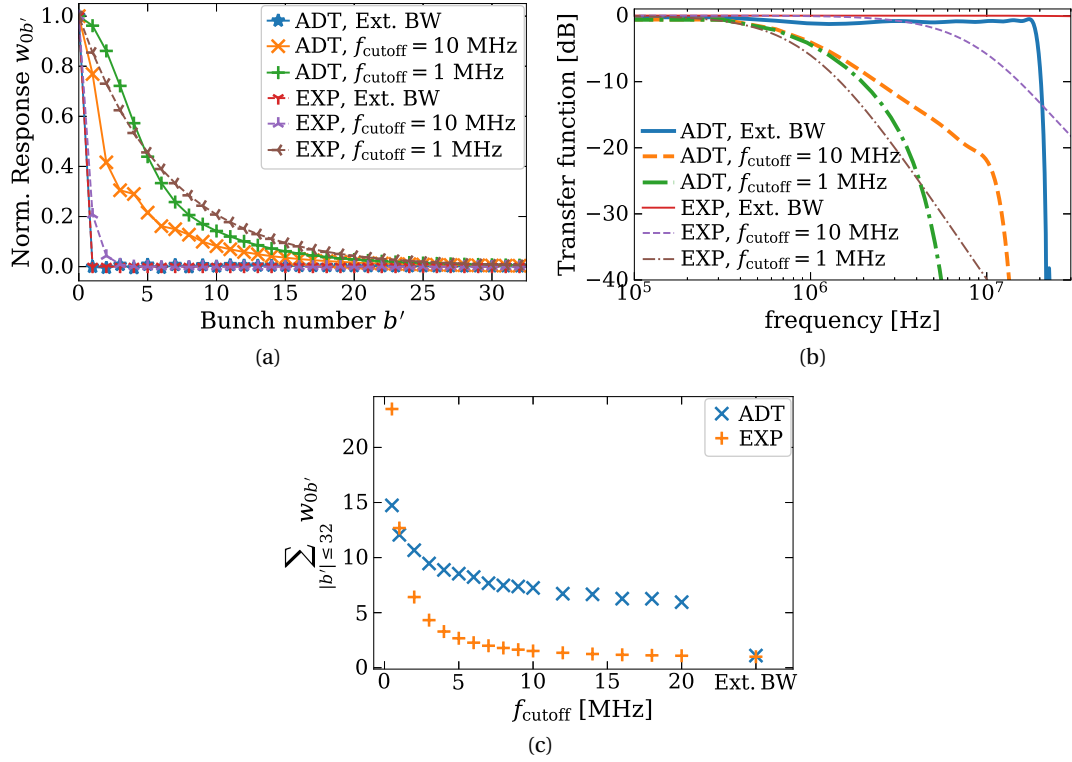


Figure 8.1: Normalized response functions of two types of filters, in time domain in (a) and in frequency domain in (b), assuming a bunch separation of $\Delta t = 25$ ns. The sum of the normalized response function in time domain, over all neighbors maximally 32 slots away, is given in (c). The EXP filter is an exponential filter, while the ADT filter replicates the transverse feedback in the LHC, both of which are fully symmetric in time domain in the range $|b - b'| \leq 32$, although only $b' - b \geq 0$ is shown in (a).

where

$$g_{bm} = g \sum_{b'} \epsilon_{b'} w_{bb'} \cos[2\pi f_m \Delta t (b' - b)] \leq g \tilde{N}, \quad (8.5)$$

$$\delta_{b\Sigma i} = - \sum_{b' \neq b} \epsilon_{b'} w_{bb'} p_{b'i} \sim \mathcal{N}(0, (\tilde{N}_b - 1) \sigma_i^2), \quad (8.6)$$

$$\delta_{b\Sigma p} = \sum_{b'} \epsilon_{b'} w_{bb'} \delta_{b'p} \sim \mathcal{N}(0, \tilde{N}_b \sigma_{BPM}^2), \quad (8.7)$$

$$\tilde{N}_b = \sum_{b'} \epsilon_{b'} w_{bb'}, \quad (8.8)$$

$$\tilde{N} = \sum_{b'} w_{0b'}. \quad (8.9)$$

The incoherent motion of the individual bunches will be damped with the single-bunch gain g as before. The coherent multi-bunch motion will be damped with an effective coherent gain g_{bm} . The incoherent motion results in an unwanted kick $g\delta_{b\Sigma i}$ per turn and the BPM noise results in a kick $g\delta_{b\Sigma p}$ per turn, both acting as a noise with the same spectrum as the feedback. The last term in Eq. (8.4) comes from the coherent multi-bunch motion of the beam. It can lead to an emittance growth if not suppressed. It can be minimized by: (i) reducing g ;

(ii) reducing A_m , which requires a larger g_{bm} ; (iii) reducing the summands, which requires $f_m \ll f_{\text{cutoff}}$, which is also required to get a large g_{bm} ; (iv) using a symmetric filter so that the summands cancel. If the bunches are gathered in trains of consecutively filled bunch slots, separated by multiple empty slots for which $\epsilon_{b'} = 0$ [1], the last alternative does not work for the bunches at either end of a train.

If the cutoff frequency is larger than the coherent frequency, $f_{\text{cutoff}} \gg f_m$, the effective coherent gain will be larger than the single-bunch gain, $g_{bm} = g\tilde{N}_b \geq g$. The sum of the peak-normalized response function is illustrated for various cutoff frequencies with both considered filter types in Fig. 8.1c. Since this is the maximum ratio between the effective coherent gain and the single-bunch gain, $\max(g_{bm}/g)$, it can be seen from this figure that reducing from the Ext. BW to standard operation of the ADT with $f_{\text{cutoff}} = 20$ MHz may already lead to a significant increase of the effective gain. The same change will only have a marginal impact with the EXP filter.

8.2.2 Emittance growth suppression with a multi-bunch feedback

The motion of the beam can more accurately be modeled as a sum of M coherent modes, as was introduced in Sec. 3.4. Mode m have coherent frequency f_m , as given by Eq. (3.25). The suppression of the emittance growth rate with incoherent detuning, which for a bunch-by-bunch feedback is given by Eq. (3.28), becomes a sum over the multi-bunch modes

$$\frac{\dot{\epsilon}}{\epsilon_0} = \sum_m \frac{S_{\text{noise}}(f_m)}{2} \left\langle \frac{(1 - \frac{g_m}{2})^2 4\pi^2 \tilde{\Delta} Q^2}{(\frac{g_m}{2})^2 + (1 - \frac{g_m}{2}) 4\pi^2 \tilde{\Delta} Q^2} \right\rangle_{\Psi}. \quad (8.10)$$

Equivalently, one gets a new expression for the suppression of the emittance growth rate with a beam-beam interaction in Eq. (3.29)

$$\frac{\dot{\epsilon}}{\epsilon_0} = \frac{1 - s_0}{2} \sum_m \frac{S_{\text{noise}}(f_m)}{2} \left(1 + \frac{g_m}{2\pi\tilde{\xi}_{\text{BB,tot}}} \right)^{-2}. \quad (8.11)$$

Here, g_m is the effective coherent gain on mode m , which depends on f_m as given by Eq. (8.5), and S_{noise} is the PSD of the noise. Note that, although the subscript b has been omitted, the sum must be taken for each bunch separately as the set of neighbors will be bunch dependent.

If the PSD of the external noise is flat up to an upper frequency f_{max} , it is, by the convention of normalization adopted in this thesis, related to the kick variance per turn as

$$S_{\text{ext}}(f) = \begin{cases} \sigma_{\text{ext}}^2 \frac{f_{\text{rev}}^2}{2f_{\text{max}}} & , f \in [0, f_{\text{max}}] \\ 0 & , \text{otherwise.} \end{cases} \quad (8.12)$$

For a single-bunch ($M = 1$) affected by white noise, one has effectively $f_{\text{max}} = f_{\text{rev}}/2$, since the bunch only samples the noise once per turn, returning Eq. (3.11). For M evenly spaced bunch positions and white noise up to $f_{\text{max}} = f_b/2$, the PSD is $S_{\text{ext}}(f \leq f_{\text{max}}) = \sigma_{\text{ext}}^2 f_{\text{rev}}/M$. Note that only the external noise is considered in Eq. (8.12). The BPM noise will be filtered by the LBW filter, and cannot therefore be included in this manner. However, for an Ext. BW feedback, one can add $g^2 \sigma_{\text{BPM}}^2$ to σ_{ext}^2 in Eq. (8.12) to get S_{noise} , and Eqs. (8.10)–(8.11) will reduce to

Eqs. (3.28)–(3.29), respectively, as the sum will be over M coherent modes. Note that the emittance growth from the BPM noise cannot be reduced by increasing the gain.

8.3 Results

Simulations have been run with the tracking code COMBI to study the emittance growth rate driven by both LF external noise and BPM noise, while damped by feedback systems with various filters. The default numerical setup is summarized in Tab. 8.1. Variations to this setup is addressed in the text. The tune spread is caused by Landau octupoles, given by Eq. (2.28), unless stated otherwise, in which case it is generated by head-on beam-beam interactions [89]. The prediction of the momentum after the feedback group delay always assumes the bare machine tunes (0.31, 0.32). The LF noise has a flat PSD up to f_{\max} , being an integer multiple of f_{rev} . The signal has been generated by filtering the Fourier transform of finite length noise signals, whereupon the signals have been concatenated in such a way as to erase the transition [90, 91]. The strongest noise is typically at the lowest betatron sideband frequency, which varies between machines. The specific choice of f_{rev} does not have a direct impact on the results. The BPM error is added to the phase space measurements before the measurements are used to calculate the responses on the various bunches. The emittance growth rate will be presented in units of a reference emittance growth rate. Unless stated otherwise, this reference is the emittance growth rate expected with full decoherence and no BPM noise,

$$\frac{\dot{\epsilon}_{\text{ref}}}{\epsilon_0} = \frac{\sigma_{\text{ext}}^2}{2\tau_{\text{rev}}}. \quad (8.13)$$

Table 8.1: Numerical parameters used in the simulations.

Parameter	Unit	Value
Bunches per beam, N_b	[1]	128
Macroparticles per bunch	[p/b]	10^6
Number of turns	[1]	10^5
Bunch spacing, Δt	[ns]	25
Revolution frequency, f_{rev}	[kHz]	11.245
Fractional transverse tunes, (Q_x, Q_y)		(0.31, 0.32)
Synchrotron tune, Q_s	$[10^{-3}]$	1.9
rms momentum spread, σ_δ	[1]	10^{-4}
Linear chromaticity, Q'	[1]	0
Octupole in-plane coefficient, a_x ¹	$[10^{-3}]$	1.09
Octupole cross-plane coefficient, b_x ¹	$[10^{-3}]$	−0.761
Total beam-beam parameter, $\xi_{\text{BB,tot}}$	$[10^{-3}]$	7.9
Single-bunch gain, g	[1/turn]	0.01
Feedback group delay	[turn]	4
External noise amplitude, σ_{ext}	$[\sigma_p \text{turn}^{-\frac{1}{2}}]$	10^{-3}
Upper noise frequency, f_{\max}	$[f_{\text{rev}}]$	1

¹ Equal in the horizontal and vertical planes.

8.3.1 Dependence on the feedback, noise, and source of detuning

The emittance growth rates of all 128 bunches, kicked by an LF noise and damped with a single-bunch gain $g = 0.01$, are presented separately in Fig. 8.2. The agreement with the theory in Eq. (8.10) is equally good for the Ext. BW feedback as after the extension of the theory to an LBW feedback. The bunches at either end of the train do not benefit maximally from the LBW configuration, due to the lack of neighbors, and thus have a smaller effective coherent gain. Note that the ADT filter reduces the emittance growth rate significantly more than the EXP filter when going from Ext. BW to $f_{\text{cutoff}} = 20$ MHz. This result was expected from the sum of the normalized response functions displayed in Fig. 8.1c.

The emittance growth rate has been calculated with $f_{\text{cutoff}} \in \{0.5, 1, 2, 5, 10, 20\}$ MHz, in addition to the Ext. BW. The average emittance growth rate of all 128 bunches, affected only by either LF noise or BPM noise, is displayed as a function of f_{cutoff} in Fig. 8.3. For the cases with only BPM noise, the reference emittance growth rate is $\dot{\varepsilon}_{\text{ref}}/\varepsilon_0 = (g\sigma_{\text{BPM}})^2/2\tau_{\text{rev}}$. The emittance growth rate driven by LF noise is suppressed further by reducing f_{cutoff} , and the difference in the dependence on f_{cutoff} for the two filter types is unmistakable. The emittance growth rate driven by BPM noise also depends on f_{cutoff} , but to a lesser extent. The main approach to reduce the BPM noise driven emittance growth rate is to reduce the single-bunch gain or the BPM error.

The average emittance growth rate with LF noise of various maximum frequencies, f_{max} , is displayed in Fig. 8.4. As long as $f_{\text{max}} \leq 1$ MHz, there is only a marginal increase in the emittance growth rate for the tested values of f_{cutoff} . As a rule of thumb, reducing the cutoff frequency of the feedback only suppresses the emittance growth rate further as long as it still covers the power spectrum of the noise. Note that the PSD is flat for all values of f_{max} in these simulations. The noise spectrum in a machine will in general be weaker at larger frequencies.

The average emittance growth rate with a beam-beam interaction, in comparison to octupole detuning, is displayed in Fig. 8.5. The agreement with the theory for a beam-beam interaction

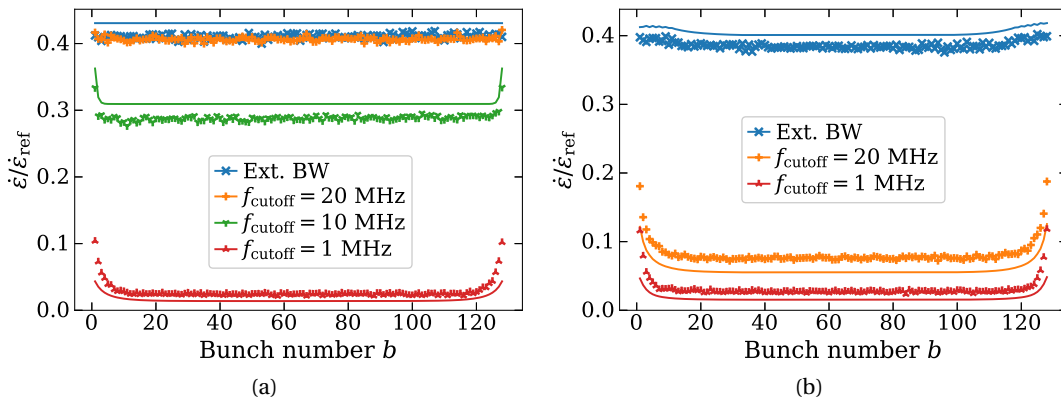


Figure 8.2: Emittance growth rate for all 128 neighboring bunches affected by only LF noise, using the EXP filter in (a) and the ADT filter in (b). The solid lines are the expected emittance growth rates, calculated with Eqs. (8.5) and (8.10).

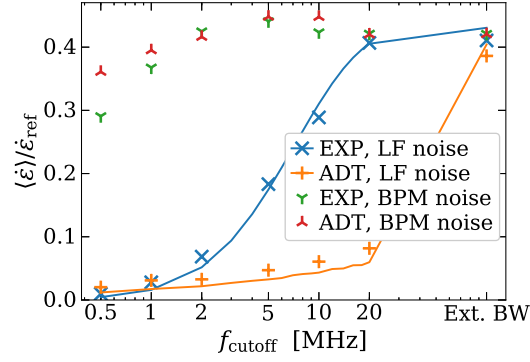


Figure 8.3: Average emittance growth rate for 128 neighboring bunches, affected by either LF noise or BPM noise, using the EXP filter and the ADT filter. The solid lines are the expected emittance growth rates due to LF noise, calculated with Eqs. (8.5) and (8.10).

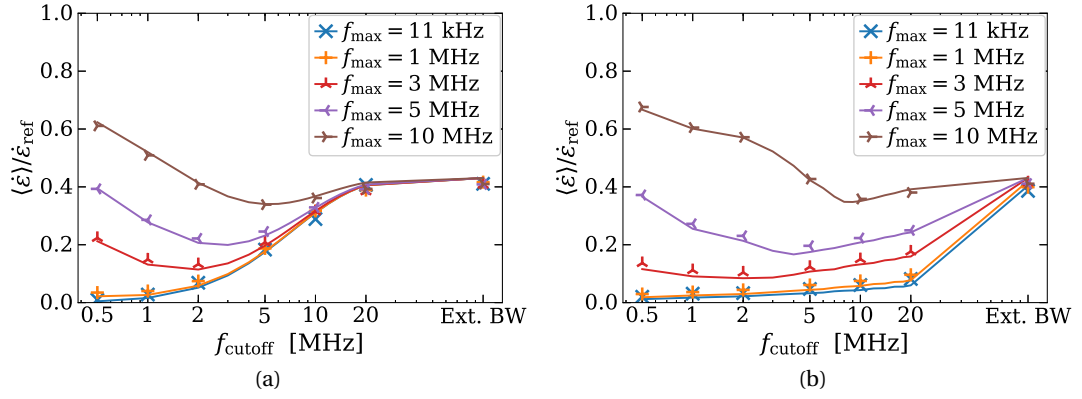


Figure 8.4: Average emittance growth rate for 128 neighboring bunches affected by LF noise of various f_{max} , using the EXP filter in (a) and the ADT filter in (b). The solid lines are the expected emittance growth rates, calculated with Eqs. (8.5) and (8.10).

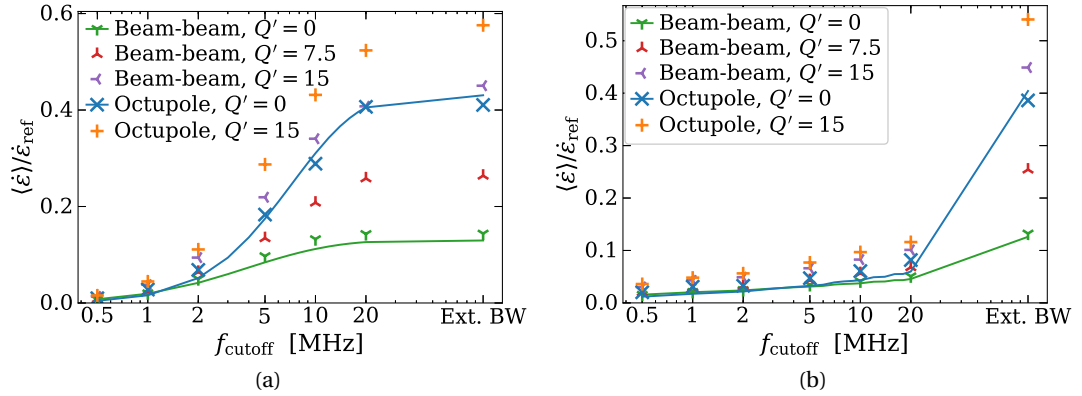


Figure 8.5: Average emittance growth rate for 128 neighboring bunches affected by LF noise, using the EXP filter in (a) and the ADT filter in (b). The solid lines are the expected emittance growth rates, calculated with Eq. (8.5) and either Eq. (8.10) for octupole detuning or Eq. (8.11) for beam-beam interactions.

in Eq. (8.11) is equally good as with the theory for octupole detuning in Eq. (8.10). The emittance growth rate with a beam-beam interaction and zero chromaticity $Q' = 0$ is significantly lower than with octupole detuning. However, with the introduction of chromaticity, the emittance growth rate increases substantially. In comparison, the emittance growth rate increases more due to the introduction of chromaticity in addition to a beam-beam interaction, than in addition to octupole detuning. This is due to a shift of the coherent beam-beam modes due to chromaticity, as was discussed in greater detail in [41].

8.3.2 Optimal feedback in the LHC and HL-LHC

The goal of this section is to find the optimal cutoff frequency and gain for the LHC in collision, both now and in the future. In the LHC as of 2018, the ratio between the BPM noise and LF noise was in both planes of both beams $\sigma_{\text{BPM}}/\sigma_{\text{ext}} \approx 50$ [41]. In this section, the emittance growth rate will be presented in units of $\dot{\epsilon}_{\text{ref}}/\epsilon_0 = \sigma_{\text{ext}}^2/2\tau_{\text{rev}}$, the relative rate expected due to the LF noise with full decoherence, also for the simulations with only BPM noise. The source of detuning will always be beam-beam interactions, as the goal is to minimize the emittance growth rate in the LHC in collision. For the same reason, all simulations are run with the ADT filter. Note that a simplified model of the LHC is used, with a single head-on interaction per turn, not multiple as was studied for the bunch-by-bunch feedback in [41], and not including long-range interactions. This is an acceptable choice here, since the main focus is the impact of the feedback bandwidth on the emittance growth rate, and the main impact of the beam-beam interactions on the feedback efficiency is through the rms tune spread. Until further notice, the total beam-beam parameter remains at $\xi_{\text{BB,tot}} = 0.0079$.

The simulated average emittance growth rate of 128 bunches with either only LF noise or BPM noise or both, is presented as a function of both the feedback's cutoff frequency and the single-bunch gain in Fig. 8.6, with $Q' = 0$ on the left and $Q' = 15$ on the right. The emittance growth rate caused by the LF noise is as expected suppressed further by either increasing g or reducing f_{cutoff} . The emittance growth rate caused by the BPM noise is strongly dependent on g , and only weakly dependent on f_{cutoff} . The trends are similar with and without chromaticity, except for a larger emittance growth rate, as was also found in Sec. 8.3.1. Especially the emittance growth rate driven by the LF noise alone is larger with chromaticity. Furthermore, some configurations have been stabilized with the introduction of the chromaticity. The emittance growth rates in the simulations with both types of noise are equal to the sum of the growth rates found with each type of noise separately, with a STD of the relative error of 4.3% with $Q' = 0$ and 3.0% with $Q' = 15$. The optimal gain with both types of noise is in general smaller for a smaller cutoff frequency. The minimal emittance growth rate at the optimal gain for cutoff frequencies 0.5 MHz, 20 MHz and Ext. BW are gathered in Tab. 8.2. It has been tested experimentally to operate the LHC with Ext. BW, but it was found that this led to a significantly increased emittance blow-up [92], in agreement with these results. Therefore, the LHC was in run 2 operated with $f_{\text{cutoff}} = 20$ MHz when in collision.

An ongoing project at CERN is to reduce the BPM error. If one could halve the BPM error, the BPM noise driven emittance growth rate would be divided by 4, leading to the total emittance growth rates presented in Fig. 8.7, with both $Q' = 0$ and $Q' = 15$. The values are weighted sums of the corresponding simulations with only one type of noise. The reduction of the BPM noise

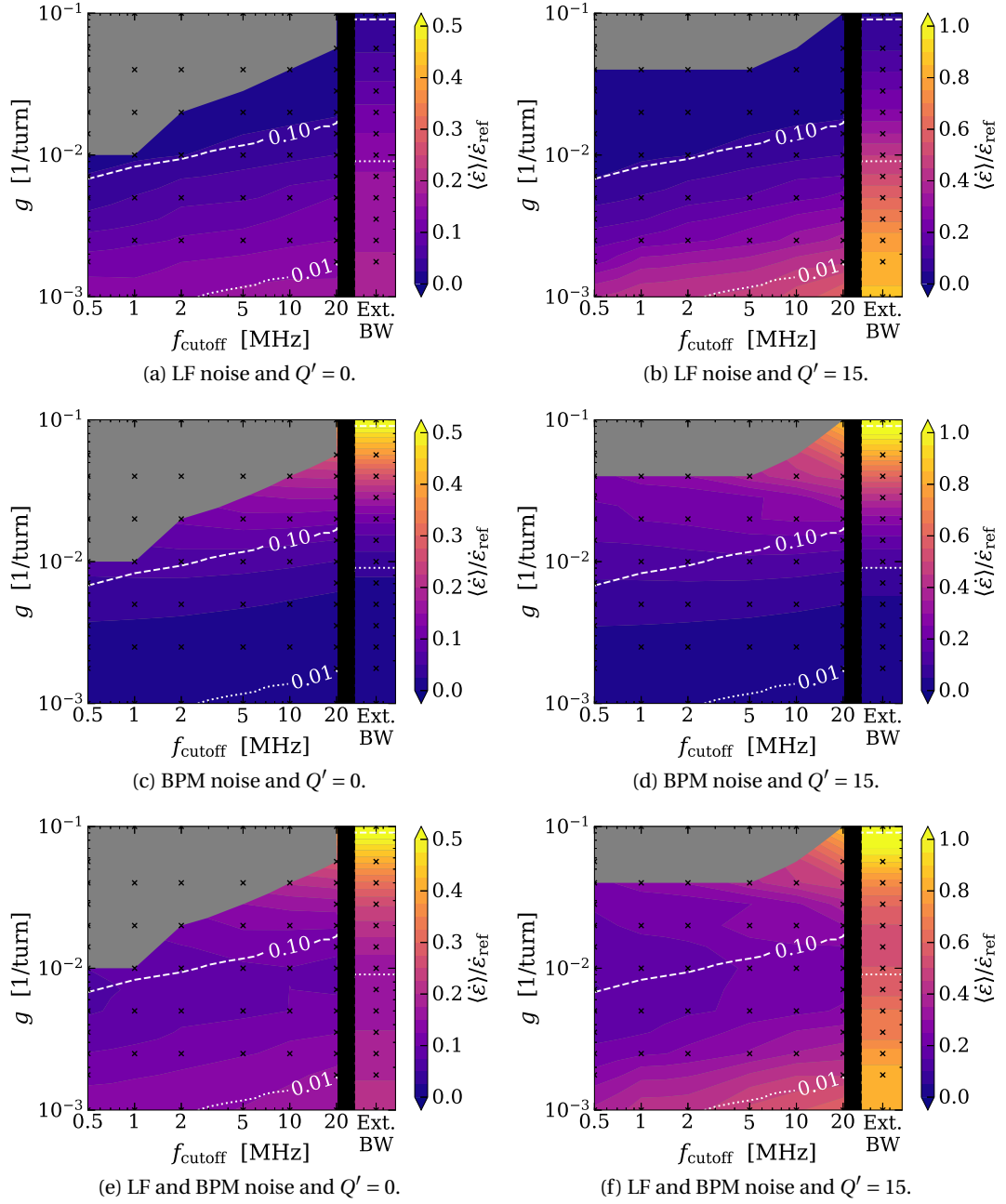


Figure 8.6: Average emittance growth rate for 128 bunches separated by 25 ns, in configurations with a beam-beam interaction of $\xi_{\text{BB,tot}} = 0.0079$. (a,b) are run with only LF noise, (c,d) are run with only BPM noise, and (e,f) are run with both such that $\sigma_{\text{BPM}} = 50\sigma_{\text{ext}}$. (a,c,e) are run with $Q' = 0$ and (b,d,f) are run with $Q' = 15$. Note the different color scales for the different chromaticities. The black crosses mark the simulations. The area marked gray contains configurations (f_{cutoff}, g) for which the feedback loop is unstable. The configurations at the edge of the gray area are stable. The white curves are contours of constant maximum coherent gain $g\tilde{N}$.

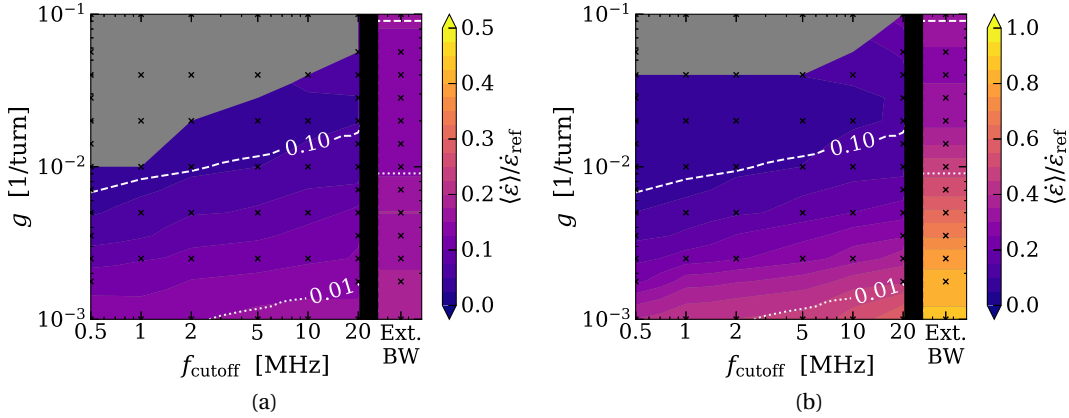


Figure 8.7: Average emittance growth rate for 128 bunches separated by 25 ns, with both LF noise and half the current BPM noise in the LHC, $\sigma_{\text{BPM}} = 25\sigma_{\text{ext}}$, in a configuration with a beam-beam interaction and $Q' = 0$ in (a) and $Q' = 15$ in (b). The black crosses mark the simulations. The area marked gray contains configurations (f_{cutoff}, g) for which the feedback loop is unstable. The configurations at the edge of the gray area are stable. The white curves are contours of constant maximum coherent gain $g\tilde{N}$.

allows for more optimal configurations with all bandwidths, and a larger single-bunch gain in general, as seen by the minimal emittance growth rates and optimal gains gathered in Tab. 8.2.

The simulations have been rerun with $\xi_{\text{BB,tot}} = 0.022$ and $Q_s = 0.0021$. This is the total head-on beam-beam parameter in the HL-LHC. With a larger tune spread, a larger gain is required to suppress the emittance growth rate. The minimal emittance growth rate and optimal gain for $Q' = 0$ and $Q' = 15$ are gathered in Tab. 8.2. With $Q' = 0$ and the current noise ratio, $\sigma_{\text{BPM}} = 50\sigma_{\text{ext}}$, the Ext. BW is not able to suppress the emittance growth rate. Note that the prediction without chromaticity by Eq. (3.29) is $\dot{\epsilon} = 0.175\dot{\epsilon}_{\text{ref}}$. With this larger beam-beam parameter, a chromaticity of 15 units increases the emittance growth rate less. For the initial noise ratio as in the LHC, $\sigma_{\text{BPM}} = 50\sigma_{\text{ext}}$, the emittance growth rate is approximately flat up to $g < 0.01$, from where it increases due to the BPM noise. The feedback is barely able to suppress the total emittance growth rate, as was also found experimentally [41], but is still needed to keep the beam stable.

If the goal of reducing the BPM error to $\sigma_{\text{BPM}} = 25\sigma_{\text{ext}}$ is achieved in the HL-LHC, the feedback does help, but less than with the smaller beam-beam parameter, as listed in Tab. 8.2. This is because more noise energy will enter discrete beam-beam modes that do not lead to emittance growth. Assuming the same external noise as in the LHC, the noise in collision in the HL-LHC is $\sigma_{\text{ext}} = 4.65 \times 10^{-5}$ in units of the beam size [5, 41], which causes a reference emittance growth rate with full decoherence of $\dot{\epsilon}_{\text{ref}}/\epsilon_0 = 4.4\%/h$. Hence, with $Q' = 15$ in the model simulated here, equivalent to two head-on beam-beam interactions with equal phase advances between the IPs for the two beams, the optimal Ext. BW feedback, with $g = 0.0163$, suppresses the emittance growth rate to $1.34\%/h$. The optimal LBW feedback, with $g = 0.0125$ and $f_{\text{cutoff}} = 0.5 \text{ MHz}$, manages to suppress it further to $0.70\%/h$. With a more realistic model of the machine, featuring in particular long-range interactions and different phases between the IPs for the two beams, the discrete beam-beam modes are expected to reach the incoherent

Table 8.2: Minimal emittance growth rate and corresponding optimal gain for a given cutoff frequency, beam-beam parameter, noise ratio, and chromaticity.

$\xi_{\text{BB,tot}} = 7.9 \times 10^{-3}$								
f_{cutoff}	$\sigma_{\text{BPM}} = 50\sigma_{\text{ext}}$				$\sigma_{\text{BPM}} = 25\sigma_{\text{ext}}$			
	$Q' = 0$		$Q' = 15$		$Q' = 0$		$Q' = 15$	
	g [10^{-2}]	$\dot{\epsilon}$ [$\dot{\epsilon}_{\text{ref}}$]	g [10^{-2}]	$\dot{\epsilon}$ [$\dot{\epsilon}_{\text{ref}}$]	g [10^{-2}]	$\dot{\epsilon}$ [$\dot{\epsilon}_{\text{ref}}$]	g [10^{-2}]	$\dot{\epsilon}$ [$\dot{\epsilon}_{\text{ref}}$]
Ext. BW	0.67	0.165	1.41	0.523	2.83	0.130	4.58	0.293
20MHz	0.92	0.095	0.94	0.225	2.07	0.049	2.01	0.105
0.5MHz	0.70	0.070	0.75	0.149	1.00 ¹	0.031	1.83	0.054
$\xi_{\text{BB,tot}} = 2.2 \times 10^{-2}$								
f_{cutoff}	$\sigma_{\text{BPM}} = 50\sigma_{\text{ext}}$				$\sigma_{\text{BPM}} = 25\sigma_{\text{ext}}$			
	$Q' = 0$		$Q' = 15$		$Q' = 0$		$Q' = 15$	
	g [10^{-2}]	$\dot{\epsilon}$ [$\dot{\epsilon}_{\text{ref}}$]	g [10^{-2}]	$\dot{\epsilon}$ [$\dot{\epsilon}_{\text{ref}}$]	g [10^{-2}]	$\dot{\epsilon}$ [$\dot{\epsilon}_{\text{ref}}$]	g [10^{-2}]	$\dot{\epsilon}$ [$\dot{\epsilon}_{\text{ref}}$]
Ext. BW	0.33	0.200	0.76	0.358	1.79	0.179	1.63	0.306
20MHz	0.55	0.161	0.62	0.267	1.88	0.107	1.72	0.194
0.5MHz	0.37	0.147	0.39	0.245	1.00 ¹	0.085	1.25	0.161

¹ Do not consider gains larger than the largest stable gain in simulations.

spectrum. In these conditions the emittance growth rate can be larger than predicted here by a factor up to 2.5 [41].

8.4 Conclusion

Transverse feedback systems are required in modern hadron colliders to maintain beam stability and a small beam emittance, and thereby a high luminosity. One main source of emittance growth is the external noise. Analytical theories have been derived in the past to calculate the suppression of the noise driven emittance growth rate with an Ext. BW/bunch-by-bunch feedback. It still remains to accurately include a linear chromaticity theoretically, even with the bunch-by-bunch feedback. In this chapter, these theories have been extended to an LBW/multi-bunch feedback, for which a coherent gain g_m has been found for each coherent mode of frequency f_m . The coherent gain will in general be larger than the single-bunch gain g , and thus further suppress the external noise driven emittance growth rate, if the cutoff frequency of the feedback is larger than the coherent mode frequency, $f_{\text{cutoff}} > f_m$. The coherent gain does not fundamentally depend on the feedback cutoff frequency, but on the discrete sum of the response function over the neighboring bunches. Thus, different feedback filters with the same cutoff frequency can have different efficiencies g_m/g . The extended theories agree quantitatively with multi-beam multi-bunch multi-particle simulations.

The predicted emittance growth rates for various feedback systems depend on the noise model used in the calculations and simulations. The PSD of the external noise is both expected by theories and measured experimentally to be strongest at low frequencies in general. In the LHC, the noise is currently believed to mainly be below the revolution frequency. Such a noise spectrum will tend to drive coherent modes of low coherent frequencies, supporting the use of an LBW feedback. There are currently several ongoing projects that aim at better describing the

Chapter 8. Optimal transverse feedback gain and bandwidth for long-term beam quality

possible sources of noise in the LHC, both what they are and how much they affect the beams, with the goal of getting a more accurate description of the PSD of the external noise. An update of the noise model will naturally prompt an update of the predicted emittance growth rates.

In addition to the external noise, the feedback introduces additional noise on its own, due to BPM errors. The corresponding emittance growth rate has been found to be only weakly dependent on the feedback bandwidth, but increases for larger single-bunch gains g . When the BPM error is non-negligible, LBW feedbacks are superior in limiting the total emittance growth rate, as one can reduce f_{cutoff} and g simultaneously, while keeping g_m constant. This has been found both in simulations and in experiments.

The ultimate goal of this study was to find the optimal configuration of a feedback, which is the value pair (f_{cutoff}, g) that minimizes the total emittance growth rate, while keeping the beam stable. The optimum depends on the amplitudes of the noise sources, the feedback type, the source and magnitude of the detuning, and thereby the machine. In the LHC in collision in 2018, both the external noise and BPM noise were non-negligible. It was found experimentally advantageous to operate with an LBW feedback with $f_{\text{cutoff}} = 20$ MHz, with respect to the Ext. BW, a result which has been reproduced here with a simplified numerical model of the LHC. Yet, the optimal feedback working point would have been an LBW feedback with the lowest possible $f_{\text{cutoff}} = 0.5$ MHz and $g = 0.0075$. This optimum would have achieved a reduction of the emittance growth rate of 72% compared to the optimal Ext. BW feedback, and a reduction of 34% compared to the optimum with $f_{\text{cutoff}} = 20$ MHz. However, this working point is close to the feedback stability limit, which must be considered in more detail, both theoretically and experimentally. Thus, this study does not encourage efforts towards further reducing the lowest possible cutoff frequency of the LBW feedback in the LHC. The linear chromaticity did not strongly affect the optimal feedback working point. However, it was found that reducing the chromaticity both suppresses the emittance growth rate further and affects the loop stability. Whether the chromaticity should be changed in operation is first and foremost a question of beam stability, and a possible reduction would have to be investigated further with this in mind. By reducing the BPM error, the emittance growth rate will be more dominated by external noise, and the LHC can be operated more optimally with a larger gain. Without reducing the BPM error, the feedback in the HL-LHC will only be able to marginally suppress the emittance growth rate. Nevertheless, the feedback will still be valuable in maintaining beam stability.

Conclusion

The bunched particle beams in high-energy hadron colliders are subject to many mechanisms that reduce or limit the beam quality, and thereby reduce the number of collisions delivered to the experiments. The scope of this thesis has been to explain how noise impacts the beam quality in high-energy hadron colliders, both in terms of beam instabilities and emittance growth. A new diffusion mechanism, leading to a loss of Landau damping of coherent instabilities with a latency, has been identified and described with an analytical model. In addition, the improved suppression of the noise driven emittance growth of colliding beams with a multi-bunch feedback system has been proposed and investigated.

Observations had been made in the past of instabilities developing in the LHC after prolonged stays in configurations that were predicted to be stable by well-established linear Vlasov theories, assuming Gaussian transverse bunch distributions. In Part II of this thesis, a detailed explanation of a mechanism causing these observations have been put forward, and such instabilities have been reproduced in a dedicated experiment in the LHC. The existence of a nonzero latency suggested that the loss of Landau damping was driven by a slow change of the bunch distribution. Such a distribution change cannot be explained by linear Vlasov theories. By expanding to second order, the distribution change, and corresponding loss of Landau damping, has been explained by a noise and wakefield driven diffusion. The diffusion is narrow in frequency and causes a local flattening of the distribution, exactly at the critical frequency of the least stable wakefield driven headtail mode. In most cases, the local flattening corresponds to the drilling of a borehole in the stability diagram at the critical frequency, which can cause a loss of Landau damping. Other mechanisms can cause a similar diffusion, but not systematically at the critical frequency. An analytical formula for the latency — Eqs. (6.34)–(6.36) — has been derived. The distribution evolution and corresponding stability evolution has also been solved numerically with the PDE solver PyRADISE, which has been developed for this specific purpose. The analytical formula and numerical solver agree well with latencies measured in the dedicated experiment conducted in the LHC.

One of the most effective techniques found to increase the latency, and thereby mitigate the loss of Landau damping, is to operate the machine with a large stability margin, i.e. with more detuning than required to stabilize a Gaussian beam. Hence, this thesis explains why it in the past has been found necessary to operate the LHC with approximately twice as high octupole current as predicted to be sufficient by linear theories, initially implemented in operation based on empirical evidence only. By exploring the parameter space in the light of this new mechanism, alternative operational settings were found that would extend the latency in the LHC by an order of magnitude, such that this mechanism would no longer be a concern

Conclusion

for safe machine operation. Furthermore, the new theory also allows to investigate future machines, such as the HL-LHC, including the estimation of the impact of new devices such as crab cavities, which will be important in the design of these machines.

The BPM noise generated by the transverse feedback system itself, caused by BPM measurements of finite accuracy, has in the past been identified as a potential performance limitation for future colliders. Since the external noise content in the LHC is at low frequencies compared to the bunch repetition frequency, a multi-bunch feedback, damping a bunch based on the measurements of its neighbors as well as itself, has been suggested as a means to reduce the overall emittance growth rate. In Part III of this thesis, the impact on the beams of a multi-bunch transverse feedback system and low-frequency external noise has been studied in general, and for the LHC in particular. To study the emittance growth rate in collision numerically, a new parallel multi-beam multi-bunch algorithm was devised and implemented in the particle tracking code COMBI. It has been found superior in terms of computing efficiency compared to the previous algorithm. To study the emittance growth rate theoretically, two theories for the suppression of the emittance growth rate with a bunch-by-bunch feedback have been extended to a multi-bunch feedback. An expression for an effective gain per multi-bunch mode has been derived — Eq. (8.5) — which is dependent on the single-bunch gain and cutoff frequency of the feedback filter, as well as the coherent frequency of the multi-bunch mode. As a rule of thumb, reducing the cutoff frequency reduces the emittance growth rate as long as it still covers the power spectrum of the noise. In the LHC, where most of the noise power is at frequencies in the order of kHz and the cutoff frequencies are in the order of MHz, this condition is always fulfilled. When the BPM error is non-negligible, multi-bunch feedbacks have been found superior to bunch-by-bunch feedbacks in limiting the total emittance growth rate in theory, simulations, and experiments. The reason is that one can reduce the cutoff frequency and single-bunch gain simultaneously, and thereby reduce the BPM noise, while keeping the effective multi-bunch gain constant.

The ultimate goal of this study was to find the optimal working point of the transverse feedback system, which has been defined as the cutoff frequency and single-bunch gain that minimizes the total emittance growth rate due to dipolar noise, while maintaining beam stability. The optimum depends on the amplitudes of the different noise signals, the feedback type, the source and magnitude of the detuning, and thereby the machine. In the LHC in collision in 2018, both the external noise and BPM noise were non-negligible. It was experimentally found advantageous to operate with a multi-bunch feedback with a cutoff frequency of 20 MHz, equal to half the bunch repetition frequency, with respect to a bunch-by-bunch feedback. Yet, it has here been found numerically, with a simplified model of the machine, that the minimal emittance growth rate would have been achieved with the currently lowest possible cutoff frequency of 0.5 MHz. This optimum would have achieved a reduction of the emittance growth rate of 72% compared to the optimal bunch-by-bunch feedback, and it is achievable with the currently implemented technology. By improving the BPM accuracy as planned, the emittance growth rate will be more dominated by external noise, and the LHC can be operated more optimally with a larger single-bunch gain. If one could halve the BPM error, it has been found that the minimal emittance growth rate would be suppressed by another factor of about 2. Without improving the BPM accuracy, the feedback in the HL-LHC would only be able to marginally suppress the emittance growth rate, due to the increased beam-beam tune shift in

comparison to the LHC. In that case, the beam quality will be limited by the BPM noise even with a multi-bunch feedback.

Future development

In this thesis, various studies have been presented that has deepened the understanding of how noise impacts the beam quality in high-energy hadron colliders. This work has opened new paths for research and development, both in the understanding of the noise and its impacts, and in improving the machine operation. For instance, investigations are currently ongoing at CERN that aim at better describing the power spectrum of the noise in the LHC, which will enable more precise predictions of the consequences of the noise. In addition, the noise amplitude in the LHC will also be reduced thanks to e.g. upgrading the BPM hardware and thereby reducing the BPM noise.

Regarding the noise and wakefield driven mechanism of loss of Landau damping due to diffusion, there are various aspects that deserve further attention:

- Investigate alternative models of the beam response, compared to the current under-damped stochastic harmonic oscillator with frequency found by a linear extrapolation.
- Study the impact of crab cavity amplitude noise, which gives a large noise moment η_{m1} to headtail modes. This is critical to understand the consequences for the HL-LHC. It may be found necessary to not crab the beams until they are brought into collision.
- Perform experiments showing the qualitative effect of the diffusion. The local flattening in 2D action space is not resolvable with beam profile measurements, but the drilling of a borehole in the stability diagram should be observable through measurements of the beam transfer function.
- This mechanism explains why it is necessary to operate a machine with a stability margin relative to the predicted *linear* stability threshold for a Gaussian bunch. The new *diffusive* stability threshold should be used in operation instead, which predicts stability also after a given latency.

Regarding the minimization of the emittance growth rate driven by external noise and BPM noise with a multi-bunch feedback, there are also aspects that deserve further attention:

- Use the new parallel algorithm to study Landau damping of multi-bunch beam-beam modes in the presence of wakefields. Including the wakefields will add stricter requirements to the stabilization of the beams and may affect the emittance growth rate.
- Use the new parallel algorithm to study more complex multi-bunch beam models, including additional beam-beam interactions per turn. This will affect the discrete beam-beam modes, and thereby the emittance growth rate.
- Understand better the role of chromaticity as a source of detuning in the suppression of the emittance growth rate. This is still an open question also for a bunch-by-bunch feedback.
- Based on the current knowledge of the noise in the LHC, it is suggested to operate the transverse feedback system with a lower cutoff frequency than the standard 20 MHz, used in 2018, to reduce the emittance growth rate. The feasibility of this option should be investigated experimentally and may, later on, prove beneficial also in operation.

A The linearized Vlasov equation and the stability diagram

In this appendix, the derivation of the stability diagram by J. S. Berg and F. Ruggiero [34] is repeated, adapted to the notation in this thesis and including some additional comments and results.

Consider a linear oscillator that is excited by impulses $\Delta p = \epsilon f_x(t)$ as in Eq. (3.17). This can be modeled with a perturbed Hamiltonian

$$\mathcal{H} = \mathcal{H}_0(J_x, J_y) - \sqrt{2J_x} \cos(\phi_x) \epsilon f_x(t), \quad (\text{A.1})$$

where $\mathcal{H}_0(J_x, J_y)$ is the equilibrium Hamiltonian, generating a 2D tune spread, and $f_x(t)$ is a weak impulse function acting in the horizontal plane. Similarly, the distribution is perturbed

$$\Psi(\phi_x, J_x, \phi_y, J_y) = \frac{1}{(2\pi)^2} [\Psi_0(J_x, J_y) + \epsilon \Psi_1(\phi_x, J_x, J_y, t)], \quad (\text{A.2})$$

where the equilibrium distribution Ψ_0 is assumed to be uniformly distributed in the transverse phases, and the perturbation Ψ_1 is uniformly distributed in the vertical phase. The linear Vlasov equation in action-phase coordinates can then be written as

$$\frac{\partial \Psi_1}{\partial t} + \omega_{x0}(J_x, J_y) \frac{\partial \Psi_1}{\partial \phi_x} - \sqrt{2J_x} \sin(\phi_x) f_x(t) \frac{\partial \Psi_0}{\partial J_x} = 0, \quad (\text{A.3})$$

where $\omega_{x0}(J_x, J_y) = \partial \mathcal{H}_0 / \partial J_x$. The equilibrium terms, which are to zeroth order in ϵ , have canceled each other by definition, and the second-order terms are negligible compared to the first-order terms that make up Eq. (A.3).

The goal is to find the response of the distribution to the excitation $f_x(t)$, which can be done per frequency. Consider in general

$$\epsilon f_x(t) = A \exp(-i\Omega t), \quad (\text{A.4})$$

with a (complex) frequency Ω . In the interesting regime when Ω is close to ω_{x0} , it can be assumed that the driven perturbation behaves like

$$\Psi_1 = h_x(J_x, J_y) \exp[-i(\phi_x + \Omega t)]. \quad (\text{A.5})$$

Appendix A. The linearized Vlasov equation and the stability diagram

Thus, the linearized Vlasov equation, after averaging over ϕ_x , gives

$$h_x(J_x, J_y) = \frac{A \sqrt{\frac{J_x}{2}} \frac{\partial \Psi_0}{\partial J_x}}{\Omega - \omega_{x0}}. \quad (\text{A.6})$$

The offset of the COM can next be calculated as

$$\begin{aligned} \langle x \rangle_\Psi &= \frac{1}{(2\pi)^2} \int_0^{2\pi} d\phi_x \int_0^{2\pi} d\phi_y \int_0^\infty dJ_x \int_0^\infty dJ_y x (\Psi_0 + \epsilon \Psi_1) \\ &= \frac{\epsilon}{(2\pi)^2} \int_0^{2\pi} d\phi_x \int_0^{2\pi} d\phi_y \int_0^\infty dJ_x \int_0^\infty dJ_y \sqrt{2J_x} \cos(\phi_x) h_x(J_x, J_y) e^{-i(\phi_x + \Omega t)} \\ &= \frac{\epsilon f_x(t)}{2} \int_0^\infty dJ_x \int_0^\infty dJ_y \frac{J_x \frac{\partial \Psi_0}{\partial J_x}}{\Omega - \omega_{x0}(J_x, J_y)} \\ &\equiv \epsilon f_x(t) R(\Omega), \end{aligned} \quad (\text{A.7})$$

where $R(\Omega)$ is defined in this thesis as the response to an excitation at frequency Ω .

Now, it is time to consider different types of excitations. First, if the excitation is driven by wakefields from rigid dipole oscillations, the excitation is proportional to the COM. The frequency of the COM is ω_0 without the wakefields, and $\omega_{\text{coh}} = \omega_0 + \Delta\omega_{\text{coh}}$ when including the wakefields. The strength of the excitation can be found by rewriting the EOM in Eq. (3.17) as

$$\langle \ddot{x} \rangle_\Psi + \omega_0^2 \langle x \rangle_\Psi = (\omega_0^2 - \omega_{\text{coh}}^2) \langle x \rangle_\Psi \approx -2\omega_0 \Delta\omega_{\text{coh}} \langle x \rangle_\Psi = -\omega_0 \epsilon f_x(t), \quad (\text{A.8})$$

where the approximation assumes a small frequency shift $\Delta\omega_{\text{coh}}$. This is equivalent to assuming that the wake force driving the instabilities is weak, known as the weak headtail approximation. Hence,

$$\epsilon f_x(t) = -2\Delta\omega_{\text{coh}} \langle x \rangle_\Psi. \quad (\text{A.9})$$

Combining Eqs. (A.7) and (A.9) gives

$$\frac{-1}{\Delta\omega_{\text{coh}}} = 2R(\Omega), \quad (\text{A.10})$$

where ω_{coh} is the complex frequency of a rigid bunch (without a frequency spread), and Ω is the complex frequency of the COM of a bunch that consists of linear oscillators with a frequency spread. In the limit $\text{Im}\{\Omega\} \rightarrow 0^+$, Eq. (A.10) is the stability diagram, the limit for how strong impedance driven modes can be stabilized by Landau damping.

Secondly, if the excitation is independent of the beam, such as due to dipolar noise

$$\epsilon f_x(t) = \xi(t), \quad (\text{A.11})$$

one finds the beam transfer function

$$\frac{\langle x \rangle_\Psi}{\xi} = R(\Omega), \quad (\text{A.12})$$

giving the response of the COM due to an excitation at frequency Ω , which is assumed to have an infinitesimal positive imaginary part.

Finally, if there is both a dipolar noise and impedance

$$\epsilon f_x(t) = \xi(t) - 2\Delta\omega_{\text{coh}} \langle x \rangle_\Psi, \quad (\text{A.13})$$

it has been suggested to model the response as [93]

$$\frac{\langle x \rangle_\Psi}{\xi} = \frac{R(\Omega)}{1 + 2R(\Omega)\Delta\omega_{\text{coh}}}. \quad (\text{A.14})$$

This expression assumes dipolar kicks from both the noise and the wakefields. That is typically not the case, and it should be verified whether this is correct for more realistic wakefields. However, such a verification study did not fit within the scope of this thesis.

B The Fokker-Planck equation

In this appendix, two different approaches are taken to derive the Fokker-Planck equation. When the noise is coherent, an essential assumption in both derivations is that the phase relaxation to a uniform distribution, due to e.g. detuning, is faster than the diffusion time.

B.1 Master equation

Disclaimer: This section was adapted from the following article — with permissions of the co-author and publisher:

[52] **S. V. Furuseth** and X. Buffat, “Long-term evolution of Landau damping in the presence of transverse noise, feedback, and detuning”, *Phys. Rev. Accel. Beams* **23**, p. 034401, 2020. doi:[10.1103/PhysRevAccelBeams.23.034401](https://doi.org/10.1103/PhysRevAccelBeams.23.034401)

It was published under CC-BY 4.0.

My contribution: All results presented here.

In this section, the goal is to derive the Fokker-Planck equation described by Eqs. (5.7)–(5.8). To do so, one can write the master equation [94, 95], a convolution of the bunch distribution before a kick, $\Psi(t)$, with the probability distribution of the action change due to the kick, $\varphi(\Delta)$,

$$\Psi(J, t + \tau) = \int_{-\infty}^{\infty} \Psi(J - \Delta, t) \varphi(\Delta; J - \Delta, \Psi) d\Delta, \quad (\text{B.1})$$

where Δ represents the change of action. The action will only change in the plane of the kick. The particles are assumed uniformly distributed in the canonical phase ϕ . The dependence of Δ on ϕ has been taken into account in the probability distribution $\varphi(\Delta)$. By doing so, the 2D problem has become a 1D problem. All terms on the RHS are evaluated at time t .

The next step is to Taylor expand the integrand around J , which to second order gives

$$\Psi(J, t + \tau) = \int_{-\infty}^{\infty} \left\{ \Psi(J, t) \varphi(\Delta; J, \Psi) - \Delta \partial_J [\Psi(J, t) \varphi(\Delta; J, \Psi)] + \frac{\Delta^2}{2} \partial_J^2 [\Psi(J, t) \varphi(\Delta; J, \Psi)] \right\} d\Delta. \quad (\text{B.2})$$

Appendix B. The Fokker-Planck equation

The distribution $\Psi(J, t)$ and the partial differentiation $\partial_J(\cdot)$ do not depend on Δ , and can be moved outside the integral, while the change magnitude Δ is a variable that does not depend on J , and can be moved inside the partial differentiations. The integral of the first term is the normalization integral, which is equal to 1, giving

$$\Psi(J, t + \tau) - \Psi(J, t) = -\partial_J \left[\Psi(J, t) \int_{-\infty}^{\infty} \Delta \varphi(\Delta; J, \Psi) d\Delta \right] + \partial_J^2 \left[\Psi(J, t) \int_{-\infty}^{\infty} \frac{\Delta^2}{2} \varphi(\Delta; J, \Psi) d\Delta \right]. \quad (\text{B.3})$$

Finally, divide by the short time τ between kicks to get a time derivative on the LHS. One then arrives at the Fokker-Planck equation [63]

$$\partial_t \Psi = -\partial_J (U \Psi) + \partial_J^2 (\tilde{D} \Psi), \quad (\text{B.4})$$

with drift and diffusion coefficients given by

$$U(J, \Psi) = \int_{-\infty}^{\infty} \frac{\Delta}{\tau} \varphi(\Delta; J, \Psi) d\Delta, \quad (\text{B.5})$$

$$\tilde{D}(J, \Psi) = \int_{-\infty}^{\infty} \frac{\Delta^2}{2\tau} \varphi(\Delta; J, \Psi) d\Delta, \quad (\text{B.6})$$

respectively. In most of this thesis, an alternative convention for the diffusion coefficient is used: $D \equiv \tilde{D}/J$. This convention is more convenient, as a constant D corresponds to a uniform diffusion in phase space.

B.2 Liouville theorem

In this section, the goal is to derive the Fokker-Planck equation described by Eqs. (6.20) and (6.21). It will be derived for one transverse plane, based on the derivation in App. A of [74]. The dynamics is modeled by a stochastic Hamiltonian

$$\begin{aligned} \mathcal{H} &= \mathcal{H}_0 + \epsilon \mathcal{H}_1 + \epsilon^2 \mathcal{H}_2 + \mathcal{O}(\epsilon^3) \\ &= \mathcal{H}_0(J) + \epsilon \xi(t) V(\phi, J) + \mathcal{O}(\epsilon^3), \end{aligned} \quad (\text{B.7})$$

where a term of $\mathcal{O}(\epsilon)$ is assumed to be weak. Note that ϵ is merely a tag denoting the size of the term it is multiplied with, it carries no physical value and can be set to 1. The stochastic factor $\xi(t)$ is assumed to have zero mean and finite correlation period

$$\langle \xi(t) \rangle_t = 0 \quad , \quad \lim_{\tau \rightarrow \infty} \langle \xi(t) \xi(t + \tau) \rangle_t = 0. \quad (\text{B.8})$$

There is assumed no term in the Hamiltonian of $\mathcal{O}(\epsilon^2)$, which is reasonable both for an external noise source and a wake force, as will be checked later.

The evolution of the bunch distribution, when acted on by the perturbed Hamiltonian in Eq. (B.7), is found by considering the Liouville theorem, given mathematically by Eq. (2.44). In

1D, it can be written as

$$\frac{\partial \Psi}{\partial t} + \frac{\partial \mathcal{H}}{\partial J} \frac{\partial \Psi}{\partial \phi} - \frac{\partial \mathcal{H}}{\partial \phi} \frac{\partial \Psi}{\partial J} = 0, \quad (\text{B.9})$$

where also the distribution will be written as a perturbation

$$\Psi = \Psi_0(J) + \epsilon \Psi_1(\phi, J) + \epsilon^2 \Psi_2(\phi, J) + \mathcal{O}(\epsilon^3). \quad (\text{B.10})$$

Without the stochastic perturbation, the distribution is equal to Ψ_0 , which is assumed uniformly distributed in ϕ due to the fast angular rotation frequency

$$\Omega = \lim_{\epsilon \rightarrow 0} \dot{\phi} = \frac{\partial \mathcal{H}_0(J)}{\partial J}, \quad (\text{B.11})$$

compared to the slow unperturbed change of action

$$\lim_{\epsilon \rightarrow 0} \dot{J} = -\frac{\partial \mathcal{H}_0(J)}{\partial \phi} = 0. \quad (\text{B.12})$$

To $\mathcal{O}(\epsilon^0)$, Eq. (B.9) reads

$$\frac{\partial \Psi_0}{\partial t} + \Omega \frac{\partial \Psi_0}{\partial \phi} = \frac{\partial \Psi_0}{\partial t} = 0, \quad (\text{B.13})$$

where the assumption of Ψ_0 being uniformly distributed in ϕ was used. Hence, without the stochastic perturbation, the distribution does not change with time.

To $\mathcal{O}(\epsilon^1)$, Eq. (B.9) reads

$$\frac{\partial \Psi_1}{\partial t} + \Omega \frac{\partial \Psi_1}{\partial \phi} = \xi(t) \left[\frac{\partial V(\phi, J)}{\partial \phi} \frac{\partial \Psi_0(\phi, J, t)}{\partial J} \right], \quad (\text{B.14})$$

which can be written as

$$\begin{aligned} \frac{\partial}{\partial \tau} \Psi_1(\phi + \Omega \tau, J, t + \tau) &= \xi(t + \tau) \left[\frac{\partial V(\phi + \Omega \tau, J)}{\partial \phi} \frac{\partial \Psi_0(\phi + \Omega \tau, J, t + \tau)}{\partial J} \right] \\ &\equiv \tilde{\xi} \left[\frac{\partial \tilde{V}}{\partial \phi} \frac{\partial \tilde{\Psi}_0}{\partial J} \right], \end{aligned} \quad (\text{B.15})$$

where the notation $\tilde{f} \equiv f(t + \tau)$, as opposed to $f \equiv f(t)$, is introduced for brevity. By assuming an unperturbed initial condition, $\Psi_1(t = 0) = 0$, Eq. (B.15) can be solved by performing the stochastic integral

$$\Psi_1(\phi, J, t) = \int_{-t}^0 d\tau \tilde{\xi} \left[\frac{\partial \tilde{V}}{\partial \phi} \frac{\partial \tilde{\Psi}_0}{\partial J} \right]. \quad (\text{B.16})$$

This first-order distribution perturbation can reach a large oscillatory amplitude, but its average value in time will be $\langle \Psi_1 \rangle_t = 0$, due to the assumption of zero mean in Eq. (B.8).

To $\mathcal{O}(\epsilon^2)$, Eq. (B.9) reads

$$\frac{\partial \Psi_2}{\partial t} + \Omega \frac{\partial \Psi_2}{\partial \phi} = \xi(t) \left[\frac{\partial V}{\partial \phi} \frac{\partial \Psi_1}{\partial J} - \frac{\partial V}{\partial J} \frac{\partial \Psi_1}{\partial \phi} \right], \quad (\text{B.17})$$

Appendix B. The Fokker-Planck equation

which after insertion of Eq. (B.16) becomes

$$\begin{aligned} \frac{\partial \Psi_2}{\partial t} + \Omega \frac{\partial \Psi_2}{\partial \phi} &= \int_{-t}^0 d\tau \xi \tilde{\xi} \left[\frac{\partial V}{\partial \phi} \frac{\partial}{\partial J} \left(\frac{\partial \tilde{V}}{\partial \phi} \frac{\partial \tilde{\Psi}_0}{\partial J} \right) - \frac{\partial V}{\partial J} \frac{\partial}{\partial \phi} \left(\frac{\partial \tilde{V}}{\partial \phi} \frac{\partial \tilde{\Psi}_0}{\partial J} \right) \right] \\ &= \int_{-t}^0 d\tau \xi \tilde{\xi} \left[\frac{\partial}{\partial J} \left(\frac{\partial V}{\partial \phi} \frac{\partial \tilde{V}}{\partial \phi} \frac{\partial \tilde{\Psi}_0}{\partial J} \right) - \frac{\partial}{\partial \phi} \left(\frac{\partial V}{\partial J} \frac{\partial \tilde{V}}{\partial \phi} \frac{\partial \tilde{\Psi}_0}{\partial J} \right) \right]. \end{aligned} \quad (\text{B.18})$$

Additional steps can be taken to make Eq. (B.18) more readily solvable: (i) Due to the fast angular rotation, it is reasonable to average over ϕ . As a consequence, the second term on both sides of Eq. (B.18) vanishes due to the fundamental theorem of calculus; (ii) It was found in Eq. (B.13) that Ψ_0 was constant, meaning that $\tilde{\Psi}_0 = \Psi_0$; (iii) Since ξ is stochastic, it is necessary to get an expectancy value over time; (iv) Unlike the stochastic evolution of Ψ_1 , of zero expected value, Ψ_2 will evolve systematically towards a non-negligible perturbation, given enough time. Hence, a new distribution named the equilibrium distribution $\Psi_{\text{eq}} \equiv \Psi_0 + \epsilon^2 \Psi_2$ is introduced. Combining all of this, the evolution of the equilibrium distribution can to leading order be written as the Fokker-Planck equation

$$\frac{\partial \Psi_{\text{eq}}}{\partial t} = \frac{\partial}{\partial J} \left[JD \frac{\partial \Psi_{\text{eq}}}{\partial J} \right], \quad (\text{B.19})$$

where the action dependent diffusion coefficient is given by

$$\begin{aligned} D &= \lim_{t_{\text{tot}} \rightarrow \infty} \frac{1}{J t_{\text{tot}}} \int_0^{t_{\text{tot}}} dt \int_{-t}^0 d\tau \epsilon^2 \left\langle \xi(t) \xi(t+\tau) \frac{\partial V(t)}{\partial \phi} \frac{\partial V(t+\tau)}{\partial \phi} \right\rangle_{\phi} \\ &= \lim_{t_{\text{tot}} \rightarrow \infty} \frac{1}{J t_{\text{tot}}} \int_0^{t_{\text{tot}}} dt \int_0^t ds \epsilon^2 \left\langle \xi(t) \xi(s) \frac{\partial V(t)}{\partial \phi} \frac{\partial V(s)}{\partial \phi} \right\rangle_{\phi} \\ &= \lim_{t_{\text{tot}} \rightarrow \infty} \frac{1}{2J t_{\text{tot}}} \int_0^{t_{\text{tot}}} dt \int_0^{t_{\text{tot}}} ds \epsilon^2 \left\langle \frac{\partial \mathcal{H}_1(t)}{\partial \phi} \frac{\partial \mathcal{H}_1(s)}{\partial \phi} \right\rangle_{\phi} \\ &= \lim_{t_{\text{tot}} \rightarrow \infty} \frac{1}{2J t_{\text{tot}}} \int_{t_0}^{t_0+t_{\text{tot}}} dt \int_{t_0}^{t_0+t_{\text{tot}}} ds \langle \dot{J}(t) \dot{J}(s) \rangle_{\phi}, \end{aligned} \quad (\text{B.20})$$

where the initial time was generalized in the last step. Equations (B.19) and (B.20) describe a diffusion mechanism. The evolution of the second-order distribution perturbation Ψ_2 constitutes the slow-and-steady evolution of the equilibrium distribution. When returning to the scope of this thesis, it can therefore be understood that Ψ_2 will not drive wakefields, and the second-order wakefield Hamiltonian \mathcal{H}_2 will therefore be zero, as was assumed here, initially.

C Change of action after a kick with decoherence and feedback

Disclaimer: This appendix was adapted from the following articles — with permissions of the co-author and publishers:

[62] **S. V. Furuseth** and X. Buffat, “Change of beam distribution due to decoherence in the presence of transverse feedback”, in *J. Phys.: Conf. Ser.* **1350**, May 2019, p. 012118. doi:[10.1088/1742-6596/1350/1/012118](https://doi.org/10.1088/1742-6596/1350/1/012118)

[52] **S. V. Furuseth** and X. Buffat, “Long-term evolution of Landau damping in the presence of transverse noise, feedback, and detuning”, *Phys. Rev. Accel. Beams* **23**, p. 034401, 2020. doi:[10.1103/PhysRevAccelBeams.23.034401](https://doi.org/10.1103/PhysRevAccelBeams.23.034401)

Both were published under a CC-BY, 3.0 and 4.0, respectively.

My contribution: All results presented here.

In this appendix, the expression in Eq. (5.2) for the change of action after an initial kick, $\Delta p = k$, when the particles are influenced by both an incoherent source of detuning and a transverse feedback system, is derived [52]. To do so, the transverse phase space coordinates of a particle after the initial kick will be referred to as

$$\rho \equiv x + ip, \quad (\text{C.1})$$

while the position just prior to the kick will be denoted $\rho_{\text{eq}} = x_0 + ip_0$, such that $\rho_0 = \rho_{\text{eq}} + ik$. It follows that the COM of the bunch is referred to as

$$\langle \rho \rangle \equiv \langle \rho \rangle_{\Psi} = \langle x \rangle_{\Psi} + i \langle p \rangle_{\Psi}, \quad (\text{C.2})$$

where the angle brackets in this appendix always refer to the average over the distribution. Equivalently, the tune of the COM is denoted $\langle Q \rangle \equiv \langle Q \rangle_{\Psi}$. The transverse offset will be reduced by the transverse feedback system towards the design trajectory by a factor called the gain g . Assuming a perfect immediate feedback, the evolution of the COM from one turn to the next is given by

$$\langle \rho_1 \rangle = \langle \rho_0 \rangle e^{-i2\pi \langle Q \rangle} \left(1 - \frac{g}{2}\right). \quad (\text{C.3})$$

Appendix C. Change of action after a kick with decoherence and feedback

The initial COM offset, $\langle \rho_0 \rangle = ik$, will after n turns be

$$\langle \rho_n \rangle = \langle \rho_0 \rangle e^{-i2\pi \langle Q \rangle n} \left(1 - \frac{g}{2}\right)^n \xrightarrow{n \rightarrow \infty} \langle \rho_0 \rangle e^{-i2\pi \langle Q \rangle n} e^{-\frac{g}{2}n}, \quad (\text{C.4})$$

with a damping time of $\tau_g = 2/g$ turns. It is assumed that the reduction of the COM amplitude due to the tune spread is negligible compared to the reduction due to the transverse feedback system.

After many turns, the COM tends to the origin in the limit $ng \gg 1$. The position of an individual particle, with a constant tune offset $\tilde{\Delta}Q = Q - \langle Q \rangle$ from the COM tune, will become

$$\begin{aligned} \rho_n &= e^{-i2\pi \sum_{j=0}^{n-1} (\langle Q \rangle + \tilde{\Delta}Q_j)} \left(\rho_0 - \langle \rho_0 \rangle \frac{g}{2} \sum_{j=0}^{n-1} \left(1 - \frac{g}{2}\right)^j e^{i2\pi \sum_{l=0}^{j-1} \tilde{\Delta}Q_l} \right) \\ &= e^{-i2\pi (\langle Q \rangle + \tilde{\Delta}Q)n} \left(\rho_0 - \langle \rho_0 \rangle \frac{\frac{g}{2}}{1 - \left(1 - \frac{g}{2}\right) e^{i2\pi \tilde{\Delta}Q}} \right) \\ &= e^{-i2\pi (\langle Q \rangle + \tilde{\Delta}Q)n} \left(\rho_{\text{eq}} + \langle \rho_0 \rangle \frac{\left(1 - \frac{g}{2}\right) \left(1 - e^{i2\pi \tilde{\Delta}Q}\right)}{1 - \left(1 - \frac{g}{2}\right) e^{i2\pi \tilde{\Delta}Q}} \right), \end{aligned} \quad (\text{C.5})$$

where $\rho_{\text{eq}} = \rho_0 - \langle \rho_0 \rangle$ is the position of the particle just prior to the kick. In going from line 1 to line 2, one has assumed that $\langle Q \rangle$ and $\tilde{\Delta}Q$ are constant during the process, and one has taken the sum of the geometric series. Assuming the kicks are small, this expression can easily be extended to include more kicks as $\langle \rho_0 \rangle \rightarrow \sum_{j=0}^m ik_j e^{i2\pi Q_j}$.

It follows from Eq. (2.23) that the action n turns after the kick is

$$2J_n = x_n^2 + p_n^2 = \overline{\rho_n} \rho_n = |\rho_n|^2, \quad (\text{C.6})$$

where the horizontal line signifies a complex conjugation. Filling in, remembering that ρ_{eq} and $\langle \rho_0 \rangle$ are complex numbers,

$$\begin{aligned} 2J_n &= e^{i2\pi (\langle Q \rangle + \tilde{\Delta}Q)n} \left(\frac{\overline{\rho_{\text{eq}}} + \overline{\langle \rho_0 \rangle}}{\overline{\rho_{\text{eq}}} + \overline{\langle \rho_0 \rangle}} \frac{\left(1 - \frac{g}{2}\right) (1 - e^{-i2\pi \tilde{\Delta}Q})}{1 - \left(1 - \frac{g}{2}\right) e^{-i2\pi \tilde{\Delta}Q}} \right) e^{-i2\pi (\langle Q \rangle + \tilde{\Delta}Q)n} \left(\rho_{\text{eq}} + \langle \rho_0 \rangle \frac{\left(1 - \frac{g}{2}\right) (1 - e^{i2\pi \tilde{\Delta}Q})}{1 - \left(1 - \frac{g}{2}\right) e^{i2\pi \tilde{\Delta}Q}} \right) \\ &= |\rho_{\text{eq}}|^2 + |\langle \rho_0 \rangle|^2 \frac{\left(1 - \frac{g}{2}\right)^2 (1 - e^{-i2\pi \tilde{\Delta}Q})(1 - e^{i2\pi \tilde{\Delta}Q})}{1 + \left(1 - \frac{g}{2}\right) \left(1 - \frac{g}{2} - e^{-i2\pi \tilde{\Delta}Q} - e^{i2\pi \tilde{\Delta}Q}\right)} + \left(\overline{\rho_0} \langle \rho_0 \rangle \frac{\left(1 - \frac{g}{2}\right) (1 - e^{i2\pi \tilde{\Delta}Q})}{1 - \left(1 - \frac{g}{2}\right) e^{i2\pi \tilde{\Delta}Q}} + \text{c.c.} \right) \\ &= 2J_0 + |\langle \rho_0 \rangle|^2 f_1 + (\overline{\rho_0} \langle \rho_0 \rangle f_2 + \text{c.c.}), \end{aligned} \quad (\text{C.7})$$

where the factors depending on g and $\tilde{\Delta}Q$ have been renamed f_1 and f_2 , and J_0 is the action prior to the kick.

It will now be made use of the well-known expressions

$$2 \cos(\theta) = e^{i\theta} + e^{-i\theta}, \quad (\text{C.8})$$

$$2i \sin(\theta) = e^{i\theta} - e^{-i\theta}, \quad (\text{C.9})$$

$$\cos(2\theta) = 1 - 2 \sin^2(\theta), \quad (\text{C.10})$$

$$e^{i\theta} = \cos(\theta) + i \sin(\theta). \quad (\text{C.11})$$

By insertion for f_1 one finds that

$$\begin{aligned} f_1 &= \frac{\left(1 - \frac{g}{2}\right)^2 (-4i^2) \sin^2(\pi \tilde{\Delta} Q)}{1 + \left(1 - \frac{g}{2}\right) \left(1 - \frac{g}{2} - 2 \cos(2\pi \tilde{\Delta} Q)\right)} \\ &= \frac{\left(1 - \frac{g}{2}\right)^2 4 \sin^2(\pi \tilde{\Delta} Q)}{\left(\frac{g}{2}\right)^2 + \left(1 - \frac{g}{2}\right) 4 \sin^2(\pi \tilde{\Delta} Q)}. \end{aligned} \quad (\text{C.12})$$

For f_2 , first multiply and divide by the complex conjugate of the denominator to get

$$\begin{aligned} f_2 &= \frac{\left(1 - \frac{g}{2}\right) (1 - e^{i2\pi \tilde{\Delta} Q})}{1 - \left(1 - \frac{g}{2}\right) e^{i2\pi \tilde{\Delta} Q}} \cdot \frac{1 - \left(1 - \frac{g}{2}\right) e^{-i2\pi \tilde{\Delta} Q}}{1 - \left(1 - \frac{g}{2}\right) e^{-i2\pi \tilde{\Delta} Q}} \\ &= \left(1 - \frac{g}{2}\right) \frac{\left(2 - \frac{g}{2} - 2 \cos(2\pi \tilde{\Delta} Q) + \left(\frac{g}{2}\right) e^{-i2\pi \tilde{\Delta} Q}\right)}{1 + \left(1 - \frac{g}{2}\right)^2 - \left(1 - \frac{g}{2}\right) 2 \cos(2\pi \tilde{\Delta} Q)} \\ &= \left(1 - \frac{g}{2}\right) \frac{(4 - g) \sin^2(\pi \tilde{\Delta} Q) - i \left(\frac{g}{2}\right) \sin(2\pi \tilde{\Delta} Q)}{\left(\frac{g}{2}\right)^2 + \left(1 - \frac{g}{2}\right) 4 \sin^2(\pi \tilde{\Delta} Q)}. \end{aligned} \quad (\text{C.13})$$

To get an expression for the last parenthesis in Eq. (C.7), note that for a complex number c , $c + \bar{c} = 2 \operatorname{Re}\{c\}$, and that $\overline{\rho_0} \langle \rho_0 \rangle = p_0 k + i x_0 k$. Dividing by 2, and setting $\Delta J = J_n - J_0$, gives

$$\Delta J = \frac{k^2}{2} \frac{\left(1 - \frac{g}{2}\right)^2 4 \sin^2(\pi \tilde{\Delta} Q)}{\left(\frac{g}{2}\right)^2 + \left(1 - \frac{g}{2}\right) 4 \sin^2(\pi \tilde{\Delta} Q)} + k \left(1 - \frac{g}{2}\right) \frac{x_0 \left(\frac{g}{2}\right) \sin(2\pi \tilde{\Delta} Q) + p_0 (4 - g) \sin^2(\pi \tilde{\Delta} Q)}{\left(\frac{g}{2}\right)^2 + \left(1 - \frac{g}{2}\right) 4 \sin^2(\pi \tilde{\Delta} Q)}, \quad (\text{C.14})$$

where $x_0 + i p_0 = \rho_{\text{eq}}$ is the position prior to the kick. This is identical to Eq. (5.2) when Taylor expanding the sine functions to first order, which is valid in the limit $\tilde{\Delta} Q \ll 1$, and using the expressions for x_0 and p_0 in Eq. (2.21).

D PyRADISE – Radial diffusion and stability evolution

Disclaimer: This appendix was adapted from the following article — with permissions of the co-author and publisher:

[52] **S. V. Furuseth** and X. Buffat, “Long-term evolution of Landau damping in the presence of transverse noise, feedback, and detuning”, *Phys. Rev. Accel. Beams* **23**, p. 034401, 2020. doi:[10.1103/PhysRevAccelBeams.23.034401](https://doi.org/10.1103/PhysRevAccelBeams.23.034401)

It was published under CC-BY 4.0.

My contribution: All results presented here.

In Part II of this thesis, the evolving single-bunch stability was studied as a consequence to an evolving transverse bunch distribution. The distribution evolution was modeled by the Fokker-Planck equation, and it was found to correspond to an action dependent diffusion in transverse action space. In the general case, the distribution evolution has to be solved numerically. Therefore, the code PyRADISE [96] has been developed to solve the Fokker-Planck equation, which is done in three steps:

1. Change the amplitude variable to $r = \sqrt{2J}$, the radius in (x, p) -phase space.
2. Solve the Fokker-Planck equation with a discrete PDE solver, using the Finite Volume Method (FVM), to get the evolution of the transverse bunch distribution [97].
3. Calculate the evolving stability due to the evolving bunch distribution, by numerically performing the integral in Eq. (2.45) with PySSD [35].

D.1 Change of independent variable

The change of the independent variables from J to r is achieved by using the chain rule, $\partial_J(\cdot) = \partial_J(r)\partial_r(\cdot)$, where $\partial_J(r) = 1/r$. Thus, the two following expressions for the 2D Fokker-Planck equation are equivalent

$$\begin{aligned}\partial_t \Psi &= \frac{\partial}{\partial J_x} \left(J_x D_{xx} \frac{\partial \Psi}{\partial J_x} - U_x \Psi \right) + \frac{\partial}{\partial J_y} \left(J_y D_{yy} \frac{\partial \Psi}{\partial J_y} - U_y \Psi \right) \\ &= \frac{1}{r_x} \frac{\partial}{\partial r_x} \left(\frac{r_x}{2} D_{xx} \frac{\partial \Psi}{\partial r_x} - U_x \Psi \right) + \frac{1}{r_y} \frac{\partial}{\partial r_y} \left(\frac{r_y}{2} D_{yy} \frac{\partial \Psi}{\partial r_y} - U_y \Psi \right),\end{aligned}\tag{D.1}$$

where D_{jj} and U_j are the diffusion and drift coefficients, respectively, in either transverse plane. Any cross-plane diffusion was found negligible in Part II, and have therefore not been included here. Note that the expressions for D_{jj} and U_j are equal in both lines of Eq. (D.1), as they are known functions of r and J .

The independent variables have been changed first and foremost because it has been found that a uniformly spaced grid in $r = \sqrt{2J}$ better represents a Gaussian bunch distribution, than a uniformly spaced grid in J does. As a consequence, the FVM that will be introduced in Sec. D.2 converges faster with the number of grid cells when using a uniform grid in r than in J .

D.2 Finite volume method

A PDE solver using the FVM has been implemented to solve the diffusion-advection problem represented by Eq. (D.1). The region of interest, and its discretization in a uniform $N_x \times N_y$ cell grid, is presented in Fig. D.1. The FVM has been applied because it ensures mass conservation in the interior region by solving the differential problem in terms of fluxes across the cell boundaries. The solver in PyRADISE has been made able to solve the differential problem both in terms of r and J . In the following, it is assumed that the solver uses the transverse actions as independent variables, but the principles are identical for both sets of independent coordinates.

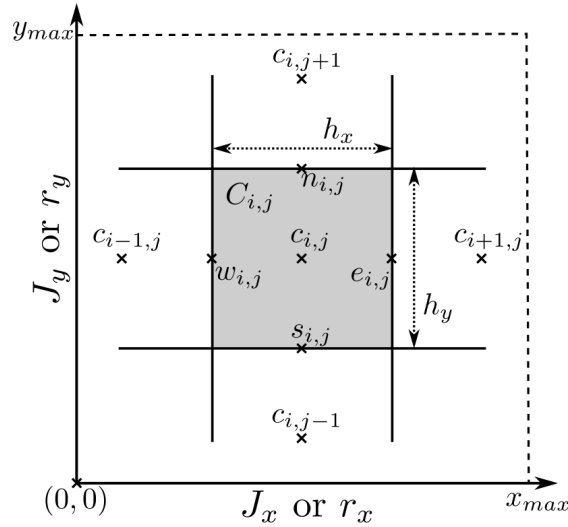


Figure D.1: Illustration of the FVM grid in PyRADISE. A uniform $N_x \times N_y$ cell grid covers the independent variables, either in the form of J or r , from 0 to their respective maximal values. Each cell $C_{i,j}$ in the grid has a center $c_{i,j} = ((i + \frac{1}{2}) \cdot h_x, (j + \frac{1}{2}) \cdot h_y)$ and four edge points $e_{i,j}$, $w_{i,j}$, $n_{i,j}$, $s_{i,j}$, which are half a cell width or height away from $c_{i,j}$ in the respective compass directions. It follows that $e_{i,j} = w_{i+1,j}$, etc.

The FVM is based on integrating the differential equation across the cell area as

$$\iint_{C_{i,j}} dJ_x dJ_y \partial_t \Psi = \iint_{C_{i,j}} dJ_x dJ_y \left[\frac{\partial}{\partial J_x} \left(J_x D_{xx} \frac{\partial \Psi}{\partial J_x} - U_x \Psi \right) + \frac{\partial}{\partial J_y} \left(J_y D_{yy} \frac{\partial \Psi}{\partial J_y} - U_y \Psi \right) \right]. \quad (\text{D.2})$$

The density in a certain cell, $\Psi_{i,j}$, is considered independent of (J_x, J_y) . Due to the divergence theorem, the density evolution in a cell depends on the diffusion and drift coefficients, as well as the distribution function itself, at the four cell edges as

$$\partial_t \Psi_{i,j} = \frac{1}{h_x} \left[J_x D_{xx} \frac{\partial \Psi}{\partial J_x} - U_x \Psi \right]_{w_{i,j}}^{e_{i,j}} + \frac{1}{h_y} \left[J_y D_{yy} \frac{\partial \Psi}{\partial J_y} - U_y \Psi \right]_{s_{i,j}}^{n_{i,j}}, \quad (\text{D.3})$$

where the values of the bracketed expressions on the RHS are added at the locations of the superscripts and subtracted at the locations of the subscripts. At the eastern edge, the distribution is evaluated as the average of the closest cell densities

$$\Psi_{e_{i,j}} = \frac{\Psi_{i+1,j} + \Psi_{i,j}}{2}, \quad (\text{D.4})$$

and the derivative is evaluated by finite differences as

$$\left. \frac{\partial \Psi}{\partial J_x} \right|_{e_{i,j}} = \frac{\Psi_{i+1,j} - \Psi_{i,j}}{h_x}, \quad (\text{D.5})$$

and equivalently for the other cell edges. Adding all the terms gives the following discretized evolution of the density in the internal cell $C_{i,j}$:

$$\begin{aligned} \partial_t \Psi_{i,j} = & + \frac{1}{h_x^2} \left[J_x^{e_{i,j}} D_{xx}^{e_{i,j}} (\Psi_{i+1,j} - \Psi_{i,j}) - J_x^{w_{i,j}} D_{xx}^{w_{i,j}} (\Psi_{i,j} - \Psi_{i-1,j}) \right] \\ & + \frac{1}{h_y^2} \left[J_y^{n_{i,j}} D_{yy}^{n_{i,j}} (\Psi_{i,j+1} - \Psi_{i,j}) - J_y^{s_{i,j}} D_{yy}^{s_{i,j}} (\Psi_{i,j} - \Psi_{i,j-1}) \right] \\ & - \frac{1}{2h_x} \left[U_x^{e_{i,j}} (\Psi_{i+1,j} + \Psi_{i,j}) - U_x^{w_{i,j}} (\Psi_{i,j} + \Psi_{i-1,j}) \right] \\ & - \frac{1}{2h_y} \left[U_y^{n_{i,j}} (\Psi_{i,j+1} + \Psi_{i,j}) - U_y^{s_{i,j}} (\Psi_{i,j} + \Psi_{i,j-1}) \right]. \end{aligned} \quad (\text{D.6})$$

From this expression, the conservation property of the FVM becomes clear. The flux out of cell $C_{i,j}$ through its eastern border is equal to the flux into cell $C_{i+1,j}$ through its western border.

The BCs, the fluxes through the borders of the global volume, must be treated carefully. At $J = 0$, physics dictates that there must be a reflective BC, i.e. with no flux through it. At the boundary at $J = J_{\max}$, one can argue between using a homogeneous or inhomogeneous Neumann or Dirichlet BC. However, it has been decided most correct to model it as an absorbing boundary (homogeneous Dirichlet), representing an aperture in a real machine. This is achieved by introducing virtual ghost cells with zero density outside the boundary, which consequently have no impact on Eq. (D.6).

The time integration is performed by `scipy.integrate.solve_ivp` [98], using a method based on a backward differentiation formula and a sparse Jacobian. Using an implicit scheme ensures the numerical stability of the integration. In the cases when the diffusion and drift coefficients depend on the distribution, the coefficients are calculated based on the distribution at time t_a , whereupon the distribution evolution from t_a to t_b is evaluated, before the coefficients are recalculated ahead of the next time step. This is acceptable due to the

small change of the distribution within each short time step. The output is an array $\Psi(i, j, k)$, containing the density in all cells $C_{i,j}$ at the desired discrete times t_k .

D.3 Stability evolution

The ultimate goal of PyRADISE is to calculate the stability evolution. Hence, the integral in Eq. (2.45) must be calculated for the distribution at each discrete time t_k , either to get the stability diagram itself or the Landau damped mode frequency, as was explained in Sec. 6.2.2. Therefore, PySSD is integrated in PyRADISE to numerically perform the integral, using a uniform trapezoidal discretization in (J_x, J_y) .

Note that it is the derivative of Ψ with respect to the action that is needed to perform the integral in Eq. (2.45). The bunch distribution can therefore no longer be assumed to be piecewise constant, as it was in the FVM. First, the derivative with respect to J_x is taken at the eastern and western edges as given by Eq. (D.5), and equivalently for the derivative with respect to J_y at the northern and southern edges. Then, the derivatives are linearly interpolated between the cell edges. Within the cell closest to the global boundary of $J = 0$, the horizontal (vertical) derivative at the western (southern) boundary is set equal to the derivative on the eastern (northern) boundary of the cell. At the other boundary, at $J = J_{\max}$, the derivative is forced to be zero. Finally, the numerical integral is performed with $\text{Im}\{\Omega_{\text{LD}}\} = \epsilon$, where $\epsilon \rightarrow 0$. The numerical non-zero value of ϵ is set proportional to the overall detuning magnitude. For now, only a linear detuning is implemented in PyRADISE, as the one driven by Landau octupoles that was described in Sec. 2.3.2.

E Harmonically driven distribution evolution

Disclaimer: This appendix was adapted from the following article — with permissions of the co-author and publisher:

[50] **S. V. Furuseth** and X. Buffat, “Loss of transverse Landau damping by noise and wakefield driven diffusion”, *Phys. Rev. Accel. Beams* **23**, p. 114401, Nov. 2020. doi:[10.1103/PhysRevAccelBeams.23.114401](https://doi.org/10.1103/PhysRevAccelBeams.23.114401)

It was published under CC-BY 4.0.

My contribution: All results presented here.

In Ch. 6 of this thesis, headtail modes driven by wakefields are modeled as under-damped stochastically driven harmonic oscillators. Due to their stochastic nature, the resulting impact can be modeled as a diffusion. However, in the limit $\text{Im}\{\Delta\Omega_m\} \rightarrow 0$, the force becomes a pure harmonic excitation. In this appendix, the focus is the resulting distribution dynamics when a bunch is affected by such a harmonic excitation.

Consider that a harmonic oscillator of angular frequency ω is harmonically driven by a real impulse $P_h \cos(\omega_h t)$, kicked once per turn, changing the one-turn Hamiltonian in Eq. (3.31) to

$$\mathcal{H} = \mathcal{H}_0 - \sqrt{2J} \cos(\phi) f_{\text{rev}} P_h \cos(\omega_h t), \quad (\text{E.1})$$

where \mathcal{H}_0 models the free motion of a simple harmonic oscillator. In the simple case of no amplitude detuning, $\mathcal{H}_0 = \omega J$, the motion of the harmonic oscillator will consist of the free and the forced motion, as due to an AC dipole [99]. The amplitude of the forced motion is

$$A(\omega) = \frac{\omega f_{\text{rev}} P_h}{|\omega^2 - \omega_h^2|}, \quad (\text{E.2})$$

which is singular for a harmonic oscillator at exactly the driving frequency.

In an accelerator, the incoherent particle frequency is typically amplitude dependent, for instance due to Landau octupoles as given by Eq. (2.29). Therefore, a particle’s amplitude will no longer be singular, because the resonance condition is disrupted as the amplitude grows. For a harmonic excitation in only one plane, only the amplitude detuning in that plane

Appendix E. Harmonically driven distribution evolution

requires consideration. Hamilton's equations of motion for ϕ and J then reads [11, 100]

$$\mathcal{H} = \omega_0 J + \frac{\tilde{a}}{2} J^2 - \sqrt{2J} \cos(\phi) f_{\text{rev}} P_h \cos(\omega_h t), \quad (\text{E.3})$$

$$\dot{\phi} = \omega_0 + \tilde{a} J - \frac{f_{\text{rev}} P_h}{\sqrt{2J}} \cos(\phi) \cos(\omega_h t) \quad (\text{E.4})$$

$$= \omega_0 + \tilde{a} J - \frac{f_{\text{rev}} P_h}{2\sqrt{2J}} [\cos(\phi + \omega_h t) + \cos(\phi - \omega_h t)],$$

$$\dot{J} = -\sqrt{2J} \sin(\phi) f_{\text{rev}} P_h \cos(\omega_h t) \quad (\text{E.5})$$

$$= -\sqrt{\frac{J}{2}} f_{\text{rev}} P_h [\sin(\phi + \omega_h t) + \sin(\phi - \omega_h t)].$$

The harmonic frequency corresponds to a harmonic action J_h such that $\dot{\phi}(J_h) = \omega_h$. One can find new conserved properties of the full Hamiltonian [100], but that is not the current goal. Here, the motion of particles, starting at the harmonic action J_h and any initial phase ϕ_0 , will be studied in terms of the original action corresponding to \mathcal{H}_0 . The goal is to get an expression for the width of the action oscillation and the period of this motion. The terms with the high angular frequency $\dot{\phi} + \omega_h$ will not produce a macroscopic change of action. The terms with the potentially low frequency $\dot{\phi} - \omega_h$ may have the same sign for an extended period of time, and can cause a macroscopic change of action for particles close to the harmonic action J_h . The beating excitation leads to a slowly oscillating action evolution of a certain width and period, which will be estimated in the following by directly solving Eqs. (E.4) and (E.5) in multiple limits.

In the limit of large harmonic excitation, $f_{\text{rev}} P_h / \sqrt{J} \gg \tilde{a}(J - J_h)$, and neglecting the high-frequency term, the equations of motion become

$$\dot{\phi} = \omega_h - \frac{f_{\text{rev}} P_h}{2\sqrt{2J}} \cos(\phi - \omega_h t), \quad (\text{E.6})$$

$$\dot{J} = -\sqrt{\frac{J}{2}} f_{\text{rev}} P_h \sin(\phi - \omega_h t). \quad (\text{E.7})$$

Regardless of the initial phase ϕ_0 , the phase will approach its one stable value at $\phi - \omega_h t = -\pi/2 + 2\pi n$, where n is an integer. The corresponding time derivative of the action is positive. The action will grow until $f_{\text{rev}} P_h / \sqrt{J} \sim \tilde{a}(J - J_h)$, breaking the initial assumption.

Alternatively, if the harmonic excitation could be treated as a weak perturbation, $f_{\text{rev}} P_h / \sqrt{J} \ll \tilde{a}(J - J_h)$, the last term in Eq. (E.4) can be neglected. If one also assumes small phase offsets $|\phi - \omega_h t| \ll 1$ and small action offsets $|J - J_h| \ll J_h$, the equations of motion read

$$\dot{\phi} = \omega_h + \tilde{a}(J - J_h), \quad (\text{E.8})$$

$$\dot{J} = -\sqrt{\frac{J_h}{2}} f_{\text{rev}} P_h (\phi - \omega_h t). \quad (\text{E.9})$$

These are the equations of motion of a simple harmonic oscillator, but it is now the phase and action that are oscillating. In the following it is assumed for simplicity, but without loss of generality, that $\tilde{a} > 0$ and that $\phi_0 \in (-\pi, \pi)$. It can be verified by insertion that the equations of

motion, combined with the initial conditions $J(0) = J_h$ and $\phi(0) = \phi_0$, are solved by

$$\phi(t) = \omega_h t + \phi_0 \cos\left(2\pi \frac{t}{\tau_{h\min}}\right), \quad (\text{E.10})$$

$$J(t) = J_h - W_{h\min} \sin\left(2\pi \frac{t}{\tau_{h\min}}\right), \quad (\text{E.11})$$

where the minimal period $\tau_{h\min}$ and action offset amplitude $W_{h\min}$ are given by

$$(\tau_{h\min} f_{\text{rev}})^2 = \frac{(2\pi)^2}{\sqrt{2J_h P_h a \pi}}, \quad (\text{E.12})$$

$$W_{h\min}(\phi_0) = \frac{(2J_h)^{1/4} \sqrt{P_h \pi}}{2\sqrt{a}} \frac{\phi_0}{\pi}, \quad (\text{E.13})$$

where the detuning coefficients have been rewritten with $\tilde{a} = \omega_{\text{rev}} a$. The initial phase ϕ_0 is the maximum phase offset, fulfilling the assumption of small $|\phi - \omega_h t|$, as long as it was fulfilled at $t = 0$. The maximum action offset $|J - J_h|$ is small if the harmonic excitation is weak. The action offset amplitude is proportional to ϕ_0 , which is assumed small.

The maximum action offset should occur for large initial phases $|\phi_0| \rightarrow \pi^-$, for which the approximation $\sin(\phi_0) = \phi_0$ in Eq. (E.9) is wrong. In this case, both ϕ and J approaches 0 initially and there is almost an asymptotic motion with an infinite period $\tau_h \rightarrow \infty$. This will, however, be prevented by the last term in Eq. (E.4). The action offset amplitude will, on the other hand, not grow until infinity. Since $|\sin(\phi - \omega_h t)| \leq |\phi - \omega_h t|$, the maximum width in action can be approximated by $|W_{h\min}(\pi)2/\pi|$ as

$$W_h = \frac{(2J_h)^{1/4} \sqrt{P_h}}{\sqrt{a\pi}}. \quad (\text{E.14})$$

Due to different harmonic periods of different particles, the corresponding distribution oscillation will decohere with time.

To test the analytical derivations, numerical tracking simulations have been run with $a = 5 \times 10^{-3}$ for particles starting at the harmonic action $J_h = 2$ with phases ϕ_0 uniformly distributed on $[-\pi, \pi]$. The peak-to-peak action variation divided by two and the period of the oscillation is presented in Fig. E.1. At small $|\phi_0|$, the expressions in Eqs. (E.12) and (E.13) are shown to be correct. At large $|\phi_0|$, the action offset amplitude approaches W_h given by Eq. (E.14), while the period grows substantially. For large P_h/aJ_h , the motion is different, but qualitatively similar. Note that the largest widths clearly breaks the assumption $W_h \ll J_h = 2$. For $a < 0$, the general picture is the same, but the particles oscillate around $\phi - \omega_h t = \pi + 2\pi n$ instead of $2\pi n$.

To study how the harmonic perturbation affects the bunch distribution, a multi-particle simulation has been run with $P_h = 10^{-2}$, $a = 5 \times 10^{-3}$, and $J_h = 2$, equal to the curve labeled $P_h/aJ_h = 1$ in Fig. E.1. The bunch evolution is presented in Fig. E.2. The action oscillation around $J_h = 2$ is clear. The full width is close to $2W_h = 2.2$, given by Eq. (E.14). For this large W_h/J_h , the amplitude is not symmetric around J_h , but slightly larger for $J > J_h$ than for $J < J_h$. The emittance period is, as expected, longer than the minimum incoherent action period,

Appendix E. Harmonically driven distribution evolution

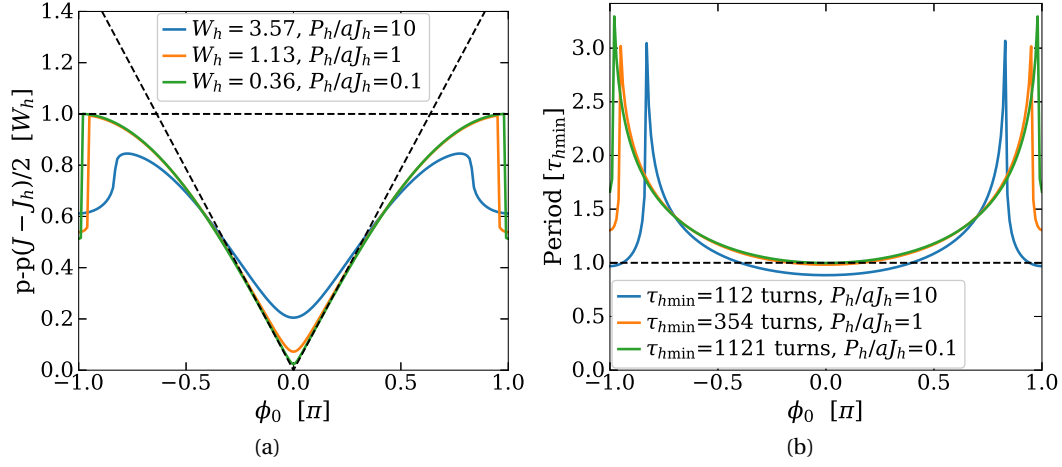


Figure E.1: Peak-to-peak (p-p) action variation in (a), and period of action oscillation in (b), for particles starting at $J_h = 2$ with various initial phases ϕ_0 . The dashed diagonal and horizontal lines in (a) correspond to Eq. (E.13) and Eq. (E.14), respectively. The dashed horizontal line in (b) corresponds to Eq. (E.12).

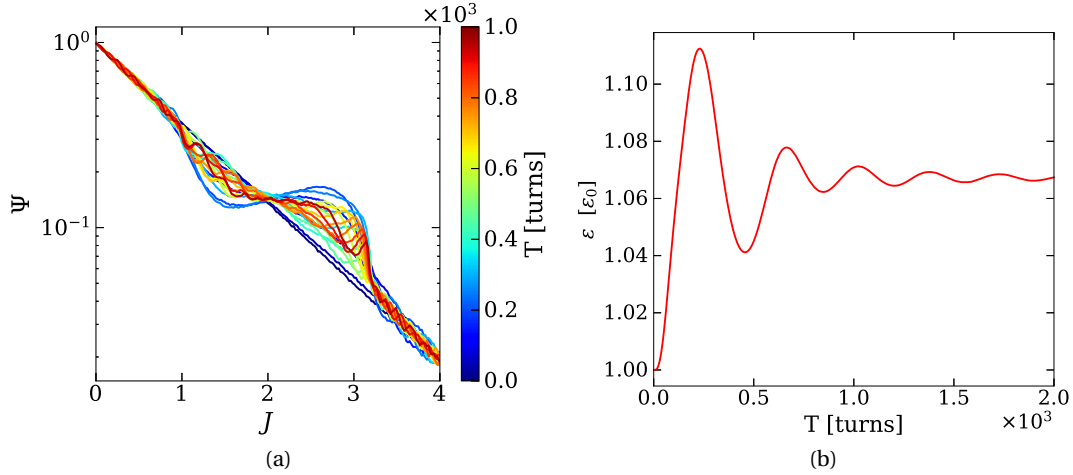


Figure E.2: Evolution of the distribution every 50 turns in (a) and emittance in (b) of a bunch that is driven by a harmonic force $P_h \cos(\omega_h t)$. The in-plane detuning coefficient is $a = 5 \times 10^{-3}$, corresponding to a detuning of aJ .

$\tau_{h\min} = 354$ turns, given by Eq. (E.12). This process cannot be modeled as a diffusion because it is deterministic and not stochastic. However, it may enhance the diffusion across J_h driven by other stochastic processes. Furthermore, the harmonic excitation does lead to a local flattening of the distribution on its own, similar to that driven by the wakefield driven diffusion studied in Ch. 6, and should therefore have an impact on the stability diagram.

Bibliography

- [1] O. S. Brüning, P. Collier, P. Lebrun, S. Myers, R. Ostojic, J. Poole, and P. Proudlock (eds.), “LHC Design Report”, CERN, Geneva, Switzerland, Rep. CERN-2004-003-V-1, Jul. 2004. doi:[10.5170/CERN-2004-003-V-1](https://doi.org/10.5170/CERN-2004-003-V-1).
- [2] R. Steerenberg, M. Albert, R. Alemany-Fernández, T. Argyropoulos, E. Bravin, G. Crookford, J.-C. Dumont, K. Fuchsberger, R. Giachino, M. Giovannozzi, G.-H. Hemelsoet, W. Höfle, D. Jacquet, M. Lamont, E. Métral, D. Nisbet, G. Papotti, M. Pojer, L. Ponce, S. Redaelli, B. Salvachua, M. Schaumann, M. Solfaroli, R. Suykerbuyk, G. Trad, J. Uythoven, S. Uznanski, D. Walsh, J. Wenninger, and M. Zerlauth, “Operation and Performance of the CERN Large Hadron Collider During Proton Run 2”, in *Proc. 10th Int. Particle Accelerator Conf. (IPAC'19)*, Melbourne, Australia, May 2019, pp. 504–507. doi:[10.18429/JACoW-IPAC2019-MOPMP031](https://doi.org/10.18429/JACoW-IPAC2019-MOPMP031).
- [3] R. Bruce, N. Fuster-Martínez, A. Mereghetti, D. Mirarchi, and S. Redaelli, “Review of LHC run 2 machine configurations”, in *Proc. of the 9th Evian Workshop on LHC Beam Operation*, Evian-les-Bains, France, Jan. 2019, to be published.
- [4] S. Papadopoulou, F. Antoniou, I. Efthymiopoulos, M. Hostettler, G. Iadarola, N. Karastathis, S. Kostoglou, Y. Papaphilippou, and G. Trad, “Monitoring and modelling of the LHC emittance and luminosity evolution in 2018”, in *J. Phys.: Conf. Ser.* **1350**, Melbourne, Australia, May 2019, p. 012011, 2019. doi:[10.1088/1742-6596/1350/1/012011](https://doi.org/10.1088/1742-6596/1350/1/012011).
- [5] E. Métral *et al.*, “Update of the HL-LHC operational scenarios for proton operation”, CERN, Geneva, Switzerland, Rep. CERN-ACC-NOTE-2018-0002, Jan. 2018.
- [6] R. Schmidt, “Machine Protection and Interlock Systems for Circular Machines – Example for LHC”, in *Proc. of the 2014 Joint International Accelerator School: Beam Loss and Accelerator Protection*, Newport Beach, USA, Nov. 2014, pp. 319–342. doi:[10.5170/CERN-2016-002.319](https://doi.org/10.5170/CERN-2016-002.319).
- [7] X. Buffat, “Transverse beams stability studies at the Large Hadron Collider”, Ph.D. thesis, École polytechnique fédérale de Lausanne, Lausanne, Switzerland, 2015, CERN-THESIS-2014-246. doi:[10.5075/epfl-thesis-6321](https://doi.org/10.5075/epfl-thesis-6321).
- [8] B. Todd, L. Ponce, A. Apollonio, and D. Walsh, “LHC Availability 2018: Proton Run”, CERN, Geneva, Switzerland, Rep. CERN-ACC-NOTE-2018-0081, Dec. 2018.
- [9] R. Widerøe, “Über ein neues Prinzip zur Herstellung hoher Spannungen”, *Archiv für Elektrotechnik* **21**(4), pp. 387–406, 1928. doi:[10.1007/BF01656341](https://doi.org/10.1007/BF01656341).

- [10] A. Wolski, *Beam dynamics in high energy particle accelerators*. London, England: Imperial College Press, 2014. doi:[10.1142/p899](https://doi.org/10.1142/p899).
- [11] Goldstein, Safko, and Poole. *Classical Mechanics*. Pearson Education, 3rd edition, 2014.
- [12] N. Mounet, “Direct Vlasov Solvers”, in *Proc. CAS-CERN Accelerator School on Numerical Methods for Analysis, Design and Modelling of Particle Accelerators*, Thessaloniki, Greece, Nov. 2018, pp. 273–304, Rep. CERN-ACC-2020-0012.
- [13] A. Chao, *Physics of Collective Beam Instabilities in High Energy Accelerators*. New York, USA: John Wiley & Sons, Inc., 1994.
- [14] J. Gareyte, J. P. Koutchouk, and F. Ruggiero, “Landau damping, dynamic aperture and octupoles in LHC”, CERN, Geneva, Switzerland, Rep. CERN-LHC-PROJECT-REPORT-091, Feb. 1997.
- [15] S. V. Furusest, X. Buffat, E. Métral, D. Valuch, B. Salvant, D. Amorim, N. Mounet, M. Söderén, S. A. Antipov, T. Pieloni, and C. Tambasco, “MD3288: Instability latency with controlled noise”, CERN, Geneva, Switzerland, Rep. CERN-ACC-NOTE-2019-0011, Apr. 2019.
- [16] S. Fartoukh, “Achromatic telescopic squeezing scheme and its application to the LHC and its luminosity upgrade”, *Phys. Rev. ST Accel. Beams* **16**, p. 111002, 2013. doi:[10.1103/PhysRevSTAB.16.111002](https://doi.org/10.1103/PhysRevSTAB.16.111002).
- [17] W. Herr and T. Pieloni, “Beam-beam effects”, in *Proc. CAS-CERN Accelerator School on Advanced Accelerator Physics*, Trondheim, Norway, Aug. 2013, pp. 431–459. doi:[10.5170/CERN-2014-009.431](https://doi.org/10.5170/CERN-2014-009.431).
- [18] G. V. Stupakov, V. V. Parkhomchuk, and V. D. Shiltsev, “Decoherence of a Gaussian Beam Due to Beam-Beam Interaction”, Rep. SSCL-Preprint-495, Aug. 1993.
- [19] K. Yokoya and H. Koiso, “Tune shift of coherent beam-beam oscillations”, *Particle Accelerators* **27**, pp. 181–186, 1990.
- [20] P. Baudrenghien and T. Mastoridis, “Transverse emittance growth due to rf noise in the high-luminosity LHC crab cavities”, *Phys. Rev. Accel. Beams* **18**, p. 101001, 2015. doi:[10.1103/PhysRevSTAB.18.101001](https://doi.org/10.1103/PhysRevSTAB.18.101001).
- [21] M. Dohlus and R. Wanzenberg, “An introduction to wake fields and impedances”, in *Proc. CAS-CERN Accelerator School on Intensity Limitations in Particle Beams* **3**, CERN, Geneva, Switzerland, Nov. 2015, pp. 15–41. doi:[10.23730/CYRSP-2017-003.15](https://doi.org/10.23730/CYRSP-2017-003.15).
- [22] N. Mounet, “Vlasov Solvers and Macroparticle Simulations”, in *Proc. ICFA Mini-Workshop on Impedances and Beam Instab. in Part. Accel.*, Benevento, Italy, Sep. 2017, pp. 77–85, CERN-2018-003-CP.
- [23] W. Höfle, F. Dubouchet, G. Kotzian, and D. Valuch, “Performance of the LHC Transverse Damper with Bunch Trains”, in *Proc. 4th Int. Particle Accelerator Conf.*, Shanghai, China, May 2013, paper WEPME043, pp. 3022–3024.

-
- [24] R. J. Steinhagen, “LHC Beam Stability and Feedback Control”, Ph.D. thesis, RWTH Aachen University, Aachen, Germany, 2007, Rep. CERN-Thesis-2007-058.
- [25] G. Kotzian, “Possibilities for Transverse Feedback Phase Adjustment by Means of Digital Filters”, in *Proc. 8th Int. Particle Accelerator Conf.*, Copenhagen, Denmark, May 2017, pp. 1924–1927. doi:[10.18429/JACoW-IPAC2017-TUPIK095](https://doi.org/10.18429/JACoW-IPAC2017-TUPIK095).
- [26] J. Komppula, X. Buffat, G. Kotzian, K. Li, and D. Valuch, “MD4036: New ADT signal processing for large tune acceptance”, CERN, Geneva, Switzerland, Rep. CERN-ACC-NOTE-2019-0008, May 2019.
- [27] G. Sterbini, A. Blas, and S. Gilardoni, “Beam-based performance of the CERN PS transverse feedback”, in *Proc. of the 54th ICFA Advanced Beam Dynamics Workshop on High-Intensity, High Brightness and High Power Hadron Beams*, East-Lansing, MI, USA, Nov. 2014, paper MOPAB10.
- [28] L. Landau, “On the vibrations of the electronic plasma”, *J.Phys.(USSR)* **10**, pp. 25–34, 1946. doi:[10.1016/B978-0-08-010586-4.50066-3](https://doi.org/10.1016/B978-0-08-010586-4.50066-3).
- [29] J. Rees and A. Chao, “Landau Damping Revisited*”, SLAC, Stanford, CA, USA, Rep. SLAC-PUB-13469, Nov. 2008.
- [30] W. Herr, “Introduction to Landau damping”, in *Proc. CAS-CERN Accelerator School on Intensity Limitations in Particle Beams* **3**, CERN, Geneva, Switzerland, Nov. 2015. doi:[10.23730/CYRSP-2017-003.137](https://doi.org/10.23730/CYRSP-2017-003.137).
- [31] A. A. Vlasov, “On the kinetic theory of an assembly of particles with collective interaction”, *Russ. Phys. J.* **9**, pp. 25–40, 1945.
- [32] G. Besnier, “Contribution à La Théorie de La Stabilité Des Oscillations Longitudinales d’un Faisceau Accéléré En Régime de Charge d’espace”, Ph.D. thesis, Université de Rennes, Rennes, France, 1978.
- [33] J. S. Berg, “Coherent modes for multiple non-rigid bunches in a storage ring”, Ph.D. thesis, Stanford University, Stanford, CA, 1996, SLAC-REPORT-478.
- [34] J. S. Berg and F. Ruggiero, “Landau damping with two-dimensional betatron tune spread”, CERN, Geneva, Switzerland, Rep. CERN-SL-AP-96-071-AP, Dec. 1996.
- [35] X. Buffat, W. Herr, N. Mounet, T. Pieloni, and S. White, “Stability diagrams of colliding beams in the Large Hadron Collider”, *Phys. Rev. ST Accel. Beams* **17**, p. 111002, 2014. doi:[10.1103/PhysRevSTAB.17.111002](https://doi.org/10.1103/PhysRevSTAB.17.111002).
- [36] L. Vos, “Ground motion in LEP and LHC”, in *Proc. of Particle Accelerators Conf.* **50**, pp. 221–231, 1995.
- [37] CERN Converter-Concepts (2018). http://te-epc-lpc.web.cern.ch/te-epc-lpc/concepts/converters/emc/emc_emissions.stm/. (accessed 28 Aug. 2020).
- [38] S. Kostoglou, “Noise effects in the Large Hadron Collider (LHC) and its High-Luminosity upgrade (HL-LHC)”, Ph.D. thesis, National Technical University of Athens, Athens, Greece, 2020, Rep. CERN-THESIS-2020-169.

- [39] M. Morrone, M. Martino, R. De Maria, M. Fitterer, and C. Garion, “Magnetic frequency response of High-Luminosity Large Hadron Collider beam screens”, *Phys. Rev. Accel. Beams* **22**, p. 013501, 2019. doi:[10.1103/PhysRevAccelBeams.22.013501](https://doi.org/10.1103/PhysRevAccelBeams.22.013501).
- [40] V. M. Juravlev, I. H. Wilson, A. Seryi, G. Ramseier, W. Coosemans, and A. I. Slepsov, “Investigations of power and spatial correlation characteristics of seismic vibrations in the CERN LEP tunnel for linear collider studies”, CERN, Geneva, Switzerland, Rep. CERN-SL/93-53, Dec. 1993.
- [41] X. Buffat, W. Herr, T. Pieloni, and D. Valuch, “Modeling of the emittance growth due to decoherence in collision at the Large Hadron Collider”, *Phys. Rev. Accel. Beams* **23**, p. 021002, 2020. doi:[10.1103/PhysRevAccelBeams.23.021002](https://doi.org/10.1103/PhysRevAccelBeams.23.021002).
- [42] X. Buffat, J. Barranco Garcia, M. Solfaroli Camillocci, P. S. Papadopolou, S. V. Furuseth, R. Suykerbuyk, D. Valuch, D. J. Walsh, L. Ponce, S. Kostoglou, T. Pieloni, and B. M. Salvachua Ferrando, “Impact of the ADT on the Beam Quality with High Brightness Beams in Collision (MD2155)”, CERN, Geneva, Switzerland, Rep. CERN-ACC-NOTE-2018-0005, Feb. 2018.
- [43] A. Piwinski, “Intra-beam-scattering”, in *Proc. 9th Int. Conf. on High Energy Accelerators*, Stanford, CA, USA, May 1974, p. 405. doi:[10.5170/CERN-1992-001.226](https://doi.org/10.5170/CERN-1992-001.226).
- [44] K. Wille, “Synchrotron radiation”, presented at Joint Universities Accelerator School, Archamps, France, Jan. 2013, unpublished.
- [45] N. Wiener, “Generalized Harmonic Analysis”, *Acta Mathematica* **55**, pp. 117–258, 1930. doi:[10.1007/bf02546511](https://doi.org/10.1007/bf02546511).
- [46] M. Lonza, “Multi-bunch feedback systems”, in *Proc. CAS-CERN Accelerator School on Digital Signal Processing*, Sigtuna, Sweden, May 2007, pp. 285–320. doi:[10.5170/CERN-2008-003.285](https://doi.org/10.5170/CERN-2008-003.285).
- [47] D. Möhl, “Sources of emittance growth”, in *Proc. CAS-CERN Accelerator School on Intermediate Accelerator Physics*, Zeuthen, Germany, Sep. 2006, pp. 245–270. doi:[10.5170/CERN-2006-002.245](https://doi.org/10.5170/CERN-2006-002.245).
- [48] V. A. Lebedev, “Emittance growth due to noise and its suppression with the feedback system in large hadron colliders”, in *Proc. Accelerator physics at the Superconducting Super Collider*, Dallas, Texas, USA, Feb. 1995, pp. 396–423. doi:[10.1063/1.47298](https://doi.org/10.1063/1.47298).
- [49] Y. Alexahin, “On the Landau Damping and Decoherence of Transverse Dipole Oscillations in Colliding Beams”, *Particle Accelerators* **59**, pp. 43–74, 1998. Rep. CERN-SL-96-064-AP.
- [50] S. V. Furuseth and X. Buffat, “Loss of transverse Landau damping by noise and wakefield driven diffusion”, *Phys. Rev. Accel. Beams* **23**, p. 114401, Nov. 2020. doi:[10.1103/PhysRevAccelBeams.23.114401](https://doi.org/10.1103/PhysRevAccelBeams.23.114401).
- [51] Y. H. Chin, “Hamiltonian formulation for transverse bunched beam instabilities in the presence of Betatron tune spread”, CERN, Geneva, Switzerland, Rep. CERN-SPS-85-9-DI-MST, May 1985.

-
- [52] S. V. Furuseth and X. Buffat, “Long-term evolution of Landau damping in the presence of transverse noise, feedback, and detuning”, *Phys. Rev. Accel. Beams* **23**, p. 034401, Mar. 2020. doi:[10.1103/PhysRevAccelBeams.23.034401](https://doi.org/10.1103/PhysRevAccelBeams.23.034401).
- [53] X. Buffat, G. Arduini, D. Amorim, S. Antipov, N. Biancacci, L. Carver, S. V. Furuseth, G. Iadarola, K. Li, L. Methner, E. Métral, N. Mounet, A. Oeftiger, A. Romano, G. Rumolo, B. Salvant, M. Schenk, T. Pieloni, and C. Tambasco, “Transverse instabilities”, in *Proc. of the 9th Evian Workshop on LHC Beam Operation*, Evian-les-Bains, France, Jan. 2019, to be published.
- [54] D. Amorim, “Study of the Transverse Mode Coupling Instability in the CERN Large Hadron Collider”, Ph.D. thesis, Université Grenoble Alpes, Grenoble, France, 2019, CERN-THESIS-2019-272.
- [55] L. R. Carver, G. Arduini, D. Astapovych, M. Barnes, J. Barranco, N. Biancacci, X. Buffat, H. Day, W. Hofle, G. Iadarola, G. Kotzian, T. Levens, K. Li, E. Métral, V. Namora, T. Persson, T. Pieloni, G. Rumolo, B. Salvant, M. Schenk, C. Tambasco, R. Tomás, D. Valuch, L. Vega Cid, N. Wang, and W. Weterings, “Instabilities and beam induced heating in 2015”, in *Proc. of the 6th Evian Workshop on LHC Beam Operation*, Evian-les-Bains, France, Dec. 2015, pp. 95–100.
- [56] L. Carver, B. Salvant, T. Pieloni, J. Barranco, T. Lefèvre, N. Wang, E. Métral, W. Höfle, X. Buffat, N. Biancacci, G. Kotzian, C. Tambasco, T. Levens, and M. Zobov, “Current Status of Instability Threshold Measurements in the LHC at 6.5 TeV”, in *Proc. 7th Int. Particle Accelerator Conf. (IPAC’16)*, Busan, South-Korea, May 2016, pp. 1434–1437. doi:[10.18429/JACoW-IPAC2016-TUPMW011](https://doi.org/10.18429/JACoW-IPAC2016-TUPMW011).
- [57] X. Buffat, G. Arduini, D. Amorim, S. Antipov, L. Barraud, N. Biancacci, L. Carver, F. Giordano, G. Iadarola, K. Li, G. Mazzacano, E. Métral, A. Romano, B. Salvant, M. Schenk, M. Söderén, D. Valuch, L. Methner, T. Pieloni, and C. Tambasco, “Our understanding of transverse instabilities and mitigation tools/strategy”, in *Proc. of the 8th Evian workshop on LHC Beam Operation*, Evian-les-Bains, France, Dec. 2017.
- [58] X. Buffat, D. Amorim, S. Antipov, L. Carver, N. Biancacci, S. V. Furuseth, T. Levens, E. Métral, N. Mounet, T. Pieloni, B. Salvant, M. Söderén, C. Tambasco, and D. Valuch, “The impact of noise on beam stability”, presented at the 8th HL-LHC Collaboration Meeting, CERN, Geneva, Switzerland, Oct. 2018, unpublished.
- [59] M. Solfaroli, T. Persson, and X. Buffat, private communication.
- [60] S. V. Furuseth, D. Amorim, S. A. Antipov, X. Buffat, N. Mounet, E. Métral, T. Pieloni, B. Salvant, and C. Tambasco, “Instability Latency in the LHC”, in *Proc. 10th Int. Particle Accelerator Conf. (IPAC’19)*, Melbourne, Australia, May 2019, pp. 3204–3207. doi:[10.18429/JACoW-IPAC2019-WEPTS044](https://doi.org/10.18429/JACoW-IPAC2019-WEPTS044).
- [61] G. Trad, A. Alexopoulos, E. Bravin, D. Butti, R. Kieffer, F. Roncarolo, S. Vlachos, and B. Wurkner, “LHC emittance measurements in Run II”, in *Proc. of the 9th Evian Workshop on LHC Beam Operation*, Evian-les-Bains, France, Jan. 2019, to be published.

- [62] S. V. Furuseth and X. Buffat, “Change of beam distribution due to decoherence in the presence of transverse feedback”, in *J. Phys.: Conf. Ser.* **1350**, Melbourne, Australia, May 2019, p. 012118. doi:[10.1088/1742-6596/1350/1/012118](https://doi.org/10.1088/1742-6596/1350/1/012118).
- [63] H. Risken and T. Frank, *The Fokker-Planck Equation: Methods of Solution and Applications*. Berlin, Heidelberg, New York: Springer-Verlag, 1996.
- [64] D. Möhl, G. Petrucci, L. Thorndahl, and S. van der Meer, “Physics and technique of stochastic cooling”, *Physics Reports* **58**, pp. 73–102, 1980. doi:[10.1016/0370-1573\(80\)90140-4](https://doi.org/10.1016/0370-1573(80)90140-4).
- [65] S. Paret and J. Qiang, “Simulation of Colliding Beams with Feedback in LHC”, in *Proc. 3rd Int. Particle Accelerator Conf. (IPAC’12)*, New Orleans, LA, USA, May 2012, paper TUPPC091, pp. 1374–1376.
- [66] N. Mounet, “The LHC Transverse Coupled-Bunch Instability”, Ph.D. thesis, École polytechnique fédérale de Lausanne, Lausanne, Switzerland, 2012, CERN-THESIS-2012-055. doi:[10.5075/epfl-thesis-5305](https://doi.org/10.5075/epfl-thesis-5305).
- [67] E. Métral and A. Verdier, “Stability diagram for Landau damping with a beam collimated at an arbitrary number of sigmas”, CERN, Geneva, Switzerland, Rep. CERN-AB-2004-019-ABP, Feb. 2004.
- [68] G. Arduini, “Potential performance reach for the HL-LHC in case of a depleted beam halo”, presented at the Review of the needs for a hollow e-lens for the HL-LHC, CERN, Geneva, Switzerland, Oct. 2016, unpublished.
- [69] S. V. Furuseth and X. Buffat, “Noise and possible loss of Landau damping – Noise Excited Wakefields”, in *Proc. of ICFA mini workshop on Mitigation of Coherent Beam Instabilities in particle accelerators*, Zermatt, Switzerland, Sep. 2019, pp. 262–269, Rep. CERN-2020-009. doi:[10.23732/CYRCP-2020-009](https://doi.org/10.23732/CYRCP-2020-009).
- [70] K. Y. Ng, *Physics of Intensity Dependent Beam Instabilities*. Singapore: World Scientific Publishing Co. Pte. Ltd., 2006.
- [71] J. L. Laclare, “Introduction to coherent instabilities – Coasting beam case”, in *Proc. CAS-CERN Accelerator School on General Accelerator Physics v.2*, Gif-sur-Yvette, France, Sep. 1984, pp. 377–414. doi:[10.5170/CERN-1985-019-V-2.377](https://doi.org/10.5170/CERN-1985-019-V-2.377).
- [72] N. G. Van Kampen, “On the theory of stationary waves in plasmas”, *Physica* **21**(6), pp. 949–963, 1955. doi:[10.1016/S0031-8914\(55\)93068-8](https://doi.org/10.1016/S0031-8914(55)93068-8).
- [73] Y. Chin and K. Yokoya, “Nonlinear perturbation approach to bunch lengthening and blow-up of energy spread”, *Nucl. Instrum. Methods Phys. Res.* **226**(23), pp. 223–249, 1984. doi:[10.1016/0168-9002\(84\)90037-8](https://doi.org/10.1016/0168-9002(84)90037-8).
- [74] A. Bazzani, S. Siboni, and G. Turchetti, “Diffusion in Hamiltonian systems with a small stochastic perturbation”, *Physica D* **76**, pp. 8–21, 1994. doi:[10.1016/0167-2789\(94\)90246-1](https://doi.org/10.1016/0167-2789(94)90246-1).

-
- [75] A. Bazzani and L. Beccaceci, “Diffusion in Hamiltonian systems driven by harmonic noise”, *J. Phys. A: Math. Gen.* **31**, pp. 5843–5854, 1998. doi:[10.1088/0305-4470/31/28/004](https://doi.org/10.1088/0305-4470/31/28/004).
- [76] S. V. Furuseth, X. Buffat, T. Pieloni, W. Herr, and F. Jones (2019), COMBIp (COherent Multi-Bunch Interactions – Pipelined). Source code: <https://gitlab.cern.ch/sfuruset/combip/>. (accessed: 11 Jan. 2020).
- [77] F. W. Jones, W. Herr, and T. Pieloni, “Parallel beam-beam simulation incorporating multiple bunches and multiple interaction regions”, in *Proc. Particle Accelerator Conf. (PAC’07)*, Albuquerque, New Mexico, USA, Jun. 2007, pp. 3235–3237. doi:[10.1109/PAC.2007.4440383](https://doi.org/10.1109/PAC.2007.4440383).
- [78] J. Coello de Portugal, Harpy. http://pylh.c.github.io/Beta-Beat.src/harmonic_analysis/. (accessed 28 Oct. 2019).
- [79] S. V. Furuseth and X. Buffat, “Parallel high-performance multi-beam multi-bunch simulations”, *Computer Physics Communications* **244**, pp. 180–186, Nov. 2019. doi:[10.1016/j.cpc.2019.06.006](https://doi.org/10.1016/j.cpc.2019.06.006).
- [80] H. Shan, E. Strohmaier, and J. Qiang, “Performance analysis of leading HPC architectures with Beambeam3D”, *Int. J. High Perform. Comput. Appl.* **22**, pp. 21–32, 2008. doi:[10.1177/1094342006085024](https://doi.org/10.1177/1094342006085024).
- [81] E. Métral, T. Argyropoulos, H. Bartosik, N. Biancacci, X. Buffat, J. F. Esteban Muller, W. Herr, G. Iadarola, A. Lasheen, K. Li, A. Oeftiger, T. Pieloni, D. Quartullo, G. Rumolo, B. Salvant, M. Schenk, E. Shaposhnikova, C. Tambasco, H. Timko, C. Zannini, A. Burov, D. Banfi, J. Barranco, N. Mounet, O. Boine-Frankenheim, U. Niedermayer, V. Kornilov, and S. White, “Beam instabilities in hadron synchrotrons”, *IEEE Trans. on Nucl. Sci.* **63**(2), pp. 1001–1050, 2016. doi:[10.1109/TNS.2015.2513752](https://doi.org/10.1109/TNS.2015.2513752).
- [82] S. V. Furuseth and X. Buffat, “Modeling of nonlinear effects due to head-on beam-beam interactions”, *Phys. Rev. Accel. Beams* **21**, p. 081002, 2018. doi:[10.1103/PhysRevAccelBeams.21.081002](https://doi.org/10.1103/PhysRevAccelBeams.21.081002).
- [83] T. Pieloni, “A study of beam-beam effects in hadron colliders with a large number of bunches”, Ph.D. thesis, École polytechnique fédérale de Lausanne, Lausanne, Switzerland, 2008. doi:[10.5075/epfl-thesis-4211](https://doi.org/10.5075/epfl-thesis-4211).
- [84] W. Clark, W. N. Polakov, and F. W. Trabold, *The Gantt chart, a working tool of management*. New York, USA: The Ronald press company, 1922.
- [85] Scientific IT and Application Support, Deneb (2018). <https://scitas.epfl.ch/hardware/deneb/>. (accessed 1 Jun. 2018).
- [86] P. S. Pacheco, *An Introduction to Parallel Programming*. Amsterdam, Netherlands: Elsevier Inc., 2011.
- [87] S. V. Furuseth, X. Buffat, J. S. Pereira-Cubillo, and D. Valuch, “Emittance growth suppression with a multibunch feedback in high-energy hadron colliders: Numerical optimization of the gain and bandwidth”, submitted for publication.

Bibliography

- [88] X. Buffat, M. Söderén, D. Valuch, J. P. O. Komppula, and S. V. Furuseth, “Emittance growth in collision with optimised ADT settings (MD3291)”, CERN, Geneva, Switzerland, Rep. CERN-ACC-NOTE-2019-0028, Jul. 2019.
- [89] W. Herr, M. P. Zorzano, and F. Jones, “Hybrid fast multipole method applied to beam-beam collisions in the strong-strong regime”, *Phys. Rev. Accel. Beams* **4**, p. 054402, 2001. doi:[10.1103/PhysRevSTAB.4.054402](https://doi.org/10.1103/PhysRevSTAB.4.054402).
- [90] J. S. Pereira-Cubillo and S. V. Furuseth, “Non-white transverse noise in COMBIp”, CERN, Geneva, Switzerland, Rep. CERN-STUDENTS-Note-2019-116, Aug. 2019.
- [91] J. Tückmantel, “Digital Generation of Noise-signals with Arbitrary Constant or Time-varying Spectra”, in *Proc. 11th European Particle Accelerator Conf. (EPAC’08)*, Genoa, Italy, Jun. 2008, paper TUPC103, pp. 1299–1301.
- [92] F. Dubouchet, W. Höfle, G. Kotzian, and D. Valuch, ““What you get” – Transverse damper”, in *Proc. of the 4th Evian workshop on LHC Beam Operation*, Evian-les-Bains, France, Dec. 2012, pp. 73–78.
- [93] V. Lebedev, “Transverse dampers with ultimate gain for suppression of instabilities in Large Hadron Colliders”, in *Proc. of ICFA mini workshop on Mitigation of Coherent Beam Instabilities in particle accelerators*, Zermatt, Switzerland, Sep. 2019, pp. 203–210, Rep. CERN-2020-009. doi:[10.23732/CYRCP-2020-009](https://doi.org/10.23732/CYRCP-2020-009).
- [94] A. Einstein, “Über die von der molekularkinetischen Theorie der Wärme geforderte Bewegung von in ruhenden Flüssigkeiten suspendierten Teilchen”, *Annalen der Physik* **322**(8), pp. 549–560, 1905. doi:[10.1002/andp.19053220806](https://doi.org/10.1002/andp.19053220806).
- [95] F. Sattin, “Fick’s law and Fokker-Planck equation in inhomogeneous environments”, *Phys. Rev. Lett. A* **372**(22), pp. 3941–3945, 2008. doi:[10.1016/j.physleta.2008.03.014](https://doi.org/10.1016/j.physleta.2008.03.014).
- [96] S. V. Furuseth (2020), PyRADISE (Python RAdial Diffusion and Stability Evolution). Source code: <https://gitlab.cern.ch/sfuruset/pyradise/>. (accessed: 9 Oct. 2020).
- [97] A. Quarteroni. *Numerical Models for Differential Problems*. Milan, Italy: Springer-Verlag, 2nd edition, 2014.
- [98] `scipy.integrate.solve_ivp`. https://docs.scipy.org/doc/scipy/reference/generated/scipy.integrate.solve_ivp.html. (accessed 28 Oct. 2019).
- [99] R. Tomás, X. Buffat, S. White, J. Barranco, P. Gonçalves Jorge, and T. Pieloni, “Beam-beam amplitude detuning with forced oscillations”, *Phys. Rev. Accel. Beams* **20**, p. 101002, 2017. doi:[10.1103/PhysRevAccelBeams.20.101002](https://doi.org/10.1103/PhysRevAccelBeams.20.101002).
- [100] S. Peggs and C. Tang, “Nonlinear diagnostics using an AC dipole”, BNL, New York, USA, Rep. RHIC/AP/159, Oct. 1998.

Sondre Vik FURUSETH

NATIONALITY: Norwegian
PHONE: +47 41 24 06 09
EMAIL: s.v.furuseth@gmail.com

Key Qualities

Natural quick learner, developed further through studying physics at NTNU, MIT, EPFL and CERN.
Creative problem solver, considering various approaches and using techniques from different fields.
Responsible and structured, from combining academia, sports, coaching and more at one time.
Compassionate and helpful. Improved pedagogically by several teaching and coaching positions.
Experienced team player from professional projects, student organizations, and team sports.

Education

01.2018 – 12.2020	Doctor of Philosophy in Physics at École Polytechnique Fédérale de Lausanne (EPFL), Switzerland Thesis: “Transverse Noise, Decoherence, and Landau damping in High-Energy Hadron Colliders”. Advisors: Prof. Olivier Schneider, Prof. Leonid Rivkin, Dr. Xavier Buffat. The thesis was written on a project in collaboration with CERN.
08.2012 – 08.2017	Master of Science in Physics and Mathematics at Norwegian University of Science and Technology (NTNU), Norway Thesis: “Head-On Beam-Beam Interactions in High-Energy Hadron Colliders: GPU-Powered Modelling of Nonlinear Effects”. Advisors: Prof. Jon Andreas Støvneng, Dr. Xavier Buffat. The thesis was written on a project in collaboration with CERN.
08.2015 – 01.2016	Exchange semester during Master studies at Massachusetts Institute of Technology (MIT), USA Taking graduate classes in physics during an exchange semester. The classes were incorporated into my Master’s degree from NTNU.

Industrial Research Experience

06.2015 – 08.2015 & 06.2014 – 08.2014	Statoil research facility, Norway <i>Research intern</i> Working on the problem of oil well integrity, and whether the integrity will remain also after the well has been closed for production. Year 1: Introductory training in O&G industry and research. Active development of 2D and 3D Comsol models for ultrasonic cement evaluation within well integrity. Year 2: Active development and use of Matlab software, intended to analyze data from well integrity logs. Worked with big data sets. Part of a multinational team.
--	---

Teaching Experience

06.2019 – 08.2019	European Organization for Nuclear Research (CERN), Switzerland <i>Supervisor</i> Supervised a student working on a scientific project relevant to my research at CERN. The outcome was a numerical generator of non-white noise signals in C.
09.2018 – 12.2018	École Polytechnique Fédérale de Lausanne (EPFL), Switzerland <i>Student assistant in PHYS-448: Introduction to particle accelerators</i> Helped students with their mandatory exercises and answered questions on different aspects of the curriculum.
05.2014 & 05.2015	Energikontakten, Norway <i>Lecturer at Exam course</i> Held lectures over 14 hours to prepare students for their exam in TMA4105, Calculus 2, at NTNU. Covered the most important curriculum and calculated previous exam problems.
09.2013 – 05.2016	Norwegian University of Science and Technology (NTNU), Norway <i>Student assistant in TFY4104, TFY4155, TMA4105, TMA4120, TMA4320</i> Helped students with their mandatory exercises, answered questions on different aspects of the curriculum, and graded their work.
09.2013 – 05.2014	ENT3R Trondheim, Norway <i>Mentor</i> Mentored students at upper secondary school. Helped them with mathematics and physics, and motivated them to continue with further studies in science.
08.2011 – 08.2013	Sandvika VGS <i>Teacher</i> Worked as a math teacher in a 1-week intensive summer school, three summers in a row, at a Norwegian upper secondary high school. The students either wanted a sneak peek on next year's curriculum, needed to restudy last year's curriculum, or had been a year abroad and needed to cover what they had missed.

Awards & Scholarships

08.2018	"Best Siv.ing./Siv.ark. at NTNU" Winnie og Ragnar Mathisens Høgskolefond Award and scholarship for having the best diploma among all the students that graduated with a degree of Siv.ing. or Siv.ark. (technological master's degree) from NTNU in 2017.
05.2017 & 05.2019	Generaldirektør Rolf Østbyes stipendfond ved NTNU Scholarship for young masters of science and technology, who graduated from NTNU, to continue their education and research abroad.
05.2017	Forsknings- og undervisningsfondet i Trondheim Scholarship to cover travel expenses to well renowned, international institutions, during Master studies in Trondheim.
05.2017	"Best Masters student of Technology 2017" Award for having the best grades among the ~ 400 graduating master students at the faculty of Natural Sciences at NTNU, prior to handing in the masters thesis.
05.2017 & 05.2018	Jansons legat Scholarship to men or women who have shown positive abilities or initiative beyond the ordinary.

Invited Talks

09.06.2020	<p>“Numerical search for optimal damper settings in collision in LHC and HL-LHC”</p> <p>Specialist talk on parallel modeling of the full LHC, applying a hybrid OpenMP-MPI code. Physics case studied was the search for optimal active transverse beam feedback settings. At “HPC user workshop” at CERN.</p>
26.09.2019	<p>“Noise and possible loss of Landau damping – Noise excited wakefields”</p> <p>Specialist talk on a new destabilizing effect in circular hadron colliders. At ICFA mini-Workshop on “Mitigation of Coherent Beam Instabilities in particle accelerators”, MCBI, Zermatt, 2019.</p>
18.07.2017	<p>“GPU-accelerated Weak-Strong Simulations of head-on beam-beam effects”</p> <p>Colloquium talk, topic of peripheral interest to the inviting party.</p> <p>Invited by Helmholtz Young Investigator Group on Hybrid gyrokinetic computations for weakly magnetized plasmas in nature and the laboratory, at the Max Planck Institute for Plasma Physics (IPP) in Garching.</p>

Technical Skills

Operating systems	Windows, Ubuntu : Advanced
Prog. languages	Matlab, Python , C, C++, Fortran: Advanced Octave: Experienced
Other programs	Latex, Inkscape, Comsol, Labview
General experience	MPI, OpenMP, CUDA, CFD, Particle tracking

Other

Languages	Norwegian:	Mother tongue
	English:	Fluent in written and oral. Level C2 (IELTS, 2015)
	French:	Intermediate (Reading, Writing), Basic (oral). A2. (Supercomm, 2018)
Sports	American Football:	I have played American football for 8 years, at Oslo Vikings U19, NTNUI Domers Elite, Geneva Whoppers Elite. Periodically on Norways national team.
	Handball:	I have played handball for 13 years, including two years at the elite program in Haslum HK. This has also led me to be a coach.

Publication List

Peer-reviewed Articles

1. S. V. Furuseth and X. Buffat, “Loss of transverse Landau damping by noise and wakefield driven diffusion”, *Phys. Rev. Accel. Beams* **23**, p. 114401, Nov. 2020.
doi:[10.1103/PhysRevAccelBeams.23.114401](https://doi.org/10.1103/PhysRevAccelBeams.23.114401)
2. S. V. Furuseth, X. Buffat, J. S. Pereira-Cubillo, and D. Valuch, “Emittance growth suppression with a multibunch feedback in high-energy hadron colliders: Numerical optimization of the gain and bandwidth”, submitted for publication.
3. S. V. Furuseth and X. Buffat, “Noise and possible loss of Landau damping – Noise Excited Wakefields”, in *Proc. of ICFA mini workshop on Mitigation of Coherent Beam Instabilities in particle accelerators*, Zermatt, Switzerland, pp. 262–269, Sep. 2019, Rep. CERN-2020-009.
doi:[10.23732/CYRCP-2020-009](https://doi.org/10.23732/CYRCP-2020-009)
4. S. V. Furuseth and X. Buffat, “Long-term evolution of Landau damping in the presence of transverse noise, feedback, and detuning”, *Phys. Rev. Accel. Beams* **23**, p. 034401, Mar. 2020.
doi:[10.1103/PhysRevAccelBeams.23.034401](https://doi.org/10.1103/PhysRevAccelBeams.23.034401)
5. S. V. Furuseth and X. Buffat, “Parallel high-performance multi-beam multi-bunch simulations”, *Computer Physics Communications* **244**, pp. 180–186, Nov. 2019.
doi:[10.1016/j.cpc.2019.06.006](https://doi.org/10.1016/j.cpc.2019.06.006)
6. S. V. Furuseth and X. Buffat, “Change of beam distribution due to decoherence in the presence of transverse feedback”, *J. Phys.: Conf. Ser.* **1350**, p. 012118, May 2019.
doi:[10.1088/1742-6596/1350/1/012118](https://doi.org/10.1088/1742-6596/1350/1/012118)
7. S. V. Furuseth and X. Buffat, “Modeling of nonlinear effects due to head-on beam-beam interactions”, *Phys. Rev. Accel. Beams* **21**, p. 081002, Aug. 2018.
doi:[10.1103/PhysRevAccelBeams.21.081002](https://doi.org/10.1103/PhysRevAccelBeams.21.081002)

Conference Articles

1. S. V. Furuseth, D. Amorim, S. A. Antipov, X. Buffat, N. Mounet, E. Métral, B. Salvant, T. Pieloni, and C. Tambasco, “Instability Latency in the LHC”, in *Proc. 10th Int. Particle Accelerator Conf. (IPAC’19)*, Melbourne, Australia, May 2019, pp. 3204–3207.
doi:[10.18429/JACoW-IPAC2019-WEPTS044](https://doi.org/10.18429/JACoW-IPAC2019-WEPTS044)
2. S. V. Furuseth and X. Buffat, “High-Performance Scheduling of Multi-Beam Multi-Bunch Simulations”, in *Proc. 10th Int. Particle Accelerator Conf. (IPAC’19)*, Melbourne, Australia, May 2019, pp. 3208–3211. doi:[10.18429/JACoW-IPAC2019-WEPTS045](https://doi.org/10.18429/JACoW-IPAC2019-WEPTS045)
3. X. Buffat, G. Arduini, D. Amorim, S. Antipov, N. Biancacci, L. Carver, S. V. Furuseth, G. Iadarola, K. Li, L. Methner, E. Métral, N. Mounet, A. Oeftiger, A. Romano, G. Rumolo, B. Salvant, M. Schenk, T. Pieloni, and C. Tambasco, “Transverse instabilities”, in *Proc. 9th LHC Operations Evian Workshop*, Evian-les-Bains, France, Jan. 2019.
4. J. Barranco, T. Pieloni, C. Tambasco, X. Buffat, and S. V. Furuseth, “Beam-Beam Studies for FCC-hh”, in *Proc. 8th Int. Particle Accelerator Conf. (IPAC’17)*, Copenhagen, Denmark, May 2017, pp. 2109–2112. doi:[10.18429/JACoW-IPAC2017-TUPVA026](https://doi.org/10.18429/JACoW-IPAC2017-TUPVA026)

Reports

1. X. Buffat, M. Söderén, D. Valuch, J. P. O. Komppula, and S. V. Furuseth, “Emittance growth in collision with optimised ADT settings (MD3291)”, CERN, Geneva, Switzerland, Rep. CERN-ACC-NOTE-2019-0028, Jul. 2019. <https://cds.cern.ch/record/2682944>
2. M. Benedikt *et al.* (eds.), “FCC-hh: The Hadron Collider”, *Eur. Phys. J. Spec. Top.* **228**, pp. 755–1107, 2019. doi:[10.1140/epjst/e2019-900087-0](https://doi.org/10.1140/epjst/e2019-900087-0)
3. F. Zimmermann *et al.* (eds.), “HE-LHC: The high-energy large hadron collider”, *Eur. Phys. J. Spec. Top.* **228**, pp. 1109–1382, 2019. doi:[10.1140/epjst/e2019-900088-6](https://doi.org/10.1140/epjst/e2019-900088-6)
4. X. Buffat, M. Albert, D. Amorim, S. Antipov, G. Crockford, S. V. Furuseth, J. P. O. Komppula, G. Kotzian, N. Mounet, A. Oeftiger, B. Salvant, M. Söderén, G. Trad, and D. Valuch, “Noise studies with new ADT pickups (MD4143)”, CERN, Geneva, Switzerland, Rep. CERN-ACC-NOTE-2019-0026, Jul. 2019. <https://cds.cern.ch/record/2682939>
5. X. Buffat, D. Amorim, S. Antipov, H. Bartosik, G. Crockford, S. V. Furuseth, G. Iadarola, T. Levens, E. Métral, N. Mounet, S. Uznanski, B. Salvant, M. Schaumann, and D. J. Walsh, “Intensity dependance of the train instability threshold and high pile-up test with 12b trains (MD3294)”, CERN, Geneva, Switzerland, Rep. CERN-ACC-NOTE-2019-0027, Mar. 2019. <https://cds.cern.ch/record/2682943>
6. S. V. Furuseth, X. Buffat, E. Métral, D. Valuch, B. Salvant, D. Amorim, N. Mounet, M. Söderén, S. Antipov, T. Pieloni, and C. Tambasco, “MD3288: Instability latency with controlled noise”, CERN, Geneva, Switzerland, Rep. CERN-ACC-NOTE-2019-0011, Mar. 2019. <https://cds.cern.ch/record/2670123>
7. X. Buffat, S. V. Furuseth, S. Kostoglou, B. M. Salvachua Ferrando, P. S. Papadopoulou, L. Ponce, M. Solfaroli Camillocci, R. Suykerbuyk, D. Valuch, D. J. Walsh, J. Barranco Garcia, and T. Pieloni, “Impact of the ADT on the beam quality with high brightness beams in collision (MD2155)”, CERN, Geneva, Switzerland, Rep. CERN-ACC-NOTE-2018-0005, Feb. 2018. <https://cds.cern.ch/record/2304603>
8. X. Buffat, S. V. Furuseth, G. Iadarola, P. S. Papadopoulou, Y. Papaphilippou, D. Pellegrini, M. Pojer, G. Crockford, B. M. Salvachua Ferrando, G. Trad, J. Barranco Garcia, T. Pieloni, and C. Tambasco, “Limitations due to strong head-on beam-beam interactions (MD1434)”, CERN, Geneva, Switzerland, Rep. CERN-ACC-NOTE-2017-0044, May 2017. <http://cds.cern.ch/record/2270590>
9. X. Buffat, N. Biancacci, S. V. Furuseth, D. Jacquet, E. Métral, D. Pellegrini, M. Pojer, G. Trad, D. Valuch, J. Barranco Garcia, T. Pieloni, C. Tambasco, and Q. Li, “Probing the behaviour of high brightness bunches in collision at 6.5 TeV and the interplay with an external source of noise (MD1433)”, CERN, Geneva, Switzerland, Rep. CERN-ACC-NOTE-2017-0030, May 2017. <https://cds.cern.ch/record/2261037>
10. S. V. Furuseth, “GPU-Powered Modelling of Nonlinear Effects due to Head-On Beam-Beam Interactions in High-Energy Hadron Colliders”, Specialization project report, Norwegian University of Science and Technology, Rep. CERN-ACC-2018-0008, Jan. 2017. <https://cds.cern.ch/record/2306183>

Theses

1. S. V. Furuseth, “Head-On Beam-Beam Interactions in High-Energy Hadron Colliders – GPU-Powered Modelling of Nonlinear Effects”, Masters thesis, Norwegian University of Science and Technology, Aug. 2017, CERN-THESIS-2017-279. <http://hdl.handle.net/11250/2460617>

Code Developments

1. S. V. Furuseth (2020), PyRADISE (Python RAdial Diffusion and Stability Evolution).
Source code: <https://gitlab.cern.ch/sfuruset/pyradise/>. (accessed: 9 Oct. 2020).
2. S. V. Furuseth, X. Buffat, T. Pieloni, W. Herr, and F. Jones (2019),
COMBIp (COherent Multi-Bunch Interactions - Pipelined).
Source code: <https://gitlab.cern.ch/sfuruset/combip/>. (accessed: 11 Jan. 2020).
3. S. V. Furuseth (2017), CABIN (Cuda-Accelerated Beam-beam Interaction).
Source code: <https://gitlab.cern.ch/sfuruset/CABIN/>. (accessed: 13 Aug. 2017).